Noble gas and CO₂ isotopic signatures of the lithospheric mantle underneath Mexico and the Canary Islands: clues from mantle xenoliths and arc lavas

IL DOTTORE
Andres Libardo Sandoval Velasquez

IL COORDINATORE
Prof. Marco Milazzo

IL TUTOR
Prof. Alessandro Aiuppa

I CO-TUTORS
Dr. Andrea Luca Rizzo
Prof.ssa Maria Luce Frezzotti

ACKNOWLEDGMENTS

ABSTRACT

Studying the isotopic composition of fluids trapped in mantle xenoliths opens avenues to understand the origin and cycling of volatiles in the Earth's upper mantle. In this PhD dissertation, new and in most cases the very first data regarding the isotopic (noble gases and CO_2) characterization of the lithospheric mantle portions of three different geodynamic environments are presented: (i) Central and NW Mexico, a continental setting dominated by extension; (ii) the Transmexican Volcanic Belt (TMVB) a subduction setting, and (iii) the Canary Islands, particularly El Hierro and Lanzarote, two oceanic islands formed by mantle plume-derived intraplate volcanism. In total 32 peridotites (including spinel lherzolites, spinel harzburgites, 1 pyroxenite and 1 dunite) and four arc lavas (from the TMVB) were investigated.

To characterize the isotopic signature of the Mexican lithospheric mantle, the present work was focused on the analysis of fluid inclusions entrapped in mantle xenoliths found in pyroclastic deposits of the Ventura Espiritu Santo Volcanic Field (VESVF), the Durango Volcanic Field (DVF), the San Quintin Volcanic Field (SQVF) (three Quaternary monogenetic volcanic fields formed in the Basin and Range extensional province). Fluid inclusions in olivine phenocrysts found in arc lavas from the Sierra Chichinautzin Volcanic Field (SCN) (a Quaternary monogenetic field located in the Transmexican Volcanic Belt (TMVB)) were also analyzed. According to the petrographic analysis, all xenoliths exhibit similar mineralogy (Ol> Opx> Cpx >> Sp). The VESVF xenoliths, in particular, bring textural evidence of interstitial glass veins bearing dendritic trails of secondary melt and fluid inclusions related to pervasive mantle metasomatism driven by carbonate-rich silicate melts. Inclusions are composed of silicate glass $\pm$ CO_2 $\pm$ Mg-Ca carbonates $\pm$ pyrite as indicated by Raman microspectroscopy. Excluding samples possibly affected by secondary processes, the averages Rc/Ra ratios ($^3He/^4He$ ratios corrected for atmospheric contamination) measured in Mexican localities are within the MORB-like range: VESVF = 7.39 $\pm$ 0.14 Ra (1σ, n = 30), DVF= 8.39 $\pm$ 0.24 Ra (1σ, n = 10), SQVF = 7.43 $\pm$ 0.19 Ra (1σ, n = 1) and SCN lavas = 7.24 $\pm$ 0.33 Ra (1σ, n = 4). This noble gas similarity between the VESVF and SCN samples supports the existence of a homogeneous mantle in central Mexico. The $^3He/^4He$ signatures observed in xenoliths suggest that (i) either the mantle He budget was scarcely modified by the Farallon plate subduction, and/or (ii) that any (large) crustal contribution was masked by a later metasomatism/refertilization episode, possibly driven by the upwelling mantle from the asthenosphere and the subsequent Basin and Range extension. The association between glass veins and fluid inclusions in VESVF xenoliths revealed that the metasomatism/ refertilization was driven by a silicate-rich melt which is consistent with a calculated helium residence time in the VESVF mantle (20 to 60 Ma) that overlaps the timing of the above geodynamic events. It is proposed that, after the refertilization event (e.g., over the last ~20 Ma), the lithospheric mantle has evolved in a steady-state, becoming slightly more radiogenic. The relative proximity between the DVF and the VESVF suggests a similar process should have happened beneath Durango, and that the difference in $^3He/^4He$ ratios with the VESVF is likely to be associated with different ages of mantle refertilization and He residence times (more recent for the DVF mantle; 4 to 10Ma). The Ar and Ne systematics reflect a mixing between MORB-like upper mantle and atmosphere-derived fluids. The mantle beneath the SQVF and the DVF seems to be more impacted by the interaction with atmospheric fluids, as proved by a systematic decrease in $^{40}Ar/^{36}Ar$ and $^4He/^{20}Ne$ ratios from central (VESVF) to western Mexico (DVF, SQVF) It is proposed that these atmospheric components were likely air-derived fluids recycled by the Farallon plate subduction. ^3He fluxes (0.027 - 0.080 mol/g), ^4He production rates (340 - 1000 mol/yr), and mantle CO_2 fluxes (3.93 x 10^7 mol/yr to 1.18 x 10^8 mol/yr) were also estimated using the helium isotopic

values measured in VESVF mantle xenoliths. Finally, DVF and VESVF nodules exhibit $CO_2/^3He$ ratios comparable to those of the upper mantle (from 3.38 x 10^8 to 3.82 x 10^9) but more positive $\delta^{13}C$ values (between -1.0 and -4.0‰), supporting the involvement of a recycled crustal carbonate component likely inherited by the Farallon plate subduction. Conversely, the SCN samples exhibit $\delta^{13}C$ values within the MORB range (comparable to other values previously reported in fluid inclusions and fumaroles from Popocatépetl, Colima and Ceboruco volcanoes) and unlike the mantle beneath VESVF-DVF, indicate a negligible mantle contamination by subduction-related crustal carbon.

The Canary Islands, in the central-eastern Atlantic, are among the most enigmatic Oceanic Island provinces on Earth, as the mantle source feeding their volcanism is spatially heterogeneous and with a multiplicity of involved components. Multi-isotope whole-rock studies have long revealed the presence of a recycled oceanic crust/lithosphere in the mantle. However, noble gas systematics have been more challenging to interpret, and carbon isotope data have remained sparse and incomplete. Our very first fluid inclusion data for El Hierro and Lanzarote nodules indicate carbon isotopic compositions of CO_2 ($\delta^{13}C$) range from –2.38 to –1.23‰ in pyroxenes and from –0.19 to +0.96‰ in olivines. These unusually positive $\delta^{13}C$ values, well above the typical upper mantle range (–8‰$<\delta^{13}C<$–4‰), prove, for the first time, the presence of a regional recycled crustal carbon component in mantle beneath the Canary Islands. We interpret this ^{13}C-rich component as inherited from a mantle metasomatism event(s) driven by fluids carrying carbon from subducted altered oceanic crust (AOC) and/or oceanic lithosphere (OL). Regarding noble gas isotopes, El Hierro xenoliths identify a depleted mantle source with MORB-like He signature. The average Rc/Ra ratio ($^3He/^4He$ normalised to air ratio and corrected for atmospheric contamination) of 7.45±0.26 Ra (2σ, n = 14) overall indicates a marginal role played by past subduction events in modifying the local mantle He budget. Instead, Lanzarote xenoliths point to a more radiogenic mantle with an average of 5.97±0.44 Ra (2σ, n = 13) which we interpret as reflecting the involvement of an EM component. When put in the context of previous $^3He/^4He$ measurements in fluid inclusions and surface gases along the Canary archipelago, these results confirm an overall west-to-east decrease of Rc/Ra ratios (from El Hierro to Lanzarote), which may reflect a combination of i) increasing contributions of the African continental lithosphere, ii) the addition of radiogenic ^4He during magma migration in the oceanic crust (whose thickness increases eastward) and/or iii) magma ageing. Finally, as proposed for Mexico, the involvement of depleted mantle-like fluids, variably admixed with air-derived components (possibly recycled via paleo-subduction event(s)), is corroborated by Ne-Ar isotopic compositions.

TABLE OF CONTENTS

TABLE OF FIGURES

TABLES

contents in fluid inclusions during noble gas analysis; [B] CO_2 contents and $CO_2/^3He$ ratios measured from the glass line after CO_2 isotopic determinations. Reported errors are 2σ uncertainties.

CHAPTER 1. INTRODUCTION

Subduction, mantle convection and volcanism are the main geological processes that govern the exchange of major volatiles between the mantle and the Earth's surface (Hier-Majumder and Hirschmann, 2017; Oppenheimer et al., 2014; Aiuppa et al., 2017, 2019; Plank and Manning, 2019; Regier et al., 2020; Bekaert et al., 2021). Such exchange affects the chemistry of the Earth's interior and governs the composition of the atmosphere/hydrosphere with implications for the evolution of life. Carbon, hydrogen (as water) and sulfur play a key role in building a habitable climate in the Earth, and small changes in their fluxes (through volcanic emissions) can produce critical impacts in the atmosphere over timescales of millions of years (Robock, 2000; Oppenheimer et al., 2014; Plank and Manning, 2019). Noble gases, on the other hand, do not have the same impact on climate, however, their relatively low concentrations in the atmosphere (especially helium) facilitate the acquisition of essential information about mantle degassing and the origin of Earth's volatiles (Burnard et al., 1997; Dunai and Porcelli, 2002; Gautheron and Moreira, 2002; Graham, 2002; Burnard, 2013; Moreira, 2013; Moreira and Kurz, 2013; Mukhopadhyay and Parai, 2019; Avice and Marty, 2020)

Volatiles can be measured in volcanic emissions or fluid inclusions trapped in volcanic materials or mantle-derived rocks. For instance, the study of the isotopic composition of fluids trapped in mantle rocks (e.g., Deines, 2002; Gautheron and Moreira, 2002; Pearson et al., 2014; Day et al., 2015) can shed light into mantle characteristics and evolution over time, as they provide clues on the cycling of volatiles in Earth's interior (e.g., Vance et al., 1989; Deines, 1992, 2002; von Gehlen, 1992; Williams and Hemley, 2001; Matsumoto et al., 2001; Dunai and Porcelli, 2002; Gautheron and Moreira, 2002; Li et al., 2008; Dasgupta and Hirschmann, 2010; Marty, 2011, 2012; Hauri et al., 2019; Regier et al., 2020). Volatiles in the mantle may exist as free elements or molecules along grain boundaries, fluid inclusions or species dispersed in mineral structures (Zhang et al., 2009). Sulfur usually occurs as sulfides (e.g., pyrrhotite; Bishop et al., 1975; von Gehlen, 1992; Guo et al., 1999; Giuliani et al., 2016); carbon has been identified in fluid inclusions as pure CO_2, CO, CH_4 and COS, forming solid phases such as graphite, diamond, carbonates, moissanite, carbonatitic melts or forming solid solutions in silicates (Murck et al., 1978; Bergman and Dubessy, 1984; Roedder, 1984; Deines, 1992, 2002; McDonough and Rudnick, 1998; Dasgupta and Hirschmann, 2010; Frezzotti and Touret, 2014; Hauri et al., 2019; Stagno, 2019; Regier et al., 2020); hydrogen is generally stored in the mantle as water in hydrous minerals (e.g., phlogopite) or as defects in anhydrous phases (Bell and Rossman, 1992; Ingrin and Skogby, 2000; Williams and Hemley, 2001); while nobles gases are usually found in fluid inclusions (e.g., Dunai and Baur, 1995; Dunai and Porcelli, 2002; Gautheron and Moreira, 2002; Gautheron et al., 2005a; Nuccio et al., 2008; Correale et al., 2015, 2016, 2019; Rizzo et al., 2018). Noble gases and carbon in mantle xenoliths, in particular, are proven tools for constraining the relative mixing proportions among different mantle reservoirs (e.g., Gurenko et al., 2006; Day and Hilton, 2011, 2021; Broadley et al., 2016; Rizzo et al., 2018; Kobayashi et al., 2019), and are key species for understanding carbon recycling in the lithospheric as well as in the deeper mantle via subduction of crustal carbon components (e.g., organic matter and sedimentary carbonate) (Dasgupta and Hirschmann, 2010; Aiuppa et al., 2017; Duncan and Dasgupta, 2017; Li et al., 2019; Plank and Manning, 2019; Bekaert et al., 2021). However, despite recent advances in the field, many questions remain yet unsolved, as mantle-derived rocks found on the Earth's surface represent a minimum portion of the mantle and the isotopic studies in fluid inclusions, particularly regarding carbon, are still limited to a relatively small number of localities.

This project arises from the need to increase our knowledge about the nature of volatile species trapped in ultramafic mantle rocks. For this purpose, two different geodynamic settings with mantle xenoliths were selected: 1) the central and northwestern Mexico and 2) the Canary Islands. The studied Mexican xenoliths come from alkaline monogenetic volcanic fields distributed along the central and northwestern portion of the country. This volcanism is closely related to the Basin and Range Province, which is the result of intense periods of continental extension likely driven by the cessation of the Farallon subduction ~30 Ma ago (Sedlock, 2003). It is believed that the thinning of the continental lithosphere favored the decompression and melting of the upper mantle (Nieto-Samaniego et al., 1999). The resulting magmas would have produced the above-mentioned monogenetic complexes bringing with them considerably amounts of mantle xenoliths. These now open a window to analyze different sections of the local lithospheric mantle (Luhr and Aranda-Gomez, 1997 and references therein). Like Mexico, volcanism in the Canary Islands has brought to the surface important quantities of ultramafic nodules, which reflect the compositional heterogeneity of the mantle source; here, I analyzed xenoliths collected in two different islands: El Hierro and Lanzarote. Several studies performed in volcanic materials and xenoliths have demonstrated that the local mantle beneath the Canaries is the result of mixing between different components including a general MORB signature mixed with a mantle plume component identified in geothermal samples from La Palma; a HIMU component recognized in the western islands (El Hierro, La Palma and La Gomera), likely derived from paleo-subduction episodes; and an Enriched mantle (EM) component in the eastern portion of the archipelago (Tenerife, Gran Canaria, Fuerteventura and Lanzarote), possibly inherited from the African Sub-Continental Lithospheric Mantle (SCLM) (Hoernle et al., 1991; Gurenko et al., 2006; Day et al., 2010; Day and Hilton, 2011, 2020).

In this doctoral dissertation, new data on the composition of noble gases and CO_2 in mantle xenoliths are reported. This new information was integrated with information on petrography, mineral chemistry and fluid inclusions' compositions from the same suite of samples. The aim is to deepen the knowledge on the characteristics and the evolution of the local lithospheric mantle in distinct geodynamic environments, as well as the occurrence of partial melting, mantle metasomatism and/or refertilization events. Another important aspect of this study regards the involvement of mantle plumes for explaining the recent magmatism, and the recycling into the mantle of noble gases and carbon related to recent or fossil subduction(s).

Chapter 2 offers a brief overview about the study of the mantle xenoliths, fluid inclusions and noble gas and carbon isotopes. Chapter 3 discusses the methodology and the analytical procedures used to analyse mantle xenoliths. Chapter 4 presents an overview of the geodynamic setting and tectonic history of the study areas. Chapters 5 and 6 discuss the noble gas and CO_2 composition of the central and northwestern Mexican lithospheric mantle based on the study of fluid inclusions trapped in mantle xenoliths collected from the Ventura Espiritu Santo (VESVF), Durango (DVF) and San Quintin (SQVF) volcanic fields. These are monogenetic volcanic complexes recognized as three of the most important mantle xenolith-bearing alkali basalt localities emplaced along the Mexican Basin and Range Province. In chapter 5, isotopic studies are coupled with petrological analysis (petrography and Raman microspectroscopy) in order to accurately determine the origin and evolution of the fluids that may have interacted with these xenoliths. The information obtained from fluid inclusions suggest a very complex history in which the lithospheric mantle composition has been modified by partial melting and metasomatism/refertilization events driven by old subduction processes and the tectonic reorganization of the western continental margin of North America during the Mesozoic and early Cenozoic. Chapter 7 explores the composition of volatiles trapped in olivine phenocrysts collected from the Sierra Chichinautzin (SCN), a Quaternary monogenetic volcanic field located in the central part of the Trans-Mexican Volcanic Belt (TMVB). The objective

of this chapter is to investigate the isotopic signature of the mantle wedge located beneath the TMVB, the effect of subduction processes in the noble gases and carbon abundances, and the main differences regarding the lithospheric mantle sampled in the Ventura Espiritu Santo, Durango and San Quintin volcanic fields.

Finally, chapters 8 and 9 report the first isotopic results for CO_2 and noble gas in mantle xenoliths collected from El Hierro and Lanzarote (Canary Islands). In these chapters, the CO_2 carbon isotopic compositions of El Hierro xenoliths prove the existence of a recycled crustal carbon component in the local source mantle. This component would reflect the infiltration of metasomatic fluids likely derived from subducted altered oceanic crust (AOC) and/or oceanic lithosphere (OL) materials. Integrating the evidence of volcanic gases and erupted rocks, noble gas compositions in fluid inclusions constrain a MORB-like signature of the mantle beneath El Hierro and indicates a more radiogenic nature for the Lanzarote mantle. A careful review of $^{3}He/^{4}He$ data available for the Canary Islands is also undertaken and offers new insights to interpret the west-to-east isotopic variation over the archipelago.

CHAPTER 2. STATE OF THE ART

The following presents a brief review about the study of mantle xenoliths, the isotopic study of noble gases and CO_2 in fluid inclusions and the structure of the thesis.

2.1. A brief review on the study of mantle xenoliths

The chemistry of the upper mantle is accessible to direct examination from analysis of mantle rocks exposed to the Earth's surface; these rocks are commonly found in peridotite massifs, in ophiolitic complexes, as xenoliths hosted in alkali-basalt- kimberlitic-lamproitic lavas or hosted in arc lavas related to subduction zones such as Kamchatka or the Philippines (Jackson, 1998; Hopp and Ionov, 2011; Pearson et al., 2014; Payot et al., 2018). Although peridotite massifs and ophiolites provide an excellent opportunity to study not only the geochemical signature of mantle rocks but also field relationships, their relative long journey to the surface may have led to modifications of the original mineralogy and chemical composition (Jackson, 1998). Conversely, even hough mantle xenoliths may be susceptible to interaction by their host melts, these are expected to retain the pristine mineralogy and geochemical/isotopic characteristics of the source due to their relative rapid ascent through the crust. Besides, one of the major advantages of mantle xenoliths, despite their small size, is their huge spatial distribution across the globe (Fig. 1); these rocks have been found in a great diversity of geodynamic environments including continental and oceanic rift, subduction and hotspots (Rodgers et al., 1975; Nixon et al., 1981; Vance et al., 1989; Arai, 1994; Downes, 1997; Luhr and Aranda-Gomez, 1997; Coltorti et al., 2000, 2010; Conceição et al., 2005; Arai et al., 2007; Arai and Ishimaru, 2008; Li et al., 2008; Nasir and Rollinson, 2009; Aldanmaz, 2012; Hopp et al., 2004; Jackson et al., 2016; Alemayehu et al., 2017; Payot et al., 2018; Snortum et al., 2019; Ionov et al., 2020; Martin et al., 2021; Mazzeo et al., 2021).

Different approaches have been employed to investigate the composition of mantle xenoliths: petrography, bulk and mineral chemistry, thermobarometry, radiogenic and stable isotope geochemistry and fluid-melt inclusion analysis. A key result of published work is that the mantle is far from being an homogeneous reservoir (Roden and Murthy, 1985; McDonough and Frey, 1989; Nadeau et al., 1990; Arai, 1994; Downes, 1997; Luhr and Aranda-Gomez, 1997; Jackson, 1998; McDonough and Rudnick, 1998; Coltorti et al., 2010; Deines, 2002; Dunai and Porcelli, 2002; Gautheron and Moreira, 2002; Gautheron et al., 2005a; Conceição et al., 2005; Arai et al., 2007; Einstein, 2007; Davies, 2011; O'Reilly and Griffin, 2013; Pearson et al., 2014; Day et al., 2015; Day and Hilton, 2020). For instance, petrological studies in mantle xenoliths suggest that the upper mantle composition is continuously modified by the effect of metasomatic and partial melting episodes (Roden and Murthy, 1985; Coltorti et al., 2000; Konzett et al., 2000; Andersen and Neumann, 2001; Frezzotti et al., 2002a, 2009; Conceição et al., 2005; O'Reilly and Griffin, 2013; Frezzotti and Touret, 2014; Kiseeva et al., 2017; McDonough and Frey, 1989; McDonough and Rudnick, 1998; Safonov et al., 2019). Such episodes are driven by the action of fluids or melts that pervade and react with the mantle, forming new minerals and/or changing its chemistry, masking previous information related to melt extraction. These fluids may come from the asthenospheric or lower mantle (plumes), the interaction with recycled SCLM (EM) or derived from the recycling of material related to subducted slabs (Jackson, 1998; Dunai and Porcelli, 2002; O'Reilly and Griffin, 2013; Howarth et al., 2014; Frezzotti and Ferrando, 2015; Kiseeva et al., 2017). Metasomatic fluids recognized in mantle xenoliths are carbonate-rich melts, silicate melts, alkali-silica rich fluids or simply H_2O/CO_2-rich fluids (Frezzotti et al., 2002b and references therein).
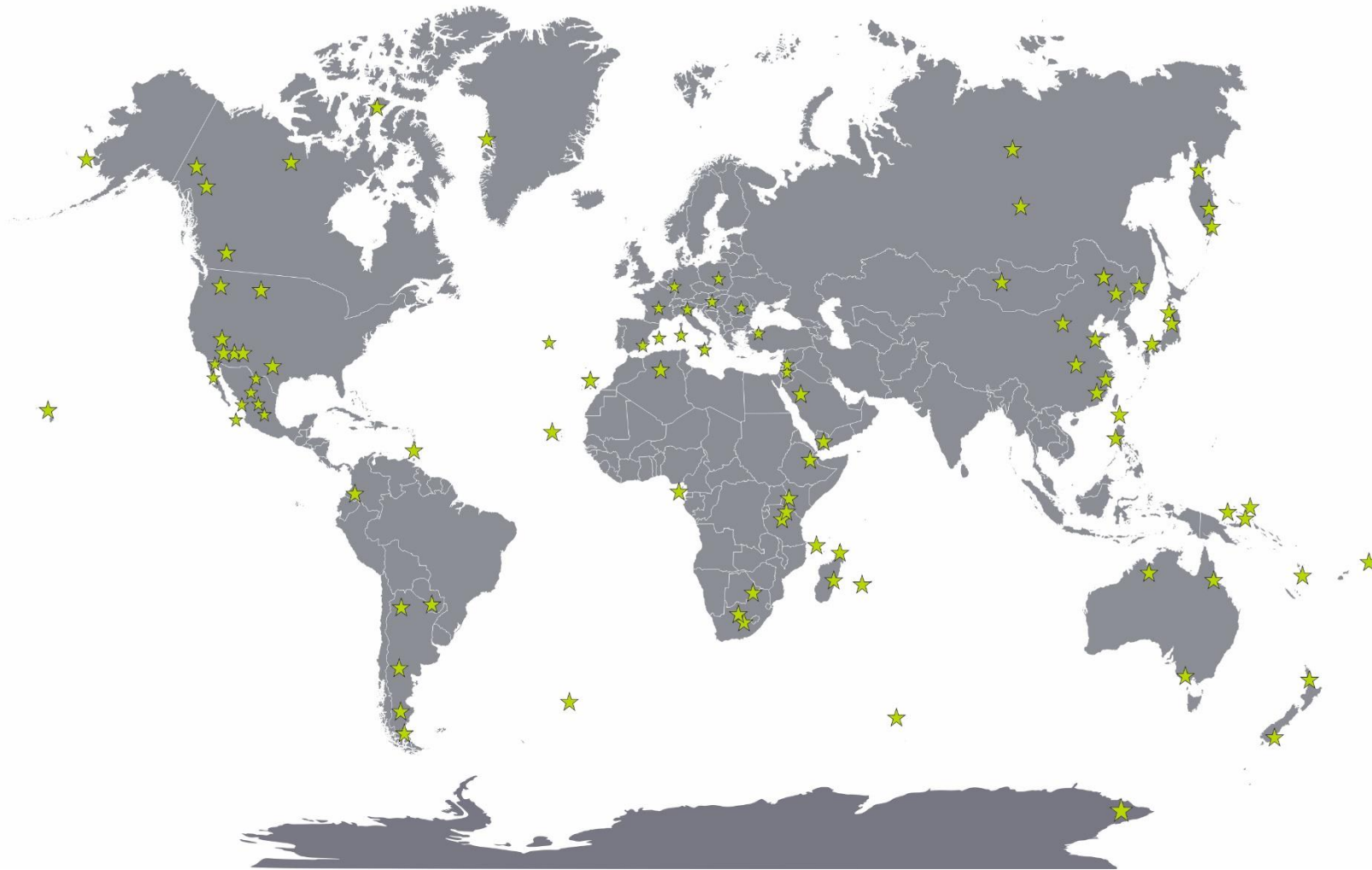
Figure 1. This map was designed based on the data reported in the literature: Vance et al. (1989), Nadeau et al. (1990), Pineau and Mathez (1990), Porcelli et al. (1992), Stern et al. (1999), Gautheron and Moreira (2002), Witt-Eickschen (2003), Hopp et al. (2004, 2007a, 2007b), Bonadiman et al. (2005), Buikin et al. (2005), Gautheron et al. (2005a), Czuppon et al. (2009), Karmalkar et al. (2009), Comin-Chiaramonti et al. (2010), Martelli et al. (2011), Correale et al. (2012, 2015, 2016, 2019), Halldórsson et al. (2014), Pearson et al. (2014), Broadley et al. (2016), Rizzo et al. (2018) and Faccini et al. (2020).

Xenoliths usually contain melt/fluid inclusions, which represent remnants of mantle melting or metasomatism; it is therefore not surprising that these are considered as valuable sources of information about the nature of fluids and the evolution of volatiles in the Earth's mantle (e.g., Andersen and Neumann, 2001; Deines, 2002; Dunai and Porcelli, 2002; Frezzotti et al., 2002a; Correale et al., 2016, 2019; Rizzo et al., 2018; Faccini et al., 2020). Scientists have developed different techniques to analyze the chemical and isotopic composition of inclusions, including non-destructive and destructive methods (Roedder, 1984). Some nondestructive methods include fluid inclusion petrography, microthermometry and Raman microspectroscopy (Roedder, 1984; Andersen and Neumann, 2001; Frezzotti et al., 2012a), while destructive methods include melting or crushing techniques that are usually employed to analyze volatile species (e.g., Deines, 2002; Graham, 2002; Burnard, 2013; Gennaro et al., 2017; Rizzo et al., 2018). Thanks to the development of these methods, today we know that fluid inclusions in mantle xenoliths exhibit a large compositional spectrum: although fluid inclusions are generally dominated by CO_2, silicate and sulphide melts, these can also contain carbonates, nitrogen, water, methane, carbon monoxide, sulphur species and noble gases (Roedder, 1984; Andersen and Neumann, 2001).

2.1.1. Mineralogy and classification of mantle xenoliths

Recently, mantle xenoliths have been classified based on tectonic setting (Pearson et al., 2014) in cratonic/circumcratonic xenoliths and non-cratonic xenoliths.

As their name implies, cratonic and circum-cratonic xenoliths are exposed on cratonic areas and are commonly associated with Kimberlite-related volcanics (Pearson et al., 2003; Kopylova and Caro, 2004; Simon et al., 2007; Ionov et al., 2010b); some examples are the kimberlites recognized in the Kaapvaal craton (Africa), Siberia craton, the Slave craton (Canada) and the Colorado-Wyoming craton (USA). An exception are the ultramafic nodules found in Cenozoic basalts erupted on the Yangtze and the North China cratons (Lu et al., 2013; Tang et al., 2014; Correale et al., 2016; Dai and Zheng, 2019). Xenoliths found in these areas predominantly belong to the spinel and garnet facies (Pearson et al., 2014) including harzburgites, garnet lherzolites (equilibrated above 2.5 GPa; Nicolas, 1986), garnet websterites, pyroxenites, dunites, phlogopite-rich mafic mantle xenoliths, eclogites, grospydes, alkremites and ultra-deep peridotites. Conversely, non-cratonic xenoliths are erupted by alkalic and potassic magmas in areas that have been affected by lithospheric thinning (Pearson et al., 2014). For instance, western Mexico and USA (Luhr and Aranda-Gomez, 1997; Li et al., 2008), Victoria (SE Australia; Yaxley et al., 1997), South America (Stern et al., 1999), Europe and the circum-Mediterranean area (Gautheron and Moreira, 2002; Gautheron et al., 2005a; Buikin et al., 2005; Martelli et al., 2011; Correale et al., 2012; Rizzo et al., 2018, 2021; Faccini et al., 2020), the Red Sea region (Hopp et al., 2004), the East African Rift system (Hopp et al., 2007b; Halldórsson et al., 2014) and the West Antarctic Rift System (WARS; Zipfel and Wörner, 1992; Day et al., 2019). Spinel lherzolites and harzburgites are the dominant xenoliths in alkali basalts erupted in continental and oceanic settings (Nicolas, 1986); other types of peridotites such as wehrlites, clinopyroxenites, dunites, websterites, lherzolites, gabbros, and garnet clinopyroxenites-websterites have been also found in non-cratonic settings.

Mantle xenoliths mainly consist of olivine, orthopyroxene and clinopyroxene with small quantities of spinel, garnet, mica (phlogopite) and in rare cases plagioclase (Mercier and Nicolas, 1975; Nicolas, 1986; Pearson et al., 2014). Although other minerals such as ilmenite, amphibole (pargasites, kaersutites and K-richterittes), apatite, monazite and zircon may be present, these are interpreted to result from secondary processes (such as metasomatism) that have modified the original composition of the mantle (e.g., Konzett et al., 2000; Kaczmarek et al., 2016; Dávalos-Elizondo et al., 2016; Safonov et al., 2019). Olivine is the most abundant mineral phase in mantle

xenoliths (>40%) and is considered the major host for Mg, Fe and Ni in these rocks (Pearson et al., 2014). The Mg# of olivines varies between 88 and 94 and is commonly used as a proxy of melt depletion or enrichment in iron produced by partial melting or metasomatic episodes. Orthopyroxenes (Opx) in mantle xenoliths generally are enstatites with Mg# similar to or higher than olivines. In spinel and garnet facies, Opx usually exhibit Al_2O_3 and CaO contents between 1 and 6 wt% and from 0.2 to 2wt%, respectively, and depend on different factors such as temperature and pressure of equilibrium of the sample, degree of partial melting and the effect of metasomatism or refertilization processes (McDonough and Rudnick, 1998; Coltorti et al., 2000; Dawson, 2002; Pearson et al., 2003; Shaw et al., 2005). Clinopyroxenes commonly exhibit a Mg# higher than olivines and are considered important host for Na, Cr and Ti in mantle xenoliths (Pearson et al., 2014). The Na_2O in clinopyroxenes varies between 0.2 and 3wt% while Al_2O_3 generally varies between 1 and 7 wt%. Xenoliths generally exhibit <2% of spinel and its Fe, Mg, Cr and Al concentrations give sensitive information about the degree of depletion of the xenolith and temperature/pressure of equilibration (Nicolas, 1986; Pearson et al., 2014). Similarly, garnet in mantle xenoliths usually are Cr-pyrope and can be use as barometer or as indicator of depletion of the host xenolith (Griffin et al., 1999).

2.1.2. Bulk geochemistry and radiogenic isotopes

Mean abundances of SiO_2, Mg# and Al_2O_3 measured in mantle xenoliths from both cratonic and non-cratonic areas show interesting trends (Fig. 2). Although no systematic variation is observed when studying the SiO_2 abundances in mantle xenoliths (SiO_2 concentrations vary in a narrow range from 41 to 47 wt%), major differences are observed in Mg# and Al_2O_3 contents. Al_2O_3 and Mg# are commonly used as depletion index in mantle-derived rocks (Pearson et al., 2014; Harvey et al., 2015; Ionov et al., 2020; Faccini et al., 2020); for example, the low Al_2O_3 observed in xenoliths from cratons and ocean settings, combined with high Mg# (in the case of cratonic xenoliths), reflect a high levels of depletion if compared with non-cratonic continental settings (Fig. 2B). It is worth noting that indicators such as Mg# may be compromised by the effect of metasomatism/refertilization processes or superficial weathering which may lead to misinterpretations about the mantle composition (O'Reilly and Griffin, 2013). Aluminium/Si and Mg/Si relationships are also recognized as good parameters to evaluate the depleted nature of mantle xenoliths. Fig. 3 shows a negative correlation between Al/Si and Mg/Si ratios measured in several nodules collected from around the globe. According to Pearson et al. (2014) this array reflects the residual character of mantle xenoliths; when pressure decreases (along the peridotite solidus), mineral phases such as pyroxenes and spinel become instable and start to melt, these reactions produce olivine and liquid, and the mantle becomes progressively depleted in Si-Al and enriched in Mg. The intersection between the xenoliths field and the chondritic array (at Mg/Si ≈ 1 and Al/Si =0.1 – 0.12) has been interpreted as the primitive upper mantle composition, i.e., the bulk composition of the silicate Earth (Pearson et al., 2014 and references therein).

Like Mg#, the trace element abundances may be compromised by the effect of secondary processes such as metasomatism, infiltration of the host magma or chemical weathering (McDonough and Frey, 1989; McDonough and Rudnick, 1998; Coltorti et al., 2000; Pearson et al., 2014). For instance, the existence of glass veins, which is a common characteristic in most xenoliths, is usually interpreted as the result of interaction with metasomatic agents that could modify the original trace-element budgets (McDonough and Frey, 1989; Coltorti et al., 2000). Coltorti et al. (2000) described three different types of metasomatized glasses found in mantle xenoliths sampled in several localities around the globe (Fig. 4A): (i) carbonatite-related glasses that show the highest CaO and Na_2O abundances, (ii) K-alkali silicate glasses that exhibit the highest TiO_2 and K_2O contents, and

(iii) Na-alkali silicate glasses with intermediate compositions. In terms of trace elements, it is also possible to make a similar distinction between carbonatite-related and N/K glasses when comparing Zr, Sm, Ti and Eu normalized abundances (Fig. 4B).
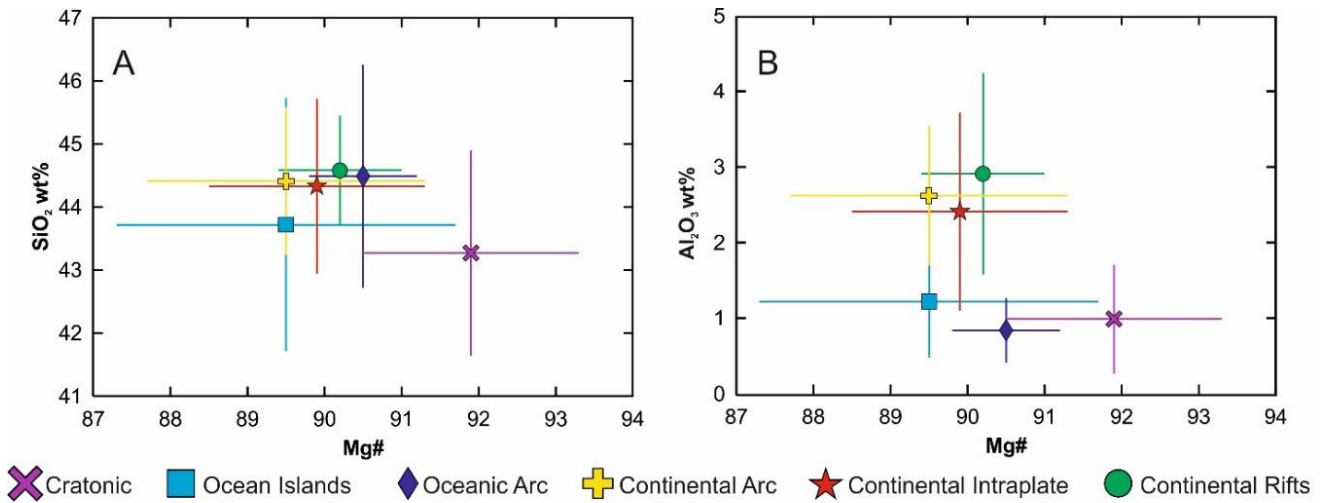
Figure 2. A) Mg# vs SiO$_2$ and B) Mg# vs Al$_2$O$_3$ abundances in mantle xenoliths from different tectonic settings. Plotted values are averages from Pearson et al. (2014). Plotted uncertainties are 1σ.
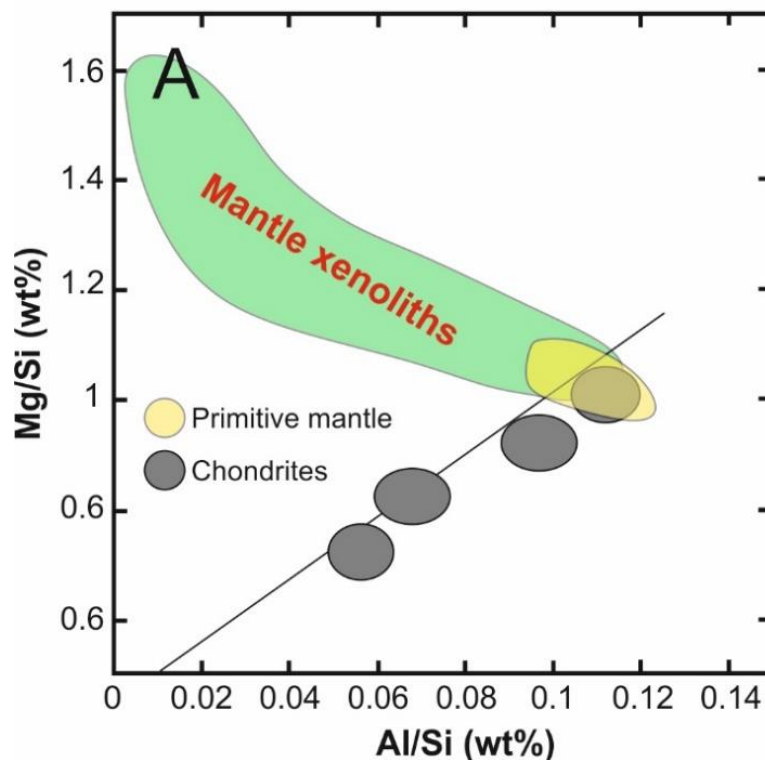
Figure 3. Al/Si vs Mg/Si abundances after whole rock analysis in mantle xenoliths. From Pearson et al. (2014).

While it is certainly possible that most of xenoliths may have suffered important chemical variations, some trace elements have proved to be particularly useful; in fact, Ni, Co and Sc often show good correlations with Al$_2$O$_3$ and MgO that make them excellent tracers of xenoliths depletion (Pearson et al., 2014). Some studies have also demonstrated the close relationship between V abundances and the variability of oxygen fugacity (fO$_2$) during partial melting episodes (e.g., Canil, 2002); this

characteristic makes V a potential proxy for paleo-redox conditions at the time of lithosphere formation. As for REE (Rare-Earth Elements) abundances, mantle xenoliths (both spinel and garnet-rich peridotites) display a great variability (McDonough and Frey, 1989; McDonough and Rudnick, 1998): xenoliths with CaO and Al_2O_3 contents >2 wt% usually show both enriched and depleted LREE patterns while xenoliths with CaO and Al_2O_3 contents <2 wt% generally are enriched in LREE relative to chondrite (Fig. 5A-B-C).
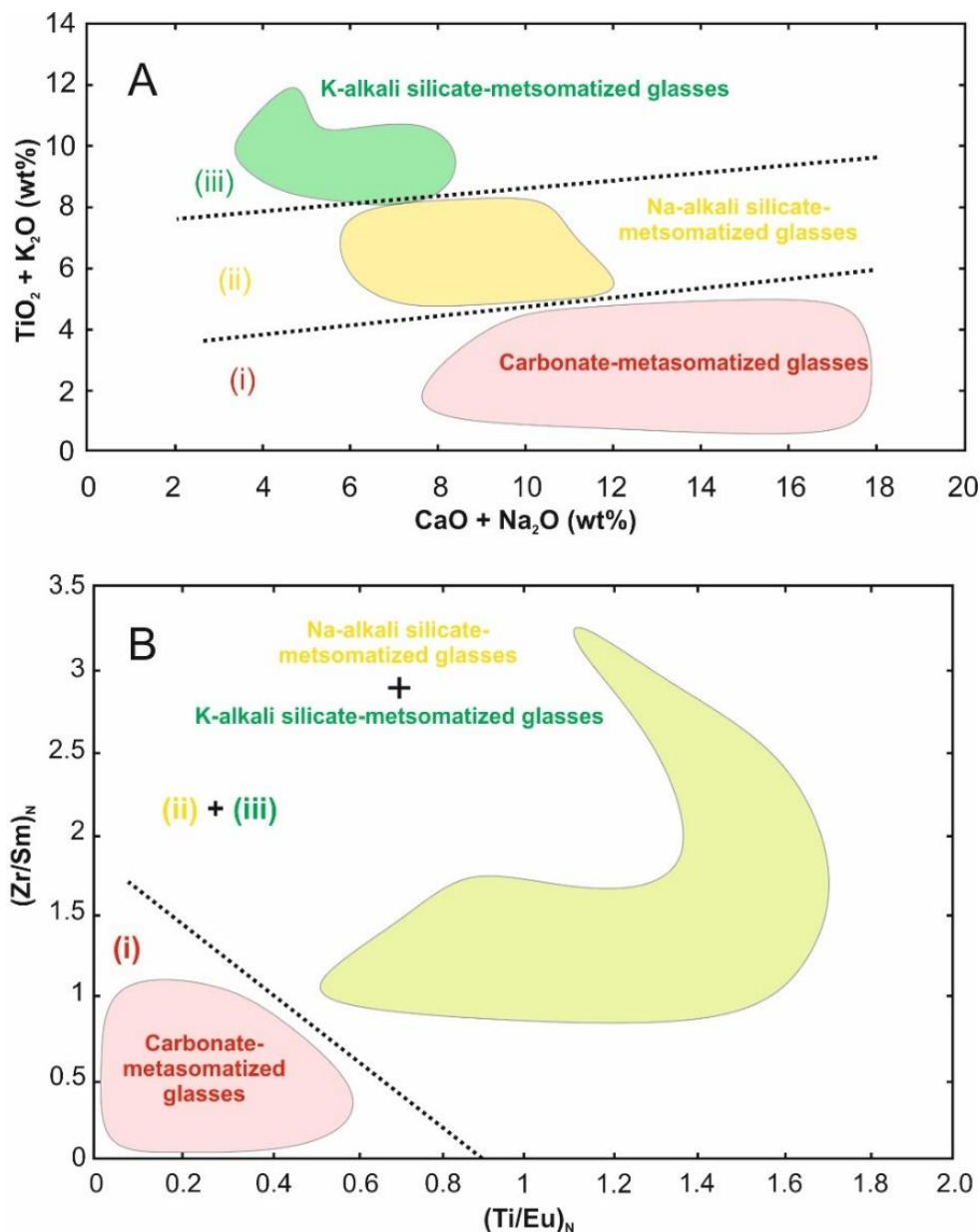
Figure 4. A) CaO, Na_2O, TiO_2 and K_2O abundances, and B) $(Ti/Eu)_N$ vs $(Zr/Sm)_N$ ratios measured in mantle glasses associated with metasomatism (values were normalized after Sun and McDonough, 1989). From Coltorti et al. (2000).

The paradox between the depletion in whole-rock major and compatible trace elements (e.g., CaO, Al_2O_3, Ni, Co and V) and the enrichment in incompatible elements (e.g., LREE, Sr, K) observed in different geodynamic settings is usually justified by a complex history, which includes different partial melting events followed by re-enrichment processes driven by the infiltration of incompatible element-rich melts (McDonough and Frey, 1989; Pearson et al., 2014). Mineral chemistry analysis have shown that Opx are typically LREE-depleted which is usually associated with partial melting (Fig. 5D); conversely, Cpx is more prone to be modified and generally exhibit enriched LREE patterns (Fig. 5E) due to silicate and/or carbonatite metasomatism (e.g., Coltorti et al., 1999; Ionov,

2002a; Bodinier, 2004; Touron et al., 2008; Ackerman et al., 2013; le Roex and Class, 2016; Touron et al., 2008). Garnets in mantle xenoliths may display two different REE patterns (Fig. 5F; Griffin et al., 1999; Gregoire, 2003; Pearson et al., 2014; le Roex and Class, 2016): (i) a normal pattern observed in melt residues defined by low LREE and high MREE and HREE, and (ii) a sinusoidal REE pattern (which is less LREE depleted and less HREE enriched) commonly linked to metasomatism.
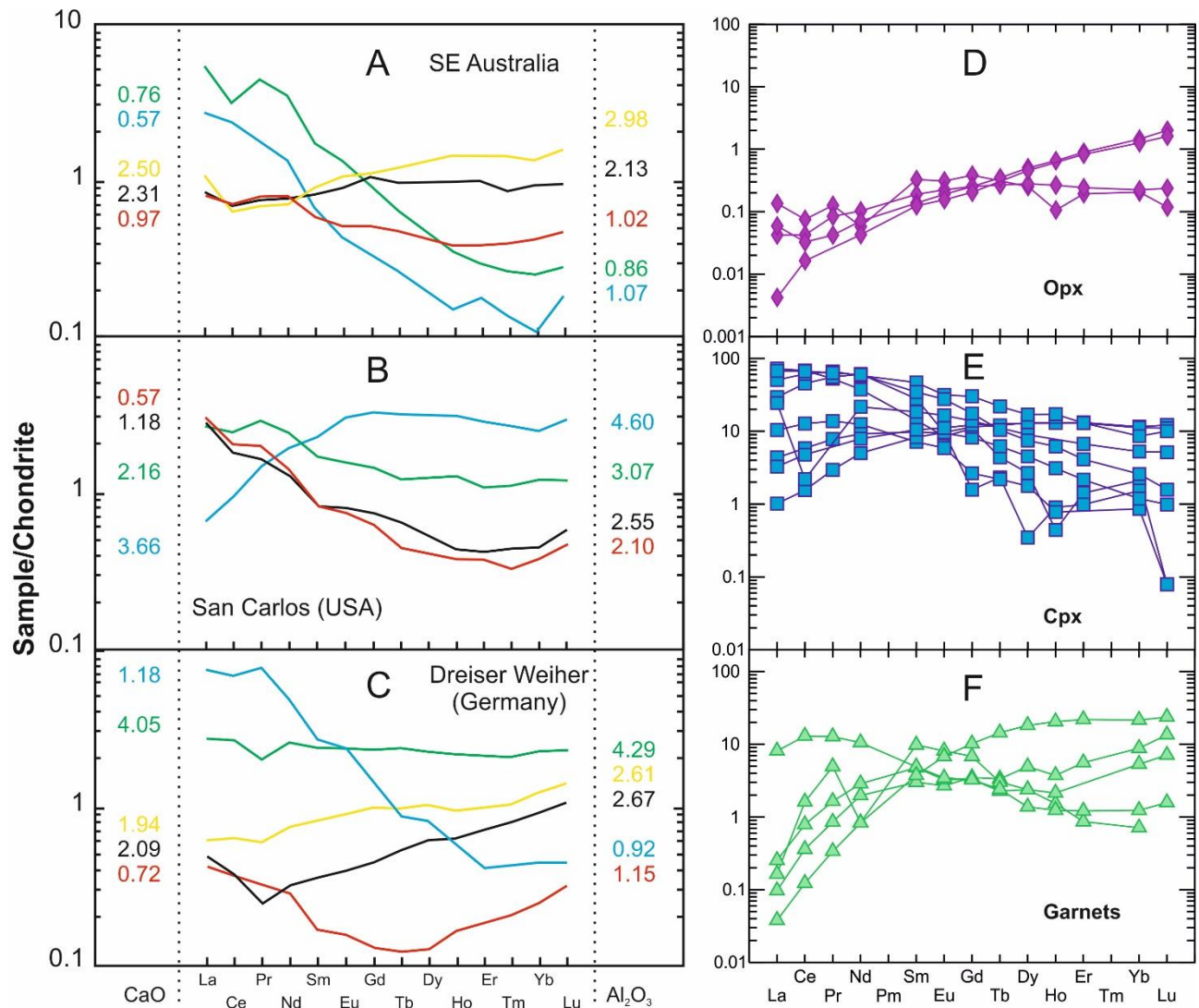
Figure 5. A, B, C: Whole-rock abundances of CaO, Al$_2$O$_3$ and REE in mantle xenoliths, from McDonough and Frey (1989). D, E, F: REE patterns obtained for Opx, Cpx and garnets in mantle xenoliths from cratonic and non-cratonic areas, data from Pearson et al. (2014).

The Sr-Nd-Pb-Os isotopic systematics of mantle xenoliths also demonstrate wide heterogeneity (Figs. 6 and 7). As shown in Fig. 6, cratonic samples display a greater variation than non-cratonic xenoliths. Cratonic samples show ^{87}Sr/^{86}Sr and ^{143}Nd/^{144}Nd ratios similar to those observed in continental rocks while non-cratonic samples exhibit a narrow field concurring with the oceanic mantle range (Fig. 6A). When comparing ^{206}Pb/^{204}Pb and ^{87}Sr/^{86}Sr ratios, cratonic xenoliths exhibit ^{87}Sr/^{86}Sr ratios even higher (>0.73; Fig. 6B) and their variability may be explained using three geochemically different mantle components as proposed by Zindler and Hart (1986): a HIMU component with high ^{206}Pb/^{204}Pb (>21) and relative low ^{87}Sr/^{86}Sr and two Enriched Mantle components (EM-I and EM-II) whose origin has been attributed to mantle metasomatism, subducted continental/oceanic crust and/or delamination of the subcontinental lithosphere (Cohen

and O'Nions, 1982; White and Hofmann, 1982; McKenzie and O'Nions, 1983; Zindler and Hart, 1986); the main difference between the two EM components is the relative high $^{87}Sr/^{86}Sr$ of EM-II at a given $^{206}Pb/^{204}Pb$ ratio which not only has been identified in mantle xenoliths but also in OIB and MORB (Zindler and Hart, 1986; Jackson and Dasgupta, 2008). The great variation of cratonic xenoliths relative to non-cratonic ones is generally explained by the antiquity of cratonic SCLM and the effect of different events of melt extraction and metasomatism (Pearson et al., 2014). The addition of agents such as silicate melts, H_2O-rich or carbonatite fluids derived from paleo-subduction events have been evoked to explain the variability of radiogenic isotopes in mantle xenoliths (e.g., Ionov, 2002b; Witt-Eickschen, 2003; Demény et al., 2004; Wu et al., 2017). A summary of the Sr-Nd-Pb-Os isotopic signatures measured in mantle xenoliths from cratonic and non-cratonic areas is presented in Fig. 7.
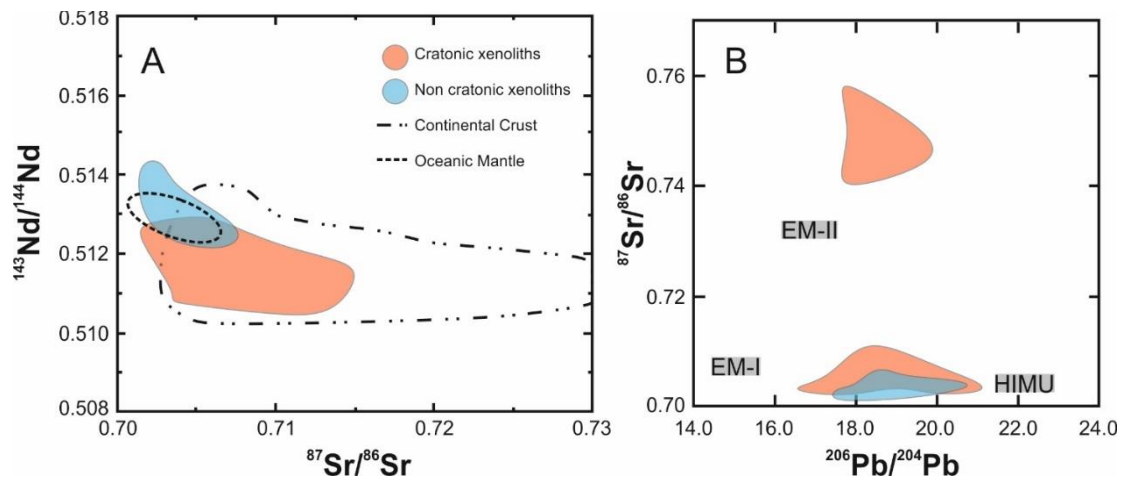
Figure 6. Strontium-Nd-Pb systematics measured in cratonic and non-cratonic mantle xenoliths. From Pearson et al. (2014).

Figure 7. Summary of the main radiogenic isotopes and Mg# measured in cratonic and non-cratonic mantle xenoliths. Modified from Pearson et al. (2014).

2.1.3. Noble gases and CO₂ isotopes in fluid inclusions

Several studies on noble gases have proved their utility as geodynamic tracers to comprehend the degassing history of the mantle, the origin of Earth's volatiles and the relationship between different mantle components (Burnard et al., 1997; Dunai and Porcelli, 2002; Gautheron and Moreira, 2002; Graham, 2002; Burnard, 2013; Moreira and Kurz, 2013; Mukhopadhyay and Parai, 2019).

Noble gases measured in ultramafic xenoliths, lavas and volcanic gases across the globe suggest the existence of at least three main volatile reservoirs in the mantle (Burnard et al., 1997; Dunai and Porcelli, 2002; Graham, 2002; Yang et al., 2009; Moreira and Kurz, 2013): (i) a less degassed lower mantle reservoir sampled in hotspots settings such as Hawaii, Iceland, la Réunion and Galapagos; (ii) a more degassed MORB-like upper mantle reservoir; and (iii) the Subcontinental Lithospheric Mantle (SCLM). In terms of helium isotopes, a lower mantle component is represented by high R/Ra ratios >9 Ra (where R is the $^3He/^4He$ ratio measured in the sample and Ra the atmospheric $^3He/^4He$ ratio equal to 1.384×10^{-6}; Clarke et al., 1976) while the MORB-like upper mantle reservoir generally display a relative low and narrow range of R/Ra values of between 7 and 9 Ra (Burnard et al., 1997; Graham, 2002; Ozima and Podosek, 2002);.

The third reservoir, the SCLM, has been defined as an isolated fraction of the upper mantle located directly beneath the continents, which has evolved separately from the convective mantle (Dunai and Porcelli, 2002). It has been proposed that the SCLM is the result of the incorporation of volatiles-rich melts coming from different mantle domains, these includes mantle plumes, the MORB-like upper mantle and the mantle wedge associated with subduction processes (Dunai and Porcelli, 2002). According to these authors, the SCLM has developed a unique geochemical and isotopic signature and may retain important amounts of noble gases. Gautheron and Moreira (2002) proposes that the mean helium isotopic signature of the SCLM is equal to 6.1 ± 0.9 Ra based on different analysis performed in fluid inclusions hosted in mantle xenoliths and lava phenocrysts from Europe, southwest USA, Antarctic, Australia and West Africa. Day et al (2015) also proposed a similar value (6.1 ± 2.1 Ra) considering peridotites from on-craton settings such as Kaapvaal (South Africa), Slave (Canada) and Siberia, and from off-craton settings such as San Carlos (USA) and Vitim (Siberia). Although this value indicates that the SCLM is more radiogenic than the MORB range (8 ±1Ra; Graham, 2002) and that the global lithospheric mantle is in steady-state for helium, recent studies in Mexico (this work) and the West Antarctic rift system (Broadley et al., 2016; Correale et al., 2019) also suggest R/Ra values higher than 7 Ra (within the MORB range) commonly associated with the action of deep metasomatism and/or refertilization events. These evidences leave open the scientific debate on the origin and the heterogeneity of the SCLM geochemical features.

The extremely low abundance of helium in the atmosphere generally prevents the $^3He/^4He$ ratios from being affected by air contamination (Farley and Neroda, 1998; Graham, 2002). This characteristic allows researchers to make accurate inferences regarding the structure and the composition of the solid earth. Conversely, heavier noble gases have accumulated in the atmosphere over the Earth's history, to the point that atmospheric contamination becomes a serious problem when interpreting isotopic ratios (Farley and Neroda, 1998; Mukhopadhyay and Parai, 2019). For instance, neon and argon isotopes measured in mantle rocks always reflect mixing trajectories between mantle and atmospheric compositions (Farley and Poreda, 1993; Matsumoto et al., 2001; Graham, 2002; Ozima and Podosek, 2002; Hopp et al., 2007a; Martelli et al., 2011; Rizzo et al., 2018). While atmospheric contamination of fluid inclusions can occur during eruption of the transporting magmas, or during exposure of mantle xenoliths to the surface, the recycling of atmospheric gases in the local mantle should also be considered. Holland and Ballentine (2006) demonstrated that important quantities of seawater-derived noble gases are continuously

introduced into the convective mantle during subduction. Besides, Matsumoto et al. (2001) and Hopp et al. (2007a) also proved the existence of a recycled atmospheric component in the lithospheric mantle from the variability of $^{3}He/^{36}Ar$, $^{4}He/^{20}Ne$, $^{20}Ne/^{22}Ne$, $^{21}Ne/^{22}Ne$, $^{36}Ar/^{22}Ne$ and $^{40}Ar/^{36}Ar$ ratios measured in fluid inclusions. According to these authors, isotopic features such as the correlation between ^{3}He and ^{36}Ar abundances, low $^{40}Ar/^{36}Ar$, low $^{4}He/^{20}Ne$ and high $^{36}Ar/^{22}Ne$ ratios, reflect mantle contamination commonly attributable to the infiltration of atmospheric fluids derived from subduction processes.

Like noble gases, carbon isotopes are also unique geochemical tracers. Carbon isotopes are commonly analyzed in volcanic gases or fluid inclusions using the $\delta^{13}C$ notation which indicates the ratio of stable isotopes ^{13}C and ^{12}C reported in parts per thousand (‰). As discussed above, fluid inclusions in mantle xenoliths are generally dominated by CO_2 and may contain carbon species such as CH_4, CO and carbonates. This characteristic makes them excellent targets to study the carbon isotopic signature of the mantle and the nature of metasomatic fluids that have modified its original composition (Deines, 2002; Gennaro et al., 2017; Boudoire et al., 2018 and references therein; Rizzo et al., 2018). Values of $\delta^{13}C$ in mantle xenoliths show a wide range of variability (from -30‰ to +1‰; Deines, 2002; Demény et al., 2010; Correale et al., 2015; Rizzo et al., 2018; this work) when compared with the range proposed for the upper mantle (-8 ‰ $< \delta^{13}C <$ -4‰; Sano and Marty, 1995). This variability is usually explained by the contribution of three different endmembers: mantle carbon ($\delta^{13}C \sim$ -5‰; Deines, 2002), organic carbon (-30‰ $< \delta^{13}C <$ -10‰; Faure, 1987), and carbonate carbon (-1‰ $< \delta^{13}C <$ +1‰; Sano and Marty, 1995). According to Deines (2002), sedimentary carbon (organic and carbonates) may represent more than the 50% of the total carbon found in ultramafic xenoliths and would be the result of carbon recycling via subduction of crustal components.

Carbon ingassing to the Earth's mantle is governed by subduction of carbonate and organic materials present in sediments, altered oceanic crust (AOC) and in the mantle layers attached to the oceanic slab (Plank and Manning, 2019). Several studies have proved that important quantities of carbon are incorporated (as carbonates) in AOC and mantle layers during hydrothermal reactions at mid ocean ridges (Fig. 8; Alt and Teagle, 1999; Alt and Shanks, 2003; Alt et al., 2013; Thomson et al., 2016; Li et al., 2019; Plank and Manning, 2019). In subduction zones, carbon can be released by mechanical removal, metamorphic decarbonation or melting at different depths depending on the temperature conditions and the carbon minerals present in the slab (Dasgupta and Hirschmann, 2010; Plank and Manning, 2019); for instance, hot slab conditions and fusible carbon minerals (siderite or ankerite) favor the release of carbon at shallow depths into the mantle wedge, while cold conditions and refractory carbon species (calcite or graphite) facilitates the introduction of carbon in the deep mantle (Fig. 8). Some studies have proposed that a little part of the subducted carbon is returned to the exosphere (after dehydration of the oceanic slab) through volcanic arcs (Thomson et al., 2016) and that most of the crustal carbon is transferred into the deep mantle. According to Thomson et al. (2016) and Regier et al. (2020), when the slab reaches the transition zone, it starts to melt and release the carbonate components present in the oceanic lithosphere, then the resulting carbonatite melts react with the overlying mantle promoting the production of diamonds and metasomatism of the surrounding peridotite (see Fig. 8). These studies argue that the transition zone acts as a barrier that retains most of the subducted carbon restricting the quantity of carbon transported into the lower mantle. The chemical reactions and the new carbon phases produced along the transition zone will influence the formation of different chemical and isotopic reservoirs in the mantle, which have huge implications for our understanding of crustal recycling and the major geological processes that governs the deep carbon cycling.

Recently, some studies of fluid inclusions in mantle xenoliths have combined the analysis of carbon and noble gases isotopes (Figs. 9 and 10). These studies suggest that the isotopic characteristics of

the SCLM are variable and strongly linked with the geodynamic history of the study area and the nature of the metasomatic/refertilization events that have affected the local mantle. For instance, Correale et al. (2012, 2015) report a complex history of melt extraction and degassing events in the upper mantle beneath the Hyblean plateau based on the variability of ^{3}He/^{4}He and ^{4}He/^{40}Ar* ratios in ultramafic nodules (Fig. 9A); besides, they report elevated δ^{13}C and CO_2/^{3}He values that reflect a mixing between MORB-like upper mantle carbon and crustal-derived carbonate fluids likely inherited from fossil subductions (Fig. 9B). Similarly, Gennaro et al. (2017) report δ^{13}C between $-2.8‰$ and $-1.5‰$ versus V-PDB in fluid inclusions trapped in ultramafic cumulates from Stromboli and suggest a contamination of the mantle wedge by recycled sediments derived from the Ionian slab. On the other hand, Rizzo et al. (2018) propose that the fluid inclusions observed in mantle xenoliths collected in SE Poland are a mix between a residual mantle (resulting from partial melting) and a metasomatizing agent (He-deleted and CO_2-rich fluid) characterized by a MORB-like ^{3}He/^{4}He and δ^{13}C signature (Fig. 9B). Moreover, these authors suggest that the European SCLM has been contaminated by the introduction of atmospheric fluids and radiogenic ^{4}He likely derived from dehydration of the subducted oceanic crust. Other reference is the investigation performed by Boudoire et al. (2018); here, although the authors focused in the usefulness of noble gas and carbon abundances to unveil the magmatic system of the Piton de la Fournaise volcano and the extent of mantle degassing, they also revealed the existence of a carbon-rich mantle plume source feeding the magmatic system of the island which differs from other OIB localities because the relative high carbon concentration identified in ultramafic enclaves.
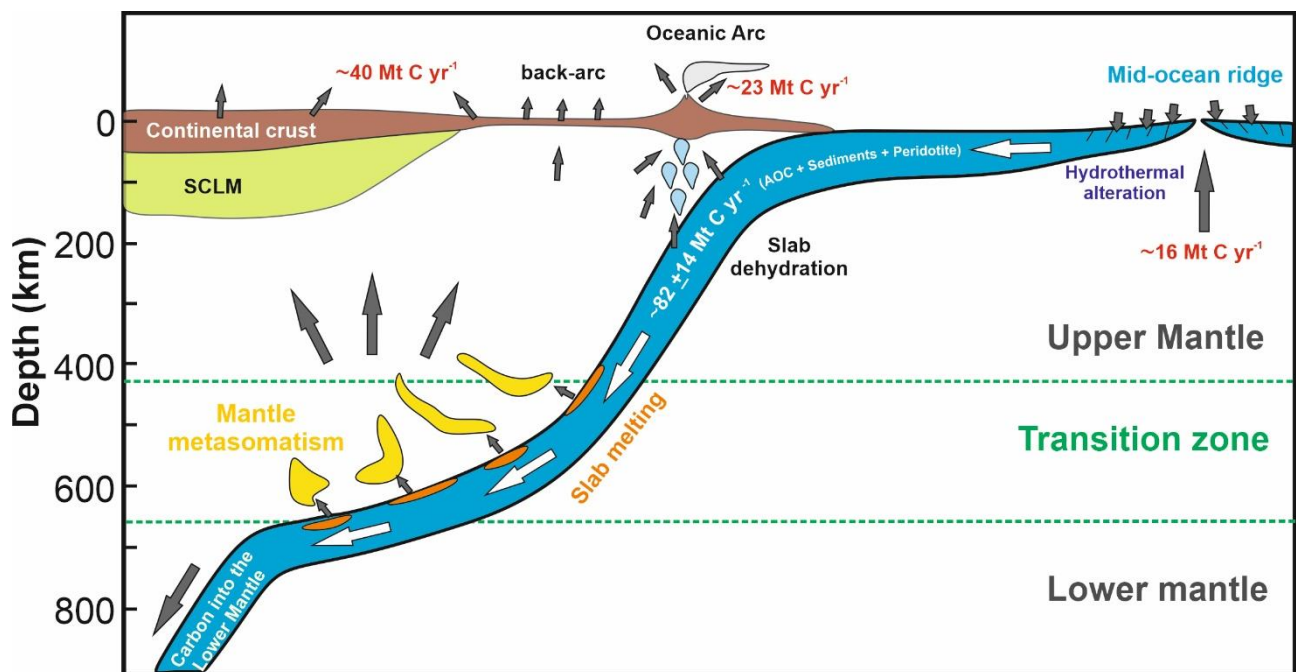
Figure 8. Model for the deep mantle carbon cycle, modified from Thomson et al. (2016). Red (inputs) and white (outputs) numbers are global carbon (C) fluxes in megatons per year (Mt yr^{-1}); values are from Plank and Manning (2019) and references therein.

Although the above-mentioned studies clearly illustrate the progress made in the study of volatiles in the Earth's mantle, some limitations prevent a complete understanding of the deep volatile cycle and several questions remain unsolved, for example: i) the disproportion between petrological and volatiles studies in mantle xenoliths that restricts the interpretations about the typology of the metasomatic agents and the relationship with the volatiles that participate in metasomatic processes; ii) the real impact of the recycled crustal material (inherited from subduction) in the

noble gas and CO_2 signature of the mantle; ii) the influence of HIMU and EM reservoirs in the variability of noble gas compositions and what signature expect considering the variability of $^3He/^4He$ ratios in some regions (e.g., Canary and Azores Islands); iii) how these isotopic signatures vary between continental and oceanic contexts and iv) how the existence of these reservoirs controls the variability of the $\delta^{13}C$ in the mantle.

As discussed in the following sections, this dissertation seeks to address these key issues combining the information from petrology and fluid inclusions composition of mantle xenoliths and gives new insights about the evolution of the lithospheric mantle in both continental and oceanic settings (i.e., Mexico and Canary Islands).
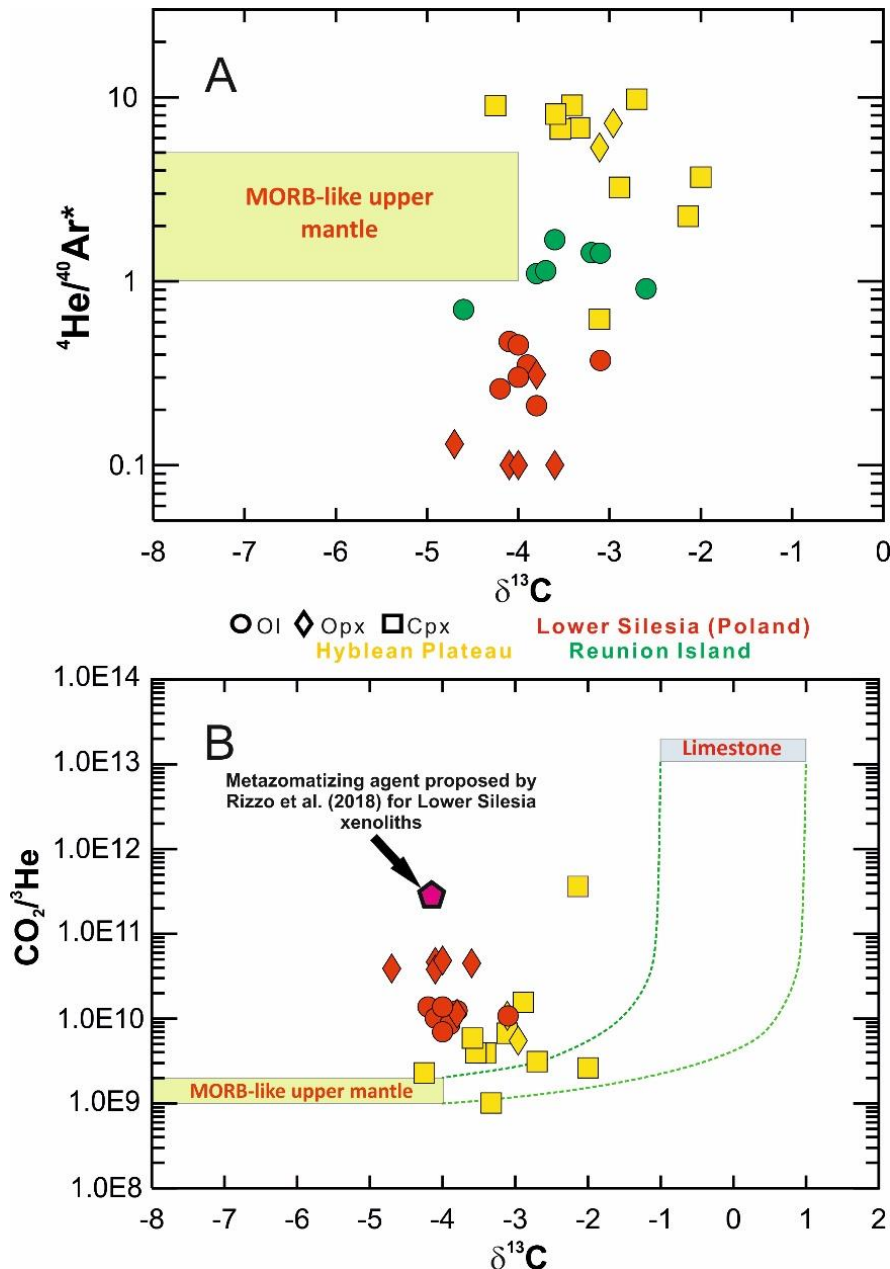
Figure 9. A) $\delta^{13}C$ vs $^4He/^{40}Ar^*$ and B) vs Rc/Ra ($^3He/^4He$ corrected for atmospheric contamination) measured in mantle xenoliths. Data from Correale et al. (2012, 2015), Boudoire et al. (2018), Rizzo et al. (2018).
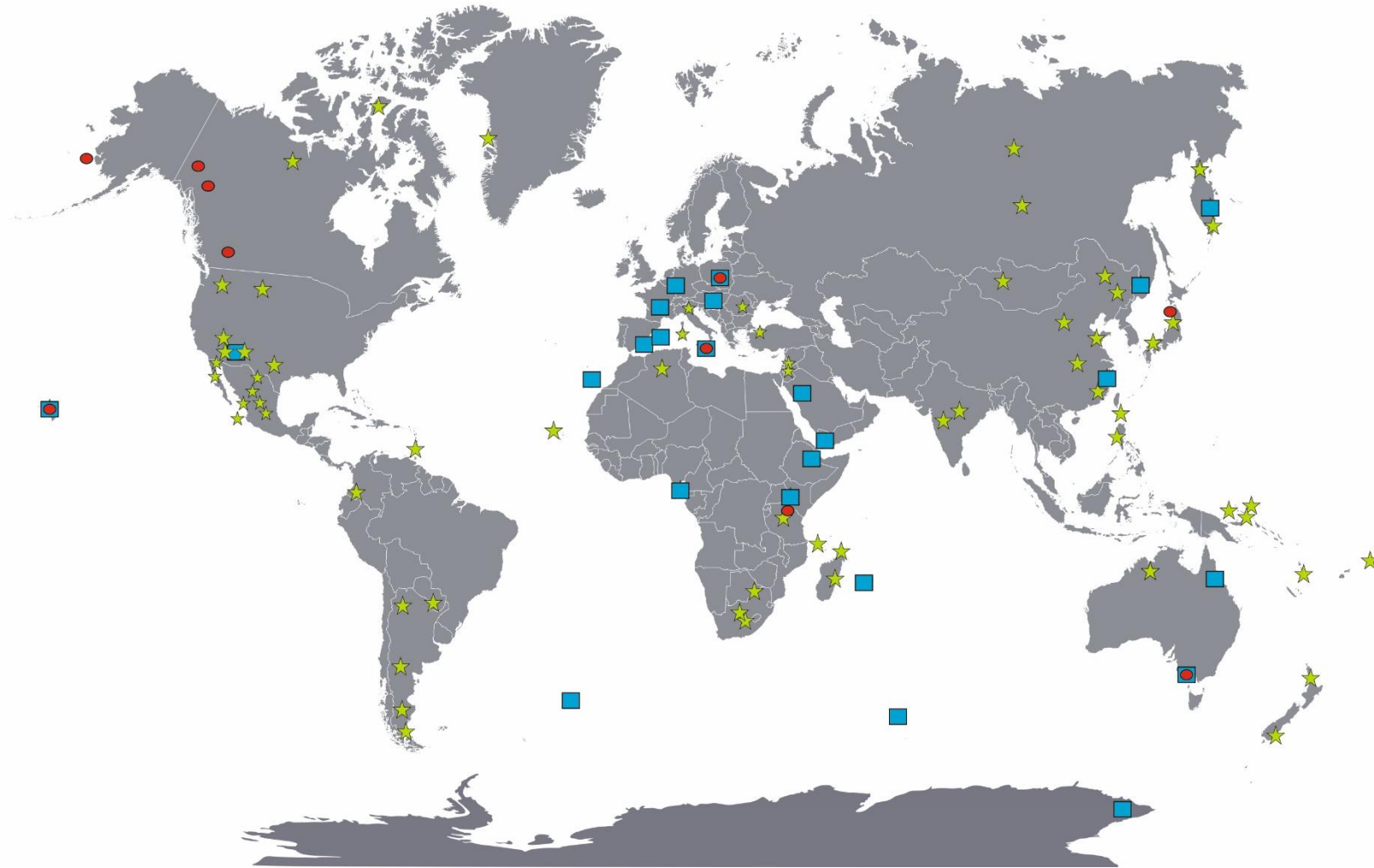
Figure 10. Blue squares and red circles represent localities where noble gas and CO_2 isotopic compositions have been measured in mantle xenoliths, respectively. Green stars represent other localities with mantle xenoliths. References are provided in Fig. 1.

CHAPTER 3. METHODOLOGY

The analyzed suite of rocks consists of 31 ultramafic nodules and four basalts: 22 samples from Mexico and 13 from the Canary Islands.

Of the 22 Mexican samples, 13 peridotites come from the VESVF (San Luis Potosi state), five from the Durango Volcanic Field (DVF; Durango state), one from SQVF (Baja California State) and four basalts from the Sierra Chichinautzin (TMVB near Mexico City). The Canarian samples consist of six peridotites from El Hierro and seven from Lanzarote.

3.1. Petrography and fluid inclusion analyses

Eight nodules from the VESVF were selected for petrographic analysis on thin and polished sections. Petrographic analysis was performed at the petrography laboratory of the University of Milano-Biccoca based on the textural classification proposed by Mercier and Nicolas (1975); the modal composition was carried out by point counting (from 4000 to 7000 points per section). Two double-polished rock sections of about 130 μm thickness were selected for the Raman of fluid inclusions. Analyzed fluid inclusions are located at 10 to 20 μm depth below the sample surface. Analyses were performed using a Labram Evolution (Horiba Scientific, Japan) at the Dipartimento di Scienze dell'Ambiente e della Terra, Università Milano Bicocca. The polarized Raman spectra were excited using a green Ar-ion laser operating at 532 nm, with 50-70 mW emission power. Spectra acquisition was performed with a backscattered geometry and a 600 g/mm diffraction grating. A transmitted light Olympus B40 microscope with a 100 × objective (Numerical aperture, N.A., = 0.90) was used for all the acquisitions (spatial resolution < = 1μm). Confocality was maintained with a pinhole of 100 μm. Spectra were collected with variable acquisition times (from 20 to 30 sec). The spectrometer was calibrated using a Silicon standard. To increase band attribution accuracy better than 0.2 cm-1, spectra were baseline corrected and processed by statistical analysis (Fityk software; Wojdyr, 2010) using a Voigt Pseudo-function, a convolution of a Lorentzian with a Gaussian line shape. Mineral and fluid identification has been based on our reference spectra database (Frezzotti et al., 2012a).

Petrological characteristics and geochemical information of mantle xenoliths and basalts from the DVF, SQVF and Sierra Chichinautzin are presented elsewhere (Luhr and Aranda-Gomez, 1997; Straub et al., 2011). Petrological, geochemical and fluid inclusion data of the same suite of mantle xenoliths from El Hierro and Lanzarote are reported in Siena et al. (1991), Oglialoro et al. (2017), Remigi et al. (2019) and Colombo (2020).

3.2. Noble gas and CO_2 isotopic analysis

Noble gas and CO_2 isotopic determinations were performed at the noble gas and stable isotopes laboratories of INGV, Sezione di Palermo, following the preparation methods and analytical procedures described in Gennaro et al. (2017), Rizzo et al. (2018), Faccini et al. (2020). All xenoliths were crushed and sieved with the aim of hand-picking crystals with diameters >0.25 mm. - aliquots (13 Ol, 11 Opx and 13 Cpx) of crystals (weights of 0.05 to 2 g) were selected for noble gas isotopic analysis. Before analysis, samples were cleaned ultrasonically in 6.5% HNO_3 (for CO_2 analysis samples were cleaned in HCl), deionized water and high-purity acetone. After drying, samples were accurately weighed and loaded into an ultra-high-vacuum (UHV) crusher (capable of holding up to six samples; holders are numbered from 1 to 6 in Fig. 11) for noble gas analyses that was pumped

and backed for 48h at 120°C. As soon as the ultra-high-vacuum was reached, fluid inclusions were released by single-step crushing at about 200 bar and room temperature (21°C). Single step technique was used to minimize the addition of secondary helium (cosmogenic ^{3}He and radiogenic ^{4}He) accumulated in the crystal lattice (Kurz, 1986; Graham, 2002; Rizzo et al., 2018; Correale et al., 2019); unlike the multistep technique, the single step is less efficient because this conservative technique crushes less sample and therefore releases less gas (more material is needed). The moles of CO_2 were quantified by measuring the total pressure of gas (generally CO_2+N_2+O_2+noble gases) released during crushing (by an IONIVAC Transmitters ITR90) in a known volume of the system, then subtracting the residual pressure of N_2+O_2+noble gases after removing CO_2 in a "cold finger" immersed in liquid nitrogen. After the manometric determination of the CO_2 concentration, the resulting gas mixture was purified in a stainless-steel ultra-high-vacuum preparation line to remove all gas species (N_2, H_2, H_2O, CO_2) except noble gases. For noble gas analysis, the residual gas mixture was purified under Zr-Al getter pumps in a UHV stainless-steel preparation line (see Fig. 11). These getters pumps base their operation on selective adsorption by a particular Zr-Al bond which has a different reactivity depending on the temperature; at room temperature, the getter pumps mainly adsorb H_2, while at temperatures around 250-300 °C they adsorb N_2, CO_2, H_2O and other carbon compounds. After then, Ar (and Kr and Xe) was removed in a "cold finger" with active charcoal immersed in liquid nitrogen. Finally, He and Ne were adsorbed in a cold head with active charcoal cooled at 10K and then moved at 40 and 80K in order to release first He and then Ne, respectively. He and Ne isotopes were analyzed using two different split-flight-tube mass spectrometers (Helix SFT-Thermo), while Ar isotopes were analyzed by a multi-collector mass spectrometer (Argus, GVI); typical blanks for He, Ne, and Ar were < 10^{-15}, <10^{-16}, and < 10^{-14} mol, respectively.

The measured ^{3}He/^{4}He ratios are expressed as R/Ra (where R is the ratio of the sample and Ra the He isotopic ratio of air = 1.39×10^{-6}); this ratio was corrected for atmospheric contamination based on the measured ^{4}He/^{20}Ne ratio and the values are expressed as Rc/Ra (eq.1):

$$Rc/Ra = ((R_M/Ra)(He/Ne)_M - (He/Ne)_A)/((He/Ne)_M - (He/Ne)_A) \qquad eq.1$$

where R_M/Ra and $(He/Ne)_M$ are the measured values and $(He/Ne)_A$ refers to the atmospheric theoretical value (0.318). ^{40}Ar values were also corrected for atmospheric contamination:

$$^{40}Ar^* = {}^{40}Ar_{sample} - ({}^{36}Ar_{sample} \cdot ({}^{40}Ar/{}^{36}Ar)_{air}) \qquad eq.2$$

where ^{40}Ar* is the corrected ^{40}Ar, ^{40}Ar/^{36}Ar$_{air}$ = 298.56 (Lee et al., 2006) and ^{21}Ne/^{22}Ne$_{air}$ = 0.029 (Steiger and Jäger, 1977; Ozima and Podosek, 2002). Values of ^{20}Ne, ^{21}Ne, ^{22}Ne, ^{36}Ar, and ^{38}Ar are also reported. Analytical uncertainties (2σ) for ^{3}He/^{4}He, ^{20}Ne/^{22}Ne, ^{21}Ne/^{22}Ne, ^{40}Ar/^{36}Ar, and ^{38}Ar/^{36}Ar ratios are <2.7%, <6.3%, <7.5%, <2.0%, and <1.7%, respectively. The ^{20}Ne/^{22}Ne and ^{21}Ne/^{22}Ne ratios are corrected for isobaric interferences at m/z values of 20 (^{40}Ar^{2+}) and 22 (^{44}CO$_2^{+2}$); corrections are performed by measuring ^{20}Ne, ^{21}Ne, ^{22}Ne, ^{40}Ar, and ^{44}CO$_2$ during the same analysis, and considering the previously determined ^{40}Ar^{2+}/^{40}Ar$^+$ and ^{44}CO$_2^{+2}$/CO$_2^+$ ratios on the same Helix SFT that run the samples (Rizzo et al., 2018; Faccini et al., 2020). For each analytical session, it is analyzed at least one standard of He, Ne, and Ar that had previously been purified from air and stored in tanks (Rizzo et al., 2018).

After noble gas analysis, the aliquots with the highest concentrations of CO_2 (2 aliquots of Ol, 4 of Opx and 1 of Cpx) were selected to determine the carbon isotopic composition of fluid inclusions (^{13}C/^{12}C) in the stable isotopes laboratory of INGV-Palermo. Selected crystals were cleaned in an ultrasonic bath in 10% HCl, weighed and loaded in a crusher system consisting of a stainless-steel sample holder, a hydraulic crusher (which exerts a single-step pressure of approximately 200 bar), a glass sampler to freeze CO_2, and a pump to ensure the vacuum inside the system (Fig. 12A).
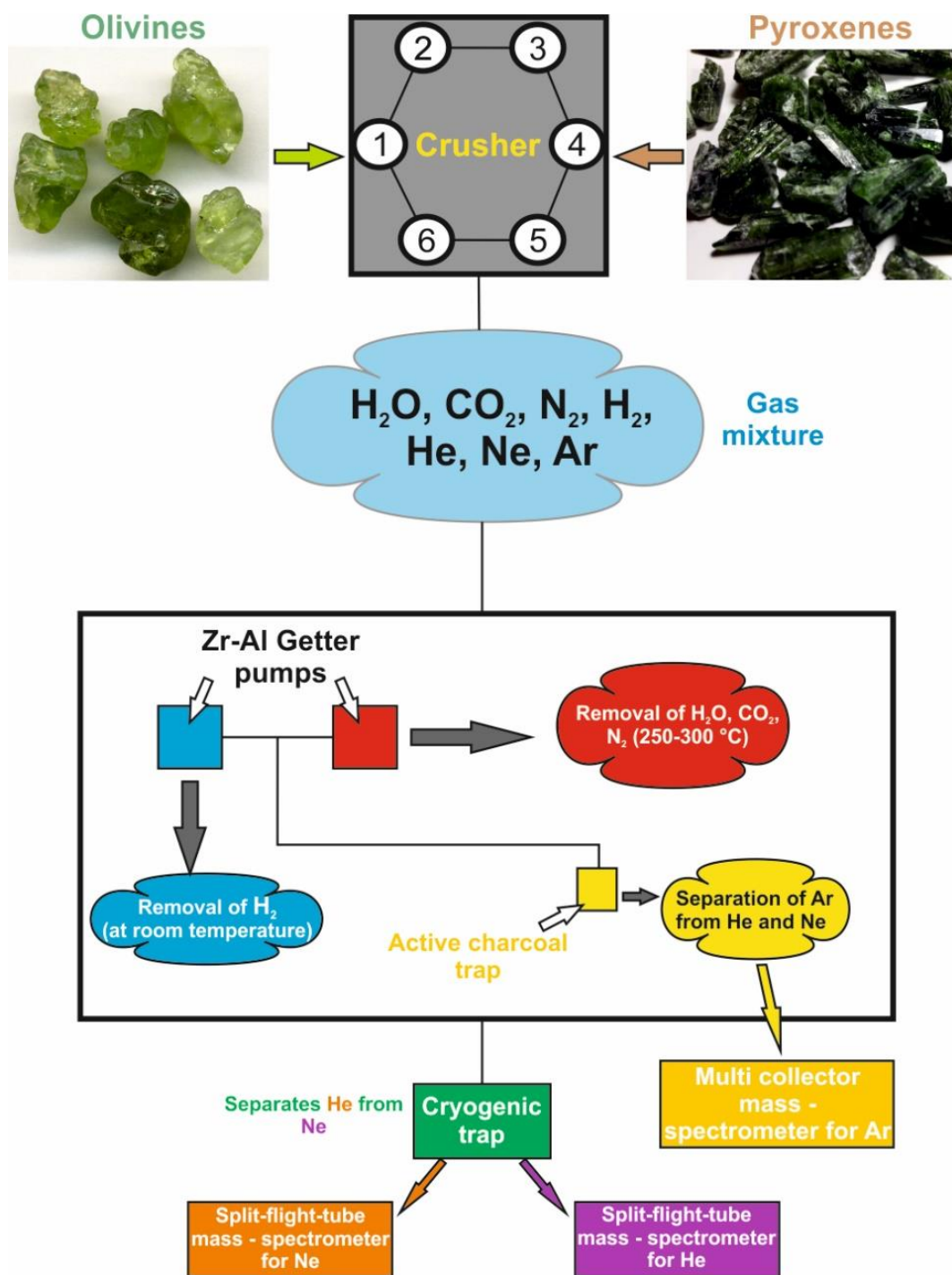
Figure 11. Schematic diagram that represents the crushing system and the purification line used for the analysis of noble gases.

During crystals crushing, a glass sampler submerged in liquid nitrogen was maintained online to freeze CO_2, and eventually, those gaseous species condensing at a temperature $\geq$ -196°C. Subsequently, the gas mixture trapped was released in a glass line equipped with a 626B Baratron® Absolute Capacitance Manometer MKS (measuring range 10^{-3}-10^{-4} mbar), for the purification procedure and quantification of CO_2 concentration (mol/g) (Fig. 12B). The released CO_2 and H_2O were condensed in the first cold trap immersed in liquid nitrogen at -196 °C, while the atmospheric and non-condensable gases (N_2 +O_2 + noble gases) were pumped away. After pumping, the cold trap was heated by a mixture of liquid nitrogen and ethyl alcohol that increased the temperature up to about -100 °C (under these conditions, CO_2 becomes gaseous while H_2O remains trapped as

ice). The purified CO_2 was then condensed in the same glass sampler immersed in liquid nitrogen (adjusted to atmospheric pressure by adding pure helium) and transferred to the laboratory of stable isotopes for the following isotopic measurements. The $^{13}C/^{12}C$ ratios were measured using a Thermo (Finnigan) Delta Plus XP CF-IRMS connected to a Trace GC gas chromatograph and a Thermo (Finnigan) GC/C III interface. Results are expressed in parts per mil (‰; relative to the V-PDB international standard) using the delta notation ($\delta^{13}C$). The analytical error estimated as 2σ was better than 0.6‰. Further details on the adopted analytical procedure can be found in Gennaro et al. (2017) and Rizzo et al. (2018) that followed analogous protocols.
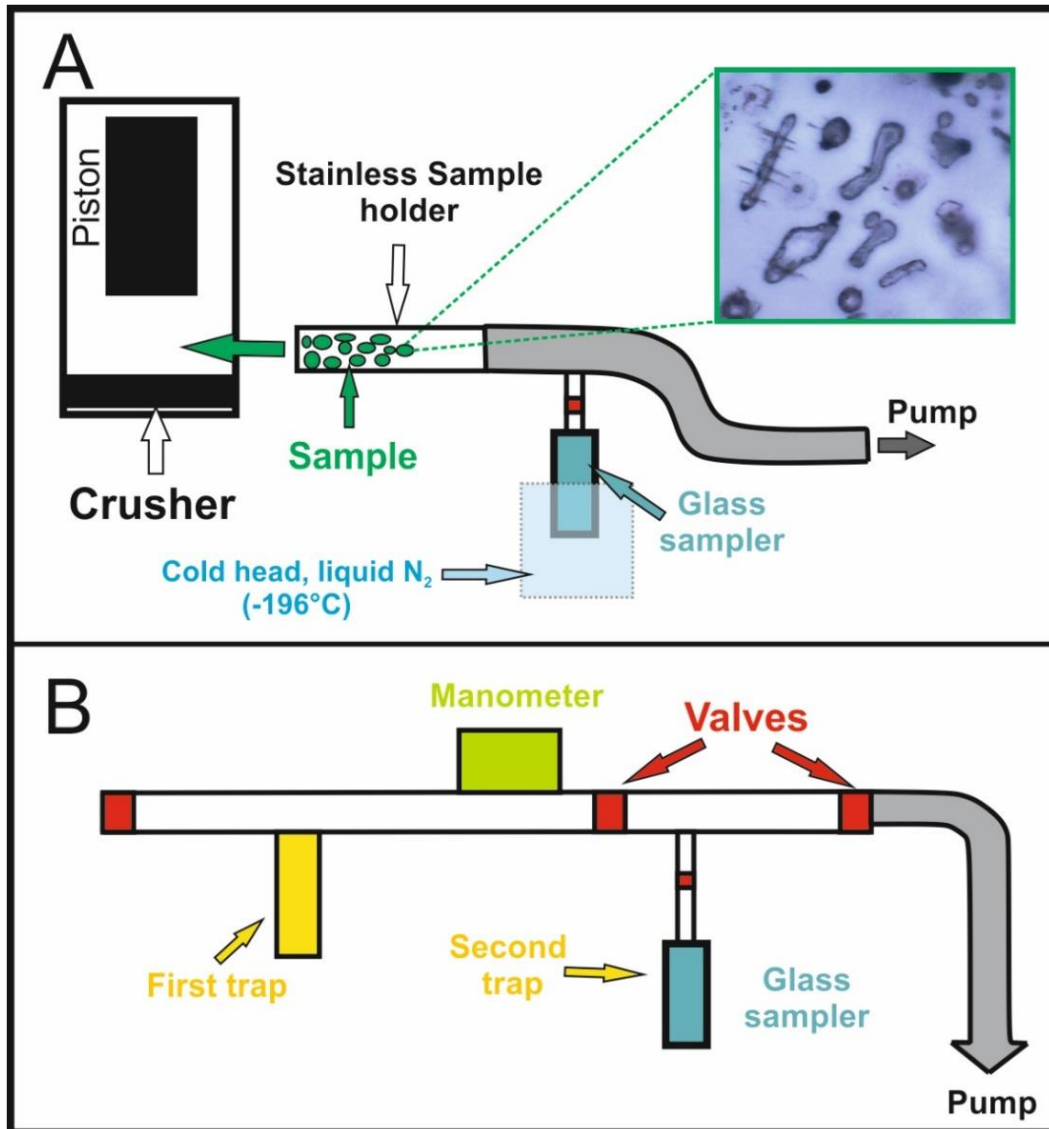
Figure 12. Schematic diagram that represents the crushing system and the purification line used for the analysis of CO_2.

CHAPTER 4. BRIEF OVERVIEW REGARDING THE GEODYNAMICS OF THE STUDY AREAS

4.1. The Basin and Range province and the intraplate volcanism along central and north-western Mexico

The Basin and Range is an extensional province identified in western North America that extends for almost 2500 km from the Idaho-Montana border (USA) to central Mexico (Dickinson, 2002; Henry and Aranda-Gomez, 1992); this gets its name from its distinctive morphology which is characterized by elongated horst alternating with alluviated basins. It is held that the evolution of Basin and Range tectonism started 30 Ma ago (during the middle-late Oligocene) as a result of the rollback and consumption of the horizontally dipping Farallon slab beneath the North American plate (Atwater, 1989; Ferrari et al., 2012; Henry and Aranda-Gomez, 1992; Sedlock, 2003); in fact, the subduction of the Farallon slab gave rise to enormous changes in the tectonic configuration of the northwestern coast of Mexico including the transition from a compressive to a transform margin (formation of the San Andreas fault system and the Mendocino and Rivera triple junctions ≈ 20Ma ago), and the beginning of a regional extension that produced the Gulf of California (≈ 10 - 5 Ma ago) and the Basin and Range Province (Figs. 13 and 14).
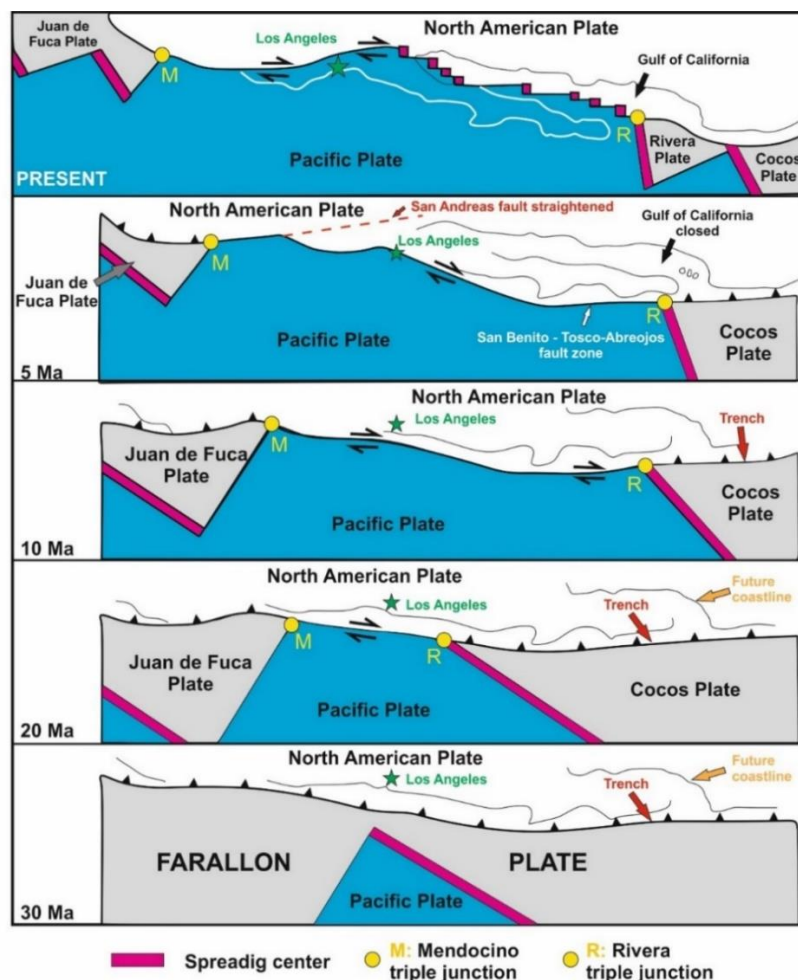
Figure 13. Evolution of the western margin of North America during the last 30 Ma. After Wallace (1990).

Like areas within the USA portion of the Basin and Range, the Mexican Basin and Range was accompanied by intraplate magmatism which generated several volcanic fields north of the

Transmexican Volcanic Belt (Fig 14A). These fields are typically monogenetic complexes associated with the eruption of alkaline basalts and basanites that have brought to the surface significant amounts of ultramafic xenoliths (mainly harzburgites and lherzolites). Their origin remains somewhat enigmatic. Some examples are the Ventura Espiritu Santo Volcanic Field (VESVF), the Santo Domingo Volcanic Field (SDVF), the Pinacate Volcanic Field (PiVF), Las Palomas Volcanic Field (PaVF), the Potrillo maar (Po), the Camargo Volcanic Field (CVF), the Durango Volcanic Field (DVF), the San Quintin Volcanic Field (SQVF) and Isla Isabel (II; Fig. 14A; Basu, 1977; Gutmann, 1986; Aranda-Gómez and Ortega-Gutiérrez, 1987; Aranda-Gómez et al., 1992; Luhr and Aranda-Gomez, 1997; Housh et al., 2010; Dávalos-Elizondo et al., 2016).

In this dissertation analyses were performed in mantle xenoliths collected from the Ventura Espiritu Santo Volcanic Field (VESVF), the Durango Volcanic Field (DVF) and the San Quintin Volcanic Field (SQVF).

4.2. The Transmexican Volcanic Belt (TMVB)

The TMVB is defined as a continental magmatic arc that extends E - W through central Mexico and contains around 8000 volcanic structures and some intrusive bodies (Fig. 14B; Gómez-Tuena et al., 2007). The province extends for about 1000 km with a variable width between 80 and 230 km from the Pacific (in Nayarit and Jalisco states) to the Gulf of Mexico (Pardo and Suárez, 1995; Ferrari et al., 1999, 2012; Gómez-Tuena et al., 2007). Although the origin of the TMVB is commonly attributed to the subduction of the Cocos and Rivera plate under the North American plate (Pardo and Suárez, 1995 and references therein), some studies suggest the existence of an active fracture zone (or a hotspot) due to the anomalous orientation of the volcanic arc relative to the trench and the existence of OIB-like volcanic rocks (Shurbet and Cebull, 1984; Moore et al., 1994; Márquez et al., 1999b).

Ferrari et al. (1999) suggest the migration of the volcanic arc from the N-NW Sierra Madre Occidental to the E-W TMVB to explain the origin of the actual volcanism in central Mexico. This transition would have taken place 30 – 7 Ma ago as a direct result of the reorganization of the western margin of North America driven by the subduction of the Farallon slab (Figs. 13); this reorientation would have also marked a compositional change of the volcanism from high silicic rhyolites and ignimbrites to mainly andesites and basalts. According to Ferrari et al. (2012), the western TMVB was built on Jurassic-Cenozoic volcanic rocks (here the crust exhibits a thickness of 35 - 40 km), conversely, the eastern portion of the TMVB (east of 101° W where the SCN is located; Fig. 14) rests on Precambrian and Paleozoic rocks where the continental crust can reach a maximum thickness of 55 km.

4.3. The Canary Islands: El Hierro and Lanzarote

The Canary Islands are an archipelago composed of seven main volcanic islands (from East to West: Lanzarote, Fuerteventura, Gran Canaria, Tenerife, La Gomera, La Palma and El Hierro) located in front of the western coast of North Africa and extended for almost 500 km (Fig. 15). The volcanic islands and seamounts formed on oceanic lithosphere of Jurassic age close to a passive continental margin (Schmincke, 1982; Carracedo et al., 1998; Anguita and Hernán, 2000; Troll and Carracedo, 2016). Although the volcanism that formed the Canary started more than 20 Ma, ages between 47 and 142 Ma have been also reported for the old seamounts located NE and SW of the archipelago (Schmincke, 1982; Carracedo et al., 1998; van den Bogaard, 2013).
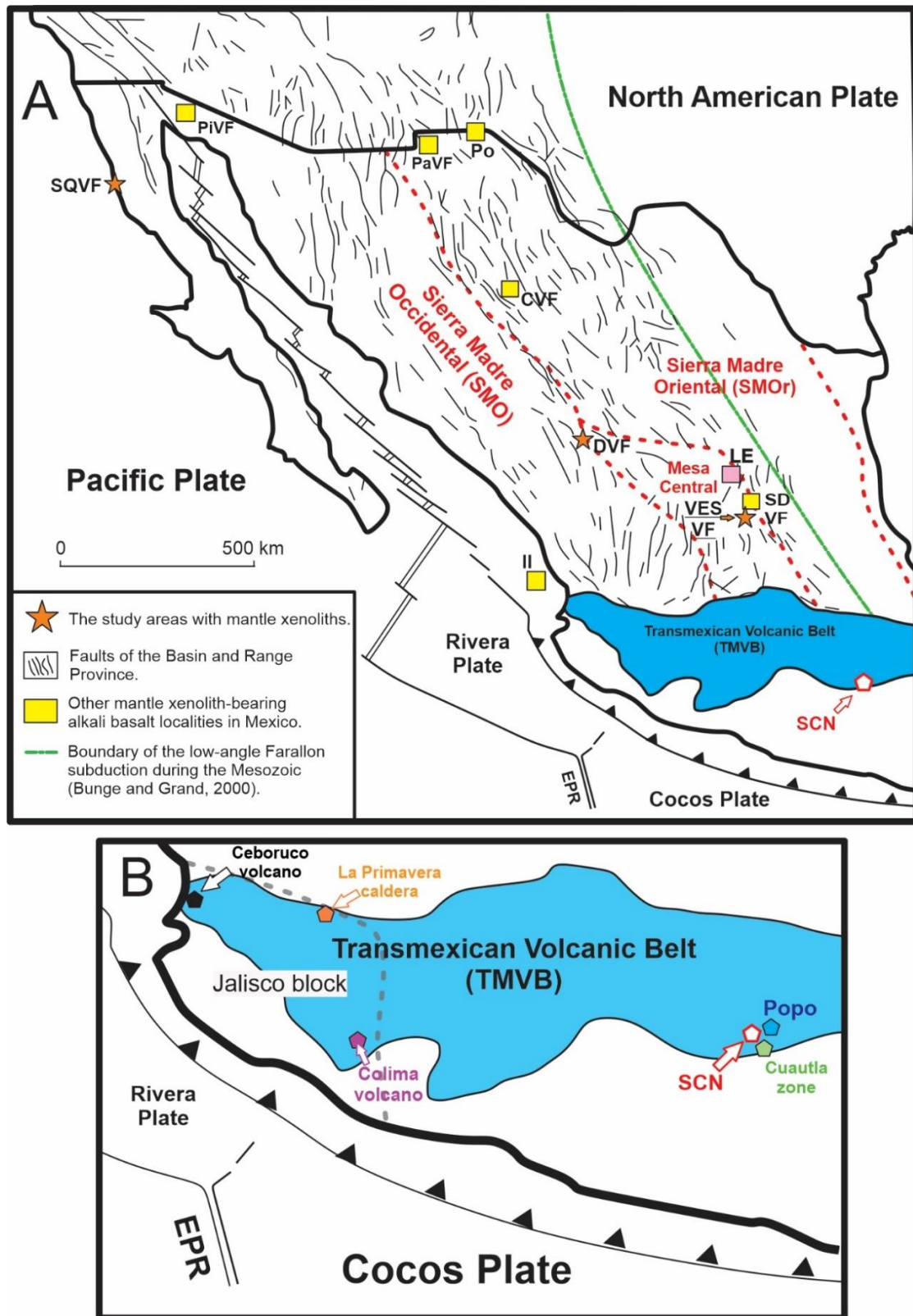
Figure 14. A) The map shows the Mexican part of the Basin and Range Province. Adapted from Aranda-Gómez et al. (2000). VESVF: Ventura Espiritu Santo Volcanic Field, SDVF: Santo Domingo Volcanic Field, PiVF: Pinacate Volcanic Field, PaVF: Las Palomas Volcanic Field, Po: Potrillo maar, CVF: the Camargo Volcanic Field, DVF: Durango Volcanic Field, SQVF: San Quintin Volcanic Field, II: Isla Isabel, SCN: Sierra Chichinautzin. Contours of Sierra Madre Occidental, Sierra Madre Oriental, the Transmexican Volcanic Belt and Mesa Central provinces were build based on Gómez-Tuena et al. (2007). B) Closer view of the Transmexican Volcanic Belt (TMVB) and location of some volcanoes where $^3He/^4He$ and $\delta^{13}C$ have been reported. The dash line represents the limit of the Jalisco block located in western Mexico.

Quaternary volcanic deposits have been reported along the Canary Islands (except for La Gomera) and most of them are considered volcanically active (Carracedo et al., 1998; Troll and Carracedo, 2016). The most recent eruptive events corresponto to the 2011-2012 submarine eruption in El Hierro (Padrón et al., 2013) and recently the September-December 2021eruption in La Palma

The Canary Islands exhibit an enormous spectrum of volcanic rocks, from carbonatites, nephelinites, basanites, tephrites, tholeiitic and alkali olivine basalts associated with shield-volcanism processes to rhyodacites, rhyolites, trachytes and phonolites related to a highly explosive felsic volcanism (Schmincke, 1982; Abratis et al., 2002; Carracedo et al., 1998; Troll and Carracedo, 2016). It is worth mentioning that this magmatic activity has brought to the surface important quantities of ultramafic xenoliths along the entire archipelago (e.g., Admunsen, 1987; Siena et al., 1991; Neumann and Wulff-Pedersen, 1997; Frezzotti et al., 2002a; Oglialoro et al., 2017).

Several hypotheses have been formulated about the origin of the Canary Islands: Anguita and Hernan (1975) proposed a connection between the Islands and the Atlas Mountains by a mega-shear that experienced a tensional phase causing decompression melting and volcanism. Araña and Ortiz (1991) suggested that compressive tectonics are the cause of the magmatism and the uplift of the archipelago; instead, Hoernle and Schmincke (1993) and Carracedo et al. (1998) described a mantle plume model where volcanism is generated by a thermal mantle anomaly (a hot-spot) which is supported by geochemical evidence, the progressive west-to-east age increase of the islands and the relative movement of the African plate (approximately 2 cm/year; Carracedo et al., 1998). Finally, Anguita and Hernán (2000) integrated these hypotheses and proposed a 'unified model' to explain the complexity of the thermal and tectonic evolution of the Canary Islands.
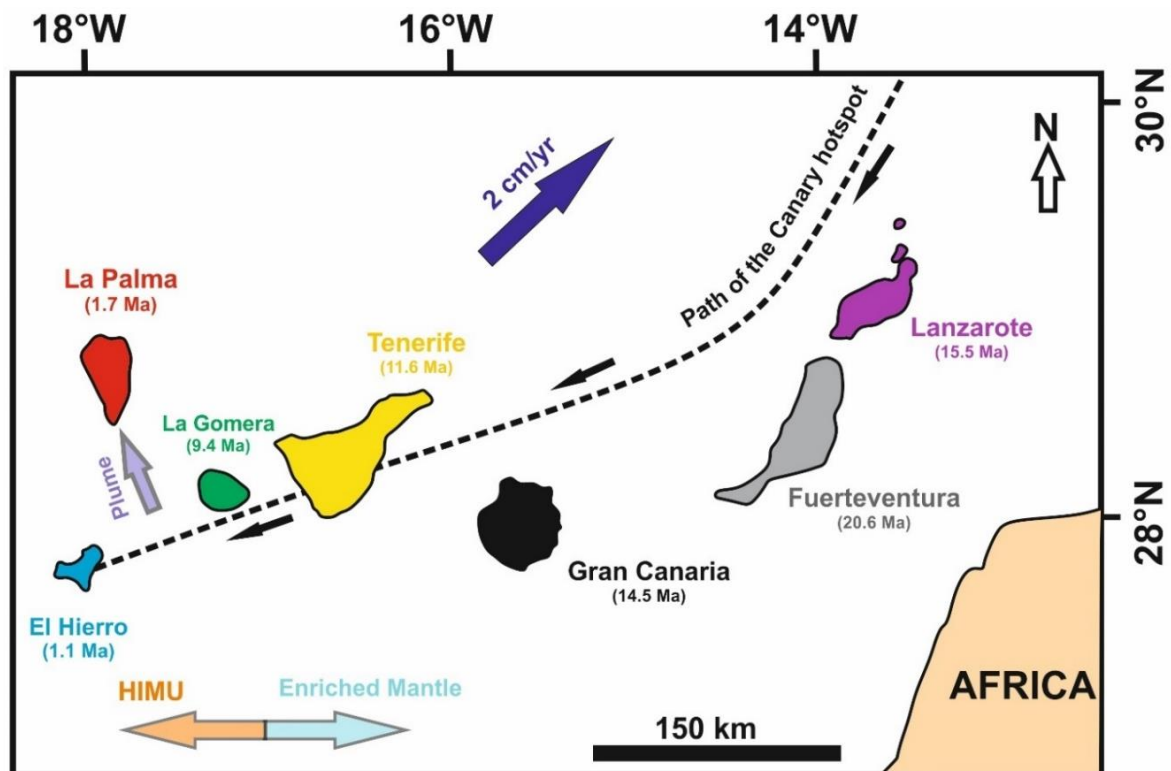
Figure 15. The Canary Islands archipelago. Modified from Anguita and Hernán (2000), Oglialoro et al. (2017) and Day and Hilton (2020). Ages in Ma represent the maximum ages reported in lavas for each Island (see Day et al., 2010). The path of the Canary hotspot was traced based on Holik et al. (1991) and Carracedo et al. (1998). Plume, HIMU and Enriched mantle arrows represent the geochemical affinity of the islands based on the data reported by Hoernle et al. (1991), Simonsen et al. (2000), Gurenko et al. (2006), Day and Hilton (2011, 2020).

The Canary Islands represent a natural laboratory for studying heterogeneities in noble gas and carbon mantle signatures, as ultramafic xenoliths, volcanic rocks, and surface emissions associated with the active volcanism of the archipelago prove the involvement of multiple sources at play in the mantle source (Gurenko et al., 2006; Day and Hilton, 2020). In terms of noble gases, only the geothermal gases of the Taburiente caldera (La Palma island), with their $^3He/^4He$ of > 9Ra (where Ra is the $^3He/^4He$ atmospheric ratio), identify a primordial component in the Canary mantle source (Pérez et al., 1994, 1996; Hilton et al., 2000; Day and Hilton, 2020; Fig. 15). In contrast, volcanic rocks of the same island mainly record a depleted mantle (MORB; Middle Oceanic Ridge Basalt) signature (some seamount series my exhibit values > 9Ra; e.g., Hilton et al., 2000; Day and Hilton, 2011), and other Islands ($^3He/^4He$ are available for El Hierro, Gran Canaria, Tenerife, La Gomera, Fuerteventura and Lanzarote) generally exhibit MORB-like, or even more radiogenic (lower $^3He/^4He$ ratios) signatures (see Table S1 for isotopic values and references). These variations have been taken as evidence of mantle heterogeneities in the sources of magmas. In particular, stemming from multi-isotope (He-Nd-Sr-Pb-Os-O) results, an Enriched Mantle (EM) component has been proposed in the eastern portion of the archipelago (Hoernle et al., 1991; Carnevale et al., 2021), while a HIMU (High-μ= elevated $^{238}U/^{204}Pb$) mantle signature has been identified in its western edge (Gurenko et al., 2006; Day and Hilton, 2011, 2020). These results indicate that recycled volatiles (e.g., derived from melting of old subducted oceanic crust/lithosphere in the case of the HIMU component) have been admixed with depleted (MORB) and plume mantle sources underneath the archipelago (Day and Hilton, 2011, 2020).

CHAPTER 5. THE COMPOSITION OF FLUIDS STORED IN THE CENTRAL MEXICAN LITHOSPHERIC MANTLE: INFERENCES FROM NOBLE GASES AND CO_2 IN MANTLE XENOLITHS FROM THE JOYA HONDA MAAR.

Published in Chemical Geology:

5.1. Geological and volcanological setting of the Ventura Espiritu Santo Volcanic Field (VESVF)

The VESVF is located in the southern portion of the province known as the Mesa Central (Raisz, 1959; Nieto-Samaniego et al., 2005); very close to the Sierra Madre Oriental province (Fig. 14A). The Mesa Central, located north of the TMVB, comprises a portion of continental crust that has a thickness of 32 km and is delimited by regional faults (Fix, 1975; Nieto-Samaniego et al., 2005). The oldest exposed rocks found in this province are muscovite schists from the Paleozoic (252 Ma), superimposed by turbiditic sequences of the Triassic and volcano-sedimentary sequences of continental origin formed during the mid-late Jurassic (Barboza-Gudino et al., 1999; Morán-Zenteno et al., 2005; Nieto-Samaniego et al., 2005). The most abundant outcrops correspond to sequences of calcareous rocks of marine origin, formed during a transgression episode during the end of the late Jurassic and the Cretaceous (Carrillo-Bravo, 1971; López-Doncel, 2003; Nieto-Samaniego et al., 2005); these rocks make up the so-called Valles-San Luis Potosí Platform (PVSLP) and the Mesozoic Basin of Central Mexico whose thickness can reach 5 km and 6 km, respectively. Cenozoic rocks are mainly volcanic and sedimentary (of continental origin), the most recent being the alkaline basalts of the VESVF, SDVF and DVF whose origin is related to a melting zone located 34 km deep under the Mesa Central (Fix, 1975).

The VESVF is comprised of some isolated scoria cones and three maars among which is the Joya Honda maar (Aranda-Gómez et al., 2007; Saucedo et al., 2017). The Joya Honda maar (JH) is located at the intersection between the PVSLP and the Mesozoic Basin of central Mexico (22 ° 25'4.97 "N and 100 ° 47'15.62" W) and is thought to have formed at about 311 ± 19 ka (Saucedo et al., 2017). This volcano is recognized as one of the most spectacular volcanic structure in Mexico (Saucedo et al., 2017), with its elliptical crater having vertical walls defining a 150 – 300 m deep depression (Fig. 16). The maar formed through a series of mixed magmatic and phreatomagmatic eruptions that emplaced a sequence of pyroclastic falls and base surge deposits (having a maximum thickness of ~100 m; Aranda-Gómez and Luhr, 1996; Saucedo et al., 2017). Magma–groundwater interaction is thought to have occurred during magma ascent through of a NE-SW normal fault system cutting folded limestones, calcareous mudstones, chert lenses and shales which are part of the Cuesta del Cura (Albian-Cenomanian) and Tamaulipas (Aptian) Formations (Aranda-Gómez and Luhr, 1996; Aranda-Gómez et al., 2000; Saucedo et al., 2017). Saucedo et al. (2017) identified five eruptive phases, the last two of which generated deposits rich in mantle xenoliths. The erupted magmas are alkaline and mafic in composition (olivine-nepheline basanites and olivine basalts), and their origin is thought to be associated with decompressional melting of the asthenosphere and lithospheric mantle under la Mesa Central, as proposed for other volcanic fields associated to the Basin and Range extension (Aranda-Gómez and Ortega-Gutiérrez, 1987; Luhr et al., 1989; Lee, 2005; Aranda-Gómez et al., 2007).

Samples were collected from the eastern part of the JH (Fig. 16), where units IV and V emerge according to the stratigraphy described by Saucedo et al. (2017). These units are composed of pyroclastic fall and flow deposits where the highest concentration of mantle xenoliths is found. The nodules are usually dispersed within or hosted in basanitic lavas. Thirteen fresh nodules were selected with diameters between 5 and 10 cm; additionally, a pyroxenite sample was studied (sample V-C) and was only used for noble gas analysis due to its small diameter (<5 cm).
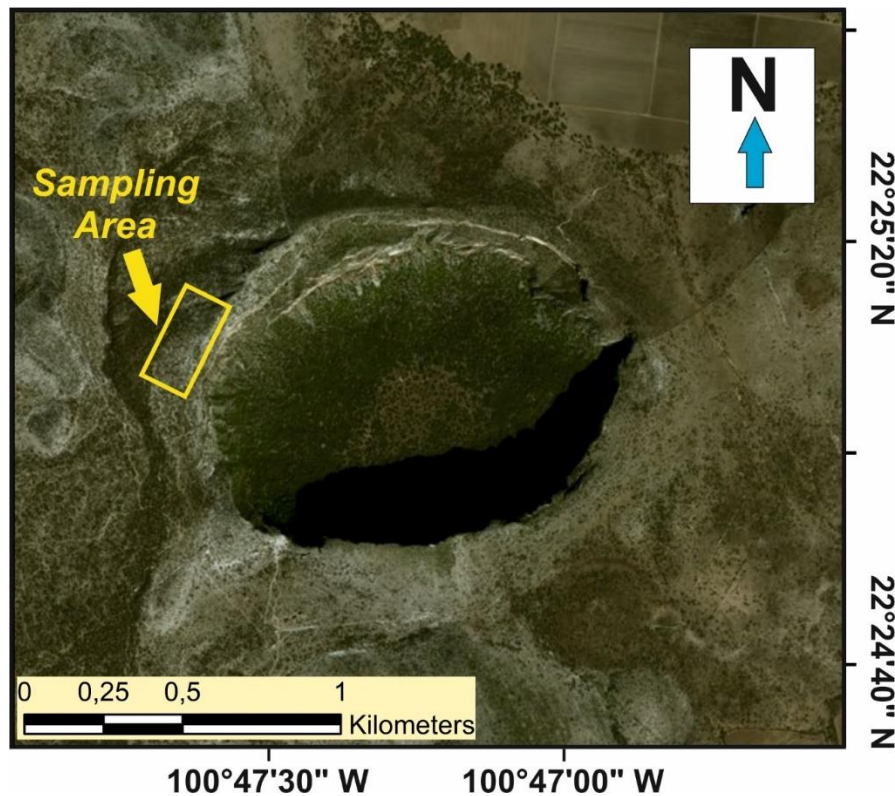
Figure 16. Image from Google Earth (February 20th, 2020) showing the Joya Honda maar (JH) morphology and sampling area.

5.2. Petrological background

The JH mantle xenoliths have been previously studied and described as spinel lherzolites and harzburgites (Aranda-Gómez and Ortega-Gutiérrez, 1987; Liang and Elthon, 1990; Luhr and Aranda-Gomez, 1997). The modal composition indicates a relatively constant paragenesis: Ol is the most abundant phase (55-88%), followed by Opx (17-32%), Cpx (1-17%) and Spinel (Sp; 0.3 - 5%); in very few cases, the presence of phlogopite is also reported with percentages below 1% (Luhr and Aranda-Gomez, 1997). Compositionally, Ol has a Mg# (Mg# = 100 x Mg/(Mg + $\sum$Fe)) ranging from 87.5 to 91, Opx from 88.6 to 91.2, Cpx from 87.7 to 91.4 and Sp from 75.5 to 82.5 (Liang and Elthon, 1990). These authors also report the development of Na-Al poor spongy rims on Opx, Cpx and spinel, explained as due to variable degrees of partial melting that have affected the local upper mantle.

Liang and Elthon (1990) classified the xenoliths into two groups based on their modal and geochemical compositions (groups Ia and Ib). Mantle xenoliths from group Ia are interpreted as mantle residues generated by different degrees of partial melting and extraction of picritic melts in the upper mantle; these authors calculated a degree of partial melting between 7% and 22% for Ia xenoliths, using melting models based on bulk-rock MgO, Ni and Sc abundances. Group Ib peridotites exhibit similar degrees of partial melting (1-20%) followed by metasomatic enrichment

27

(Liang and Elthon, 1990). One of the most important characteristic of Ib xenoliths is the extreme core-to-rim chemical zoning (and LREE-enriched patterns; $(La/Yb)N > 0.8$) in clinopyroxene, revealed by a decrease of of Al_2O3 and Na_2O towards the rim, while Mg#, CaO, TiO_2 and Cr_2O_3 tend to increase (Liang and Elthon, 1990). According to these authors, high $FeO-Na_2O$ contents in the cores of Ib minerals and LREE enrichment in Cpx crystals suggest interaction between silicate melts (basanitic in composition) and a residual mantle similar to group Ia xenoliths. Additionally, they explain the extreme core-to-rim chemical zoning, and reaction rims in Cpx, by the reaction with H_2O-rich fluids depleting Cpx rims in Na_2O and Al_2O_3 (also increasing TiO_2 contents).

5.3. Results

5.3.1. Petrography

The suite of xenoliths exhibits the same mineralogy: Ol> Opx> Cpx >> Sp. All samples are plagioclase-free and are classified as spinel lherzolites and harzburgites (Table 1, Fig. 17). Peridotites show protogranular to porphyroclastic textures, in which two generations of Ol, Opx and Cpx crystals are observed (Fig. 18): the first generation corresponds to large, elongated and deformed crystals of sizes greater than 3 mm (porphyroclasts); the second generation corresponds to smaller crystals with polygonal shapes (neoblasts < 3mm), which occur in the rock as a consequence of an intense recrystallization process.

Table 1. Modal composition of JH mantle xenoliths.

Sample	Rock type	Ol (%)	Opx (%)	Cpx (%)	Sp (%)
VE	Lherzolite	54.47	28.96	14.37	2.2
VJ	Lherzolite	52.01	32.31	13.39	2.29
IVA	Lherzolite	72.48	15.86	10.45	1.21
VF	Lherzolite	52.08	33.97	11.93	2.02
VI	Lherzolite	53.41	23.48	19.79	3.32
VG	Harzburgite	68.14	30.04	1.26	0.56
VK	Lherzolite	61.27	24.59	13.69	0.44
VH	Harzburgite	62.08	31.26	4.47	2.18
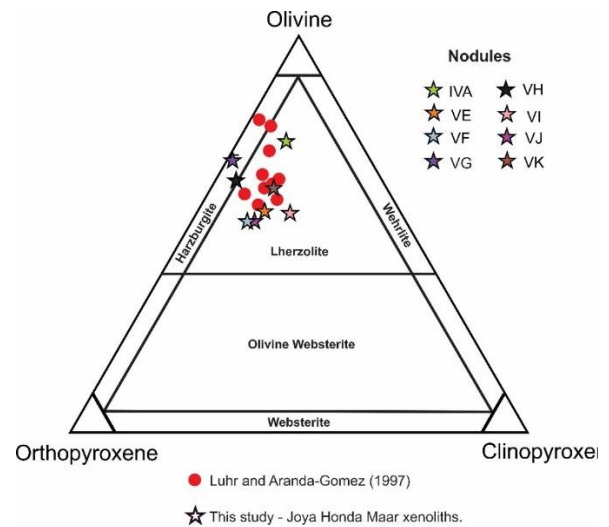
Figure 17. Ternary classification for ultramafic and mafic rocks, from Streckeisen (1976).

Olivines are present as translucent crystals without alteration. Ol porphyroclasts exhibit anhedral forms (size <4.5 mm) with curved grain boundaries, kink bands and numerous fractures due to deformation (Fig. 18A); some crystals have Opx and Cpx inclusions (<1mm) with rounded shapes. Most of the neoblasts are less than 2 mm long and are characterized by straight borders and subhedral forms. Orthopyroxenes exhibit light brown colours without alteration; opx porphyroclasts are characterized by anhedral and elongated forms with curved grain boundaries and diameters < 4.5 mm (Fig. 18B-C-D). Neoblasts exhibit euhedral forms with well-developed straight boundaries and sizes less than 2 mm; Opx tends to concentrate forming clusters of three or more crystals, where vermicular spinel is commonly observed (Fig. 18E-F); some Opx may contain small Cpx inclusions (<0.2mm). Opx may exhibit a rough areas (especially over the rims) that resembles spongy rims,

which may expand over the entire crystal (Fig. 18B-C-F). Cpx crystals are light green, with subhedral to anhedral forms, sizes < 2 mm (rare crystals with diameters greater than 4 mm are present). Spongy textures along crystal rims in Cpx are very common and varies in thickness, this texture sometimes develops as bands or affecting the entire crystal surface (Fig. 18C-G). Finally, spinel occurs as dark brown crystals with irregular shapes (anhedral forms with curved grain borders), sizes < 2 mm and develop as vermicular intergrowths in pyroxene clusters (Fig. 18E-F).

Peridotites are cut by glass veins that develop along the crystal borders, extending into single crystals as micro-fractures. Veins have variable thicknesses, the largest being 0.3 mm thick (Fig. 18D-F-H). Veins do not show a genetic relation with the host lava and are mainly formed by glass and may contain relatively large (<0.25 mm) crystals of Cpx, tiny crystals with high birefringence, identified as carbonates; and rare opaque minerals.

5.3.2. Fluid and melt inclusions

Olivine crystals contain abundant dendritic trails of secondary inclusions consisting of glass, mineral phases, and a fluid phase. Dendritic inclusion trails are intragranular and typically originate from the glass/carbonate microveins permeating the rocks (Fig. 19A). Fig. 19 shows this peculiar texture resulting from the association of large (15-30 μm) irregularly-shaped inclusions containing silicate glass (melt) with subordinate crystals and a fluid phase in variable proportions, along with smaller (<20 μm) inclusions dominated by glass (melt) or fluid, ± crystals. Similar inclusion textures are also observed in orthopyroxene and clinopyroxene, while fluid inclusions in the absence of glass, generally observed in peridotites (Andersen and Neumann, 2001; Frezzotti and Touret, 2014), are extremely rare. In inclusions, the silicate glass is colorless, isotropic, and does not show any devitrification (Fig. 19B). Mineral phases (< 30 μm) are high birefringent and texturally associated with the glass (Fig. 19C). The fluid is CO_2-rich, one or two phases (L, or L+V). Fluid-dominated inclusions may contain tiny mineral grains, among which there is an opaque phase (Fig. 19D).

5.3.3. Raman microspectroscopy

Raman microspectroscopy analyses of dendritic inclusions reveal that mineral phases texturally associated with silicate glass are Mg-calcite (Fig. 20A; vibrations at 1088, 714, 284, 158 cm^{-1}). The fluid is pure CO_2 (Fig. 20B; Fermi doublet at about 1282 -1387 cm^{-1}). Interestingly, in most CO_2 inclusions, Raman spectra also reveal the presence of dolomite (Fig. 20C; vibrations at 1094-1096, 722-723, 299-300 cm^{-1}). Dolomite vibrations, however, are unexpectedly weak (likely linked to disorder; Frezzotti et al., 2012a) and broad (full width at half maximum up to 15 cm^{-1}) (Fig. 20C). Also, the main vibration at 1098 cm^{-1} is downshifted from 2 to 4 cm^{-1}. These spectral characteristics indicate a relevant order decrease in the crystalline structure as it occurs in decomposing carbonates (Frezzotti and Peccerillo, 2007; Carteret et al., 2009; Frezzotti et al., 2012a). The tiny mineral grains observed in a few CO_2 inclusions are magnesite (Fig. 20D; vibrations at 1094, 723, 322, 202 cm^{-1}). An opaque mineral has been identified as pyrite (Fig. 20D; vibrations at 342 and 377 cm^{-1}). The association of Mg-carbonate ± pyrite in CO_2-rich inclusions is suggestive of fluid inclusion-host olivine reactions at low temperatures (Frezzotti et al., 2012b), probably during host lava cooling at the surface.
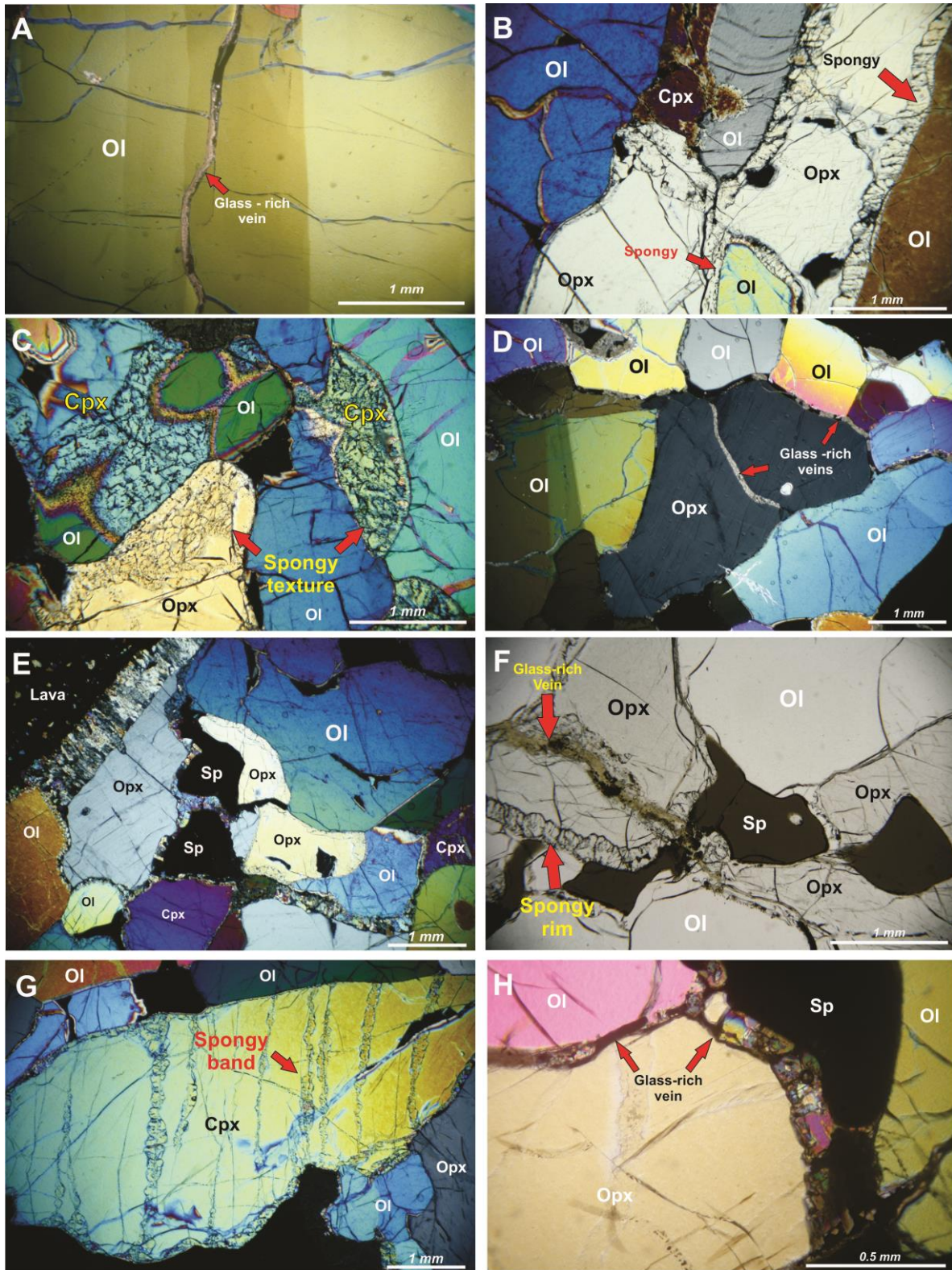
Figure 18. Microphotographs of the JH mantle xenoliths in cross-polarized light (A, B, C, D, E, G, H) and transmitted plane-polarized light (F). Ol: olivine, Opx: orthopyroxene, Cpx: clinopyroxene, Sp: spinel. A) Ol porphyroclast with well-developed kink bands and glass-rich veins. B) Spongy rims developed in Opx crystals; C) Cpx and Opx crystals are almost and totally replaced by the spongy rim. D) Porphyroclastic texture; Opx crystal being cut by a glass-rich vein. E) Opx cluster. F) Opx cluster cut by a vein composed of light brown glass and some opaque minerals, note the presence of spongy rims in Opx. G) Cpx porphyroclast with development of spongy bands. H) Glass-rich veins around Opx porphyroclast.
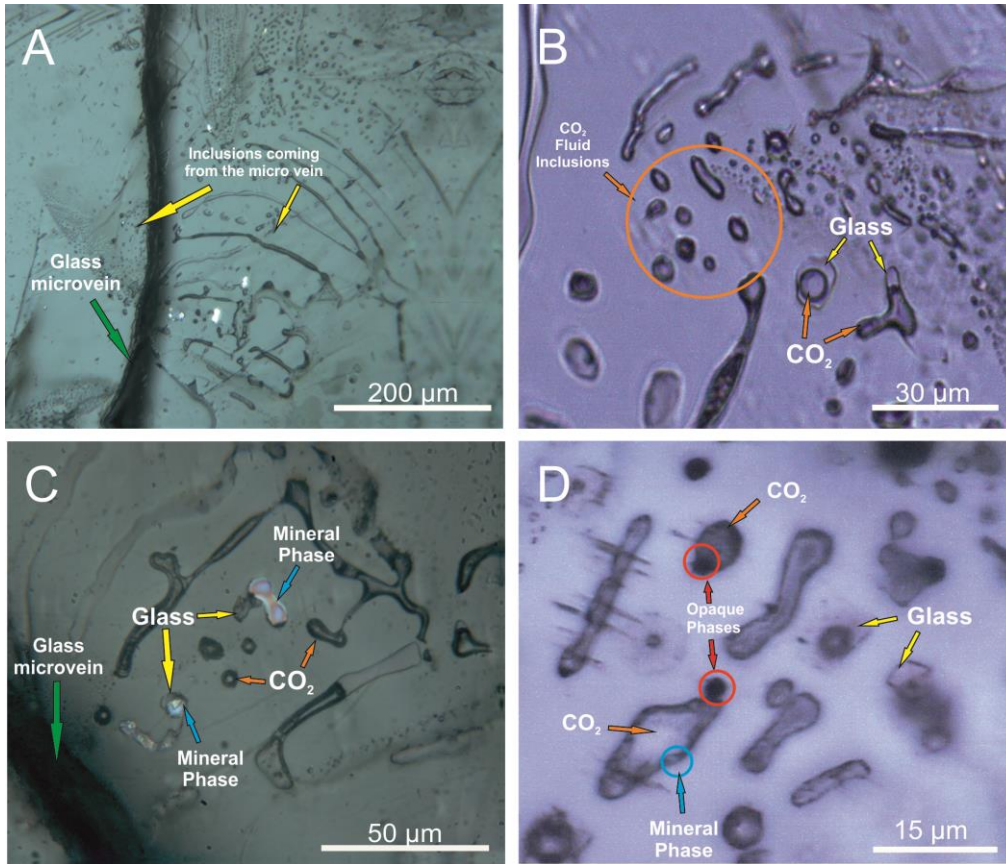
Figure 19. Microphotographs of inclusions identified in olivine. A) Melt and fluid inclusions originating from microveins. B) Intragranular trail of dendritic inclusions. C) Inclusions composed by glass and high birefringent mineral phases (cross-polarized light illumination). D) Opaque phases associated to fluid inclusions.
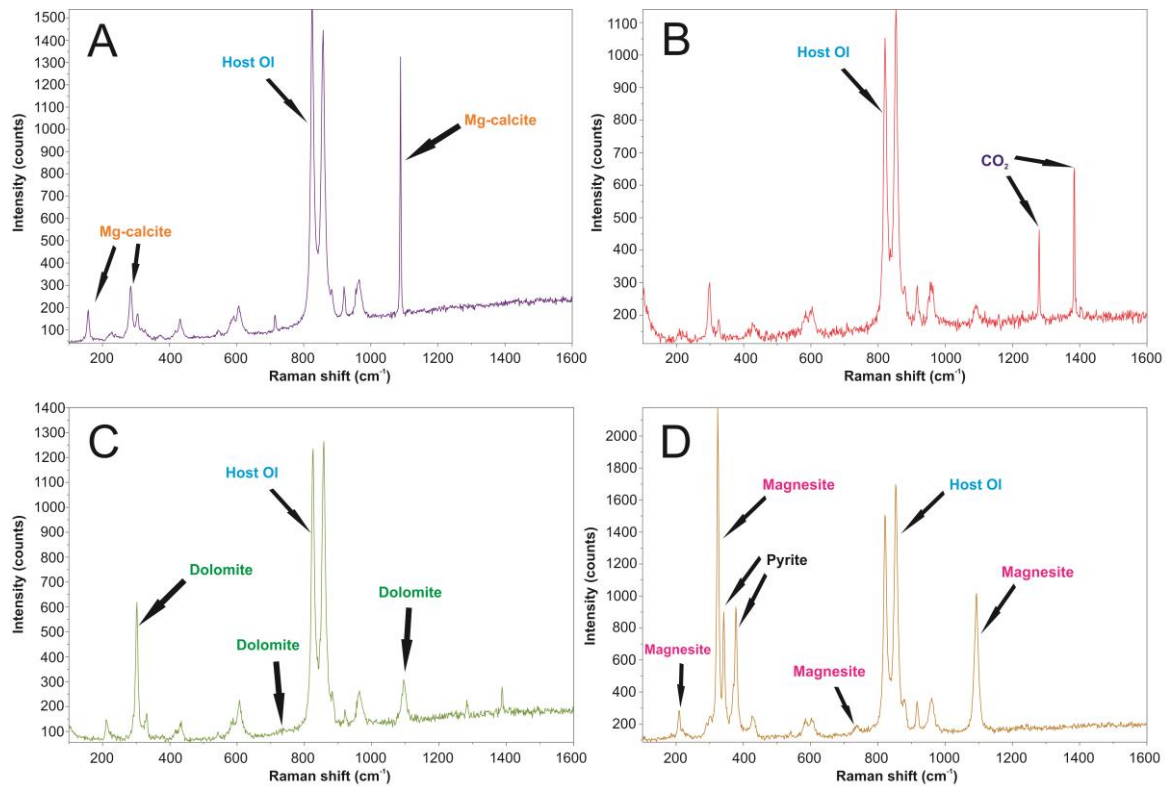
Figure 20. Raman spectroscopy applied in olivine inclusions. A) Raman spectra of birefringent mineral phases (Mg-calcite) observed in Fig. 19C. B) Raman spectra of pure CO_2 fluid inclusions identified in Fig. 19D. C) Raman spectra of dolomite contained in some inclusions of Fig. 19B. D) Raman spectra of magnesite and pyrite contained in olivine inclusions.

5.3.4. Elemental and Isotopic composition

The elemental and isotopic composition of the crystal-hosted fluid inclusions (bulk mineral crushes) in the JH mantle xenoliths are reported in Table 2; reported errors are 1σ uncertainties, except for $^{21}Ne/^{22}Ne_{ext}$ ratios whose errors are 2σ uncertainties. Concentrations of ^{4}He range between 8.56 x 10^{-14} and 1.29 x 10^{-11} mol/g where the highest concentrations are observed in Cpx (~4.28 x 10^{-12} mol/g) followed by Ol (~2.21 x 10^{-12} mol/g) and Opx (~2.06 x 10^{-12} mol/g). ^{4}He concentrations for the V-I crystals are significantly lower than those measured in other nodules. $^{40}Ar^{*}$ content ranges from 5.37 x 10^{-14} to 1.08 x 10^{-11} mol/g; in general, both $^{40}Ar^{*}$ and ^{4}He values are similar to those previously reported in mantle xenoliths from the European Subcontinental Lithospheric Mantle (European SCLM), the West Antarctic Rift System (WARS), the Eastern Australia SCLM and some regions belonging the East African Rift (Northern/Southern Kenya rifts and the Ethiopia-Afar region; Fig. 21A; Matsumoto et al., 1998, 2000; Hopp et al., 2004, 2007a, 2007b; Buikin et al., 2005; Gautheron et al., 2005a; Czuppon et al., 2009; Martelli et al., 2011; Halldórsson et al., 2014; Broadley et al., 2016; Rizzo et al., 2018; Correale et al., 2019; Faccini et al., 2020). ^{20}Ne, ^{21}Ne and ^{22}Ne values tend to be high in Cpx and Opx; ^{20}Ne ranges from 1.42 x 10^{-16} to 5.08 x 10^{-14} mol/g, ^{21}Ne from 5.22 x 10^{-19} to 1.21 x 10^{-16} mol/g and ^{22}Ne from 1.34 x 10^{-17} to 4.90 x 10^{-15} mol/g. CO_2 is the most abundant gas, on average its contents are higher in Cpx and Opx (1.02 x 10^{-7} ± 1.03 x 10^{-7} and 3.18 x 10^{-8} ± 3.71 x 10^{-8} mol/g, respectively) than in Ol (3.43 x 10^{-9} ± 6.36 x 10^{-9} mol/g); CO_2 contents are positively correlated with ^{4}He, $^{40}Ar^{*}$, ^{20}Ne, ^{21}Ne and ^{22}Ne, but are lower than those observed in European SCLM xenoliths (Fig. 21B-C). In detail, the Rc/Ra values vary as follows: Ol from 7.13 ± 0.10 to 7.68 ± 0.07 Ra (1σ), Opx from 6.15 ± 0.08 to 7.54 ± 0.08 Ra (1σ), and Cpx from 5.40 ± 0.14 to 7.59 ± 0.07 Ra (1σ). The $^{4}He/^{40}Ar^{*}$ ratios vary between 0.14 and 3.11 (Fig. 22), which overlaps in part the typical production ratio of the mantle ($^{4}He/^{40}Ar^{*} = 1-5$; Yamamoto et al., 2009; Marty, 2012); on average the highest values belong to Ol crystals (1.51 ± 0.76; 1σ), compared to Opx (0.72 ± 0.25; 1σ) and Cpx (0.78 ± 0.40; 1σ). $^{4}He/^{20}Ne$ values range from 2.4 to 10483; the highest values are recorded in Cpx and Ol (on average 2223.2 ± 3196.8 and 1498.6 ± 1306.1 (1σ), respectively), while Opx exhibits considerably lower ratios (<639). This tendency is also observed for $^{40}Ar/^{36}Ar$ ratios that vary from 303.48 ± 0.08 to 8231.50 ± 13.81 in Cpx, from 391.97 ± 1.17 to 2518.41 ± 13.00 in Ol, and from 339.74 ± 0.26 to 1436.20 ± 1.91 in Opx (1σ). It should be noted that those samples with the lowest values of Rc/Ra, also are depleted in $^{4}He/^{40}Ar^{*}$, $^{40}Ar/^{36}Ar$ and $^{4}He/^{20}Ne$. On average $^{20}Ne/^{22}Ne$ and $^{21}Ne/^{22}Ne$ ratios are 10.2 ± 0.50 and 0.0332 ± 0.0058 (1σ), respectively; in both cases, the values are slightly higher in Cpx compared to Ol and Opx. Finally, the isotope composition of CO_2 expressed as $\delta^{13}C$ values (V-PDB) varies between -0.97 and -2.86‰ and does not exhibit a systematic variation between Ol, Opx and Cpx. The most negative value (-2.86‰) was reported in IV-A Opx while the most positive values belong to two aliquots of the same nodule: V-K Ol (-1.10) and V-K Opx (-0.97).

5.4. Discussion

Present textural and Raman spectroscopy observations indicate that the JH fluid inclusions are CO_2-dominated (Figs. 19 and 20) and, even more importantly, that they are strictly associated with the pervasive infiltration of glass veins (Figs. 18 and 19). The inclusions typically exhibit the coexistence of glass, mineral phases, and a fluid phase, and form dendritic trails of fluid inclusions originating from the glass/carbonate microveins permeating the rocks (Fig. 19A). The close association between glass and fluid inclusions, and their originating from the glass microveins, are strongly suggestive of trapping of fluids delivered by degassing of a carbonate-rich silicate melt at mantle depth. Textural observations and preliminary compositional information (indicating that glass veins contain 59±3 wt % SiO_2) clearly exclude that the glass veins are related to the basanitic to basaltic host magma.
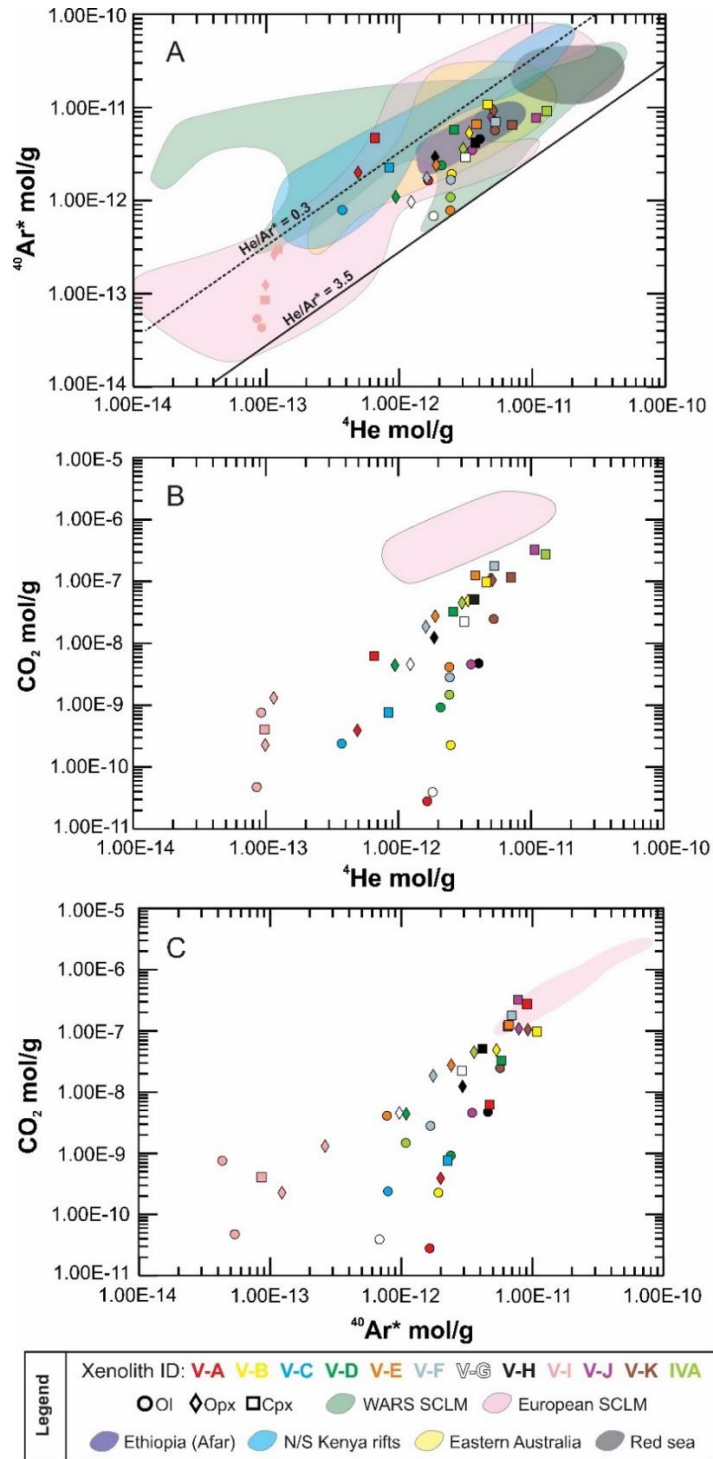
Figure 21. ^{4}He, ^{40}Ar* and CO_2 contents measured in fluid inclusions hosted in JH mantle xenoliths. SCLM: Subcontinental Lithospheric Mantle. The West Antarctic Rift System (WARS) SCLM compositional range was built using fluid inclusions data measured by Broadley et al. (2016) and Correale et al. (2019). European SCLM range includes fluid inclusions values measured in mantle xenoliths from the Rhenish Massif (Germany), Pannonian basin, Massif Central (Central France), Tallante - Calatrava (Spain), Lower Silesia (Poland) and the Eastern Transylvanian Basin; data was taken from Buikin et al. (2005), Gautheron et al. (2005a), Martelli et al. (2011), Rizzo et al. (2018) and Faccini et al. (2020). Eastern Australia SCLM data was taken from Matsumoto et al. (1998, 2000) and Czuppon et al. (2009). Red sea region data from Hopp et al. (2004, 2007a) and Halldórsson et al. (2014). Northern/Southern Kenya rifts data was taken from Hopp et al. (2007b) and Halldórsson et al. (2014). The Ethiopia (afar) field was designed after Halldórsson et al. (2014).

Table 2. Fluid inclusions compositions from JH mantle xenoliths. Concentrations are reported in mol/g. r*: reply made in sample V-I. Estimated errors for ^{3}He, ^{4}He, ^{20}Ne, ^{21}Ne, ^{22}Ne, ^{40}Ar, ^{36}Ar and CO_2 are <5%, <0.03%, <7%, <5%, <0.7%, <0.07%, <0.1% and <5%, respectively.

Sample	Phase	Weight (g)	^{3}He	^{4}He	^{20}Ne	^{21}Ne	^{22}Ne	CO_2[a]	^{40}Ar	^{36}Ar	^{40*}Ar	^{4}He/^{20}Ne	^{4}He/^{40}Ar*	R/Ra	Rc/Ra	error +/- (1σ)
V-A	Ol	0.95855	1.67E-17	1.65E-12	9.11E-16	2.72E-18	9.26E-17	2.80E-11	2.09E-12	1.50E-15	1.65E-12	1814.0	1.00	7.26	7.26	0.06
V-A	Opx	0.26388	4.74E-18	4.91E-13	8.90E-15	2.59E-17	9.00E-16	3.91E-10	3.61E-12	5.45E-15	2.00E-12	55.2	0.25	6.91	6.94	0.13
V-A	Cpx	0.21991	6.45E-18	6.57E-13	5.81E-16	2.62E-18	5.41E-17	6.23E-09	5.16E-12	1.55E-15	4.70E-12	1131.4	0.14	7.06	7.06	0.13
V-B	Ol	0.99706	2.53E-17	2.48E-12	1.84E-15	5.52E-18	1.88E-16	2.26E-10	3.70E-12	6.01E-15	1.92E-12	1349.7	1.29	7.32	7.33	0.06
V-B	Opx	0.4776	3.43E-17	3.36E-12	6.75E-15	1.97E-17	6.61E-16	4.88E-08	7.67E-12	7.95E-15	5.32E-12	497.5	0.63	7.34	7.35	0.06
V-B	Cpx	0.48584	4.67E-17	4.62E-12	4.41E-16	2.00E-18	3.61E-17	9.70E-08	1.12E-11	1.36E-15	1.08E-11	10483.3	0.43	7.27	7.27	0.06
V-C	Ol	0.59294	3.71E-18	3.74E-13	2.35E-16	n.a	2.61E-17	2.38E-10	8.96E-13	3.56E-16	7.91E-13	1593.9	0.47	7.13	7.13	0.10
V-C	Cpx	0.5587	8.55E-18	8.40E-13	5.73E-16	1.82E-18	5.87E-17	7.61E-10	2.57E-12	1.02E-15	2.27E-12	1466.6	0.37	7.32	7.33	0.07
V-D	Ol	1.02241	2.08E-17	2.08E-12	3.76E-16	1.25E-18	3.67E-17	9.18E-10	2.76E-12	1.27E-15	2.38E-12	5534.0	0.87	7.19	7.19	0.06
V-D	Opx	0.49922	9.46E-18	9.43E-13	2.33E-15	7.04E-18	2.39E-16	4.39E-09	2.07E-12	3.30E-15	1.09E-12	404.4	0.86	7.21	7.22	0.08
V-D	Cpx	0.47389	2.66E-17	2.59E-12	3.02E-16	1.23E-18	2.73E-17	3.25E-08	6.01E-12	7.58E-16	5.78E-12	8576.0	0.45	7.37	7.37	0.07
V-E	Ol	1.02916	2.51E-17	2.42E-12	1.22E-15	3.90E-18	1.19E-16	4.11E-09	8.79E-13	3.38E-16	7.79E-13	1982.0	3.11	7.47	7.47	0.07
V-E	Opx	0.51352	1.98E-17	1.90E-12	5.12E-15	1.56E-17	5.16E-16	2.74E-08	3.03E-12	2.11E-15	2.41E-12	371.6	0.79	7.49	7.50	0.07
V-E	Cpx	0.32954	3.96E-17	3.81E-12	3.93E-15	1.27E-17	3.81E-16	1.25E-07	7.06E-12	1.50E-15	6.62E-12	970.0	0.58	7.48	7.48	0.07
V-F	Ol	1.01203	2.57E-17	2.44E-12	3.49E-15	1.05E-17	3.55E-16	2.81E-09	2.50E-12	2.81E-15	1.67E-12	700.6	1.46	7.57	7.57	0.07
V-F	Opx	0.52681	1.66E-17	1.61E-12	4.91E-15	1.51E-17	4.98E-16	1.85E-08	2.37E-12	2.11E-15	1.75E-12	328.5	0.92	7.41	7.42	0.08
V-F	Cpx	0.31734	5.58E-17	5.29E-12	2.01E-14	6.07E-17	1.99E-15	1.78E-07	1.06E-11	1.24E-14	6.98E-12	262.9	0.76	7.58	7.59	0.07
V-G	Ol	1.00336	1.94E-17	1.81E-12	7.91E-16	2.44E-18	7.78E-17	3.91E-11	1.19E-12	1.72E-15	6.81E-13	2292.1	2.66	7.68	7.68	0.07
V-G	Opx	0.50526	1.29E-17	1.23E-12	3.20E-15	9.62E-18	3.26E-16	4.54E-09	1.47E-12	1.69E-15	9.68E-13	384.5	1.27	7.53	7.53	0.08
V-G	Cpx	0.32136	3.21E-17	3.15E-12	1.57E-15	5.55E-18	1.52E-16	2.24E-08	3.17E-12	9.41E-16	2.89E-12	2003.4	1.09	7.32	7.32	0.07
V-H	Ol	1.0181	4.21E-17	4.03E-12	4.72E-15	1.47E-17	4.66E-16	4.72E-09	6.44E-12	6.29E-15	4.58E-12	853.7	0.88	7.51	7.52	0.08
V-H	Opx	0.53853	1.95E-17	1.86E-12	4.01E-14	1.16E-16	3.94E-15	1.23E-08	1.52E-11	4.14E-14	2.93E-12	46.5	0.64	7.47	7.52	0.08
V-H	Cpx	0.30754	3.92E-17	3.73E-12	3.52E-15	1.13E-17	3.46E-16	5.09E-08	4.74E-12	1.93E-15	4.17E-12	1062.1	0.90	7.56	7.56	0.07
V-I	Ol	1.0437	8.62E-19	8.56E-14	1.42E-16	5.22E-19	1.39E-17	4.74E-11	2.25E-13	5.78E-16	5.37E-14	604.6	1.59	7.24	7.25	0.13
V-I	Opx	0.5057	9.92E-19	9.93E-14	1.55E-16	6.59E-19	1.34E-17	2.26E-10	3.77E-13	8.58E-16	1.23E-13	639.0	0.8	7.18	7.19	0.15
V-I	Cpx	0.49525	9.34E-19	1.23E-13	5.08E-14	1.46E-16	4.90E-15	n.a	1.13E-11	3.72E-14	2.97E-13	2.4	0.41	4.84	5.46	0.14
V-I r*	Ol	1.01139	9.47E-19	9.25E-14	4.09E-16	1.32E-18	4.07E-17	7.54E-10	1.75E-13	4.48E-16	4.32E-14	226.0	2.14	7.36	7.37	0.17
V-I r*	Opx	0.50086	9.81E-19	1.15E-13	1.13E-14	3.37E-17	1.14E-15	1.31E-09	2.02E-12	5.94E-15	2.63E-13	10.1	0.44	5.98	6.15	0.08
V-I r*	Cpx	0.57112	7.37E-19	9.81E-14	9.68E-15	2.89E-17	9.72E-16	4.07E-10	5.64E-13	1.62E-15	8.59E-14	10.1	1.14	5.26	5.40	0.14
V-J	Ol	1.0333	3.63E-17	3.53E-12	3.77E-15	1.15E-17	3.76E-16	4.55E-09	5.30E-12	6.20E-15	3.47E-12	937.0	1.02	7.38	7.38	0.07
V-J	Opx	0.5061	5.02E-17	4.93E-12	7.60E-15	2.36E-17	7.58E-16	1.08E-07	1.02E-11	7.88E-15	7.87E-12	649.1	0.63	7.32	7.33	0.08
V-J	Cpx	0.30875	1.11E-16	1.07E-11	6.19E-15	2.02E-17	6.07E-16	3.23E-07	8.59E-12	2.87E-15	7.75E-12	1726.7	1.38	7.50	7.50	0.07
V-K	Ol	1.0225	5.42E-17	5.24E-12	4.99E-15	1.58E-17	4.99E-16	2.46E-08	7.72E-12	6.93E-15	5.67E-12	1049.9	0.92	7.45	7.45	0.08
V-K	Opx	0.52687	5.37E-17	5.13E-12	2.48E-14	7.37E-17	2.38E-15	1.05E-07	1.54E-11	2.07E-14	9.25E-12	206.6	0.55	7.53	7.54	0.08
V-K	Cpx	0.30567	7.40E-17	7.07E-12	4.08E-14	1.21E-16	4.11E-15	1.16E-07	1.06E-11	1.40E-14	6.47E-12	173.4	1.09	7.52	7.53	0.07
IV A	Ol	1.03046	2.52E-17	2.43E-12	4.47E-15	1.29E-17	4.34E-16	1.47E-09	2.09E-12	3.40E-15	1.08E-12	543.9	2.24	7.45	7.45	0.08
IV A	Opx	0.49715	3.04E-17	3.02E-12	1.05E-14	3.07E-17	1.03E-15	4.49E-08	5.48E-12	6.38E-15	3.59E-12	286.9	0.84	7.23	7.23	0.10
IV A	Cpx	0.47966	1.29E-16	1.29E-11	1.25E-14	3.82E-17	1.22E-15	2.73E-07	1.20E-11	9.65E-15	9.11E-12	1033.2	1.42	7.21	7.21	0.06

Table 2. Continued. [a.] First estimation of CO_2 during noble gases analysis; [b.] CO_2 measured from glass line.

Sample	Phase	$^{40}Ar/^{36}Ar$	error +/- (1σ)	$^{20}Ne/^{22}Ne$	error +/- (1σ)	$^{21}Ne/^{22}Ne$	error +/- (1σ)	$(^{21}Ne/^{22}Ne)$ EX to 12.5	error +/- (2σ)	$CO_2/^3He$	$^3He/^{36}Ar$	$CO_2/^3He$	CO_2[b]	$δ^{13}C$
V-A	Ol	1391.46	1.24	9.93	0.06	0.0297	0.00135	0.043	0.003	1.68E+06	0.0111	n.a	n.a	n.a
V-A	Opx	662.11	0.93	9.87	0.04	0.0288	0.00050	n.a	n.a	8.24E+07	0.0009	n.a	n.a	n.a
V-A	Cpx	3320.08	9.83	n.a	n.a	n.a	n.a	n.a	n.a	9.66E+08	0.0041	n.a	n.a	n.a
V-B	Ol	614.85	0.37	9.87	0.04	0.0296	0.00082	0.053	0.003	8.93E+06	0.0042	n.a	n.a	n.a
V-B	Opx	964.58	0.65	9.97	0.03	0.0298	0.00045	0.041	0.001	1.42E+09	0.0043	2.58E+09	1.17E-07	-2.30
V-B	Cpx	8231.50	13.81	12.18	0.26	0.0553	0.00431	n.a	n.a	2.07E+09	0.0343	n.a	n.a	n.a
V-C	Ol	2518.41	13.00	n.a	n.a	n.a	n.a	n.a	n.a	6.43E+07	0.0104	n.a	n.a	n.a
V-C	Cpx	2511.64	5.81	n.a	n.a	n.a	n.a	n.a	n.a	8.90E+07	0.0084	n.a	n.a	n.a
V-D	Ol	2177.87	2.53	10.57	0.16	0.0354	0.00227	n.a	n.a	4.41E+07	0.0164	n.a	n.a	n.a
V-D	Opx	626.23	0.62	n.a	n.a	n.a	n.a	n.a	n.a	4.64E+08	0.0029	n.a	n.a	n.a
V-D	Cpx	7926.55	24.39	11.03	0.39	0.0452	0.00659	n.a	n.a	1.22E+09	0.0350	1.61E+09	4.27E-08	-1.55
V-E	Ol	2598.15	11.14	10.37	0.07	0.0332	0.00107	0.049	0.003	1.64E+08	0.0743	n.a	n.a	n.a
V-E	Opx	1436.20	1.91	10.00	0.04	0.0306	0.00046	0.050	0.002	1.39E+09	0.0094	n.a	n.a	n.a
V-E	Cpx	4719.85	15.56	10.25	0.05	0.0338	0.00115	0.058	0.004	3.16E+09	0.0265	9.17E+08	3.63E-08	-2.66
V-F	Ol	889.63	0.69	9.87	0.04	0.0297	0.00064	n.a	0.003	1.09E+08	0.0091	n.a	n.a	n.a
V-F	Opx	1123.07	1.53	9.93	0.04	0.0307	0.00072	0.063	0.003	1.11E+09	0.0079	1.15E+09	1.91E-08	-1.34
V-F	Cpx	856.84	0.53	10.12	0.03	0.0306	0.00045	0.042	0.001	3.18E+09	0.0045	1.12E+09	6.22E-08	-1.66
V-G	Ol	690.44	0.68	10.23	0.06	0.0316	0.00117	0.045	0.003	2.02E+06	0.0112	n.a	n.a	n.a
V-G	Opx	866.39	1.50	9.85	0.04	0.0296	0.00062	n.a	n.a	3.52E+08	0.0076	n.a	n.a	n.a
V-G	Cpx	3371.87	14.57	11.06	0.11	0.0390	0.00227	n.a	n.a	6.97E+08	0.0341	n.a	n.a	n.a
V-H	Ol	1023.71	0.63	10.18	0.03	0.0317	0.00041	0.048	0.001	1.12E+08	0.0067	n.a	n.a	n.a
V-H	Opx	366.42	0.00	10.11	0.02	0.0301	0.00027	0.039	0.001	6.33E+08	0.0005	n.a	n.a	n.a
V-H	Cpx	2457.00	6.70	10.15	0.05	0.0326	0.00104	0.056	0.004	1.30E+09	0.0203	n.a	n.a	n.a
V-I	Ol	388.43	0.86	n.a	n.a	n.a	n.a	n.a	n.a	5.50E+07	0.0015	n.a	n.a	n.a
V-I	Opx	439.10	1.49	11.59	0.73	0.0492	0.01944	n.a	n.a	2.28E+08	0.0586	n.a	n.a	n.a
V-I	Cpx	303.48	0.16	10.24	0.01	0.0323	0.00025	n.a	n.a	0.00E+00	0.0000	n.a	n.a	n.a
V-I r*	Ol	391.97	1.17	10.39	0.16	0.0336	0.00251	n.a	n.a	7.95E+08	0.0021	n.a	n.a	n.a
V-I r*	Opx	339.74	0.26	9.91	0.03	0.0296	0.00029	n.a	n.a	1.33E+09	0.0002	n.a	n.a	n.a
V-I r*	Cpx	348.57	0.56	9.98	0.03	0.0298	0.00034	n.a	n.a	5.52E+08	0.0005	n.a	n.a	n.a
V-J	Ol	854.91	0.48	10.05	0.03	0.0307	0.00053	0.047	0.002	1.25E+08	0.0058	n.a	n.a	n.a
V-J	Opx	1294.25	0.87	10.08	0.03	0.0313	0.00056	0.051	0.002	2.15E+09	0.0064	3.82E+09	1.92E-07	-2.13
V-J	Cpx	2993.26	5.58	10.24	0.03	0.0335	0.00071	0.056	0.002	2.90E+09	0.0388	2.10E+09	2.34E-07	-1.30
V-K	Ol	1114.13	0.00	10.07	0.03	0.0319	0.00049	0.058	0.002	4.54E+08	0.0078	3.82E+08	2.07E-08	-1.10
V-K	Opx	741.96	0.00	10.32	0.02	0.0316	0.00031	0.042	0.001	1.95E+09	0.0026	1.88E+09	1.01E-07	-2.08
V-K	Cpx	756.34	0.50	9.92	0.02	0.0296	0.00029	0.041	0.001	1.57E+09	0.0053	3.38E+08	2.50E-08	-0.97
IV A	Ol	614.05	0.43	10.14	0.04	0.0303	0.00050	0.039	0.001	5.84E+07	0.0074	n.a	n.a	n.a
IV A	Opx	858.77	0.49	10.10	0.03	0.0298	0.00045	n.a	n.a	1.48E+09	0.0048	2.22E+09	6.76E-08	-2.86
IV A	Cpx	1238.93	24.70	10.25	0.03	0.0314	0.00047	0.043	0.001	2.11E+09	0.0134	1.18E+09	1.52E-07	-1.25

In view of the above, and in line with previous work (Liang and Elthon, 1990; Luhr and Aranda-Gomez, 1997), we relate the fluid inclusions trapped in JH xenoliths to a melt-related metasomatic event deep in the source mantle. The overprinted textures in Cpx along crystal rims (named as spongy rims by Luhr and Aranda-Gómez, 1997) (see Fig. 18) have also been associated to this metasomatic event (Liang and Elthon, 1990).

In the discussion below, we combined the above petrographic evidence and the isotopic signatures (noble gases and CO_2) of the JH fluid inclusions to constrain volatile origin and mantle characteristics. However, an initial screening of the dataset was necessary to filter out samples that have suffered from to secondary processes affecting fluid inclusion compositions. The filtered dataset is used below to infer volatile sources ad processes deep in the mantle.

5.4.1. Diffusive Fractionation

As shown in Fig. 21, the lowest noble gas concentrations (especially helium) were measured in V-I crystals and, to a minor extent, in V-A and V-C ($^4He < 10^{-12}$ mol/g). Some CO_2 depletion is also evident in sample V-I (Fig. 21C). When plotting ^3He, ^4He, $^{40}Ar^*$, and $^4He/^{40}Ar^*$ vs. Rc/Ra (Figs. 22 and 23), we find that in sample V-I the He and Ar depletion is also accompanied by $^3He/^4He < 6.15$ Ra, which are sensibly lower than the dataset average (7.39 ± 0.14 Ra; 1σ, n = 30). In samples V-A and V-C, the $^3He/^4He$ decrease is less important. It is worth noting that the lower Rc/Ra values mostly correspond to pyroxenes (Opx and Cpx) from the same nodule, while Ol crystals are less or not modified. Indeed, Ol from V-I show $^3He/^4He$ values (7.25 – 7.37 Ra) that are within the above reported average of the dataset.

Following Burnard et al. (1998), Burnard (2004) and Yamamoto et al. (2009), this data variability can be interpreted as due to preferential loss of He (relative to Ar and CO_2) due to diffusive fractionation. In fact, in case of radiogenic ^4He in-growth or addition to fluid inclusions, an increase of ^4He concentration with decreasing $^3He/^4He$ values should be expected, without any relative decrease of ^3He, $^{40}Ar^*$, and $^4He/^{40}Ar^*$. We highlight that He diffusion into the fast flowing melt-filled dissolution channels cutting the mantle is commonly invoked during partial melting (Burnard, 2004; Yamamoto et al., 2009; Faccini et al., 2020) and/or metasomatism of solid mantle that prevalently affects pyroxene crystals. Previous studies suggest that the ^4He diffusion coefficient is considerably higher than that of ^{40}Ar ($D^4He/D^{40}Ar$ = 3.16 in solid mantle; Burnard, 2004; Yamamoto et al., 2009); this is fundamentally based on the assumption that the difference in the atomic masses of the two elements are the key controls of their different diffusion coefficients. Likewise, the difference in mass between ^3He and ^4He implies important differences in their diffusivities (D^3He/D^4He = 1.15; Trull and Kurz, 1993; Burnard, 2004; Yamamoto et al., 2009). Hence, in case of diffusive loss of He, a decrease in $^3He/^4He$ and $^4He/^{40}Ar^*$ is expected, as observed in V-A and V-I pyroxenes. Because the clearest evidence of diffusive fractionation is observed in pyroxenes, we exclude V-C because Ol from this sample show $^3He/^4He$ values (7.13 Ra) comparable to Opx (7.33 Ra) from the same nodule (although Ol have lower He concentrations). In any case, in order to properly interpret the origin of the He in the following sections of the discussion, pyroxenes from V-I and V-A nodules will not be discussed further.

To support the hypothesis of a diffusive fractionation, in Figs. 22 and 23A-B-C we model this process based on the approach proposed by Burnard et al. (1998), Burnard (2004), Yamamoto et al. (2009), and already applied in Boudoire et al. (2020) and Faccini et al. (2020). We consider a starting mantle composition of ^3He = 1.56 x 10^{-17} mol/g, ^4He = 1.5 x 10^{-12} mol/g, and $^{40}Ar^*$ = 6 x 10^{-13} mol/g, which corresponds to the lowest concentrations of these species in nodules not evidently modified by diffusion. We additionally use a starting $^4He/^{40}Ar^*$ = 2.5 (the average mantle production ratio),

and a $^3He/^4He = 7.5$ Ra, which is within the Rc/Ra variability of the dataset. According to our modeling, diffusive fractionation is able to justify the data variability observed in pyroxene from V-A and V-I samples, which will not be discussed anymore.
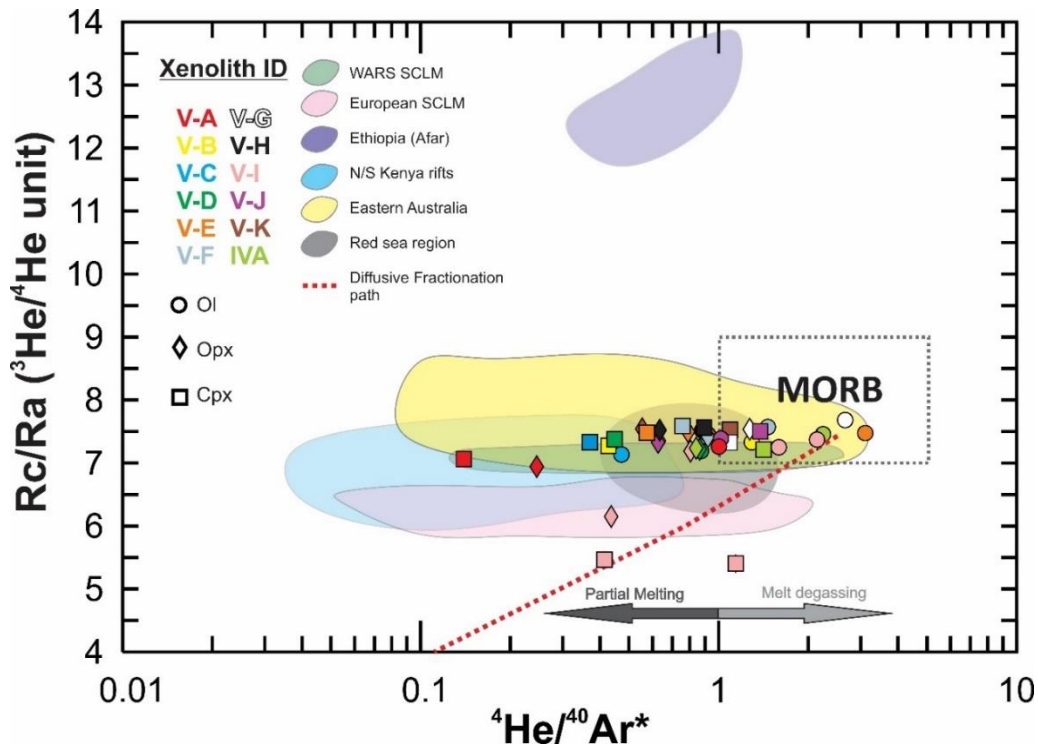
Figure 22. $^4He/^{40}Ar^*$ vs $^3He/^4He$ corrected for air contamination (Rc/Ra) ratios of fluid inclusions from JH mantle xenoliths. MORB range is reported at Rc/Ra = 8 ± 1 (Graham, 2002) and $^4He/^{40}Ar^*$ from 1 to 5 (Yamamoto et al., 2009). The WARS SCLM, European SCLM, Ethiopia (Afar), N/S Kenya rifts, Eastern Australia SCLM and Red sea compositional ranges were built using fluid inclusions data cited in Fig. 21. The diffusive fractionation path is modeled using the diffusion coefficient (D) of ^3He, ^4He, and $^{40}Ar^*$ ($D^3He/D^4He=1.15$ and $D^4He/D^{40}Ar=3.16$ in solid mantle (Burnard, 2004; Yamamoto et al., 2009). Partial melting (see arrow) can lead to decreasing $^4He/^{40}Ar^*$ (see subsection 5.4.3).

5.4.2. *Exposure to cosmic rays*

Several studies have shown that rocks exposed to cosmic rays (i.e. after eruption) favor the accumulation of ^3He in the crystal lattices shifting the original $^3He/^4He$ ratios to higher values (Kurz, 1986; Lal, 1987; Dunai and Baur, 1995; Dunai, 2010; Broadley et al., 2016; Nesterenok and Yakubovich, 2016; Correale et al., 2019). According to e.g. Dunai and Baur (1995) and Correale et al. (2019 and references therein), crystals with low He concentrations are more prone to changes due to the diffusion of ^3He from lattices into the fluid inclusions. However, in the case of the JH mantle xenoliths, the aliquots with the lowest He contents ($^3He <10^{-17}$ and $^4He < 10^{-12}$; Fig. 23A-B) generally show an opposite effect, that is a decrease in $^3He/^4He$ compared to the samples with the highest helium concentrations that we interpreted as the result of diffusive fractionation. The eruption time of JH xenoliths (311 ± 19 ka; Saucedo et al., 2017) limits the exposure time to cosmic rays. Finally, the single step crushing method prevents the contribution of secondary He accumulated in the crystal lattice (cosmogenic ^3He and radiogenic ^4He), as evidenced by other authors (Kurz, 1986; Graham, 2002; Rizzo et al., 2018; Correale et al., 2019; Faccini et al., 2020). We therefore conclude that the effect of cosmogenic ^3He in our samples is negligible.
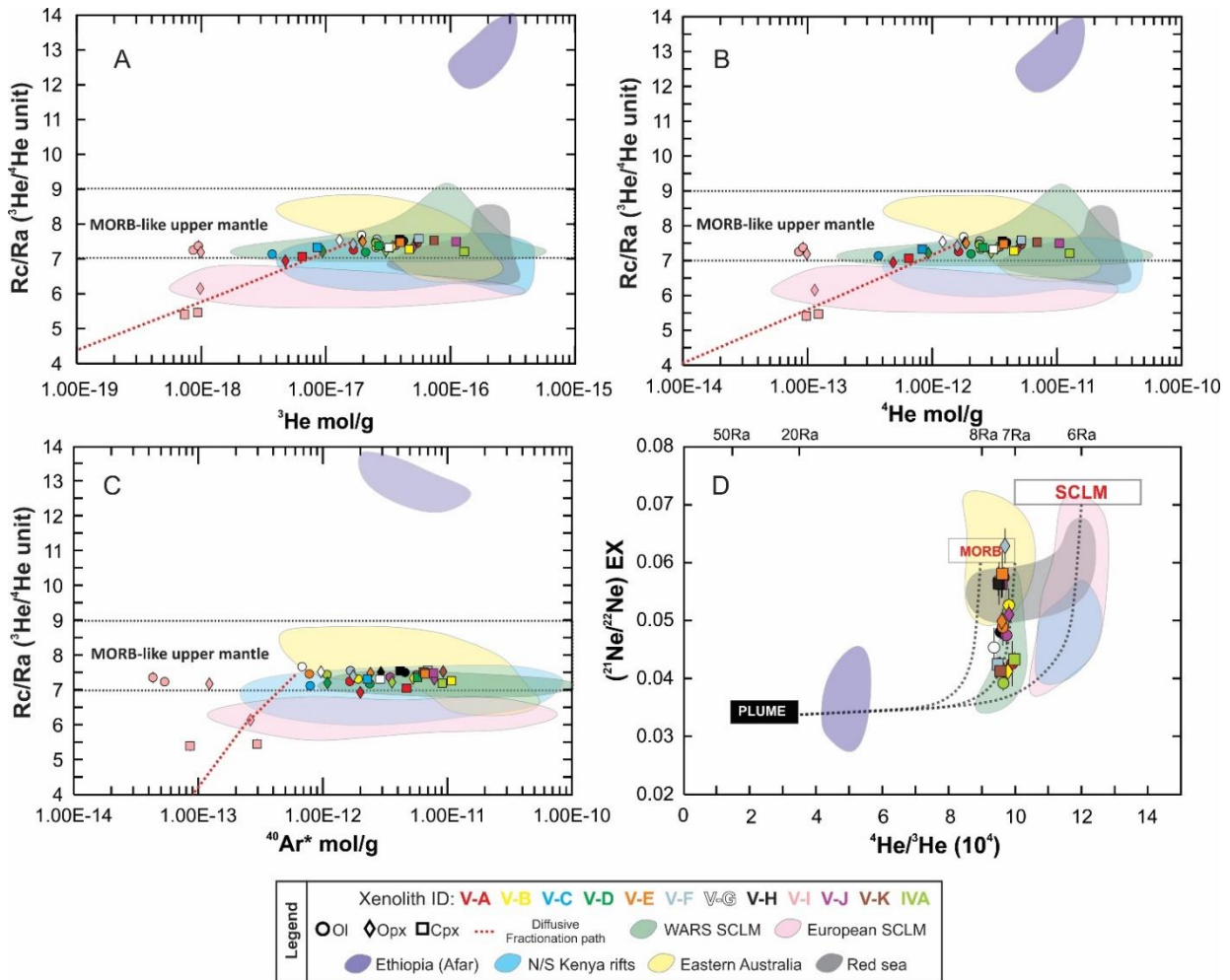
Figure 23. A) [3]He, B) [4]He and C) [40]Ar* vs [3]He/[4]He corrected for air contamination (Rc/Ra). MORB range is report ed at Rc/Ra = 8 ± 1 (Graham, 2002). D) [21]Ne/[22]Ne $_{EX}$ ratios vs [4]He/[3]He ratios, adapted from Hopp et al. (2004) and Halldórsson et al. (2014). Values with 2σ uncertainties <10% are plotted. Dotted lines are binary mixing between three endmembers: 1) Plume, at 20Ra and [21]Ne/[22]Ne $_{EX}$ = 0.034 ± 0.001, 2) MORB-like upper mantle at 8 Ra, 7 Ra and [21]Ne/[22]Ne $_{EX}$ = 0.06 ± 0.001 and SCLM at 6.1 ± 0.9 Ra and [21]Ne/[22]Ne $_{EX}$ = 0.07 ± 0.001.

5.4.3. Effects on fluid inclusions by mantle melting and/or fluid-melt partitioning

It has been previously inferred that the noble gas signature of mantle xenoliths can depend to some extent on the melting history of the mantle source, and that the [4]He/[40]Ar* ratio is a useful tracer to recognize relative variations of partial melting degree in mantle xenoliths (Graham, 2002; Burnard, 2004; Yamamoto et al., 2009; Correale et al., 2012, 2016, 2019; Rizzo et al., 2018; Faccini et al., 2020). The utility of [4]He/[40]Ar* stands on the different mineral/melt partition coefficients of the two elements (e.g., olivine, DHe =0.00017 and DAr =0.0011; Heber et al., 2007). In detail, it is suggested that, even considering the wide uncertainties in the derived partition coefficients (Heber et al., 2007), He is more incompatible than Ar, and can thus escape the mantle more effectively during partial melting, ultimately causing a [4]He/[40]Ar* decrease in the mantle residuum (Burnard, 2004; Heber et al., 2007; Yamamoto et al., 2009). This possible mantle partial melting trend is indicated in Fig. 22.

In the JH nodules, the majority of Ol crystals have [4]He/[40]Ar* values within the typical production ratio of a fertile mantle ([4]He/[40]Ar* = 1-5; Marty, 2012), while Opx and Cpx crystals exhibit slightly lower [4]He/[40]Ar* ratios, from 0.4 to 1.4. In general, the [4]He/[40]Ar* population of our samples could

imply that mantle melting may have to some extent impacted the Opx and Cpx noble gas signature, but not that of Ol, ultimately suggesting a low degree of partial melting. However, any detailed consideration on this process is prevented by the lack of mineral chemistry in our samples to be compared to the composition of fluid inclusions. In addition, we stress that the degrees of partial melting are not well constrained on petrological basis for the JH spinel lherzolites, as a wide range (7-22%) has been proposed in previous work (Liang and Elthon, 1990).

The mentioned behavior of ^{4}He/^{40}Ar* in relation to partial melting is valid if fluid inclusions trapped in mantle minerals represent a residuum rather than inclusions degassed from melt(s) percolating and metasomatizing the local mantle. Nevertheless, our suite of samples exhibits textural evidence of interstitial glass veins bearing dendritic trails of secondary melt and fluid inclusions related to pervasive mantle metasomatism driven by carbonate-rich silicate melt. This suggests that the composition of fluid inclusions (e.g., ^{4}He/^{40}Ar*) could also, or alternatively (to mantle melting), be influenced by fluid-melt partitioning from the metasomatizing melt. In fact, assuming a mantle with ^{4}He/^{40}Ar*=1, and considering the olivine/melt partition coefficient proposed by Heber et al. (2007), the first melt should have ^{4}He/^{40}Ar*=6.5 while the first gas exsolved from the melt should have ^{4}He/^{40}Ar*=0.92 (assuming a solubility ratio SHe/SAr~7; Lux, 1987). This implies, that a metasomatizing melt poorly or slightly degassed would equally fit most of the dataset. According to the petrographic evidence, metasomatic melt degassing seems the most reasonable process to explain most of our fluid inclusions compositional variability.

5.4.4 Inferences on the noble gas signature of the JH source mantle

5.4.4.1. Interaction with atmospheric fluids and evidence for a recycled atmospheric component

In order to correctly interpret the noble gas data obtained in fluid inclusions from the JH mantle xenoliths, it is necessary to evaluate the interaction with atmospheric fluids. It is well known that Ar and Ne are more susceptible (relative to He) to contamination, due to their higher abundances in atmosphere relative to the mantle fluids. For this reason, tracers such as ^{40}Ar and ^{36}Ar, ^{4}He/^{20}Ne, ^{20}Ne/^{22}Ne, ^{21}Ne/^{22}Ne, and ^{40}Ar/^{36}Ar are normally used to investigate the isotopic contribution from the atmosphere (Matsumoto et al., 2001; Gurenko et al., 2006; Hopp et al., 2004, 2007a, 2007b; Nuccio et al., 2008; Martelli et al., 2014; Oppenheimer et al., 2014; Rizzo et al., 2018). Helium, Ne and Ar systematics suggest the existence of an atmospheric component in our samples (especially in nodule V-I). In general, the measured R/Ra and ^{4}He/^{20}Ne values fall along an air-MORB mixing curve, and overlap with those measured in mantle xenoliths from the European SCLM, the West Antarctic Rift System (WARS), Eastern Australia, Red sea region and N/S Kenya rifts (Fig. 24A). The existence of such an atmospheric component is corroborated by ^{40}Ar/^{36}Ar and ^{20}Ne/^{22}Ne ratios significantly below the expected MORB values (44,000 and 12.5, respectively; Burnard et al., 1997; Moreira et al., 1998; Sarda, 2004). As shown in Fig. 24B, ^{40}Ar/^{36}Ar and ^{3}He/^{36}Ar values also fall along a two-component mixing between a MORB-like upper mantle and atmosphere (He/Ar* ratios of 0.14 to 3.5 explain the whole data variability; see also Fig. 25B). Likewise, samples fit the binary mixing air-MORB when using the three-isotope neon plot (Fig. 24C), confirming the existence of atmospheric fluids in our inclusions. The atmospheric component is especially notable in nodule V-I that exhibits an isotopic signature close to that of air with ^{4}He/^{20}Ne ratios below 10 (for Opx and Cpx) and ^{40}Ar/^{36}Ar values below 392. These compositions confirm that this nodule likely suffered secondary processes that modified its pristine mantle signature. This sample is therefore not considered representative of the local SCLM (and omitted from the following discussion).
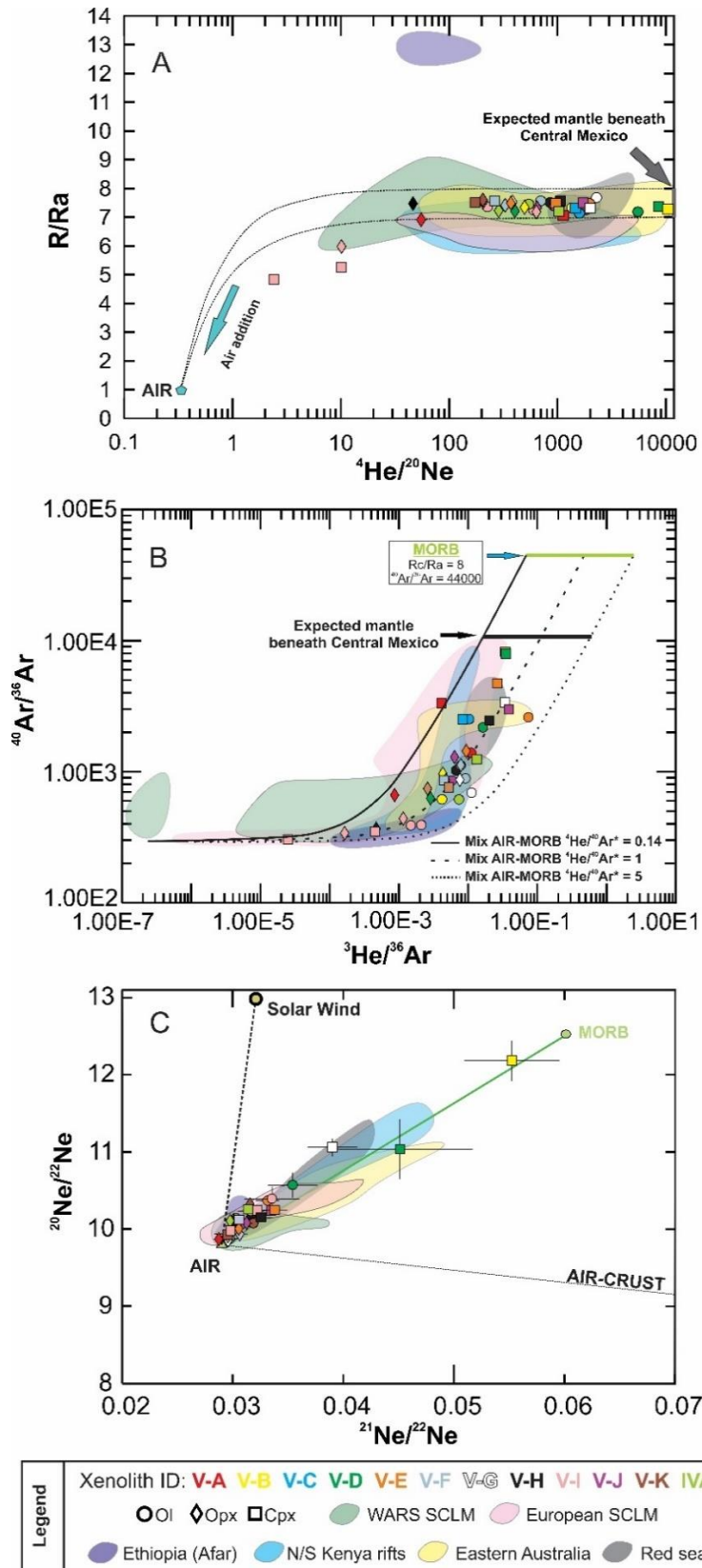
Figure 24. A) $^4He/^{20}Ne$ vs R/Ra diagram, the solid lines represent the binary mixing between air and an upper mantle source with R/Ra values between 7 and 8, B) $^3He/^{40}Ar$ vs $^{40}Ar/^{36}Ar$ diagram. C) $^{21}Ne/^{22}Ne$ vs. $^{20}Ne/^{22}Ne$ diagram in which the green line represents the binary mixing air-MORB mantle as defined by Sarda (2004) and Moreira et al. (1998) at $^{21}Ne/^{22}Ne_{air} = 0.029$ and $^{20}Ne/^{22}Ne_{air} = 9.8$ and $^{21}Ne/^{22}Ne = 0.06$ and $^{20}Ne/^{22}Ne = 12.5$; the primordial neon composition is reported as Solar wind at $^{21}Ne/^{22}Ne = 0.0328$ and $^{20}Ne/^{22}Ne = 13.8$ (Heber et al., 2009); the crust endmember was plotted at $^{21}Ne/^{22}Ne = 0.6145$ and $^{20}Ne/^{22}Ne = 0.3$ (Kennedy et al., 1990). The WARS SCLM, European SCLM, Ethiopia (Afar), N/S Kenya rifts, Eastern Australia SCLM and Red Sea compositional ranges were built using fluid inclusions data cited in Fig. 21.

The atmospheric component identified in the fluid inclusions may derive from two main possible processes, as summarized by Nuccio et al. (2008), Martelli et al. (2011), Correale et al. (2012), Rizzo et al. (2018), Faccini et al. (2020): a) air entrapment in crystal fractures during or after eruption of transporting lava, and b) the interaction with subducted atmospheric fluids recycled in the upper mantle.

Although air entrapment in crystals microcracks cannot be totally discarded due to surface exposure of the xenoliths over the last 300 ky, the positive relation between ^{3}He and ^{36}Ar suggests a deep origin (Fig. 25A), i.e., a recycled atmospheric component in the lithospheric mantle likely inherited from subduction (Matsumoto et al., 2001). In view of the above, and with the aim of constraining the ^{40}Ar/^{36}Ar signature expected for the local mantle, we also evaluate the relationship between ^{20}Ne/^{22}Ne and ^{40}Ar/^{36}Ar ratios (Fig. 25B), using the approach used by Langmuir et al. (1978) and Hopp et al. (2007a). Considering an upper mantle ^{20}Ne/^{22}Ne equal to 12.5 (Sarda et al., 1988; Moreira et al., 1998), ^{36}Ar/^{22}Ne ratios between 4.21 and 93.5, a maximum ^{4}He/^{20}Ne ratio of 11,000 and ^{4}He/^{40}Ar* ratios between 0.14 and 3.11 (as observed in our samples; see Figs. 22 and 24A), we calculate a ^{40}Ar/^{36}Ar signature of about 10,500 for the local upper mantle (see Fig. 25B and Table 3). Assuming a MORB-like ^{40}Ar/^{36}Ar signature of the pristine upper mantle (~44,000; Moreira et al., 1998), these calculations further support the existence of an atmospheric component in the Mexican lithospheric mantle, likely recycled during subduction events. Similar indications were observed in SCLM xenoliths from European localities, West Antarctic Rift System (WARS), Eastern Australia, Red sea region, N/S Kenya rifts and Ethiopia (Afar) (Matsumoto et al., 1998, 2000; Hopp et al., 2004, 2007a, 2007b; Buikin et al., 2005; Gautheron et al., 2005a; Czuppon et al., 2009; Martelli et al., 2011; Halldórsson et al., 2014; Broadley et al., 2016; Rizzo et al., 2018; Correale et al., 2019; Faccini et al., 2020).

Petrological evidence also highlights the interaction of the local upper mantle with metasomatic fluids possibly coming from the subducted oceanic crust (Pier et al., 1989; Luhr and Aranda-Gomez, 1997; Dávalos-Elizondo et al., 2016). Even though the present-day plate geometry in central and southern Mexico implies that the oceanic crust subduction terminates beneath the TMVB (Fig. 14; Pardo and Suárez, 1995; Ferrari et al., 2012) i.e. 200 km south JH, subduction of the Farallon plate beneath the western part of North America during the Mesozoic and Paleogene could have potentially modified the Mexican lithospheric mantle directly below la Mesa Central (Pier et al., 1989; Bunge and Grand, 2000). Therefore, we consider realistic that the presence of an atmospheric component in fluid inclusions from JH is mostly attributable to a local SCLM feature.

Table 3. Expected noble gas isotopic ratios for the Mexican lithospheric mantle. ^{20}Ne/^{22}Ne$_{air}$ ^{40}Ar/^{36}Ar$_{air}$ ratios after Steiger and Jäger (1977), Ozima and Podosek (2002) and Lee et al. (2006).

Locality	R/Ra	^{4}He/^{40}Ar*	^{4}He/^{20}Ne	^{36}Ar/^{22}Ne	^{40}Ar/^{36}Ar	^{20}Ne/^{22}Ne	^{20}Ne/^{22}Ne $_{air}$	^{40}Ar/^{36}Ar $_{air}$
VESVF	7.39 ± 0.14	0.14 - 3.11	11000	4.21 - 93.5	10500	12.5	9.8	298.56
DVF	8.39 ± 0.24	0.10 – 3.00	2000	8.33 – 93.50	1000	-	-	-

5.4.4.2. Noble gas signature of the JH mantle source.

Neon isotopes can additionally be used, in combination with He isotopes, to resolve any potential influence of a mantle plume on the isotopic signature of the JH mantle xenoliths. To this aim, the relationship between the extrapolated neon isotope ratio (i.e. the air-free mantle ^{21}Ne/^{22}Ne ratio expressed as ^{21}Ne/^{22}Ne$_{EX}$) and the ^{3}He/^{4}He values was evaluated (e.g., Hopp et al., 2004, 2007b; Halldórsson et al., 2014). The ^{21}Ne/^{22}Ne$_{EX}$ values were calculated by extrapolating the measured

^{21}Ne/^{22}Ne ratios to Neon-B (^{20}Ne/^{22}Ne=12.5) using the methodology proposed by Graham (2002) and Halldórsson et al. (2014). Only those samples with ^{40}Ar/^{36}Ar ratios > 500 and ^{20}Ne/^{22}Ne ratios distinguishable from air were selected. For comparison, the same calculation was made using the Ne isotopes previously reported for the European SCLM (Buikin et al., 2005; Gautheron et al., 2005a; Martelli et al., 2011; Rizzo et al., 2018; Faccini et al., 2020), the WARS (Broadley et al., 2016; Correale et al., 2019), Eastern Australia SCLM (Matsumoto et al., 1998, 2000), Red Sea region (Hopp et al., 2004; Halldórsson et al., 2014), Ethiopia (Afar) region (Halldórsson et al., 2014) and N/S Kenya rifts (Hopp et al., 2007b; Halldórsson et al., 2014); as a result, the graph reported in the Fig. 23D was obtained.
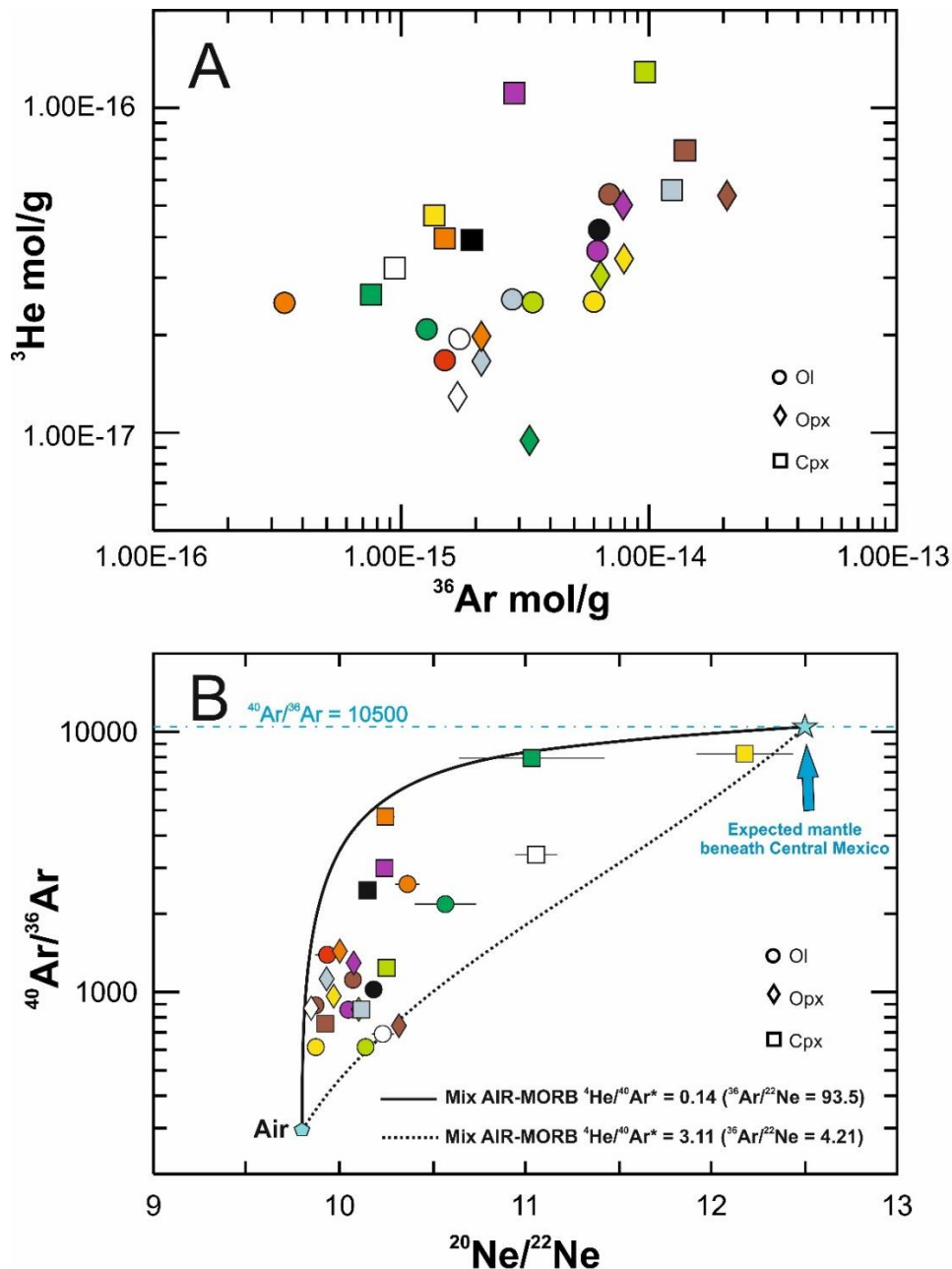
Figure 25. A) ^{36}Ar vs ^{3}He concentration. Plotted values correspond to samples with ^{40}Ar/^{36}Ar > 500. B) ^{20}Ne/^{22}Ne vs ^{40}Ar/^{36}Ar. Mixing curves are the result of mass-balance and isotopic mass balance equations using the parameters reported in Table 3.

As evidenced in Fig. 23D, samples V-K/VF Ol, VF Opx and V-E/V-H Cpx exhibit $(^{21}Ne/^{22}Ne)_{EX}$ and $^4He/^3He$ ratios close to the theoretical value for a MORB-like upper mantle (as observed for some mantle xenoliths from the Easter Australia SCLM and the Red Sea region), the remaining values fall along the MORB-Plume mixing line. When comparing our samples with other portions of SCLM on Earth, we notice that JH nodules have similar $(^{21}Ne/^{22}Ne)_{EX}$ but lower $^4He/^3He$ values, confirming the presence of a dominating MORB component. Instead, the Ethiopian xenoliths more clearly exhibit both $(^{21}Ne/^{22}Ne)_{EX}$ and $^4He/^3He$ ratios close to the Plume endmember.

In the case of JH mantle xenoliths, $(^{21}Ne/^{22}Ne)_{EX}$ ratios <0.05 would suggest a deep-mantle contribution of Neon (<10%). However, it must be considered that the samples less contaminated by the atmospheric component fall within the AIR-MORB line when considering their error bars (Fig. 24C). In addition, the $^3He/^4He$ ratios reflect a homogeneous MORB-like signature. Based on this evidence, we conclude that the upper mantle beneath JH is predominantly MORB-like with a minimum contamination by a recycled crustal component, although we cannot totally discard a deep-mantle contribution. This conclusion supports the idea that the VESVF originates from extension and melting of the lithospheric mantle under the Mesa Central province.

As discussed above, the relative invariance of the Rc/Ra values suggests that the upper mantle under this portion of La Mesa Central is relatively homogeneous in terms of noble gases (Rc/Ra = 7.39 ± 0.14; Fig. 23A - C). This $^3He/^4He$ signature is similar to that measured at the WARS (7.5 ± 0.5 Ra, 7.1 ± 0.4 Ra and 6.8 ± 0.3 Ra Broadley et al., 2016; Correale et al., 2019; Day et al., 2019) and at the upper range of that inferred at the N/S Kenya rifts and Red Sea region (6.6 ± 0.7 Ra and 7.0 ± 0.9 Ra, respectively; Hopp et al., 2004, 2007b; Halldórsson et al., 2014), but manifestly less radiogenic than the European SCLM (6.1 ± 0.9; Gautheron and Moreira, 2002; Buikin et al., 2005; Gautheron et al., 2005a; Martelli et al., 2011; Rizzo et al., 2018; Faccini et al., 2020).

The MORB-type $^3He/^4He$ signature at JH deserves some consideration in relation to the past geodynamic history of the area. We envisage two possible scenarios.

In scenario 1, the relatively homogeneous (MORB-like) $^3He/^4He$ ratios for the JH mantle xenoliths might be taken as indicative of a low-to-negligible recycling of crustal materials during the subduction of Farallon plate (20-40 Ma). A limited input of U-Th-bearing crustal materials would in fact explain well the low contribution of radiogenic ^4He in the local mantle. If this interpretation is correct, then past subduction events would only have added a recycled atmospheric component into the mantle (cfr 6.1.1). Alternatively, one may consider a scenario (scenario 2) in which any addition of (subduction-related) materials during subduction of the Farallon plate was later (during the <20 Ma Basin and Range extensional phase) overprinted by an influx of MORB-like materials, rising from deeper (asthenospheric to deep SCL) mantle domains. This latter scenario is supported by the geodynamic reconstructions that indicate a metasomatism/refertilization of the lithospheric mantle during the Basin and Range extensional phase. Paleo-subduction reconstructions indicate that the Farallon plate subducted horizontally underneath Western North-America and Northern-Central Mexico between 74 - 40Ma, producing the Laramide orogeny in the United States and the mountain range known as the Sierra Madre Oriental (SMOr) east of the JH (Fig. 14A; Atwater, 1989; Cserna, 1989; Severinghaus and Atwater, 1990; Bunge and Grand, 2000; Eguiluz de Antuñano et al., 2000; Lee, 2005). This tectonic configuration would have changed at ~40-20Ma, however, when the retreat of the Farallon slab occurred, a commonly invoked cause for initiation of the Basin and Range extension (Leeman and Harry, 1993; Nieto-Samaniego et al., 1999, 2005; Sedlock, 2003; Lee, 2005). According to Nieto-Samaniego et al. (1999), retreating of the oceanic slab favored the influx of younger and hotter asthenospheric material that ultimately led to melt generation and extension at the base of the Mesa Central. Evidence of this process comes from the intense normal faulting in the Mesa Central registered 30Ma, 23-24Ma 12-13Ma ago, and from the

transition from calc-alkaline volcanism (in the so-called Sierra Madre Occidental; SMO; Fig. 14A) to intraplate alkaline volcanism (Henry and Aranda-Gómez, 1992; Nieto-Samaniego et al., 1999; Aranda-Gómez et al., 2000). Injection of ^{3}He-rich (MORB-like) asthenospheric melts during the mid-Cenozoic could well have caused re-fertilization/re-juvenation of the Mexican lithospheric mantle in a model similar to that proposed for the lithospheric mantle beneath the Yangtze craton and the WARS (Correale et al., 2016, 2019; Faccini et al., 2020). This scenario is possible if we assume that almost all ^{3}He comes from asthenospheric melts, as proposed by Gautheron and Moreira (2002) and Gautheron et al. (2005a) to explain the noble gases systematics of the European SCLM (a steady-state model).

Irrespective of subduction is considered to have (scenario 2) or have not (scenario 1) impacted the He mantle budget, there is unquestionable petrographic evidence (this study; Liang and Elthon, 1990; Luhr and Aranda-Gomez, 1997) for a melt-related metasomatic event affecting the JH, potentially during Basin and Range extensional phase (Nieto-Samaniego et al., 1999).

5.4.5. ^{3}He fluxes, ^{4}He production and the helium residence time for the Mexican lithospheric mantle

The MORB-type He signature of JH xenoliths can quantitatively be interpreted in light of the SCLM model of Gautheron and Moreira (2002). According to the authors (see also Griffin et al., 1999, 2009), the geochemical and isotopic characteristics of the SCLM are the ultimate result of any past interaction with fluids and melts coming from (i) deeper mantle sources and/or (2) recycled slab components that have alternated over geological time (Griffin et al., 1999). In terms of helium isotopes, Gautheron and Moreira (2002) argued that the SCLM is globally homogeneous (6.1±0.9 Ra). They based this inference on the study of suites of ultramafic xenoliths and alkali basalts collected from different continental settings (Europe, USA, Antarctic, Australia, and West Africa).

In order to explain its helium isotopic homogeneity, Gautheron and Moreira (2002) proposed the global lithospheric mantle is in steady state for helium. In their model, the global SCLM is continuously metasomatized by melts and fluids with a MORB-like helium signature coming from the asthenosphere (affecting the entire reservoir); eventually, this signature becomes more radiogenic due to U and Th decay resulting in lower ^{3}He/^{4}He ratios (e.g., 6.1 ± 0.9 Ra). Thus, the steady-state model is based on the balance between the He flux from the asthenosphere and the in-situ production in the lithosphere of radiogenic ^{4}He. From this model, it is possible to estimate the helium residence time in the lithospheric mantle (Rt), the ^{3}He flux (F) and the ^{4}He production (P*). The model uses the dimensions of the SCLM (thickness, surface and density) assuming a constant U + Th concentration. These authors reported a Rt = ~200 Ma, F= 270 mol/yr and P* = 6.8×10^6 mol/yr for the global SCLM, while Gautheron et al. (2005a) obtained a Rt = 5-150 Ma, F= 3.5 $\times 10^4$ at/m^2/s (~ 1 mol/yr) and P* ~ 3 x 10^4 mol/yr for the European SCLM.

However, some studies on noble gas systematics (including our results) support a more fertile signature (^{3}He/^{4}He> 7.0 Ra) for some portions of the SCLM on Earth (e.g., Southern Australia and West Antarctic Rift; Matsumoto et al., 1998; Broadley et al., 2016; Correale et al., 2019). Therefore, we argue that the steady state model proposed by Gautheron and Moreira (2002) should be applied in local portions of SCLM to eventually detail their interactions with the asthenosphere. Using this steady-state model, and considering the ^{3}He/^{4}He signature of the JH mantle xenoliths, we estimated the helium residence time, the ^{3}He flux and the ^{4}He production for the lithospheric mantle located under the San Luis Potosí state (central Mexico):

$$F = \frac{P^*}{\left(\frac{^4He}{^3He}\right)_{SCLM} - \left(\frac{^4He}{^3He}\right)_{MORB}} \qquad \text{eq.3}$$

In eq. 3, F is the ^{3}He flux (cc STP/yr) and P* is the ^{4}He production (P*= 2.8 *10^{-14} * (4.35+Th/U) * U * M). U is the concentration of uranium in ppm and M is the mass of the subcontinental mantle. The helium residence time Rt is defined as:

$$Rt = \frac{Total\ ^3He\ in\ the\ SCLM\ (cc\ STP)}{F} \qquad \text{eq.4}$$

The parameters used in the calculation are as follows: 1) the average of the ^{4}He/^{3}He ratios measured in JH mantle xenoliths equal to 97,500 (7.38 Ra) and a MORB endmember equal to 84,600 (8.5 Ra). The latter value is higher than that assumed by Gautheron and Moreira (2002) (8.0 Ra) because preliminary results for mantle xenoliths from other localities in central Mexico yield Rc/Ra values of < 8.39 (please see subsection 6.3); 2) U contents between 0.01 and 0.03 ppm as previously reported for mantle xenoliths from central Mexico (Dávalos-Elizondo et al., 2016) and a Th/U = 3 as assumed by Gautheron and Moreira (2002); 3) A subcontinental mantle mass equal to 3.66x10^{21} g. This mass was estimated assuming a thickness of the local lithospheric mantle of ~150km (density of 3.3x10^6 g/m^3; Gautheron and Moreira, 2002) and a surface of 7.4x10^9 m^2 that includes all the Cenozoic intraplate monogenetic volcanic fields located in the San Luis Potosí state (VESVF, SDVF and Los Encinos volcanic field; see Fig. 14A; Aranda-Gómez et al., 2007); 5) A upper mantle ^{4}He concentration equal to 1 x 10^{-6} ccSTP/g (4.5 x 10^{-11} mol/g), which corresponds to the maximum value identified for continental mantle xenoliths (Gautheron and Moreira, 2002); this value is equivalent to a ^{3}He concentration =1.0 x 10^{-11} ccSTP/g (4.5 x 10^{-16} mol/g) assuming a Rc/Ra = 7.38; thus the total ^{3}He estimated for the local SCLM is 1.64x10^6 mol (3.66x10^{10} cc STP). The results obtained are reported in Table 4.

The calculated ^{3}He fluxes for the Mexican lithospheric mantle vary from 0.027 to 0.080 mol/g (Fig. 26A). These fluxes are very low if compared with the values reported for the global SCLM, the European SCLM or MORB values (800-1300 mol/g; Marty and Jambon, 1987; Javoy et al., 1989; Michael and Graham, 2015; Tucker et al., 2018). When scaled to the surface area (7.4x10^9 m^2) of volcanism in the San Luis Potosí state, our specific fluxes vary between 6.9 and 20.7 at/s/cm^2 (Fig. 26B) which are well above the MORB and the global SCLM values (4.8 at/s/cm^2 and 3.5 at/s/cm^2, respectively; Craig et al., 1975; Gautheron and Moreira, 2002) confirming a high ^{3}He contribution from the asthenosphere under central Mexico.

The associated Rt values range from 20 to 60 Ma. These estimates are lower if compared to the global SCLM and would explain the less radiogenic character of the Mexican lithospheric mantle. In this model, the Rt values do not depend on the area but have a close relationship with the average of the ^{3}He/^{4}He ratios measured in the mantle xenoliths. It is reasonable to think that the smaller the ^{3}He/^{4}He ratio measured in the xenoliths (7.38 Ra for JH xenoliths and 6.1Ra for the SCLM), the longer the helium residence time in the lithospheric mantle should be. Therefore, low Rt values implies low ^{4}He production and high ^{3}He/^{4}He ratios, as observed in JH mantle xenoliths. Moreover, our estimated Rt range overlaps with the inferred age range for the retreating subduction of the Farallon slab (40-20 Ma ago) processes, which may have triggered the injection of asthenospheric melts in the lithospheric mantle and the generation of the Basin and Range province (Nieto-Samaniego et al., 1999; Lee, 2005). If correct, our results would independently indicate that the last major geodynamic modification in the lithospheric mantle underneath the JH occurred during the lower and mid-Cenozoic. We argue that the refertilization event was able to increase the ^{3}He/^{4}He signature within the MORB-like range, overprinting the pre-Cenozoic signature recorded by the Mexican lithospheric mantle. Since then, the latter would have evolved in a similar way to that

proposed by Gautheron and Moreira (2002), i.e., in a steady state becoming slightly more radiogenic during the last ~20Ma down to the measured ^{3}He/^{4}He values.

In conclusion, both the low production of ^{4}He and the relative lower Rt (compared to other areas) could explain the high ^{3}He/^{4}He ratios measured in JH mantle xenoliths. However, we caution these are local estimates; therefore, in order to minimize the effect generated by the area and possible mantle heterogeneities, future work will target obtaining isotopic data for mantle xenoliths from other localities of the Basin and Range extension in Mexico. This will allow a more realistic reconstruction of the evolution of the Mexican lithosphere in terms of noble gases.

Table 4. ^{4}He production rates, ^{3}He fluxes, helium residence time and CO_2 fluxes calculated for the lithospheric mantle beneath central Mexico. P*, F and Rt values were calculated based on mathematical formulations proposed y Gautheron and Moreira (2002). P*: ^{4}He production, F: ^{3}He flux, Rt: Helium residence time.

U (ppm)	P* (ccSTP/g)	P* (mol/yr)	F (ccSTP/year)	F (mol/yr)	Rt (Ma)	CO₂ flux (mol/yr)	CO₂ flux (g/yr)
0.01	7.69E+06	3.43E+02	5.99E+02	0.027	61.17	3.93E+07	1.73E+09
0.012	9.23E+06	4.12E+02	7.19E+02	0.032	50.97	4.72E+07	2.08E+09
0.014	1.08E+07	4.81E+02	8.38E+02	0.037	43.69	5.50E+07	2.42E+09
0.016	1.23E+07	5.49E+02	9.58E+02	0.043	38.23	6.29E+07	2.77E+09
0.018	1.38E+07	6.18E+02	1.08E+03	0.048	33.98	7.07E+07	3.11E+09
0.02	1.54E+07	6.87E+02	1.20E+03	0.053	30.58	7.86E+07	3.46E+09
0.022	1.69E+07	7.55E+02	1.32E+03	0.059	27.80	8.65E+07	3.80E+09
0.024	1.85E+07	8.24E+02	1.44E+03	0.064	25.49	9.43E+07	4.15E+09
0.026	2.00E+07	8.93E+02	1.56E+03	0.070	23.53	1.02E+08	4.50E+09
0.028	2.15E+07	9.62E+02	1.68E+03	0.075	21.84	1.10E+08	4.84E+09
0.03	2.31E+07	1.03E+03	1.80E+03	0.080	20.39	1.18E+08	5.19E+09

5.4.5.1. Mantle CO_2 fluxes

We combine the ^{3}He flux estimated above with the CO_2/^{3}He ratios measured in the JH xenoliths (e.g., Marty and Jambon, 1987; Tucker et al., 2018) to calculate the mantle-derived CO_2 fluxes in the area. Taking U concentrations between 0.01 ppm and 0.03 ppm and a CO_2/^{3}He(avg) ~1.47 x 10^9, the calculated CO_2 fluxes range from 3.93 x 10^7 mol/yr (1.02 x 10^{10} at/s/cm^2) to 1.18 x 10^8 mol/yr (3.05x10^{10} at/s/cm^2; Fig. 26C-D). Our estimated fluxes are lower than previously estimated for other continental rift localities (such as the EAR), consistent with the small area of the San Luis Potosí volcanic filed (considered in the model), and correspond to <0.1% of the MORB CO_2 fluxes; similarly, our fluxes are lower than estimated for hot spot settings such as Hawaii or Canary Islands (Hauri et al., 2019). Additional studies on noble gas and CO_2 isotopic data from other mantle xenoliths locations in central and northwestern Mexico are required to further validate our results.

5.4.6. Inferences on CO_2 origin.

In JH peridotites, fluids are dominated by CO_2 (Fig. 21), as typically recorded by other worldwide mantle xenoliths (Andersen and Neumann, 2001; Deines, 2002; Frezzotti and Touret, 2014). Thus, the CO_2 isotopic composition can be used to constrain carbon origin. Our samples exhibit δ^{13}C ratios between −0.97 and −2.86‰ (Fig. 27A); they are therefore isotopically more positive (^{13}C-rich) than found in European mantle xenoliths in alkaline intra-plate and extensional contexts, such as in the Hyblean plateau (southeast Sicily, Italy; ranging from-4 to -2‰; Correale et al., 2015) and Lower Silesia (southwest Poland; ranging from -4.7 to -3.1‰; Rizzo et al., 2018).

The CO_2 isotopic composition in the JH peridotites is also well above the $\delta^{13}C$ MORB mantle range ($-8‰ < \delta^{13}C < -4‰$; Sano and Marty, 1995). When $\delta^{13}C$ values are plotted against Rc/Ra and $CO_2/^3He$ ratios (Fig. 27B-C), our samples fall along a MORB-Limestone mixing line, suggesting source mantle Carbon contamination by C-rich fluids with a crustal carbonate signature.

The crustal carbon component found in fluid inclusions of JH xenoliths may in principle derive from two main distinct processes: (i) infiltration of CO_2 rich fluids derived by assimilation of carbonates by host magmas during ascent through the continental crust, and (ii) mantle metasomatism by CO_2-rich fluids and melts derived from subducted oceanic crust and sediments.
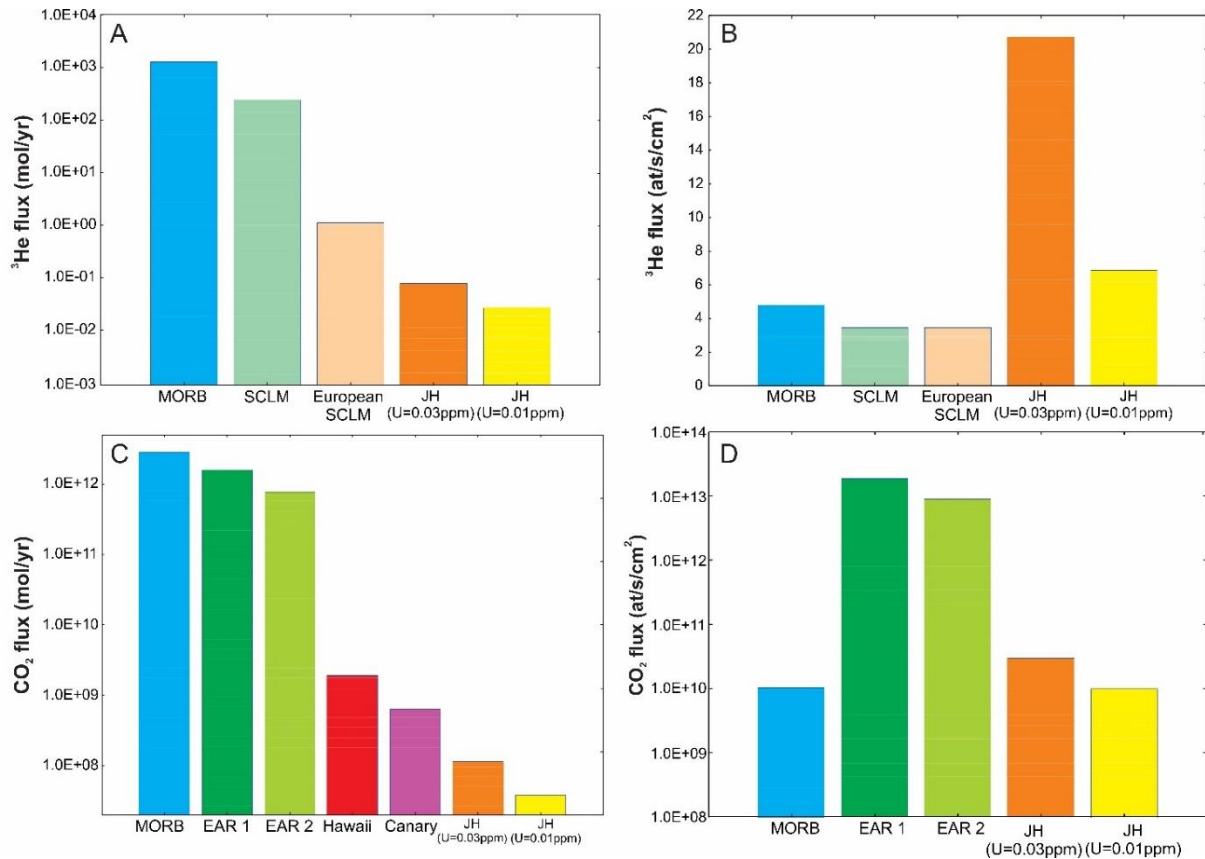
Figure 26. A) Comparison between ^3He fluxes measured in central Mexico based on JH mantle xenoliths analysis (at U=0.01 and 0.03 ppm) and other localities. MORB value was estimated using data from Michael and Graham (2015) and using a $CO_2/^3He$ ratio =2.2 x 10^9 (Marty and Tolstikhin, 1998); SCLM value was taken from Gautheron and Moreira (2002); the European SCLM flux was calculated based on Gautheron et al. (2005a). B) ^3He fluxes scaled to the surface area. See the text for more details. C) Associated CO_2 fluxes (mol/yr) for central Mexico compared with other tectonic localities. MORB CO_2 flux was calculated after Michael and Graham (2015); EAR1 and EAR2 values were taken from Lee et al. (2016) and Foley and Fischer (2017), respectively; Hawaii and Canary fluxes were obtained from Hauri et al. (2019). D) CO_2 fluxes scaled to the surface area.

Infiltration of CO_2 fluids in mantle xenoliths outgassed during assimilation of carbonates in basanitic magmas in the continental crust should be considered since JH maar formed on carbonate deposits (the Valles-San Luis Potosí calcareous platform (PVSLP) and the Mesozoic Basin of central Mexico). However, the relatively fast ascent rates of the host magma through the continental crust (Luhr et al., 1989; Pier et al., 1989), and the lack of carbonate xenoliths in the host lava, argue against a crustal component inherited during sin-eruptive magma ascent. Conversely, petrographic and Raman evidence indicates pervasive infiltration of carbonate-bearing silicate melts and CO_2-fluids in peridotites (Figs. 18-19-20), strongly supporting deep carbon mobility during a metasomatic event in the lithospheric mantle. We, therefore, conclude that the carbonate component identified in JH

CO$_2$ fluids was trapped under mantle conditions and is related to CO$_2$ degassing of metasomatic carbonate-rich silicate melts on reaction with mantle minerals. Metasomatic processes occurred well before entrainment by the host magma and eruption (as proposed by Liang and Elthon, 1990).

As mentioned in the previous sections, northwestern Mexico's current tectonic configuration indicates that the Cocos and Rivera plates do not directly affect the mantle under the Mesa Central, making it difficult to consider involvement of present subduction (Fig. 14). Moreover, some studies suggest that the contribution of carbonate sediments from the subducting slab is minimal. The CO$_2$-rich plume gases released by arc volcanoes (e.g., Popocatepetl) come from the assimilation of limestone deposits, as evidenced by trace element analysis performed in mafic rocks and the presence of carbonate xenoliths in volcanic deposits (Goff et al., 1998, 2001; Aiuppa et al., 2017). A low contribution of subducted Carbon in fluids has also been proposed for other volcanic fields belonging to the TMVB, such as the Sierra Chichinautzin Volcanic Field (SCVF; Verma, 2000) and the Michoacan-Guanajuato Volcanic Field (MGVF; Verma and Hasenaka, 2004).
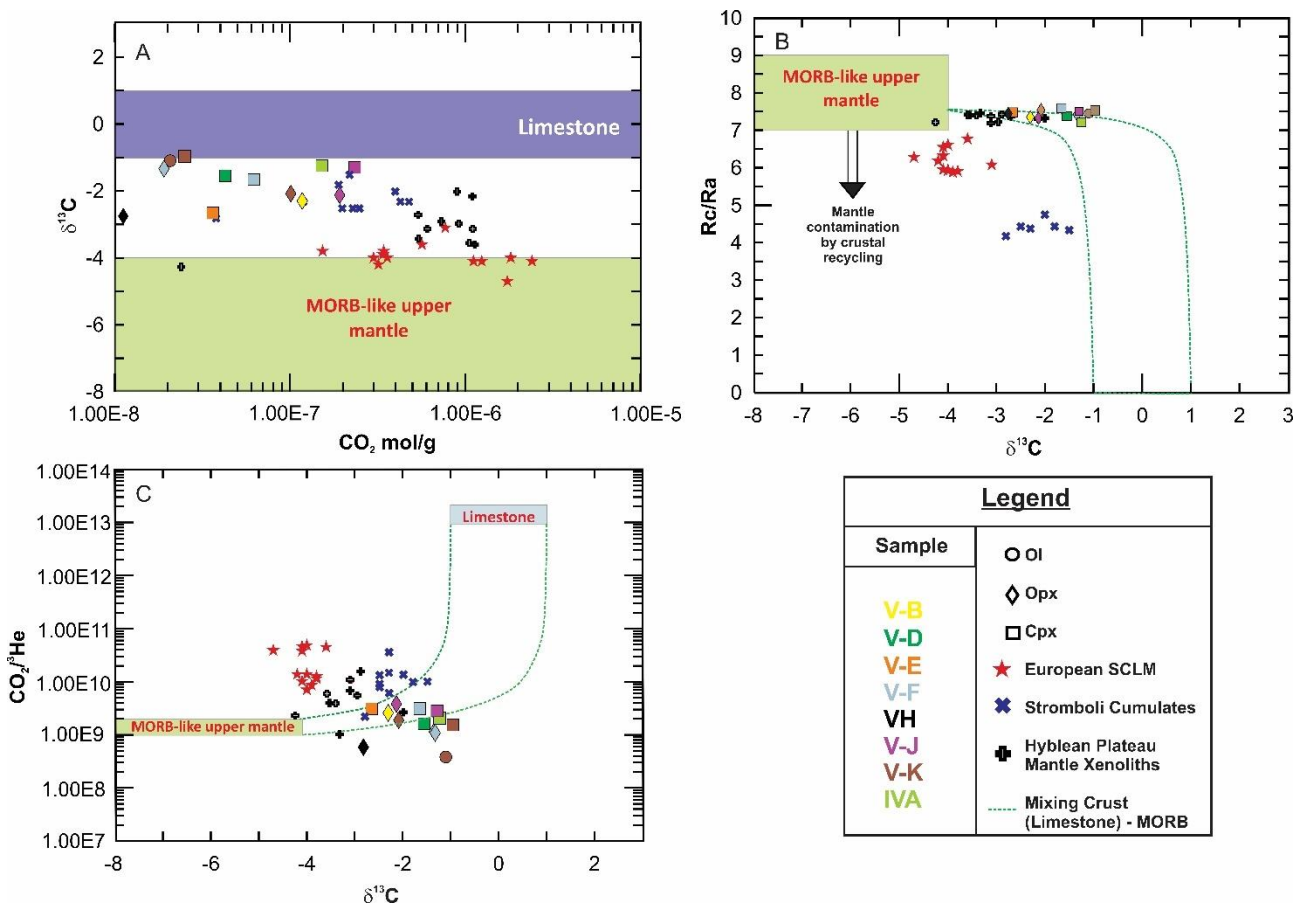
Figure 27. A) CO$_2$ vs δ^{13}C. Hyblean, Stromboli and European SCLM data from Correale et al. (2015), Gennaro et al. (2017) and Rizzo et al. (2018), respectively. B) δ^{13}C vs ^{3}He/^{4}He corrected for air contamination (Rc/Ra). Dotted lines are binary mixing between two endmembers: 1) Limestone at δ^{13}C =-1, 1 and Rc/Ra= 0.01 and 2) MORB-like upper mantle at δ^{13}C = -4 and Rc/Ra = 7.38. C) δ^{13}C vs CO$_2$/^{3}He. Dotted lines are binary mixing between two endmembers: 1) Limestone at δ^{13}C =-1, 1 and CO$_2$/^{3}He = 10^{-13} and 2) MORB-like upper mantle at δ^{13}C = -4 and CO$_2$/^{3}He = 1.00 x 10^{-9}, 2.00 x 10^{-9}.

In contrast to present-day subduction being an unlikely driver, we emphasize a possible major role played by older subduction of the Farallon underneath the northwestern margin of North America during the Mesozoic and early Cenozoic (Atwater, 1989; Ferrari et al., 2012; Henry and Aranda-Gómez, 1992; Sedlock, 2003). Several authors claim that the North American lithospheric mantle could have been hydrated by fluids or melts released by flat subduction of the Farallon plate, as

evidenced by petrological studies of mantle xenoliths from the Sierra Nevada and the Colorado Plateau (Smith et al., 1999; Lee, 2005; Li et al., 2019). "Farallon hydration" (Lee, 2005) is suggested to have occurred during the late Cretaceous and early Cenozoic, and to have affected the lithospheric mantle up to 800 km inboard of the trench (Li et al., 2008). This metasomatic event is also well documented in Mexican xenoliths (Liang and Elthon, 1990; Dávalos-Elizondo et al., 2016; Levresse et al., 2016). For example, Luhr and Aranda-Gomez (1997) interpreted the systematic east to west oxygen fugacity increase in Cenozoic mantle xenoliths from central and northern Mexico as induced by the progressive oxidation of the lithospheric mantle by fluids released by the Farallon oceanic slab.

In light of the above, the interaction between subducted fluids delivered by the Farallon plate and the Mexican lithospheric mantle could represent a feasible mechanism to explain the heavy $\delta^{13}C$ signatures of JH mantle fluids. We argue that the crustal carbon component identified in the fluid inclusions would reflect a mantle feature induced by an old subduction-related carbonate component inherited during the mid-Cenozoic before the Basin and Range extension (Middle Miocene; (Henry and Aranda-Gómez, 1992; Sedlock, 2003) and recycled in the local mantle.

5.5. Conclusions

We investigate the petrography and noble gas-CO_2 composition of fluid inclusions in ultramafic mantle xenoliths collected from JH, in central Mexico. Peridotites are classified as spinel-lherzolites and harzburgites. Petrographic observations and Raman microspectroscopy analyses of fluid and melt inclusions reveal the coexistence of glass/carbonate microveins and a CO_2 fluid phase permeating the rocks, suggesting interaction between peridotites and degassing carbonate-rich silicate melts at mantle depth.

The $^4He/^{40}Ar^*$ range (0.14 - 3.11) partially overlaps that of fertile mantle (1-5), which could indicate either a low degree of partial melting or the occurrence of a metasomatism/refertilization process by melts degassing fluids ultimately entrapped in the mantle as secondary fluid inclusions.

Neon and Ar systematics reveal a mixing between atmospheric and MORB-like fluids, strongly supporting the presence of an atmospheric component eventually recycled from the Farallon plate subduction; $^{40}Ar/^{36}Ar$ ratios that vary from 303 to 8231 while $^{20}Ne/^{22}Ne$ and $^{21}Ne/^{22}Ne$ ratios are 10.2 ± 0.50 and 0.0332 ± 0.0058, respectively. Although, $(^{21}Ne/^{22}Ne)_{EX}$ ratios suggest the existence of plume-derived neon in our fluid inclusions, JH mantle xenoliths exhibit homogeneous $^3He/^4He$ signature (7.39 ± 0.14 Ra) that is comparable to that of the MORB-like mantle and similar to other worldwide SCLM localities (eg., Eastern Australia, N/S Kenya rifts and WARS). This isotopic signature results from a low recycling of crustal components in the local mantle possibly overprinted by a metasomatism/refertilization episode reasonably occurred after the retreat of the Farallon slab during the early and mid-Cenozoic.

Based on the "Steady-state" model proposed by Gautheron and Moreira (2002), we estimated a helium residence time in the local SCLM between 20-60Ma, which overlaps the geodynamic evolution of the area and the metasomatism/refertilization event. Since then, the lithospheric mantle would have evolved in a steady state for helium (from a MORB signature ~8.5 Ra) becoming slightly more radiogenic during the last ~20Ma. We also calculated ^3He fluxes between 0.027 - 0.080 mol/g, ^4He production rates from 340 to 1000 mol/yr and mantle CO_2 fluxes from 3.93 x 10^7 mol/yr to 1.18x10^8 mol/yr represent less than the 0.1% of the MORB CO_2 fluxes.

The $\delta^{13}C$ values measured in JH fluid inclusions reveal a binary mixing between a MORB-like upper mantle and a crustal carbonate component (limestone). We propose that the crustal CO_2/carbonate

component identified in JH xenoliths was trapped under mantle conditions through metasomatic reactions between peridotites ad C-bearing silicate melts. These would have acted as carriers in the local mantle of a recycled carbon component inherited from the Mesozoic to early Cenozoic Farallon subduction.

CHAPTER 6. THE ISOTOPIC COMPOSITION OF VOLATILES PRESENT IN MANTLE XENOLITHS FROM DURANGO (DVF) AND THE SAN QUINTIN (SQVF) VOLCANIC FIELDS, NW MEXICO.

6.1. Geological setting of the DVF and the SQVF

The DVF is located in the Mesa Central province, near the eastern border of the Sierra Madre Occidental (Fig. 14A). This field covers more than 2000 km^2 and is composed of approximately 100 Pleistocene and Quaternary volcanic structures including maars, lava flows and cinder cones that represent at least 20 km^3 of extruded magma (Albritton, 1958; Swanson, 1989; Aranda-Gómez et al., 1992; Luhr and Aranda-Gomez, 1997). In this work, the studied mantle xenoliths are from La Breña-El Jaguey maar complex, the most important xenolith locality recognized along the DVF (Aranda-Gómez et al., 1992).

La Breña -El Jaguey maar complex is located 45 km to the NW of the Durango city (24 ° 25' 04.69"N and 104 ° 32' 04.86"W) and exhibits a particular morphology generated by the intersection of two different maars (Fig. 28): El Jaguey and La Breña. El Jaguey is identified as a funnel-shaped maar with a diameter of 0.75 km while La Breña is a nearly circular maar of 1.4 km in diameter (Swanson, 1989; Aranda-Gómez et al., 1992). Like the JH, it is thought that these maars were produced due to the interaction between a superficial aquifer and a basanitic magma originated in the lithospheric mantle (Aranda-Gómez and Ortega-Gutiérrez, 1987; Henry and Aranda-Gómez, 1992; Luhr and Aranda-Gomez, 1997); no radiometric ages have been reported for these events, however, it is believed that the maar-related eruptions are Quaternary (Swanson, 1989; Aranda-Gómez et al., 1992). The oldest outcropping rocks identified in the complex are the volcanic rocks of the Sierra Madre Occidental (Albritton, 1958; Swanson, 1989; Aranda-Gómez et al., 1992). These rocks form a calc-alkaline sequence characterized by the occurrence of basalts, basaltic andesites, andesites and rhyolitic ignimbrites dating back to the Oligocene (Albritton, 1958; Demant et al., 1989; Nieto-Samaniego et al., 2005). Over these rocks, Albritton (1958) proposed a sequence of Quaternary rocks composed of continental sedimentary sequences alternating with basaltic lava flows; it has been suggested that the area that comprises both El Jaguey and La Breña was initially occupied by a cluster of Pleistocene scoria cones and related lava flows that are now exposed in the internal walls of the maars. According to Aranda-Gómez et al. (1992), El Jaguey maar formed first as the result of a series of phreatomagmatic explosions producing several pyroclastic surge layers that now fill the crater and cover the surrounding areas. The eruptions associated with the formation of La Breña maar also generated a thick pyroclastic sequence (up to 45m thick;) including surge beds and scoria/ash fall layers (Swanson, 1989; Aranda-Gómez et al., 1992). The La Breña sequence is exposed in the upper walls of the complex and suggest that during the maar formation, the hydromagmatic eruptions alternated with purely magmatic activity (Swanson, 1989; Aranda-Gómez et al., 1992). The eruption of the complex ended with the formation of small lava and scoria cones within La Breña maar.

Unlike the VESVF and the DVF, the SQVF is situated in northwestern Mexico, more precisely in the Baja California state, near the Mexico-USA border (Fig. 14A). The SQVF is the unique mantle-xenolith bearing alkaline basalt complex identified in the Baja California Peninsula and its origin is also closely related with the cessation of the Farallon subduction and the opening of the Gulf of California (Aranda-Gómez and Ortega-Gutiérrez, 1987; Luhr et al., 1995a; Luhr and Aranda-Gomez, 1997). When the Farallon subduction ended approximately 12Ma ago, two triple junctions were formed along the western margin of North America (Wallace, 1990; Luhr et al., 1995a; Sedlock, 2003): the Mendocino and Rivera triple junctions (Fig. 13). Once formed, these would

have migrated northward and southward, respectively, favoring the development of a transform boundary between the Pacific and the North American plate (Luhr et al., 1995a). In the Mexican region this transform system is known as the San Benito - Tosco-Abreojos fault zone. The relative plate motion between the Pacific and the North American plates not just triggered the development of the transform system but also promoted the progressive extension of the proto-gulf of California and the formation of several spreading centers that erupted new MORB seafloor at about 3.5 Ma ago (Luhr et al., 1995a; Sedlock, 2003). Some authors suggest that the deformation style was similar to the Basin and Range extension. In fact, the geochemical signatures of the SQVF magmas and the presence of mantle xenoliths closely resemble the volcanic fields developed along the central and northern Mexico during the same period (e.g., the VESVF and the DVF; Aranda-Gómez and Ortega-Gutiérrez, 1987; Luhr et al., 1989; Pier et al., 1989; Luhr et al., 1995a).
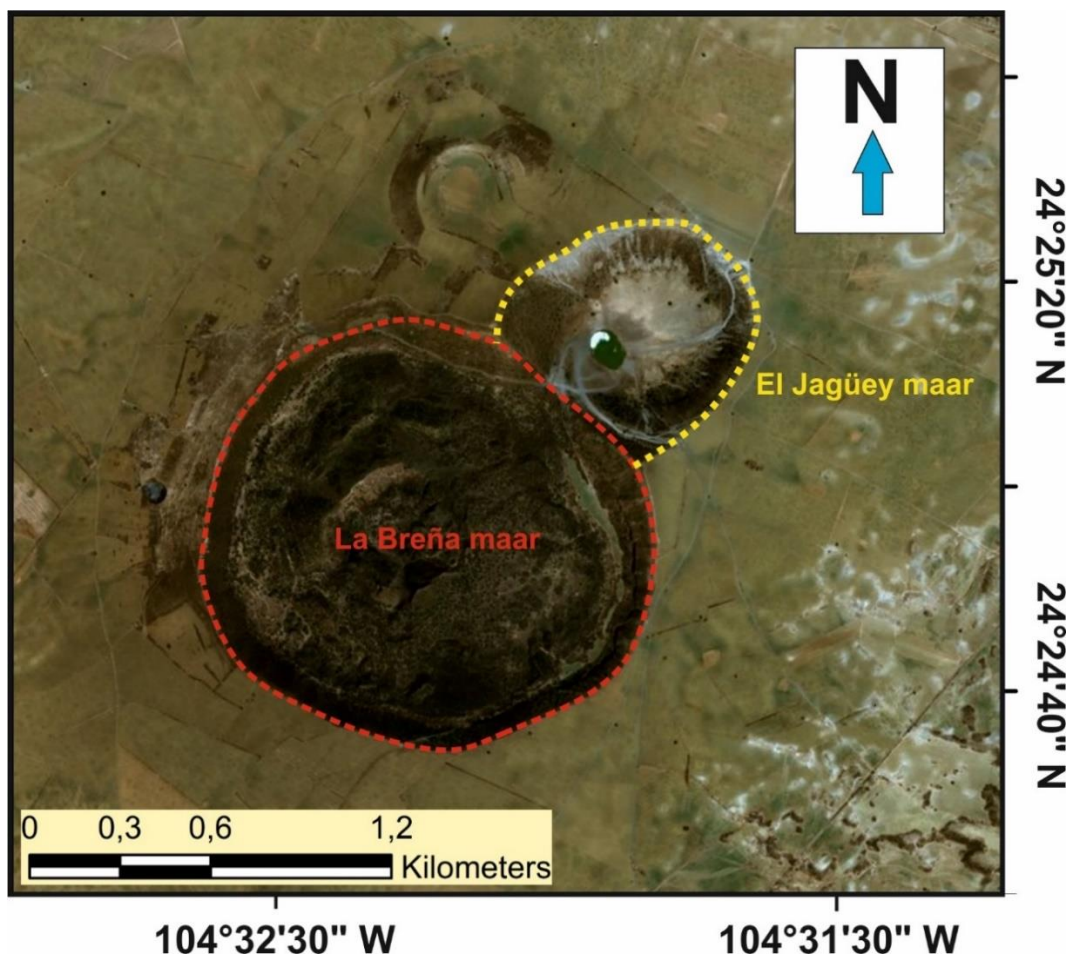
Figure 28. Image from Google Earth (June 23rd, 2021) showing La Breña-El Jagüey maar complex.

The SQVF is located the Yuma terrane defined by Sedlock et al. (1993). This terrane was formed in the early Cretaceous by the junction of two different subterranes composed of Triassic, Jurassic and Cretaceous volcanic and sedimentary rocks. According to Sedlock et al. (1993), the Yuma terrane was intruded by batholithic bodies during the middle and late Cretaceous. The youngest rocks reported in the vicinity of the SQVF are marine clastic deposits, calc-alkaline rocks (associated with the Farallon subduction) and alkalic monogenetic fields including the SQVF (Luhr et al., 1995a). It is though that the volcanic activity of the SQVF started during the Pleistocene and continued through the Holocene (Luhr et al., 1995a; Luhr and Aranda-Gomez, 1997); some deposits of pepperites and pillow lavas have been also identified in the volcanic field suggesting that the SQVF

initiated as a group of subaqueous volcanoes that later emerged. The SQVF consists of 10 different volcanic complexes, each complex is characterized by a well-preserved scoria cone, several eruptive vents and lava flows (Fig. 29; Luhr et al., 1995a; Luhr and Aranda-Gomez, 1997). The volcanic complexes are: the Media Luna (L), Woodford (W), Basu (B), Riveroll (R), Kenton (K), Picacho Vizcaíno (P), Sudoeste (S), Ceniza (C), Monte Mazo (M) and Isla San Martin (I). Mantle xenoliths analyzed in this work comes from the Media Luna cone.
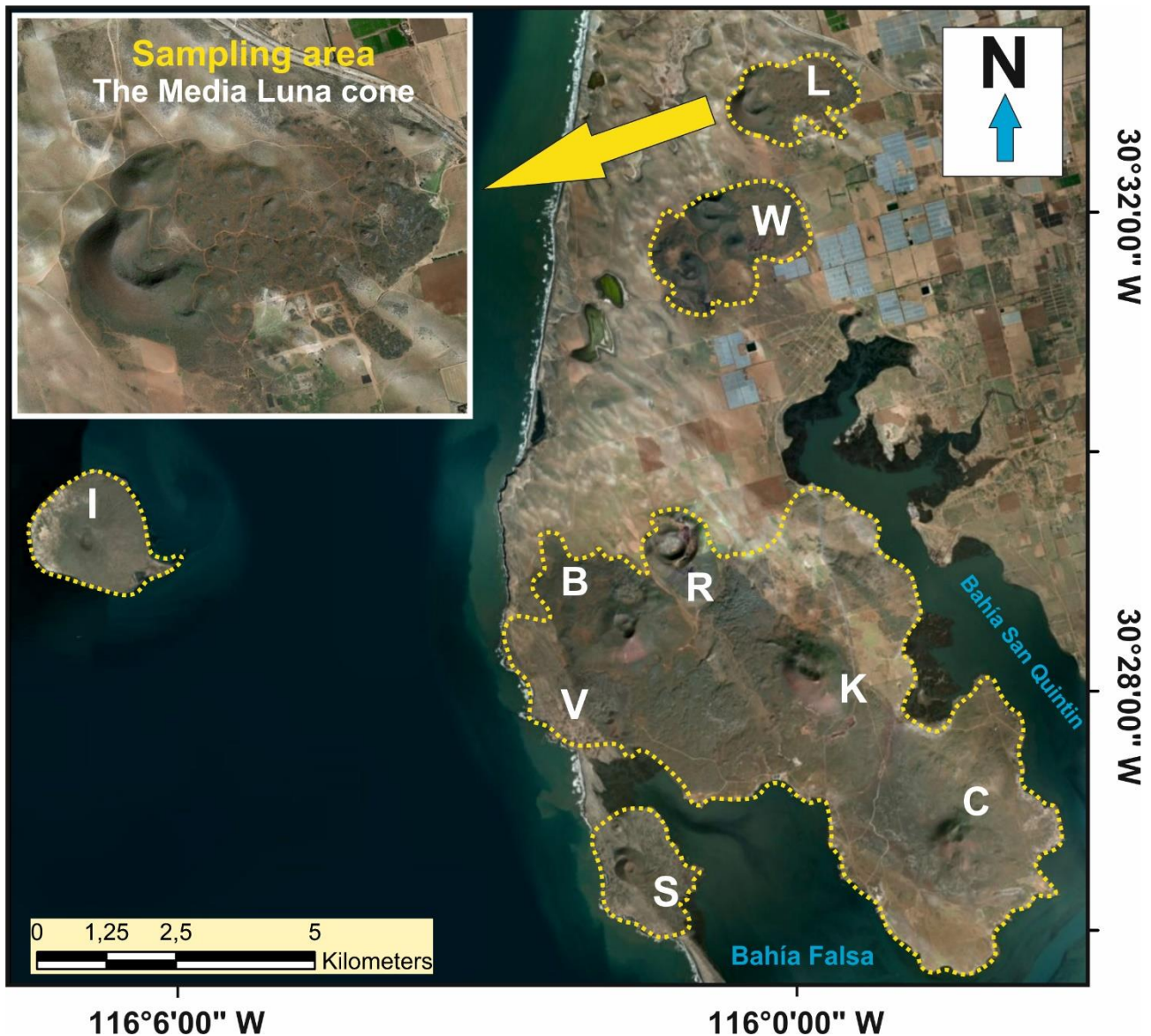
Figure 29. Image from Google Earth (June 23th, 2021) showing the San Quintín Volcanic Field (SQVF) and sampling area. Media Luna (L), Woodford (W), Basu (B), Riveroll (R), Kenton (K), Picacho Vizcaíno (P), Sudoeste (S), Ceniza (C), Monte Mazo (M) and Isla San Martin (I).

6.2. Petrological background of mantle xenoliths

Peridotites samples were provided by the Department of Mineral Sciences belonging to the Smithsonian Institution. Samples NMNH-18, NMNH-20 and NMNH-27 were previously analyzed by Luhr and Aranda-Gomez (1997). Mantle xenoliths from the DVF are dominated by coarse-tabular and protogranular textures characterized by the presence of clusters of Sp, Opx and Cpx (possibly

originated from the decompressive reaction of olivine and garnet). Ol and Opx crystals from DVF samples usually have diameters >2mm while Cpx and Sp exhibit variable diameters between 1 – 2 mm. SQVF xenoliths generally show strongly deformed fabrics with a bimodal grain-size distribution (porphyroclastic texture); samples may exhibit porphyroclasts of Ol and Opx with diameters greater than 5 mm surrounded by recrystallized neoblasts (diameters< 1 mm) of Ol, Opx, Cpx and Sp. A common characteristic between DVF and SQVF xenoliths is the presence of interstitial glass veins and spongy rims in Cpx. Glasses have elevated SiO_2 (54 - 57 wt%), Al_2O_3 (18 - 21 wt%), Na_2O (2.5 - 6.1 wt%), K_2O (1.5 - 5.7 wt%), P_2O_5 (0.06 - 0.81 wt%) and depleted MgO (2.5 - 3.6 wt%). Spongy rims in Cpx are enriched in CaO and depleted in Al_2O_3 and N_2O as observed in VESVF xenoliths. Luhr and Aranda-Gomez (1997) proposed that both glasses and spongy rims may be the result of two different processes: 1) the development of internal melts derived from partial melting or 2) the infiltration of volatile-rich melts reacting with the lithospheric mantle. These authors report pressures of 17.7 ± 1.7 kbar and fO_2 values (ΔFMQ) of -0.2 ± 0.3 for the DVF xenoliths and pressures around 10.7 ± 2.5 kbar and fO_2 (ΔFMQ) of 0.0 ± 0.2 for the SQVF samples. Luhr and Aranda-Gomez (1997) argue that the systemic increase of the fugacity of mantle xenoliths from the DVF to the SQVF could be associated with a subduction-related oxidation of the lithospheric mantle due to the release of fluids from the subducted Farallon slab beneath the North American plate.

6.3. Results

The studied samples consist of six ultramafic nodules: four lherzholites and one harzburgite from the DVF and one lherzolite from the SQVF. The composition of fluid inclusions are reported in Table 5 and Fig. 30. Samples from the DVF generally exhibit higher gas concentrations (e.g., ^{4}He, $^{40}Ar^*$ and CO_2) than the SQVF aliquots but lower than the concentrations obtained in most of the pyroxenes analyzed in the VESVF xenoliths. In general, ^{3}He and ^{4}He concentrations vary from 1.38×10^{-19} to 1.32×10^{-17} mol/g and 1.96×10^{-14} to 1.51×10^{-12} mol/g, respectively. $^{40}Ar^*$ range from 3.02×10^{-14} to 2.17×10^{-12} mol/g. CO_2 is the dominant phase in the fluid inclusions, and ranges from 8.33×10^{-11} to 1.54×10^{-8} mol/g. The concentration of CO_2 exhibits a positive correlation with noble gases as shown in Fig. 30. Rc/Ra values vary from 5.10 to 8.40 with the lowest values reported for the SQVF samples. On average, the Rc/Ra ratios obtained in DVF xenoliths are higher than the ratios observed in the SQVF nodules. Xenoliths from both localities do not exhibit systematic differences in $^{4}He/^{20}Ne$ and $^{4}He/^{40}Ar^*$ ratios, which range from 11.5 to 205 and from 0.11 to 2.5, respectively. Although, $^{40}Ar/^{36}Ar$ ratios measured in all samples are higher than the air value (<338), the maximum value reported is 1031 which is much lower than the MORB range (~44,000; Moreira et al., 1998). $^{20}Ne/^{21}Ne$ and $^{21}Ne/^{22}Ne$ values vary from 9.80 ± 0.01 (1σ) to 12.57 ± 0.10 (1σ) and from 0.0290 ± 0.0003 (1σ) to 0.056 ± 0.0024 (1σ), respectively.

6.4. Discussion

6.4.1. Processes that modified the pristine composition of fluid inclusions

Considering the petrological information of mantle xenoliths exposed above, it is reasonable to argue that the original isotopic composition of fluid inclusions has been modified by the effect of partial melting or metasomatism, especially in Cpx where textures such as spongy rims have been identified (Luhr and Aranda-Gomez, 1997). Diffusive fractionation of noble gases may derive from these processes affecting DVF and SQVF xenoliths and must be carefully evaluated in order to study the real nature of the lithospheric mantle beneath these localities.

Pyroxenes generally show lower ^{3}He/^{4}He ratios than olivines, except for the sample NMNH-37 Cpx which exhibit the highest ratio of the dataset at 8.40Ra (Table 5 and Fig. 31A-B). Samples NMNH – 27 Opx/Cpx from the SQVF (red symbols) show an evident decrease in ^{3}He/^{4}He ratios accompanied by a depletion in ^{4}He concentrations that are clear evidence of diffusive fractionation (Fig. 31); this decrease is also observed in CO_2 contents, particularly Cpx (Fig. 30B). A depletion in ^{3}He/^{4}He is also noted in Cpx and some Opx from nodules NMNH-36, NMNH-39, NMNH-20 and NMNH-18, at comparable or even higher helium concentrations than those measured in Ol (Fig 31A-B); in the case of sample NMNH-20, pyroxenes exhibit the maximum helium concentrations of the dataset which are similar to some concentrations measured in the VESVF xenoliths. Comparing our results with the mineral chemistry data from Luhr and Aranda-Gomez (1997), it is possible to see that the decrease in ^{3}He/^{4}He ratios observed in Cpx (nodules NMNH 18, 20 and 27) is accompanied by an increase in Mg# (from Ol to Cpx) which may be interpreted as a result of partial melting (Fig. 32A); Ol from nodules NMNH 20 and 27 are near the mantle range while the Ol from nodule NMNH-18 exhibit higher Mg# likely representing a more depleted mantle.

The ^{4}He/^{40}Ar* variability supports the partial melting hypothesis. Ol and Opx crystals (except samples NMNH-39 Ol/Opx and NMNH-27 Opx) exhibit ^{4}He/^{40}Ar* within the mantle production range and are higher than the values reported for Cpx (Fig. 31C). This trend is also observed in Fig. 32B where samples NMNH-18, 20 and 27 also show a decrease in ^{4}He/^{40}Ar* as the Mg# increase (from Ol to Cpx). As discussed in subsection 5.4.3, He is more incompatible than Ar, and can escape from the mantle more effectively during partial melting, causing a ^{4}He/^{40}Ar* decrease in the mantle residuum (Burnard, 2004; Heber et al., 2007; Yamamoto et al., 2009). Following the petrological observations made by Luhr and Aranda-Gomez (1997), it is reasonable to infer that low ^{3}He/^{4}He and ^{4}He/^{40}Ar* ratios in Cpx are the result of a partial melting/metasomatism trend which are probably connected with modifications in the pristine concentrations and isotopic ratios of fluid inclusions; Opx crystals from nodules NMNH- 20 and 39 also exhibit a similar behavior. Considering the above and the lack of fluid inclusion studies that confirm the origin of fluids trapped in ^{3}He/^{4}He-depleted pyroxenes, samples NMNH – 27 Opx/Cpx, NMNH-36 Cpx, NMNH-39 Opx/Cpx, NMNH-20 Opx/Cpx and NMNH-18 Cpx were excluded from the following sections of this dissertation.

6.4.2. Recycled atmospheric fluids in the local mantle

^{4}He/^{20}Ne vs R/Ra (^{3}He/^{4}He ratio not corrected for atmospheric contamination), and ^{3}He/^{36}Ar vs ^{40}Ar/^{36}Ar diagrams clearly suggest that fluid inclusions are composed of both mantle and atmospheric fluids (Figs. 33A-B). It is worth noting that the Ar and Ne systematics measured in VESVF xenoliths also exhibit a mixing between MORB and air, with the latter being interpreted as a recycled atmospheric component possibly inherited from the Farallon subduction (see subsection 5.4.4). When comparing with the VESVF xenoliths, nodules from the DVF and SQVF show lower ^{4}He/^{20}Ne and ^{40}Ar/^{36}Ar ratios; on average DVF xenoliths exhibit ^{4}He/^{20}Ne = 73.18 ± 50.07 and ^{40}Ar/^{36}Ar = 462.52 ± 128.51 while the VESVF xenoliths show ^{4}He/^{20}Ne = 1716.80 ± 2416.13 and ^{40}Ar/^{36}Ar = 1962.54 ±1958.53. Besides, as for VESVF xenoliths, there is a correlation between ^{3}He and ^{36}Ar abundances (Fig. 33C) that supports the hypothesis that the atmospheric component identified in both (DVF and SQVF nodules) would have been trapped at mantle conditions (e.g., Matsumoto et al., 2001).

Table 5. Fluid inclusions compositions from DVF and SQVF mantle xenoliths. Concentrations of noble gases isotopes and CO_2 are reported in mol/g. [a.] First estimation of CO_2 during noble gases analysis; [b.] CO_2 measured from glass line. Estimated errors for ^3He, ^4He, ^{20}Ne, ^{21}Ne, ^{22}Ne, ^{40}Ar, ^{36}Ar and CO_2 are <5%, <0.03%, <7%, <5%, <0.7%, <0.07%, <0.1% and <5%, respectively.

Sample	Phase	Locality	Weight (g)	^3He	^4He	^{20}Ne	^{21}Ne	^{22}Ne	CO_2[a]	^{40}Ar	$^{40}Ar*$	$^4He/^{20}Ne$	$^4He/^{40}Ar*$	R/Ra
NMNH-18	Ol	DVF	1.08003	2.87E-18	2.47E-13	2.10E-15	6.13E-18	2.10E-16	1.75E-09	1.72E-13	9.82E-14	117.6	2.52	8.33
NMNH-18	Opx	DVF	1.03656	3.50E-18	3.24E-13	3.51E-15	1.02E-17	3.65E-16	3.10E-09	9.20E-13	2.26E-13	92.3	1.44	7.74
NMNH-18	Cpx	DVF	0.69300	1.03E-17	1.13E-12	1.67E-14	4.85E-17	1.69E-15	1.56E-08	6.63E-12	1.84E-12	67.7	0.61	6.53
NMNH-20	Ol	DVF	1.03079	5.68E-18	5.00E-13	1.52E-14	4.57E-17	1.57E-15	5.28E-09	5.62E-12	3.94E-13	32.8	1.27	8.10
NMNH-20	Opx	DVF	1.39776	2.08E-19	2.74E-14	9.98E-16	2.80E-18	1.02E-16	2.34E-09	1.30E-13	5.36E-14	27.5	0.51	5.39
NMNH-20	Cpx	DVF	0.41756	1.39E-19	1.96E-14	1.18E-15	5.26E-18	4.36E-16	8.33E-11	4.23E-14	3.02E-14	16.5	0.65	5.02
NMNH-27	Ol	SQVF	1.07264	5.69E-19	5.51E-14	1.59E-15	4.63E-18	1.60E-16	2.36E-09	3.08E-13	3.88E-14	34.8	1.42	7.37
NMNH-27	Opx	SQVF	1.11606	1.65E-18	1.74E-13	1.10E-14	3.26E-17	1.13E-15	1.39E-08	4.38E-12	1.52E-12	15.8	0.11	6.68
NMNH-27	Cpx	SQVF	0.55603	6.51E-18	6.45E-13	3.23E-14	9.66E-17	3.29E-15	1.44E-08	1.23E-11	1.35E-12	20.0	0.48	7.16
NMNH-36	Ol	DVF	1.07046	1.15E-18	1.01E-13	3.14E-15	9.13E-18	3.22E-16	3.81E-09	8.88E-13	1.08E-13	32.2	0.93	8.13
NMNH-36	Opx	DVF	1.13955	1.78E-18	1.67E-13	2.02E-15	7.49E-18	3.90E-16	2.14E-09	3.44E-13	1.70E-13	82.5	0.98	7.65
NMNH-36	Cpx	DVF	0.57902	5.40E-18	4.63E-13	4.04E-14	1.19E-16	4.13E-15	1.54E-08	1.37E-11	1.32E-12	11.5	0.35	8.18
NMNH-37	Ol	DVF	1.07363	5.29E-19	4.80E-14	6.17E-16	1.94E-18	6.26E-17	8.83E-10	1.37E-13	4.61E-14	77.8	1.04	7.90
NMNH-37	Opx	DVF	1.10433	8.94E-18	9.15E-13	4.42E-14	1.30E-16	4.47E-15	9.87E-09	9.48E-12	n.a	20.7	n.a	6.93
NMNH-37	Cpx	DVF	0.52719	2.72E-18	2.95E-13	1.23E-14	3.60E-17	1.27E-15	1.21E-08	4.79E-12	2.17E-12	24.0	0.14	6.56
NMNH-39	Ol	DVF	1.01815	1.28E-18	1.16E-13	3.38E-15	9.90E-18	3.45E-16	2.02E-09	6.35E-13	3.35E-13	34.5	0.35	7.84
NMNH-39	Opx	DVF	1.01739	7.41E-18	7.00E-13	3.41E-15	9.37E-18	3.55E-16	3.04E-09	9.52E-13	4.93E-13	205.2	1.42	7.60
NMNH-39	Cpx	DVF	0.50192	1.76E-18	1.95E-13	2.56E-15	6.87E-18	2.74E-16	7.53E-09	1.24E-12	8.43E-13	76.2	0.23	6.46

Sample	Phase	Rc/Ra	error +/- (1σ)	$^{40}Ar/^{36}Ar$	error +/- (1σ)	$^{20}Ne/^{22}Ne$	error +/- (1σ)	$^{21}Ne/^{22}Ne$	error +/- (1σ)	$CO_2/^3He$	$^3He/^{36}Ar$	$CO_2/^3He$	CO_2[b]	δ^{13}C
NMNH-18	Ol	8.35	0.14	690.34	0.62	10.02	0.04	0.0293	0.0009	6.11E+08	0.0115	n.a	n.a	n.a
NMNH-18	Opx	7.77	0.18	391.54	0.08	9.91	0.04	-	-	8.87E+08	0.0015	n.a	n.a	n.a
NMNH-18	Cpx	6.56	0.19	409.01	0.07	9.95	0.02	0.0290	0.0003	1.52E+09	0.0006	n.a	n.a	n.a
NMNH-20	Ol	8.17	0.10	317.79	0.07	-	-	0.0291	0.0002	9.30E+08	0.0003	n.a	n.a	n.a
NMNH-20	Opx	5.44	0.25	503.73	0.44	9.91	0.12	-	-	1.13E+10	0.0008	n.a	n.a	n.a
NMNH-20	Cpx	5.10	0.52	1031.96	1.65	12.57	0.10	0.0562	0.0024	6.00E+08	0.0034	n.a	n.a	n.a
NMNH-27	Ol	7.43	0.19	338.17	0.16	9.91	0.05	0.0290	0.0008	4.14E+09	0.0006	n.a	n.a	n.a
NMNH-27	Opx	6.80	0.16	452.62	0.07	9.88	0.02	0.0293	0.0003	8.44E+09	0.0002	n.a	n.a	n.a
NMNH-27	Cpx	7.27	0.14	332.06	0.35	9.80	0.01	0.0294	0.0002	2.21E+09	0.0002	n.a	n.a	n.a
NMNH-36	Ol	8.20	0.16	336.63	0.05	-	-	-	-	3.31E+09	0.0004	n.a	n.a	n.a
NMNH-36	Opx	7.68	0.18	585.04	0.65	10.76	0.04	0.0400	0.0007	1.20E+09	0.0030	n.a	n.a	n.a
NMNH-36	Cpx	8.40	0.16	327.04	0.30	9.84	0.01	0.0291	0.0002	2.85E+09	0.0001	n.a	n.a	n.a
NMNH-37	Ol	7.93	0.24	445.15	0.42	9.85	0.10	0.0311	0.0020	1.67E+09	0.0017	n.a	n.a	n.a
NMNH-37	Opx	7.03	0.14	278.99	0.27	9.94	0.01	0.0294	0.0002	1.10E+09	0.0003	n.a	n.a	n.a
NMNH-37	Cpx	6.64	0.17	540.20	0.07	9.90	0.02	0.0291	0.0003	4.43E+09	0.0003	n.a	n.a	n.a
NMNH-39	Ol	7.90	0.14	626.51	0.16	-	-	0.0287	0.0006	1.58E+09	0.0013	n.a	n.a	n.a
NMNH-39	Opx	7.62	0.16	612.69	0.13	9.94	0.05	-	-	4.10E+08	0.0048	2.08E+09	1.05E-07	-2.57
NMNH-39	Cpx	6.48	0.20	926.66	0.20	9.92	0.08	-	-	4.29E+09	0.0013	3.32E+09	6.55E-09	-3.80

56
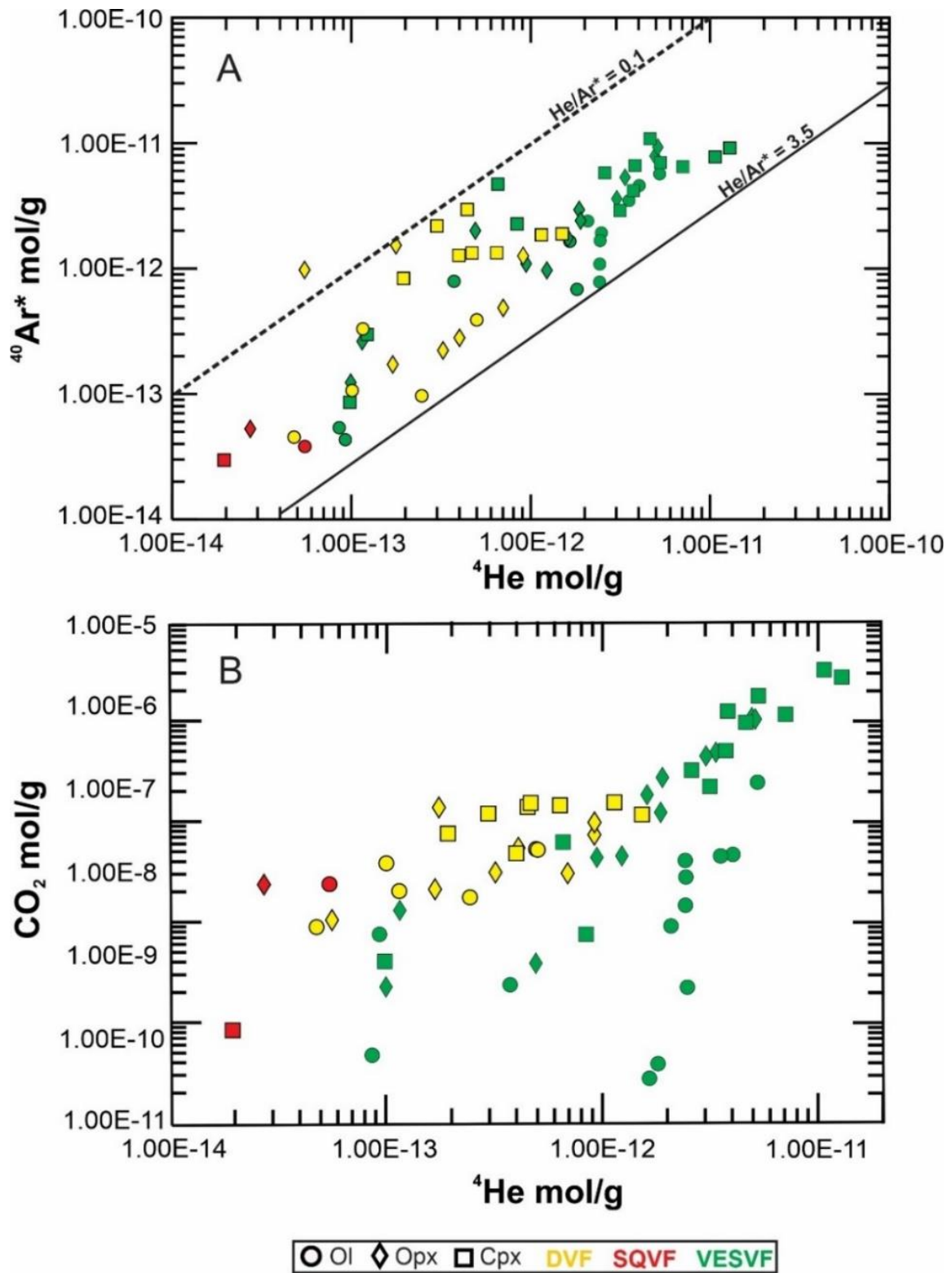
Figure 30. ^{4}He, ^{40}Ar* and CO_2 abundances measured in mantle xenoliths from the DVF, SQVF and VESVF.
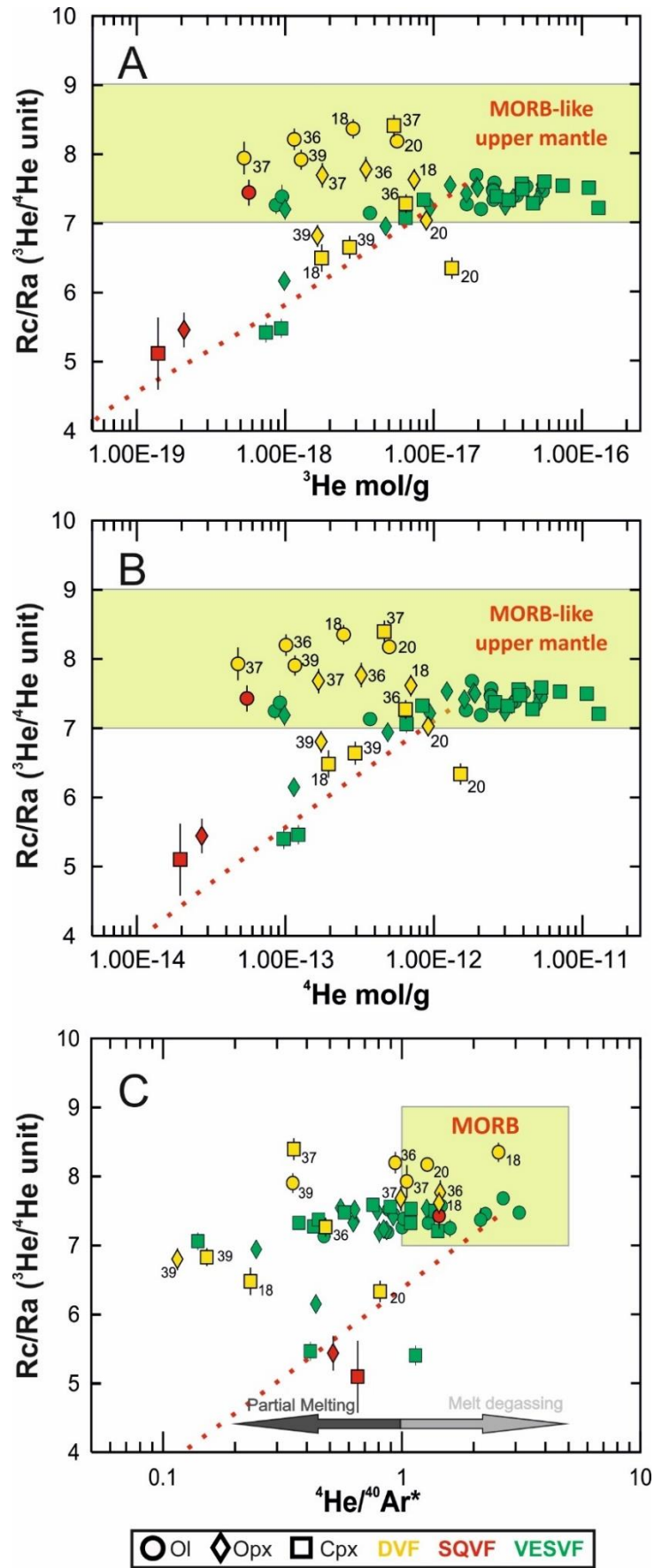
Figure 31. A) [3]He, B) [4]He and C) [4]He/[40]Ar* vs [3]He/[4]He ratios corrected for atmospheric contamination (Rc/Ra). MORB range is report ed at Rc/Ra = 8 ± 1 (Graham, 2002) and [4]He/[40]Ar* from 1 to 5 (Yamamoto et al., 2009).
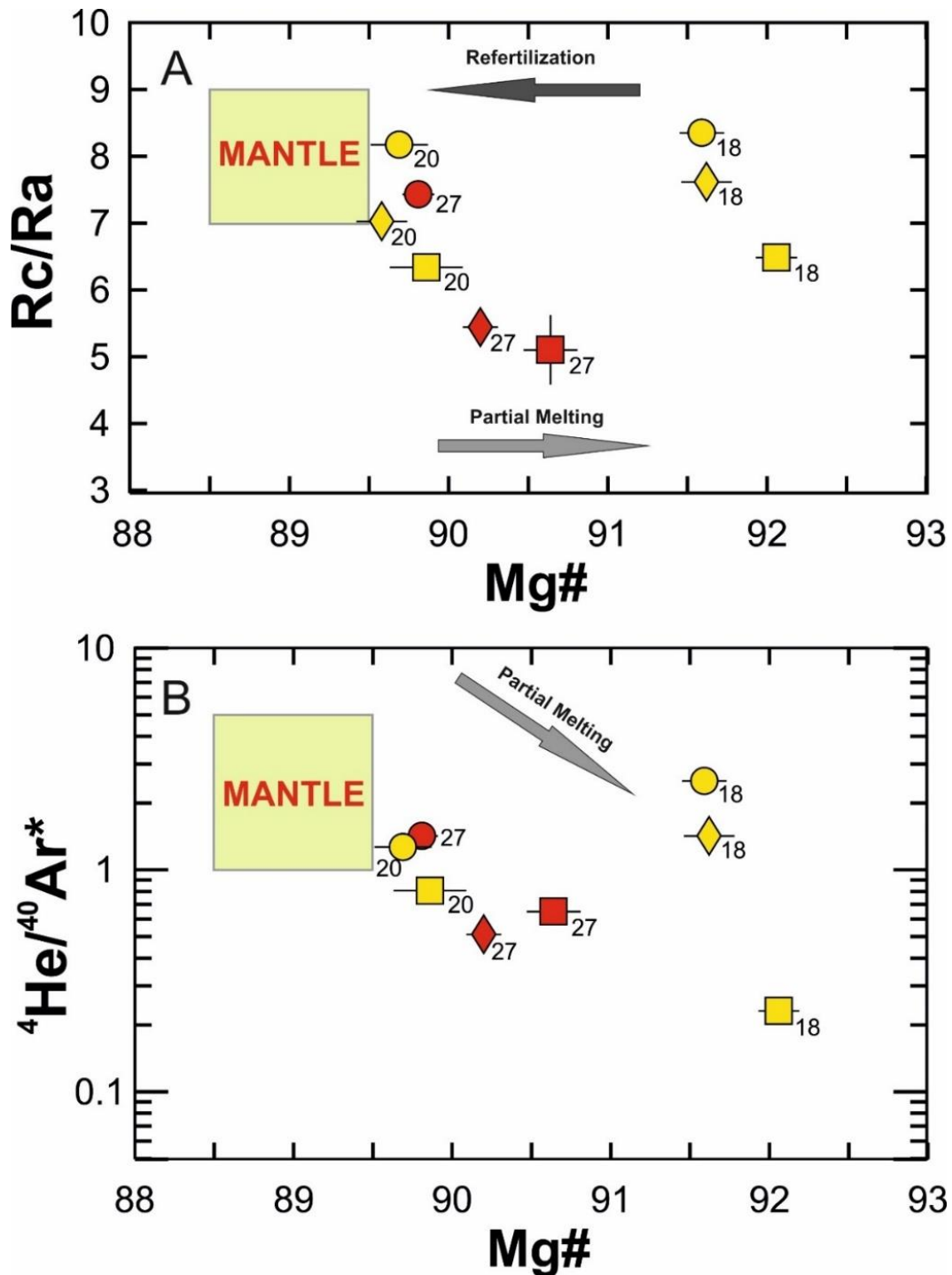
Figure 32. Mg# vs A) Rc/Ra (^{3}He/^{4}He ratio corrected for atmospheric contamination) and vs B) ^{4}He/^{40}Ar*. Mg# values were obtained from Luhr and Aranda-Gomez (1997).

Following the modelling presented in section 5.4.4, the isotopic characteristics of the mantle beneath the DVF were determined using the approach proposed by Langmuir et al. (1978) and Hopp et al. (2007a). The model was only applied to the DVF xenoliths given the data scarcity for the SQVF. Considering a theorical ^{20}Ne/^{22}Ne equal to 12.5 for the upper mantle (Sarda et al., 1988; Moreira et al., 1998), ^{4}He/^{40}Ar* ratios between 0.10 and 3.10 (Fig. 33B) and ^{36}Ar/^{22}Ne ratios between 8.33 and 93.5, it was possible to estimate a ^{40}Ar/^{36}Ar ≈ 1000 for the local upper mantle (with ^{4}He/^{20}Ne ratios <2000; Fig. 34; Table 3) which is clearly lower than the ^{40}Ar/^{36}Ar reported for the VESVF mantle (10,500). The difference in ^{4}He/^{20}Ne and ^{40}Ar/^{36}Ar ratios between these Mexican localities indicates different extends of mantle contamination. The SQVF and the DVF xenoliths (that

represent the west portion of the Mexican lithospheric mantle) are evidently more impacted by the interaction with atmospheric fluids than the VESVF samples.

The above is supported by the fact that DVF xenoliths show equilibration pressures comparable to those reported for VESVF (19.6 ± 3.0 kbar; Luhr and Aranda-Gomez, 1997) that excludes a possible compositional variation related to depth and coincides with the observations made by Luhr and Aranda-Gomez (1997) who identified a systematic east-west increase in fO_2 values measured in mantle xenoliths from the three localities. According to these authors, the increase in fO_2 is the consequence of a subduction-related oxidation of the Mexican lithospheric mantle during the eastward descent of the Farallon slab beneath the North American plate. This oxidation was likely driven by the release of fluids from the oceanic slab that would have transported variable amounts of atmospheric components into the mantle. The process would be controlled by the shifts in the arc-trench gap (occurred during the Mesozoic and early Cenozoic) and produced a greater impact on the mantle regions near the paleo-trench, i.e., the west portion of the Mexican mantle as observed by $^4He/^{20}Ne$, $^{40}Ar/^{36}Ar$ and fO_2 values. This interpretation assumes a direct relationship between fO_2 values obtained by Luhr and Aranda-Gomez (1997) and the extent of atmospheric contamination observed in the samples here analyzed.

However, it is important to clarify that this hypothesis is based on the study of nodules from three localities and must be complemented by future studies on noble gas in other mantle xenolith-bearing volcanic fields belonging to the Mexican Basin and Range Province.

6.4.3. $^3He/^4He$ signature of the mantle beneath DVF and SQVF

The $^3He/^4He$ average of the lithospheric mantle beneath the DVF is 8.39 ± 0.24 Ra (1σ). In the case of the SQVF, only the olivine aliquot is representative of the local mantle with a $^3He/^4He$ ratio = 7.4 ± 0.2 Ra. Both values fall within the MORB-like upper mantle range, which excludes the influence of a lower mantle component (plume hypothesis) beneath these localities and reinforces the hypothesis that the Quaternary monogenetic volcanism of the DVF and the SQVF was produced by continental extension.

Compared with the VESVF, the SQVF olivine falls within the same $^3He/^4He$ range while the DVF average is clearly higher and suggests the existence of a less radiogenic mantle. In section 5.4.5 the role of the Farallon plate was discussed to explain the $^3He/^4He$ signature of VESVF xenoliths. In this scenario, the retreating of the Farallon slab (~40 Ma ago) would have triggered the refertilization of the lithospheric mantle through the injection of ^3He-rich asthenospheric melts (Nieto-Samaniego et al., 1999; Lee, 2005). Assuming the same geodynamic scenario and the relative proximity between the DVF and the VESVF, a similar process should have also occurred beneath Durango (Fig. 35). If we consider the tectonic configuration of the western margin of North America at the time of the Laramide Orogeny (74-40 Ma), in which the Farallon plate acted as a natural barrier between the lithospheric mantle and the asthenosphere (Fig. 35B), it is reasonable to suppose that during the subsequent rollback and retreating, the VESVF mantle could have been exposed to, and refertilized by, the hot asthenosphere first (40-20 Ma ago Fig. 35C); since then, the VESVF lithospheric mantle would have evolved in steady state becoming more radiogenic during the last 20 Ma (starting from a $^3He/^4He$ ratio ~8.5 Ra). As the retreating process continued, the mantle beneath the DVF would have been refertilized at a later stage, which might explain the higher $^3He/^4He$ ratios observed there. These arguments imply a shorter residence time (Rt) of helium in the local subcontinental mantle (see subsection 5.4.5; Figs. 14A and 35D-E).
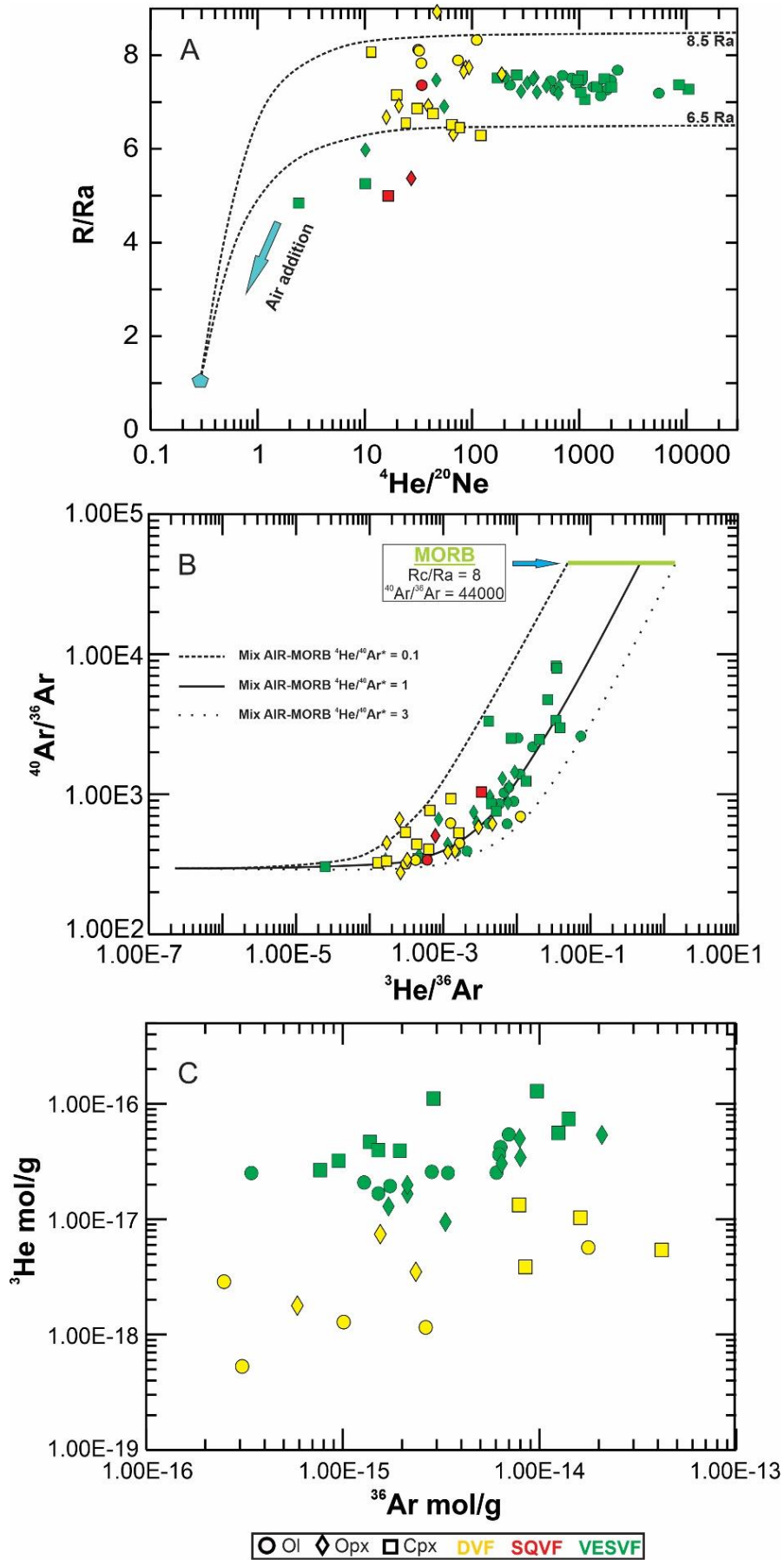
Figure 33. A) ^{4}He/^{20}Ne vs R/Ra diagram, the dotted lines represent the binary mixing between air and an upper mantle source with R/Ra values between 6.5 and 8.5. B) ^{3}He/^{40}Ar vs ^{40}Ar/^{36}Ar diagram. C) ^{36}Ar vs ^{3}He concentrations.
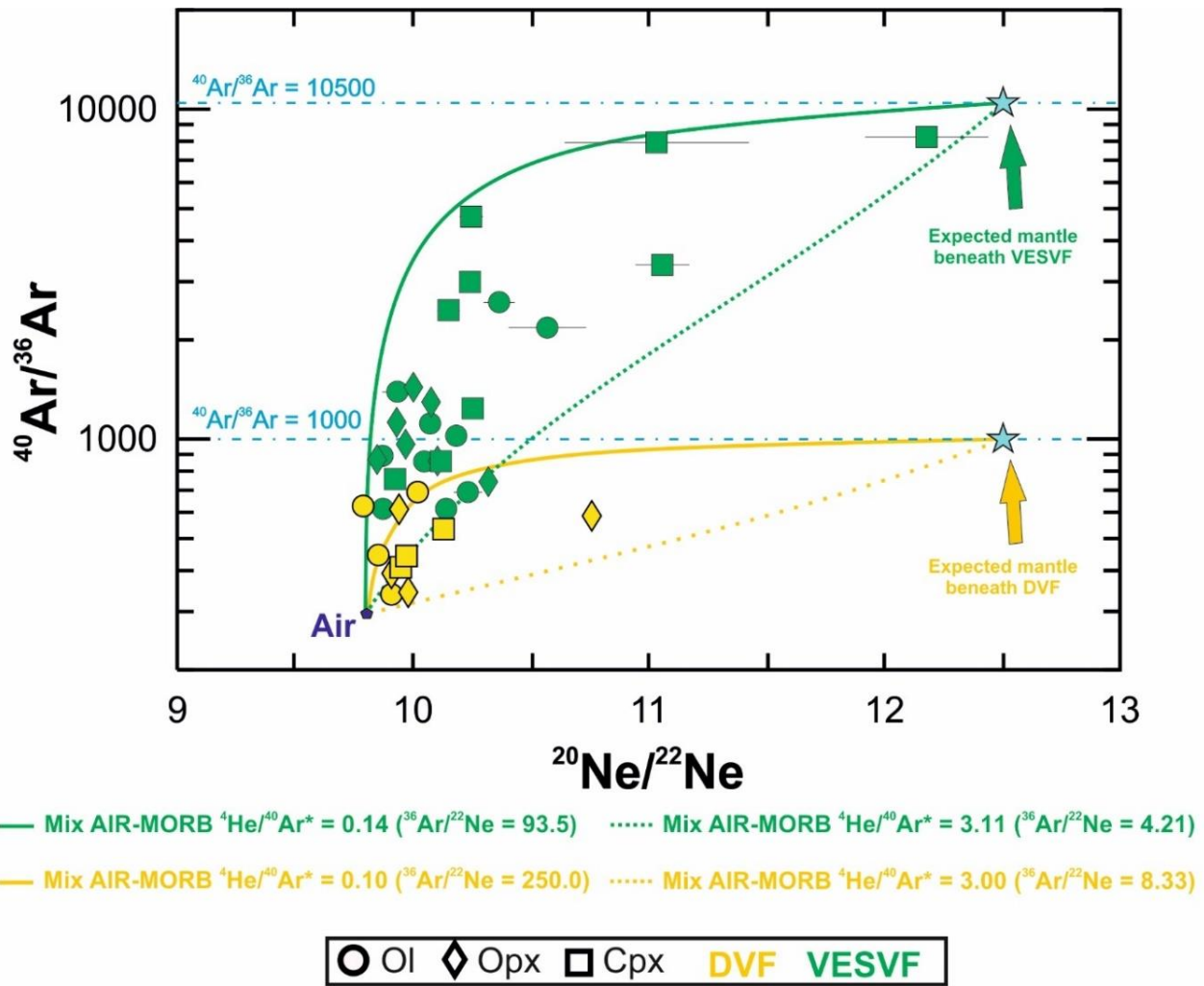
Figure 34. B) $^{20}Ne/^{22}Ne$ vs $^{40}Ar/^{36}Ar$. Mixing curves are the result of mass-balance and isotopic mass balance equations using the parameters reported in Table 3.

The above hypothesis can be tested estimating the refertilization age of the DVF mantle following the formula proposed by Ballentine and Burnard (2002) for the ^{4}He production rate:

$$^{4}He \text{ atoms } g^{-1} yr^{-1} = (3.115 \times 10^{6} + 1.272 \times 10^{5})[U] + 7.710 \times 10^{5}[Th] \quad \text{eq. 5}$$

where [U] and [Th] are concentrations in ppm. Assuming a U concentration between 0.01 and 0.03 ppm (and a Th/U = 3; Gautheron and Moreira, 2002) for the Mexican mantle xenoliths (Dávalos-Elizondo et al., 2016), it is possible to estimate a ^{4}He production rate between 9.23×10^{-20} - 2.77×10^{-19} mol/g*yr. Considering a steady state model (same as proposed for the VESVF, see subsection 5.4.5) for the lithospheric mantle beneath the DVF, the above-estimated ^{4}He production rate, a starting $^{3}He/^{4}He$ =8.5 Ra and a ^{4}He concentration = 4.5×10^{-11} mol/g (the maximum value identified for continental mantle xenoliths; Gautheron and Moreira, 2002), we find that a residence time (Rt) of 4 to 10Ma is needed to decrease the helium ratio from 8.5 to 8.39 Ra (the average $^{3}He/^{4}He$ values measured in DVF xenoliths). In other words, these ages support the idea that the DVF mantle was more recently refertilized than the mantle located beneath the VESVF, where a Rt of 40 - 20Ma was estimated (subsection 5.4.5). This would explain the higher $^{3}He/^{4}He$ ratios observed in Ol and Opx crystals from DVF xenoliths.
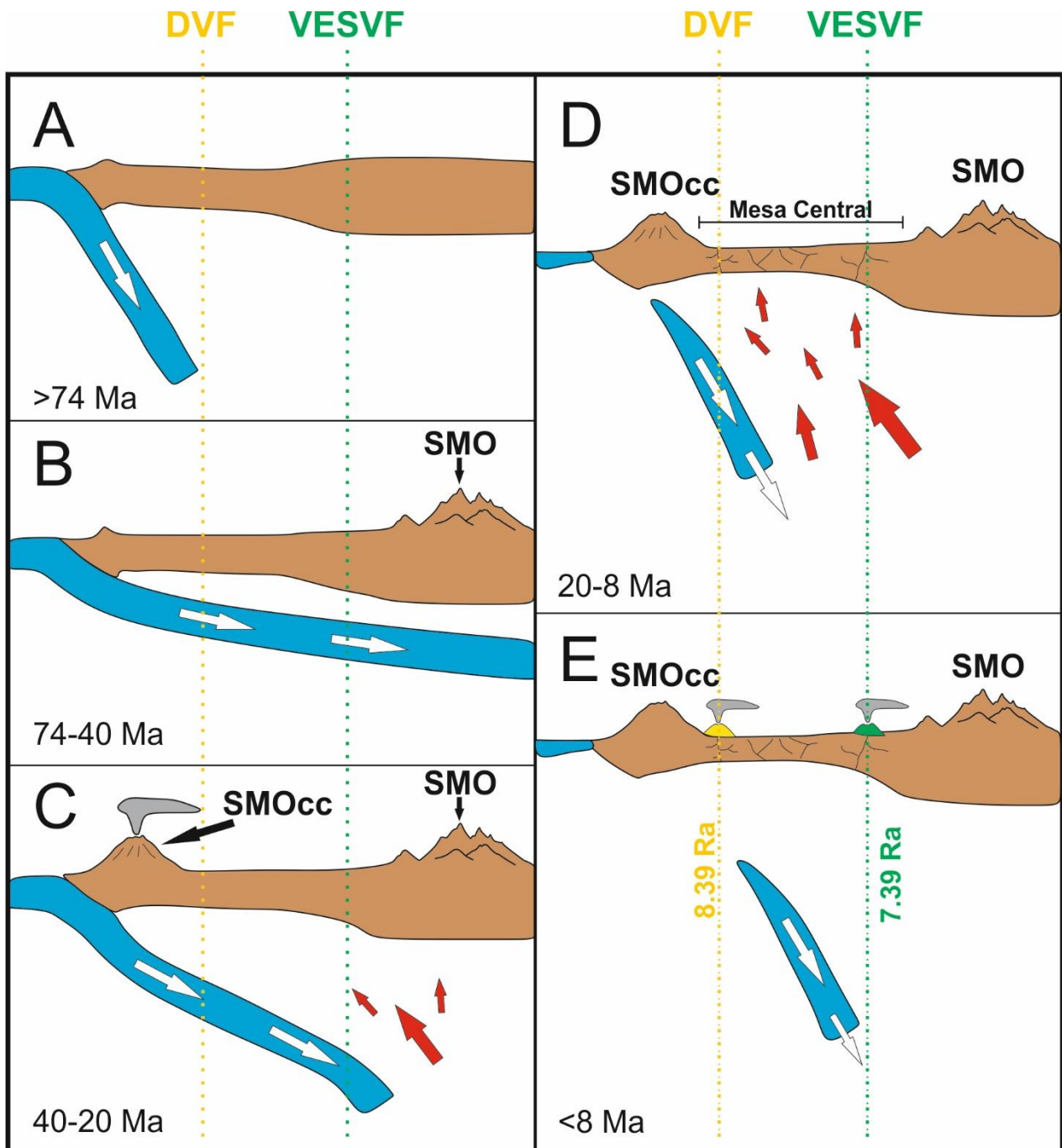
Figure 35. Evolution of the western margin of the North American plate during the Late Mesozoic and Cenozoic. A) Subduction of the Farallon slab beneath North America during the Mesozoic. B) Shallowing of the subduction angle and tectonic uplift of the Sierra Madre Oriental (SMO; Laramide Orogeny). C) Rollback of the Farallon slab causing the introduction of asthenospheric fluids in the lithospheric mantle beneath the VESVF. This process also caused extension at the base of the crust favoring the ignimbrite flare-up of the Basin and Range Province and the formation of the Sierra Madre Occidental (SMOcc). D) Over time, the subduction angle increased and ceased which favored the refertilization of the lithospheric mantle beneath DVF. E) The lithospheric mantle beneath the DVF and VESVF evolves in steady-state becoming more radiogenic over time. The Basin and Range extension facilitated the formation of mantle xenolith-bearing alkali basalt localities (e.g., the VESVF and DVF) in the Mesa Central. Adapted from Lee (2005).

6.4.4. CO_2 contents

In all Mexican xenoliths, CO_2 is the dominant phase in fluid inclusions (see Tables 2 and 5). CO_2 is positively correlated with noble gases which means that those samples with the highest contents of

He and Ar commonly exhibit the highest CO_2 concentrations. This is not a new observation since different studies (where fluid inclusions were extracted using the same technique) have reported similar results in European ultramafic xenoliths (Gennaro et al., 2017; Rizzo et al., 2018, 2021). Comparing with these European localities, VESVF samples exhibit a wide range of variability (Fig. 36); pyroxenes show similar gas concentrations to those reported in mantle xenoliths from SW Poland and the Hyblean plateau but olivines manifest the lowest CO_2 contents.
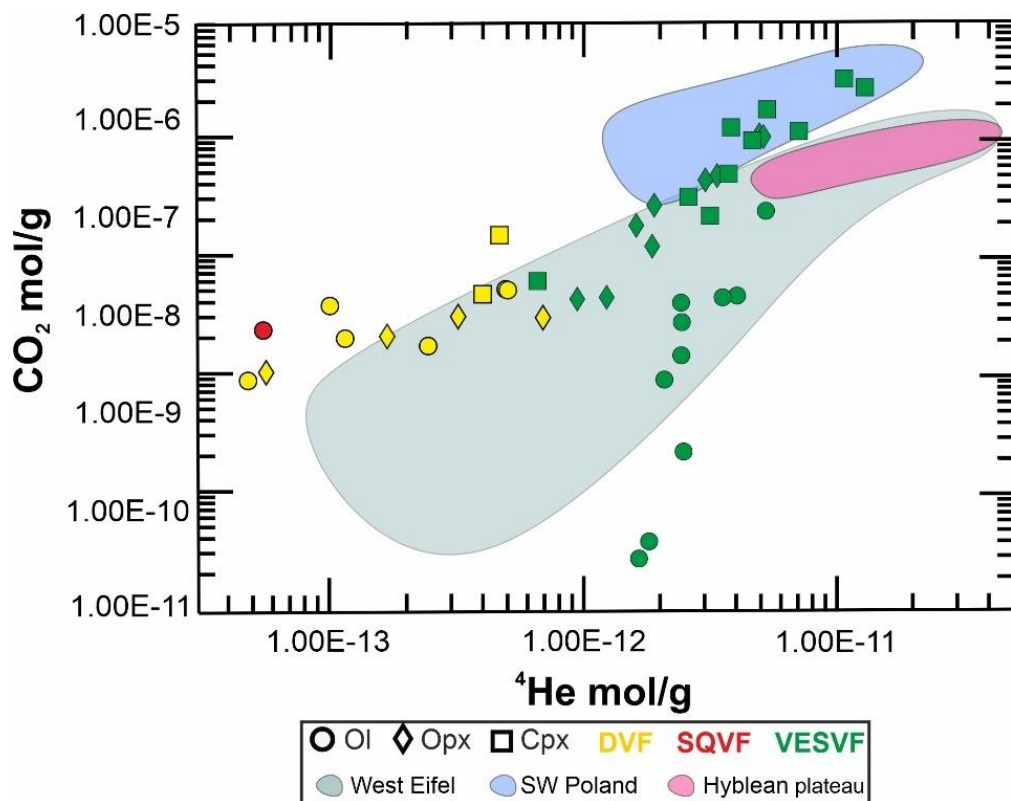
Figure 36. ^{4}He vs CO_2 concentrations. Those samples suspicious of diffusive fractionation were not considered. Compositional field for the Hyblean plateau, SW Poland and West Eifel were designed based after Correale et al. (2015), Gennaro et al. (2017) and Rizzo et al. (2018, 2021).

Fig. 36 also indicates that DVF and SQVF samples show a narrow range of CO_2 concentrations and are among the most depleted in both helium and CO_2. As discussed in previous sections, DVF and VESVF xenoliths show similar equilibration pressures and different metasomatic processes that would explain the differences in ^{3}He/^{4}He and ^{40}Ar/^{36}Ar ratios and rules out a compositional variability related to depth. Although, it is not possible to discard that the difference in CO_2 could be associated with microscopic factors such as the quantity and volume of the fluid inclusions, the entrapment of different metasomatic agents characterized by different carbon contents could explain the difference in CO_2 concentrations observed in mantle xenoliths (e.g., Rizzo et al., 2021). In this respect, the range of He/Ar* values overlapping in the SQVF, DVF and VESVF (Fig. 31) is a further indication that different degassing pressures (i.e., depths) are not able to justify the observed CO_2 concentration variability.

6.5. Conclusions

DVF and SQVF xenoliths offer a wider view of the variability of noble gas and carbon in the Mexican lithospheric mantle. ^{4}He/^{40}Ar* ratios suggest a systematic decrease from olivines to pyroxenes. This

depletion is accompanied by a general increase in the Mg# and may be explained as the effect of partial melting and/or metasomatic processes affecting the local mantle. Like VESVF xenoliths, Ne and Ar systematics revealed a mixing between atmospheric and MORB-like fluids, strongly supporting the presence of an atmospheric component eventually recycled via paleo-subduction. Comparing with the VESVF samples, DVF and SQVF nodules describe a more impacted mantle by atmospheric-derived noble gases which agrees well with the east-to-west increase of the oxygen fugacity in mantle xenoliths previously studied in the Basin and Range Province. This oxidation was likely driven by the release of fluids from the Farallon slab that would have transported variable amounts of atmospheric components that mainly impacted the west portion of the Mexican upper mantle.

The average Rc/Ra ratios for the DVF is 8.39 ± 0.24 Ra and for SQVF xenoliths is 7.43 ± 0.19 Ra (1σ). The difference in $^{3}He/^{4}He$ ratios between the VESVF and the DVF is likely associated with different ages of mantle refertilization possibly triggered by the retreating of the Farallon slab (~40 Ma ago). It is worth noting that the SQVF results were not included in the model because the scarcity of data. While for VESVF xenoliths the refertilization was approximately between 40-20Ma ago, the respective age for the DVF mantle is <10Ma. Considering a mantle evolution governed by a steady-state model in which the mantle becomes more radiogenic over time, the above hypothesis is a feasible explanation for the variability of He isotopes observed along the central and NW Mexican lithospheric mantle.

CHAPTER 7. NOBLE GAS AND CARBON ISOTOPIC SIGNATURE OF THE SUBARC MANTLE LOCATED BENEATH THE SIERRA CHICHINAUTZIN VOLCANIC FIELD (SCN).

7.1 Geological setting of the SCN

The SCN is a Quaternary monogenetic volcanic field located along the Trans-Mexican Volcanic Belt (TMVB) front, and in between two Quaternary stratovolcanoes: Popocatepetl and Nevado de Toluca (Figs. 37; Márquez et al., 1999a, 1999b; Schaaf et al., 2005; Meriggi et al., 2008). The SCN has been active during the last 40 ka producing more than 200 monogenetic structures (including several scoria cones, lava flows, lava domes, shield volcanoes and hydromagmatic craters) and approximately 470 km^3 of extruded magma (Márquez et al., 1999b; Schaaf et al., 2005; Meriggi et al., 2008). Erupted rocks include basalts, basaltic andesites, andesites and dacites that overlie lavas and pyroclastic deposits of the Popocatepetl and Nevado del Toluca, sedimentary rocks of the Sierra Madre Oriental and sediments of the Mexico, Toluca and Cuernavaca basins (Márquez et al., 1999b; Meriggi et al., 2008). The origin of the SCN is still controversial and different hypothesis have been set out in the literature. One model typified by Meriggi et al. (2008) suggests that the calc-alkaline affinity and the LILE-Pb enrichments identified in evolved rocks are the result of partial melting of a subduction-related metasomatized mantle wedge that feeds the volcanism of the SCN. In contrast, other studies (Márquez et al., 1999a, 1999b) propose an extensional origin for the monogenetic SCN; these authors point to an OIB geochemical affinity of the SCN basalts (interpreted as the result of partial melting of a mantle not affected by subduction), and that the calc-alkaline affinity of the most evolved rocks is the result of magma mixing between the above-mentioned basaltic magmas and crustal-derived felsic magmas.
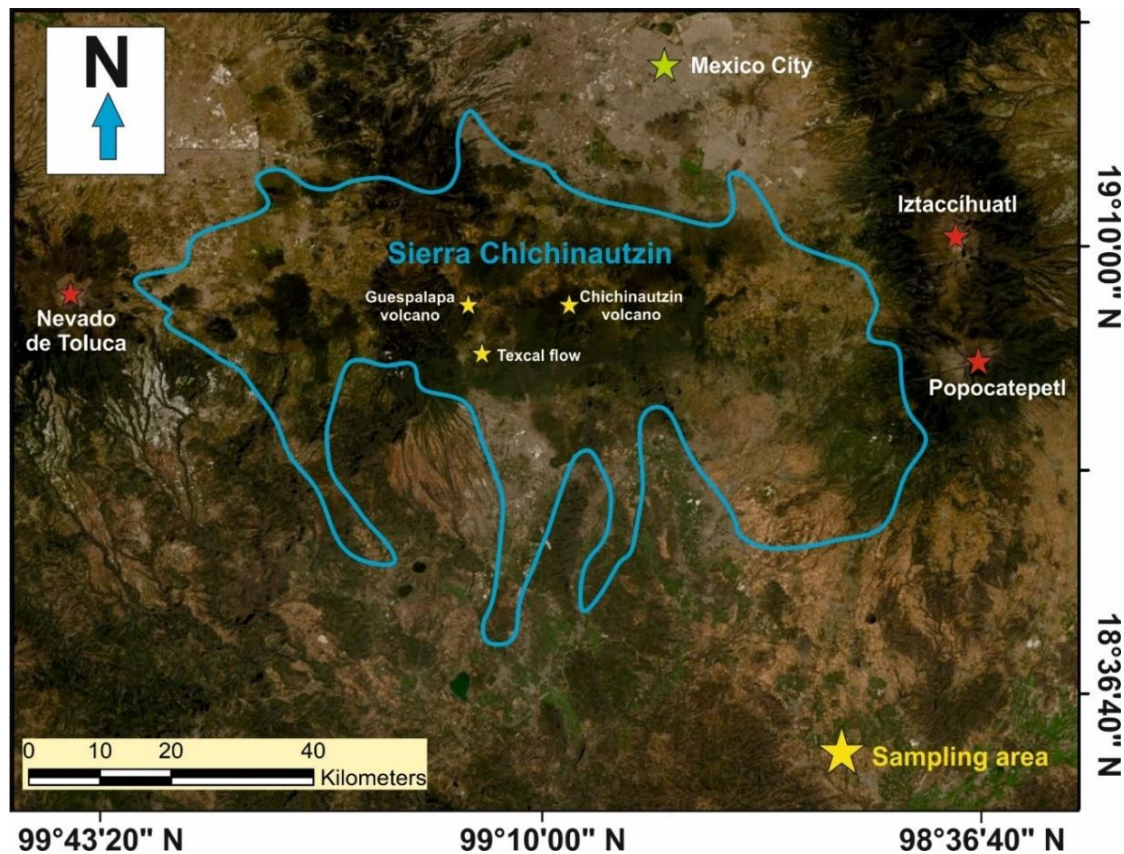
Figure 37. Image from Google Earth (June 23rd, 2021) showing the Sierra Chichinautzin (SCN) and sampling areas.

7.1. Results

Four samples were analyzed including two calc-alkaline basaltic andesites (samples CH09-1 and CH09-9) and two high-Nb arc basalts (samples CH05-16 and MCH06-5). Sample CH09-1 was collected from the Texcal Flow, samples CH05-16 and CH09-9 were collected in the Guespalapa volcano while sample MCH-06-5 was obtained from the Chichinautzin volcano (Fig. 37). The geochemical characteristics and the petrogenesis of the same suite of volcanic rocks is discussed elsewhere (Straub et al., 2011). The noble gas and CO_2 compositions of the olivine phenocrysts-hosted fluid inclusions are reported in Table 6 and Fig. 38. As mantle xenoliths, fluid inclusions in SCN phenocrysts are dominated by CO_2 (with concentrations that vary between 1.17×10^{-8} and 1.29×10^{-6} mol/g). Helium concentrations are also elevated: ^{3}He and ^{4}He contents vary from 9.98×10^{-18} to 3.94×10^{-16} and from 1.00×10^{-12} to 3.99×10^{-11} mol/g, respectively. Rc/Ra values are within the mantle range (7.00 ± 0.07– 7.36 ± 0.10 Ra; 1σ) while ^{4}He/^{40}Ar* ratios (varying between 3.68 to 8.71 are higher than those observed in Mexican xenoliths. In general, the samples exhibit ^{4}He/^{20}Ne >500 and ^{40}Ar/^{36}Ar >650 (except for sample MCH06-5) and δ^{13}C values between -6.3 and -5.0‰.

7.2. Discussion

7.2.1. Comparison with noble gas signatures obtained from Mexican mantle xenoliths (VESVF, DVF and SQVF)

Petrological and isotopic analysis performed in SCN lavas have proved that both andesites and basalts directly derive from the local mantle. According to Straub et al. (2008, 2011), these rocks show common geochemical characteristics that suggest a similar genetic mechanism; andesites and basalts are consistently enriched in Ni and MgO (with melt Mg# $\approx$ 70), they show similar ratios of trace elements (e.g., Sr/Y and Gd/Yb), and contain Ni-rich olivines with ^{3}He/^{4}He MORB-like ratios. Sr-Pb-Nd isotopes are more heterogeneous, and are interpreted to reflect the existence of different mantle components (Schaaf et al., 2005; Straub et al., 2011) rather than crustal assimilation processes. Straub et al. (2008, 2011) propose that both andesites and basalts originated after the partial melting of coexisting silica-deficient and quartz-normative pyroxenites (located below the Moho) that were produced by the infiltration of silicic slab materials in the local mantle. After melting, a broad spectrum of high-Mg# basaltic, andesitic and dacitic melts were generated; during their ascent through the crust, these can suffer from some differentiation by fractional crystallization and crustal melt mixing episodes (just before the eruption), explaining the occurrence of lavas with Mg#<65.

The lavas studied in this work have relative high Mg# (>60) and ^{3}He/^{4}He ratios within the MORB-like upper mantle range (Fig. 39), so it is reasonable to assume that the fluid inclusions hosted in our olivine separates represent the fluids present in the SCN subarc mantle. This consideration allows to compare the isotopic signature of the lavas with the fluid inclusion data obtained from the VESVF, DVF and SQVF xenoliths. In terms of gas concentrations, olivines from the calc-alkaline basaltic andesites (samples CH09-1 and CH09-9) exhibit the greatest He and CO_2 contents when compared with the rest of the Mexican dataset (Fig. 38); regarding samples MCH05-16 and CH05-16 (alkaline basalts), these show higher values than in DVF and the SQVF nodules and comparable contents relative to the VESVF mantle xenoliths. The fact that SCN olivines exhibit gas concentrations comparable or even higher than the VESVF nodules indicate a volatile-rich parental melt.

Despite of the differences in gas contents observed in CH09-1 and CH09-9, all samples exhibit Rc/Ra values (^{3}He/^{4}He ratios corrected for atmospheric contamination) within the MORB range

(Fig. 39) suggesting that the olivines derive from an upper mantle similar to that beneath the VESVF with comparable ^{3}He/^{4}He ratios (on average 7.24±0.33Ra; 1σ).

Both basaltic andesites and alkaline basalts show higher ^{4}He/^{40}Ar* ratios than those reported for mantle xenoliths (Fig. 39B), consistent with the magmatic nature of the olivine-phenocrysts; in silicate melts, Ar is less soluble than He so high ^{4}He/^{40}Ar*ratios are expected during melt degassing processes (Jambon et al., 1985; Moreira and Sarda, 2000; Paonita and Martelli, 2007; Paonita, 2009; Boudoire et al., 2018). It is worth noting that the four olivine samples (CH09-1, CH09-9 and MCH05-16) exhibit ^{4}He/^{20}Ne ratios higher than 500 and fall within the range reported for the VESVF mantle xenoliths (Fig. 40A). The remaining sample CH06-9 shows a ^{4}He/^{20}Ne of 52.82, and while this is the lowest ratio identified in the SCN dataset, it is considerably higher than the air value and is comparable with the DVF samples and some VESVF nodules with ^{3}He/^{4}He>7 Ra. Based on the gas concentrations and isotopic ratios of noble gases, the SCN olivines likely reflect a subarc mantle with similar characteristics to those described for the VESVF mantle. Probably both localities evolved under similar geodynamic conditions due to their proximity (Fig. 14). This scenario would have changed when the Mexican volcanic arc starter to migrate from a NW-SE to an almost E-W continental arc (see subsections 4.1 and 4.2) as a result of the tectonic reorganization of the western margin of the North American plate that came after the subduction of the Farallon slab (30 - 7 Ma ago).
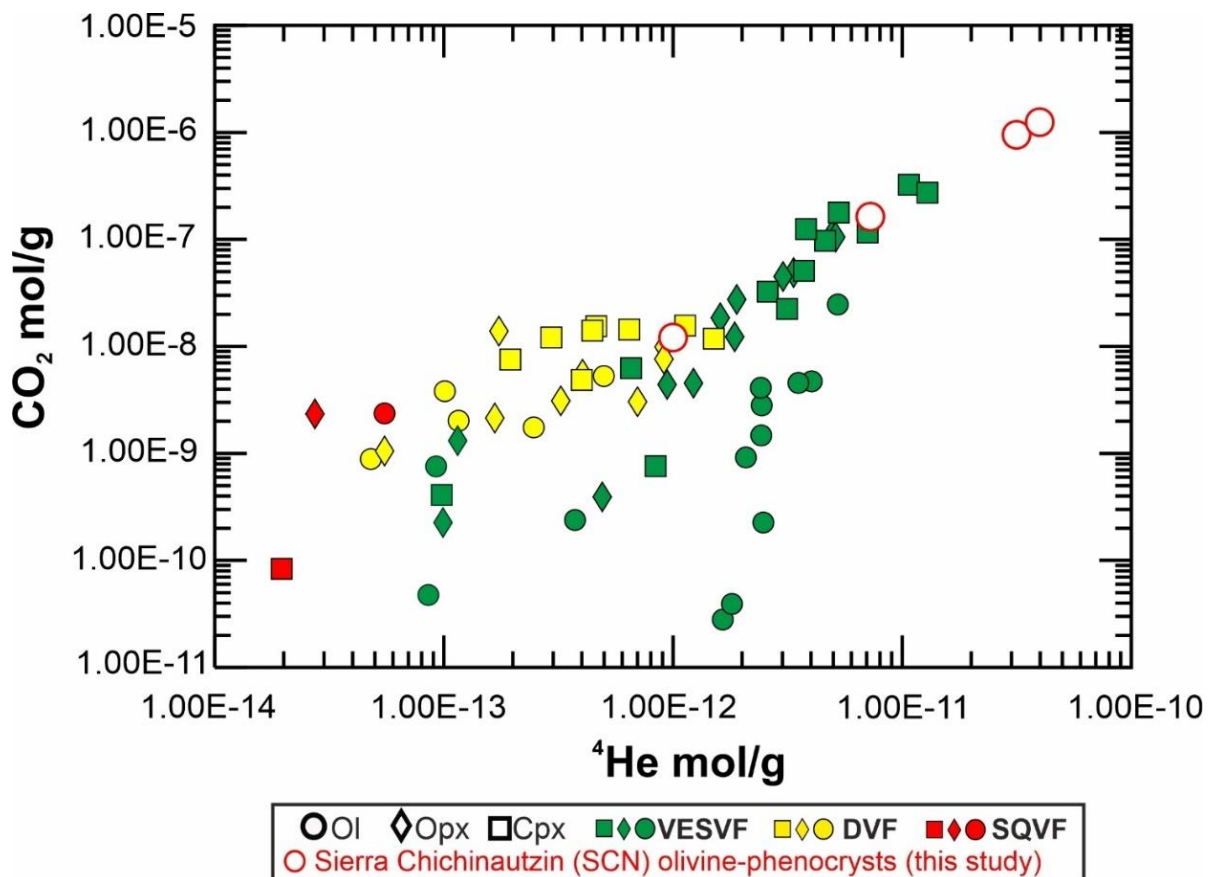
Figure 38. ^{4}He vs CO_2 abundances measured in fluid inclusions from mantle xenoliths and SCN olivines. VESVF: Ventura Espiritu Santo Volcanic Field, DVF: Durango Volcanic Field, SQVF: San Quintin Volcanic Field.

Table 6. Fluid inclusions compositions of the Sierra Chichinautzin (SCN) olivine phenocrysts. [a.] First estimation of CO_2 during noble gases analysis; [b.] CO_2 measured from glass line. Estimated errors for ^3He, ^4He, ^{20}Ne, ^{21}Ne, ^{22}Ne, ^{40}Ar, ^{36}Ar and CO_2 are <5%, <0.03%, <7%, <5%, <0.7%, <0.07%, <0.1% and <5%, respectively.

Sample	Phase	Weight (g)	^3He	^4He	^{20}Ne	^{21}Ne	^{22}Ne	CO_2[a]	^{40}Ar	$^{40}Ar*$	$^4He/^{20}Ne$	$^4He/^{40}Ar*$	R/Ra
CH09-1	Ol	0.48322	2.38E-16	2.46E-11	9.08E-15	2.77E-17	9.33E-16	7.17E-07	4.89E-12	2.82E-12	2704.2	8.71	6.99
CH09-9	Ol	0.51047	3.94E-16	3.99E-11	1.39E-14	4.26E-17	1.44E-15	1.29E-06	1.24E-11	7.21E-12	2879.6	5.54	7.10
CH05-16	Ol	0.48009	7.43E-17	7.26E-12	1.36E-14	4.02E-17	1.37E-15	1.60E-07	2.68E-12	1.97E-12	535.8	3.68	7.36
MCH06-5	Ol	0.71327	9.98E-18	1.00E-12	1.90E-14	5.50E-17	1.90E-15	1.17E-08	8.79E-13	2.51E-13	52.8	3.98	7.13

Sample	Rc/Ra	error +/- (1σ)	$^{40}Ar/^{36}Ar$	error +/- (1σ)	$^{20}Ne/^{22}Ne$	error +/- (1σ)	$^{21}Ne/^{22}Ne$	error +/- (1σ)	$CO_2/^3He$	$^3He/^{36}Ar$	$CO_2/^3He$	CO_2[b]	$\delta^{13}C$
CH09-1	6.99	0.07	697.30	0.07	9.74	0.03	0.0298	0.0005	3.01E+09	0.0340	4.08E+09	9.74E-07	-6.13
CH09-9	7.10	0.06	706.09	0.76	9.65	0.02	0.0297	0.0004	3.26E+09	0.0224	3.61E+09	1.42E-06	-6.31
CH05-16	7.36	0.10	1117.31	0.10	9.93	0.02	0.0295	0.0003	2.15E+09	0.0310	3.88E+09	2.88E-07	-5.00
MCH06-5	7.17	0.10	414.01	0.08	10.06	0.01	0.0292	0.0002	1.18E+09	0.0047	n.a	n.a	n.a
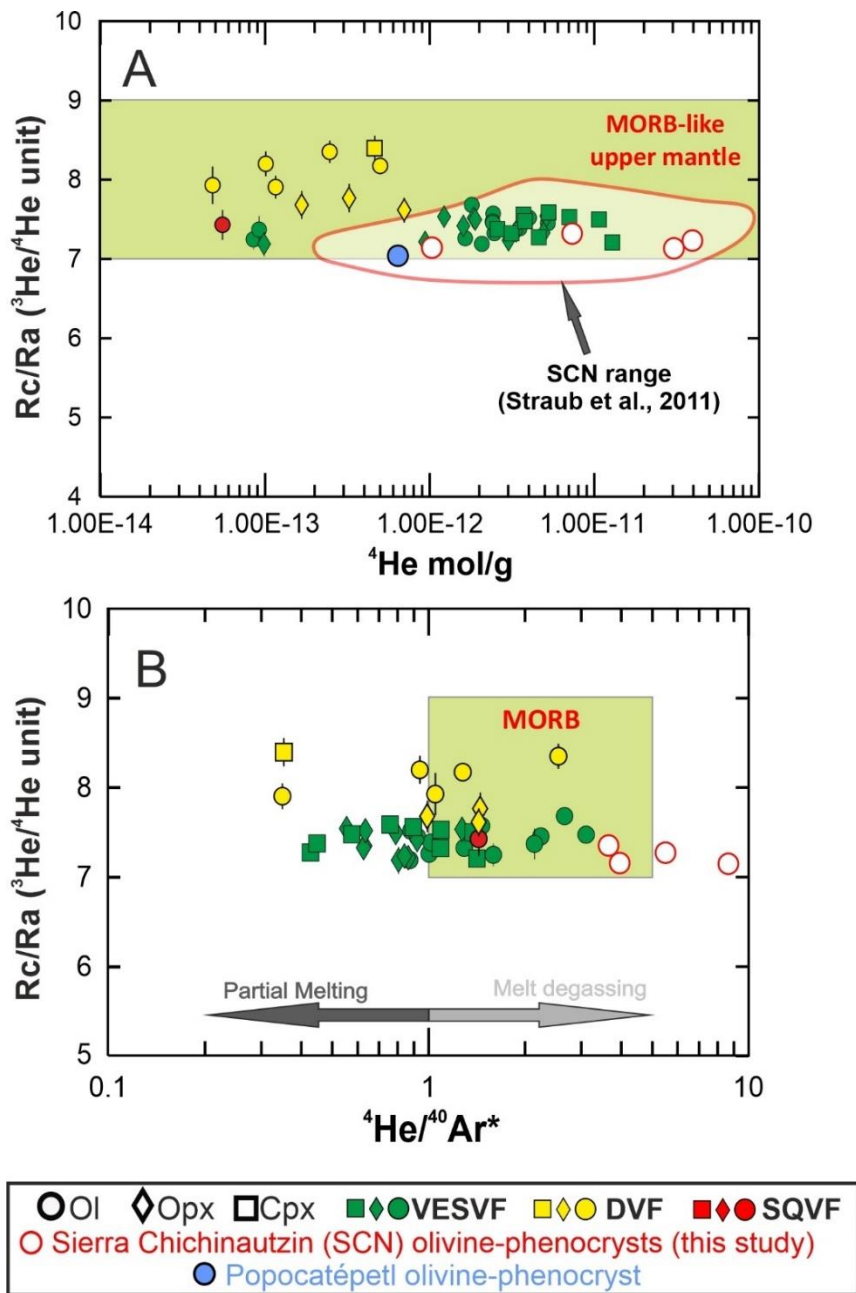
Figure 39. A) ^{4}He, B) ^{4}He/^{40}Ar* vs Rc/Ra (^{3}He/^{4}He ratios corrected for atmospheric contaminations) for the SCN samples and comparison with the Mexican mantle xenoliths analyzed in chapters 5 and 6. The value for Popocatépetl volcano is from Straub et al. (2011). Plotted values of VESVF and DVF correspond to samples not modified by secondary processes such as diffusive fractionation (see subsections 5.4 and 6.4.1).

7.2.2. Comparison with other noble gas information reported for the TMVB

Despite of the great variability of volcanic structures and deposits identified along the TMVB, very few data have been reported regarding the isotopic study of noble gases and δ^{13}C (e.g., Taran et al., 2002; Inguaggiato et al., 2005; Straub et al., 2011). The isotopic data reported in the literature is mainly obtained from the analysis of superficial gas emissions including fumaroles, bubbling and dissolved gas and, to a minor extent, from fluid inclusions (e.g., SCN and Popocatepetl lavas; Straub et al., 2011). The available information for the TMVB is presented in Figs. 40 and 41 and include

samples collected in the Jalisco block, Colima and Ceboruco volcanoes, La Primavera caldera, Popocatepetl and Iztaccihuatl volcanoes and the Cuautla zone (see Fig. 14B).
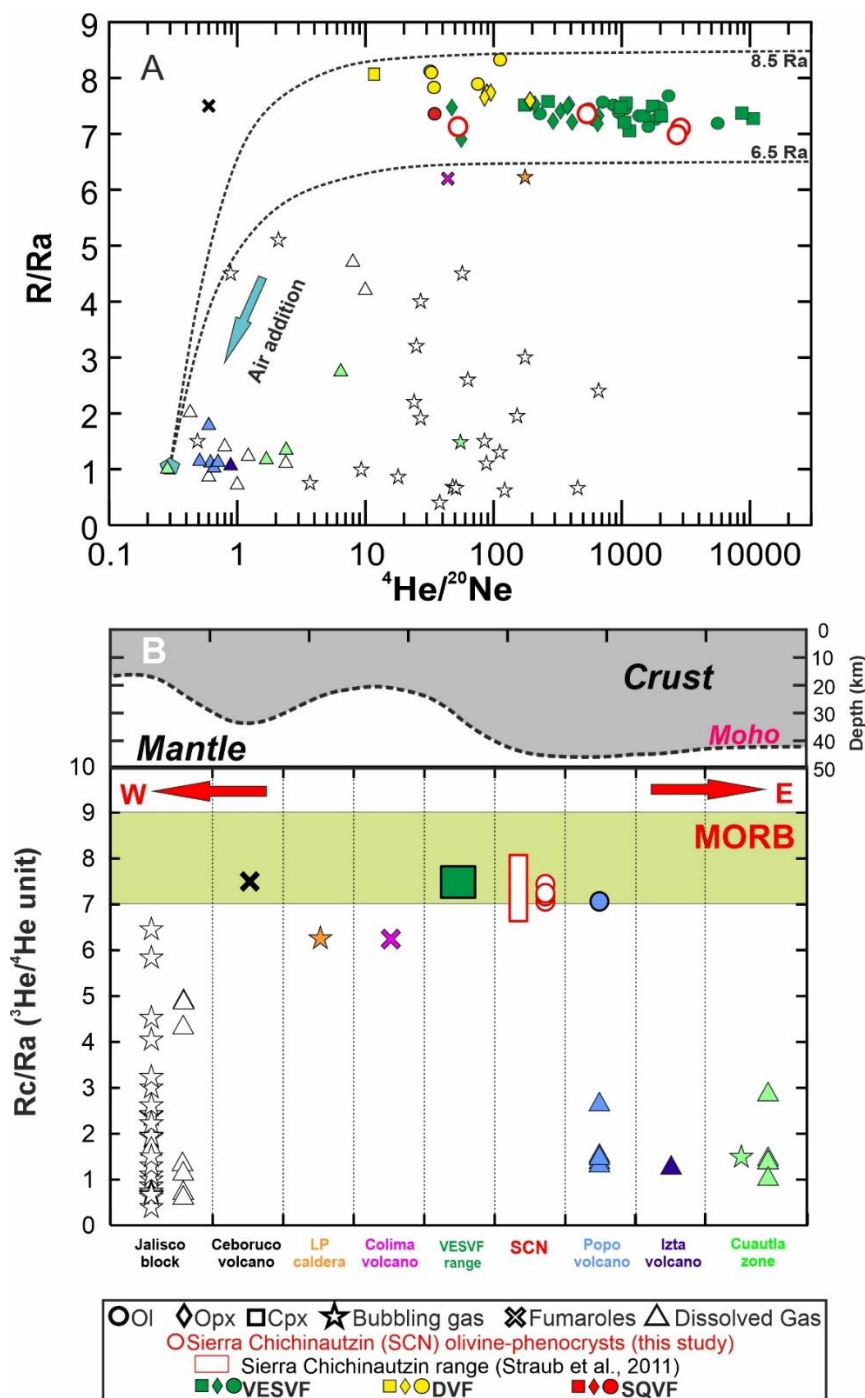
Figure 40. A) $^{4}He/^{20}Ne$ vs R/Ra ratios ($^{3}He/^{4}He$ not corrected for atmospheric contamination) estimated for the SCN olivines. B) Variability of 3He/4He ratios along the Transmexican Volcanic Belt (TMVB). Values for the Jalisco block, La Primavera caldera (LP) and Ceboruco and Colima volcanoes are from Taran et al. (2002). FluId inclusion value for the Popocatépetl volcano is from Straub et al. (2011). Bubbling and surface gas for Popocatépetl-Izztaccíuatl volcanoes and for the Cuautla zones are from Inguaggiato et al. (2005). The crustal thickness profile was designed after Urrutia-Fucugauchi and Böhnel (1988) and Urrutia-Fucugauchi et al. (1999).

In a $^{4}He/^{20}Ne$ vs R/Ra plot, it is straighforward to distinguish fluid inclusion results from superficial gas information (Fig. 40A): gas manifestations exhibit lower $^{3}He/^{4}He$ values than fluid inclusions. This is commonly attributed to the interaction of magmatic fluids with superficial fluids during gas-water-rock interactions in the shallow crust, including the addition of crustal radiogenic fluids (e.g.,

71

Lages et al., 2021 and references therein). These processes are especially relevant for dissolved water samples that also exhibit the lowest $^4He/^{20}Ne$ ratio (very close to the air value = 0.318; Ozima and Podosek, 2002) confirming a dominant contamination by atmospheric-derived gases. In the case of Popocatepetl volcano, the difference in Rc/Ra between fluid inclusion and dissolved water (Fig. 40B) shows the utility of the former to investigate the source mantle helium isotopic signature. Similar studies performed in arc volcanoes have revealed that volatiles sampled in peripheral geothermal fields or low-temperature bubbling springs are subjected to shallow contamination from (meteoric, biogenic) fluids, resulting in lower $^3He/^4He$ signatures relative to high-temperature fumarole emissions (Sano et al., 1984; Williams et al., 1987; Lages et al., 2021). Thus, we consider that bubbling and dissolved gas data observed in Figs. 40-41 underestimate the real $^3He/^4He$ signature of the local mantle (as proved for dissolved gas samples from Popocatépetl volcano; on average 1.65 ± 0.49 Ra, 1σ. Other averages are 2.24 ± 1.69 Ra (1σ) and 1.66 ± 0.70 Ra (1σ) calculated for bubbling/dissolved gas samples from the Jalisco block and the Cuautla zone, respectively), which prevents a direct comparison with the SCN lavas. In the case of Popocatepetl, the $^3He/^4He$ value measured in fluid inclusions is comparable with those measured in SCN olivines and in the VESVF mantle xenoliths, which indicates a similar mantle signature (at least in terms of helium isotopes) supported by the vicinity of these volcanic zones (Fig. 14).

Some of the highest helium isotopic ratios (Rc/Ra >6) are observed in fumaroles from the Ceboruco and Colima volcanoes, it is worth mentioning that fumaroles from Ceboruco exhibit MORB-like signature with a value similar to those reported in SCN olivines and Popocatepetl, thus these can be considered as representative of the local mantle. Conversely, those from Colima, although obtained from a high-temperature fumarole (850℃), are characterized by low $^3He/^4He$ ratios (around 6 Ra), which may reflect a more radiogenic portion of the sub-arc mantle, possibly associated with a crustal contribution from the subducted slab, or the addition of ^4He-rich crustal fluids during the magma ascent considering the thickness of the crust in the western TMVB (20-30 km; Figs. 14B and 40B; Urrutia-Fucugauchi and Böhnel, 1988; Urrutia-Fucugauchi et al., 1999).

7.2.3. The $\delta^{13}C$ signature of the local subarc mantle

Reported $\delta^{13}C$ values for the TMVB are illustrated in Fig. 41. As for helium ratios, the low $\delta^{13}C$ ($\delta^{13}C$ <8‰; Fig 41A) reported in bubbling gas and dissolved water of the Jalisco block, the Popocatepetl and Iztaccíhuatl volcanoes suggest that these samples were likely affected by secondary processes occurred at shallow depths. Negative $\delta^{13}C$ may derive from contamination with organic carbon, and/or isotopic fractionation related to magmatic degassing (in samples not modified by secondary processes) or the interaction with superficial water. SCN olivines clearly shows a MORB-like upper mantle $\delta^{13}C$ signature similar to the values reported for the crateric fumaroles of the Popocatépetl and the high-temperature fumaroles of Colima volcano (Fig. 41B). MORB-like values can be explained using two hypotheses: 1) MORB ratios could be associated with magmatic degassing processes; high $^4He/^{40}Ar^*$(3-9) suggest that fluids present in SCN olivines are likely remnants of degassing, if this is truth, then these should derive from a melt with more positive $\delta^{13}C$ signatures similar to those observed in VESVF xenoliths. The latter is reasonable considering that $\delta^{13}C$ fractionates towards lower values during magmatic degassing (Javoy et al., 1978; Trull et al., 1993; Boudoire et al., 2018); 2) On the other hand, $\delta^{13}C$ could point to a subarc mantle with a carbon signature that varies between -4‰ and -7‰ suggesting a negligible contamination by crustal carbon derived from subduction which is consistent with the data reported for other arc volcanoes such as Ceboruco and La Primavera. The helium ratios observed along the TMVB support the presence of a little more radiogenic mantle (locally uniform) when compared with the Basin and Range volcanic fields (VESVF, DVF and SQVF). The fact that the SCN show comparable noble gas systematics to

the VESVF nodules but different $\delta^{13}C$ could also indicate that SCN lavas are not directly related with the partial melting of a VESVF-like mantle, instead these may come from the fusion of a deeper mantle domain characterized by similar noble gas compositions and different carbon signatures evidently not affected by subduction-related carbonate recycling.
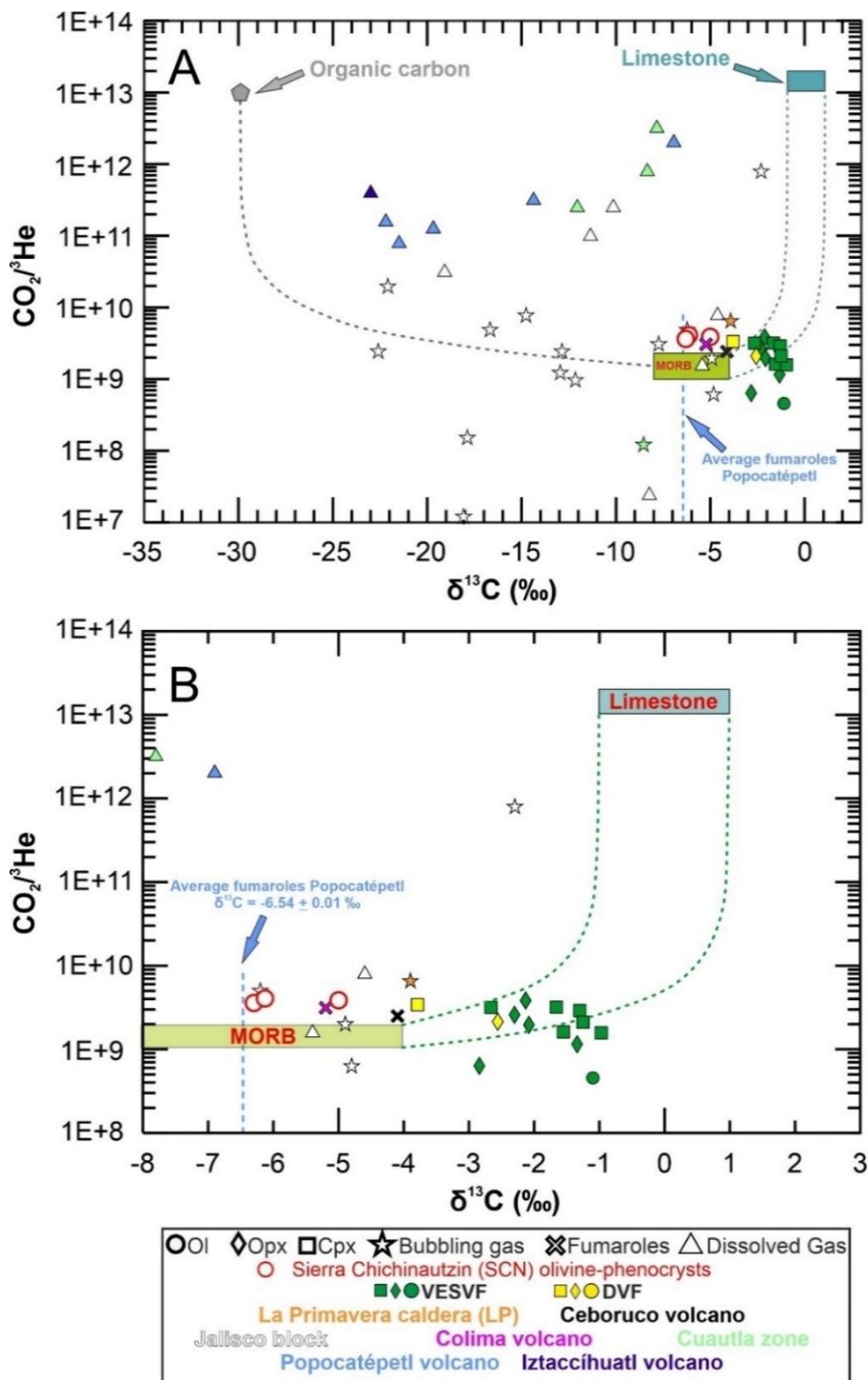
Figure 41. A) $\delta^{13}C$ vs $CO_2/^3He$ ratios. B) Closer view of A between -8 and +3‰. Because no information of $CO_2/^3He$ is available for the Popocatépetl fumaroles, the $\delta^{13}C$ average (blue dotted line) was plotted considering the highest $CO_2/^3He$ value reported for the TMVB within the MORB-like range. This average is reported in Goff et al. (1998). Bibliographic references are provided in Fig. 40.

7.3. Conclusions

In this chapter the fluid inclusion composition of olivine-phenocrysts from SCN lavas were investigated. Fluids analyzed in SCN olivines are considered representative of the local mantle since fluid inclusions analysis revealed similar (or even higher) He and CO_2 concentrations to those previously reported in VESVF mantle xenoliths. Rc/Ra and $^4He/^{20}Ne$ ratios also fall within the same range. The above suggests a homogeneity of the isotopic signatures (in terms of helium) and indicates that the mantle beneath both localities evolved under similar geodynamic conditions; this scenario would have changed during the migration of the Mexican volcanic arc to its actual E-W position. Comparing with other volcanic areas belonging the TMVB, the Rc/Ra ratios of the SCN can be compared to fluid inclusions (hosted in olivines) and fumarolic samples from the Popocatépetl and Ceboruco volcanoes, respectively. The similarity with the Popocatépel is interpreted as an isotopic homogeneity of the mantle located beneath the central TMVB.

$\delta^{13}C$ measured in SCN samples falls within the MORB-like range and are comparable to $\delta^{13}C$ results reported for the Popocatépel, Ceboruco and Colima fumaroles and bubbling gas obtained from La Primavera caldera. Unlike the mantle beneath VESVF, carbon isotopes indicate the existence of a subarc mantle with carbon signatures between -4‰ and -7‰, which points to a negligible mantle contamination by subduction-related crustal carbon. The difference between the mantle sampled in the VESVF and the SCN mantle may be interpreted as the result of magmatic degassing processes that modified the original $\delta^{13}C$ values or that the SCN lavas come from the fusion of a deeper mantle domain (with MORB-like $^3He/^4He$ ratios) marked by carbon compositions not affected by subduction-related carbonate recycling.

CHAPTER 8. RECYCLED CRUSTAL CARBON IN THE DEPLETED MANTLE SOURCE OF EL HIERRO VOLCANO, CANARY ISLANDS.

8.1. Volcanism and evolution of El Hierro Island

El Hierro is the youngest (oldest exposed lavas at 1.12 Ma;Guillou et al., 1996) and westernmost island of the Canary archipelago (Fig. 15) and its history is summarized in three stages (Troll and Carracedo, 2016 and references therein): (i) the formation of the Tiñor Volcano (1.12 Ma to 1.03 Ma); (ii) the collapse of the latter and the emplacement of a new volcanic structure (the El Golfo volcano; 545 – 176 ka), and (iii) the development of a triple rift system. This volcanism is mainly dominated by high alkali silica-undersaturated rocks (extruded during the El Golfo volcano eruption), which can contain ultramafic xenoliths (Neumann, 1991; Oglialoro et al., 2017). The analyzed suite of mantle xenoliths consists of three spinel lherzolites and three spinel harzburgites selected among over 35 peridotite samples from El Julan cliff valley, El Hierro (Canary Islands; Fig. 42), and erupted 30 – 40 ka ago (Oglialoro et al., 2017). Sampling details and petrographic characteristics of these rocks are already presented elsewhere (Oglialoro et al., 2017; Colombo, 2020).
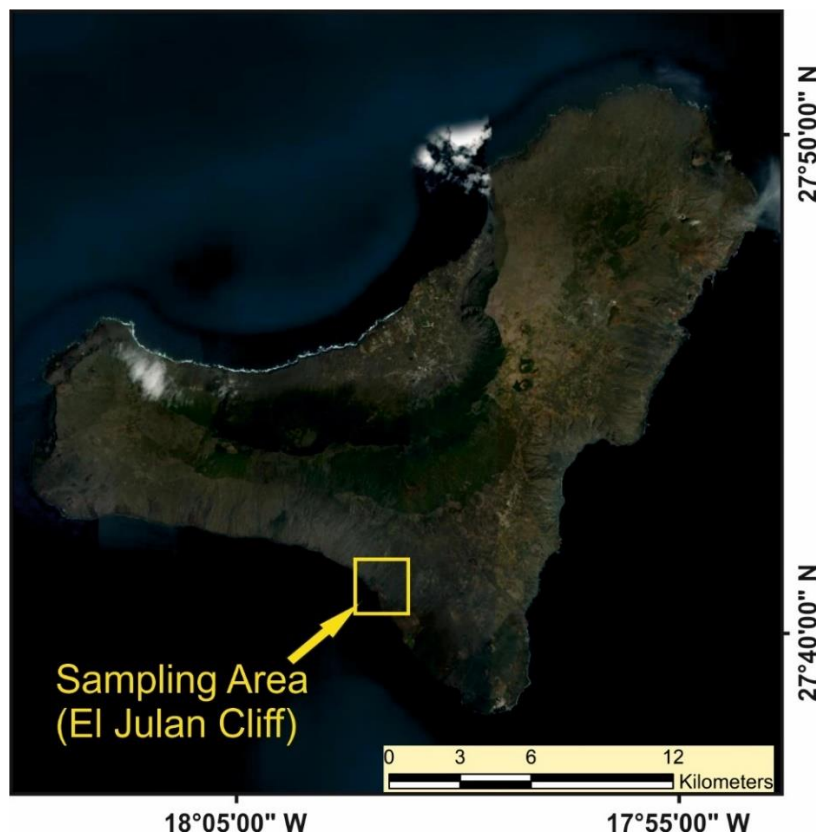
Figure 42. El Hierro island and sampling locality in El Julan Cliff Valley.

8.2. Results

The elemental and isotopic compositions of noble gases and CO_2 in El Hierro mantle xenoliths are reported in Table 7. The fluid inclusion composition is dominated by CO_2, as found previously

(Oglialoro et al., 2017). CO_2 exhibits a broad positive correlation with noble gas and nitrogen concentrations (Fig. 43). Both CO_2 estimates, during noble gases analysis and CO_2 isotopic determinations (see Table 7), are similar and vary from 5.31×10^{-10} to 2.17×10^{-6} mol/g. The highest CO_2 concentrations are observed in Cpx (from 7.70×10^{-8} to 2.17×10^{-6} mol/g), followed by Opx (from 1.65×10^{-8} mol/g to 6.92×10^{-7} mol/g) and Ol (from 5.31×10^{-10} mol/g to 8.45×10^{-8} mol/g). $^4He/^{20}Ne$ ratios vary between 5.9 and 776.1, with the lowest values measured in sample 1.1 (Opx and Cpx) and sample 1.23 Cpx. These samples also have low Rc/Ra (<6) and $^4He/^{40}Ar^*$ (<0.07) values, indicating isotopic fractionation during diffusive He loss from fluid inclusions (see section 8.3.1 for details). These samples are thus disregarded in the further discussion below. The remaining sample aliquots exhibit Rc/Ra values in the 7 to 8 Ra range within the MORB range (Graham, 2002). The $^{40}Ar/^{36}Ar$, $^{20}Ne/^{22}Ne$ and $^{21}Ne/^{22}Ne$ ratios values range from 805.0 to 5328.4, from 9.84 to 10.49, and from 0.0286 to 0.0330, respectively. The spread of Ar and Ne isotopic signatures is well reproduced by mixing between a depleted mantle (MORB) source and an atmospheric component (see section 8.3.2 for details). The isotopic composition of CO_2 (expressed as $\delta^{13}C = R_{Sample}/R_{Standard} - 1$, where $R = {}^{13}C/{}^{12}C$ and the standard is the Vienna Pee Dee Belemnite, VPDB) reveals the highest $\delta^{13}C$ values in Ol (-0.19‰ and +0.96‰), while Opx and Cpx exhibit somewhat more negative compositions, ranging from -2.38‰ to -1.23‰. These C isotope compositions are well above the typical depleted mantle (MORB) range (Sano and Marty, 1995).
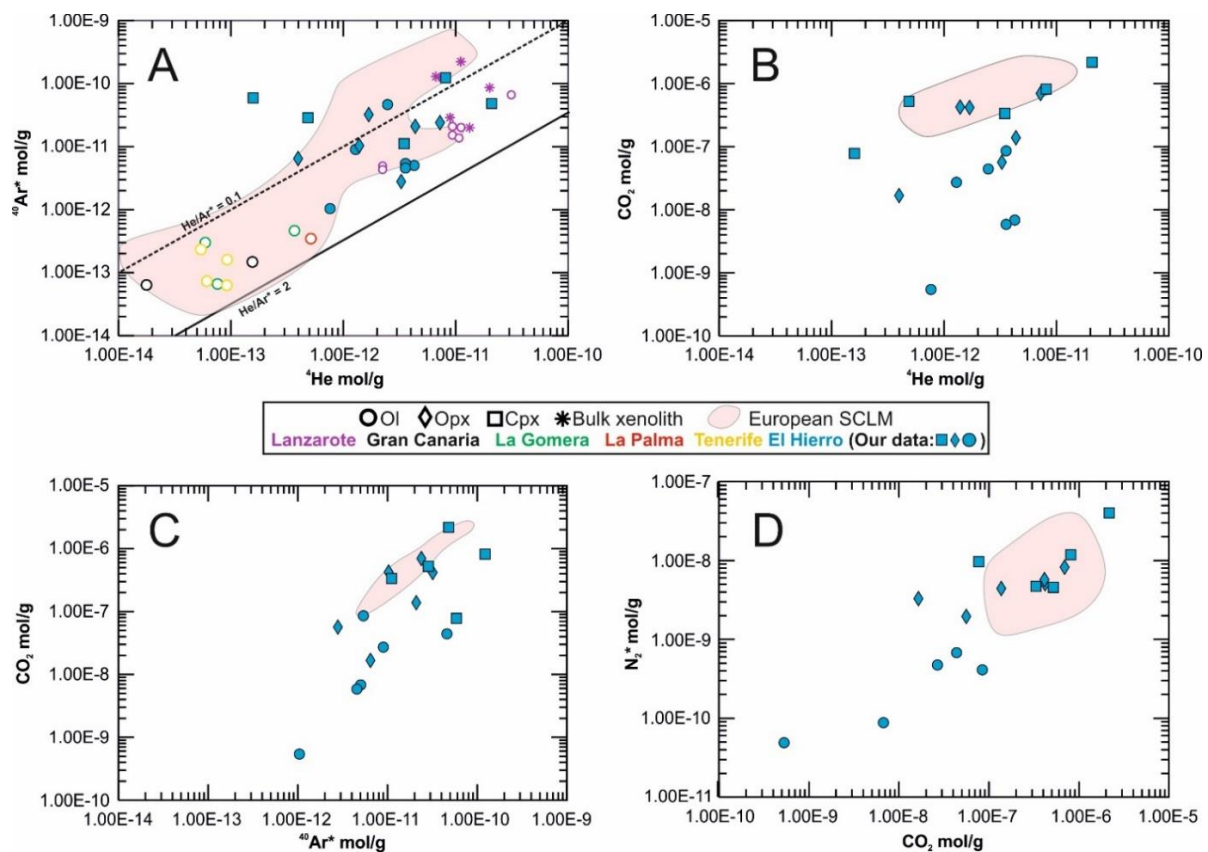
Figure 43. ^4He, $^{40}Ar^*$, CO_2 and $^*N_2$ abundances in fluid inclusions hosted in El Hierro mantle xenoliths and other Canary Islands. European SCLM compositional range was designed using fluid inclusions data of mantle xenoliths from the Rhenish Massif (Germany), Eifel region (Germany), Pannonian basin, Massif Central (Central France), Tallante - Calatrava (Spain), and Lower Silesia (Poland); data was taken from Buikin et al. (2005), Gautheron et al. (2005a), Martelli et al. (2011), Rizzo et al. (2018) and Faccini et al. (2020). White symbols are lava phenocrysts, the outline colours represent the island where the samples come from (see legend). Plotted CO_2 values correspond to the first concentrations estimated in fluid inclusions during noble gas analysis (see Table 7).

Table 7. Noble gas and CO_2 compositions of fluid inclusions hosted in El Hierro mantle xenoliths. Concentrations of noble gases isotopes, CO_2 and N_2 are reported in mol/g. [A] First estimation of CO_2 contents in fluid inclusions during noble gas analysis; [B] CO_2 contents and $CO_2/^3He$ ratios measured from the glass line after CO_2 isotopic determinations. Reported errors are 2σ uncertainties. Estimated errors for ^3He, ^4He, ^{20}Ne, ^{21}Ne, ^{22}Ne, ^{40}Ar, ^{36}Ar and CO_2 are $<10\%$, $<0.06\%$, $<14\%$, $<10\%$, $<1.5\%$, $<0.14\%$, $<0.2\%$ and $<10\%$, respectively.

Sample	Mineral	Rock type	ID (Oglialoro et al., 2017; Colombo, 2020)	Weight (g)	^3He	^4He	^{20}Ne	^{21}Ne	^{22}Ne	CO_2[A]	N_2*	^{40}Ar	^{40}Ar*	$^4He/^{20}Ne$	$^4He/^{40}Ar$*
1.1	Ol	Sp Lherzolite	XML3	0.52644	1.28E-17	1.28E-12	5.67E-15	1.70E-17	5.65E-16	2.68E-08	4.73E-10	9.72E-12	9.03E-12	225.9	0.14
1.1	Opx	Sp Lherzolite	XML3	0.12869	2.48E-18	4.03E-13	6.74E-15	2.14E-17	6.82E-16	1.65E-08	3.29E-09	7.26E-12	6.48E-12	59.8	0.06
1.1	Cpx	Sp Lherzolite	XML3	0.08996	1.29E-18	1.58E-13	8.39E-15	2.56E-17	8.53E-16	7.70E-08	9.66E-09	6.27E-11	5.92E-11	18.9	0.003
1.15	Ol	Sp Harzburgite	XML11	0.51344	3.73E-17	3.60E-12	1.13E-14	3.35E-17	1.13E-15	8.45E-08	4.11E-10	6.09E-12	5.41E-12	317.9	0.67
1.15	Opx	Sp Harzburgite	XML11	0.11766	1.38E-17	1.42E-12	2.25E-14	6.73E-17	2.28E-15	4.20E-07	5.08E-09	1.37E-11	1.03E-11	62.8	0.14
1.15	Cpx	Sp Harzburgite	XML11	0.05385	3.62E-17	3.55E-12	2.73E-14	7.92E-17	2.79E-15	3.33E-07	4.70E-09	1.76E-11	1.11E-11	129.9	0.32
1.2	Ol	Sp Lherzolite	XML6	0.52471	4.80E-17	4.32E-12	7.10E-15	2.19E-17	7.06E-16	6.73E-09	8.79E-11	6.89E-12	5.04E-12	608.5	0.86
1.2	Opx	Sp Lherzolite	XML6	0.10331	4.72E-17	4.39E-12	1.06E-14	3.30E-17	1.05E-15	1.37E-07	4.42E-09	2.25E-11	2.10E-11	415.8	0.21
1.2	Cpx	Sp Lherzolite	XML6	0.04105	8.66E-17	8.21E-12	1.45E-14	4.49E-17	1.42E-15	8.12E-07	1.18E-08	1.33E-10	1.24E-10	565.4	0.07
1.22	Ol	Sp Lherzolite	XML8	0.50752	7.62E-18	7.66E-13	9.87E-16	3.10E-18	9.38E-17	5.31E-10	4.89E-11	1.31E-12	1.04E-12	776.1	0.73
1.22	Opx	Sp Lherzolite	XML8	0.31254	3.26E-17	3.29E-12	6.44E-15	1.91E-17	6.48E-16	5.59E-08	1.95E-09	3.91E-12	2.81E-12	511.8	1.17
1.23	Ol	Sp Harzburgite	XML5	0.50783	2.58E-17	2.49E-12	1.24E-14	3.74E-17	1.24E-15	4.38E-08	6.77E-10	4.92E-12	4.64E-11	200.7	0.05
1.23	Opx	Sp Harzburgite	XML5	0.10976	1.80E-17	1.71E-12	2.59E-14	7.87E-17	2.61E-15	4.13E-07	5.74E-09	3.55E-11	3.22E-11	66.0	0.05
1.23	Cpx	Sp Harzburgite	XML5	0.058	3.64E-18	4.93E-13	8.37E-14	2.50E-16	8.53E-15	5.19E-07	4.57E-09	4.47E-11	2.87E-11	5.9	0.02
1.3	Ol	Sp Harzburgite	-	0.52935	3.76E-17	3.57E-12	6.05E-15	1.82E-17	6.03E-16	5.75E-09	n.a	6.39E-12	4.58E-12	589.8	0.78
1.3	Opx	Sp Harzburgite	-	0.10888	7.71E-17	7.27E-12	3.62E-14	1.07E-16	3.63E-15	6.92E-07	8.23E-09	2.83E-11	2.40E-11	200.7	0.30
1.3	Cpx	Sp Harzburgite	-	0.05363	2.26E-16	2.13E-11	3.37E-14	1.06E-16	3.33E-15	2.17E-06	4.02E-08	5.81E-11	4.85E-11	631.8	0.44

Sample	Mineral	R/Ra	Rc/Ra	Error (+/-)	$^{40}Ar/^{36}Ar$	Error (+/-)	$^{20}Ne/^{22}Ne$	Error (+/-)	$^{21}Ne/^{22}Ne$	Error (+/-)	$CO_2/^3He$	$^3He/^{36}Ar$	CO_2 [B]	$CO_2/^3He$[B]	$\delta^{13}C$ (‰)
1.1	Ol	7.20	7.21	0.16	4141.0	0.0	10.11	0.07	0.0304	0.00106	2.09E+09	5.47E-03	n.a	n.a	n.a
1.1	Opx	4.41	4.43	0.25	2734.4	97.7	10.04	0.16	0.0319	0.00249	6.64E+09	9.33E-04	n.a	n.a	n.a
1.1	Cpx	5.76	5.85	0.57	5328.4	76.0	9.87	0.14	0.0302	0.00161	5.98E+10	1.09E-04	n.a	n.a	n.a
1.15	Ol	7.44	7.45	0.15	2620.4	0.0	9.99	0.04	0.0296	0.00081	2.26E+09	1.60E-02	5.53E-08	1.48E+09	0.96
1.15	Opx	6.98	7.01	0.21	1210.0	11.8	9.94	0.06	0.0297	0.00120	3.04E+10	1.22E-03	2.75E-07	1.99E+10	-1.23
1.15	Cpx	7.33	7.34	0.21	805.0	6.4	9.84	0.11	0.0286	0.00121	9.19E+09	1.66E-03	n.a	n.a	n.a
1.2	Ol	7.99	7.99	0.15	1103.1	0.0	10.12	0.05	0.0312	0.00095	1.40E+08	7.69E-03	n.a	n.a	n.a
1.2	Opx	7.72	7.73	0.18	4516.6	76.2	10.40	0.13	0.0325	0.00230	2.90E+09	9.48E-03	2.67E-07	5.65E+09	-1.43
1.2	Cpx	7.59	7.59	0.20	3979.1	39.8	10.43	0.24	0.0323	0.00245	9.38E+09	2.58E-03	n.a	n.a	n.a
1.22	Ol	7.16	7.16	0.17	1465.4	0.0	10.49	0.24	0.0330	0.00390	6.96E+07	8.55E-03	n.a	n.a	n.a
1.22	Opx	7.11	7.11	0.16	1044.6	12.7	9.98	0.09	0.0296	0.00143	1.72E+09	8.70E-03	n.a	n.a	n.a
1.23	Ol	7.46	7.47	0.15	5187.2	0.0	10.09	0.04	0.0304	0.00081	1.69E+09	2.73E-03	1.28E-08	4.95E+08	-0.19
1.23	Opx	7.52	7.55	0.19	3137.1	37.6	10.01	0.07	0.0304	0.00136	2.30E+10	1.59E-03	3.64E-07	2.03E+10	-2.38
1.23	Cpx	5.07	5.32	0.40	826.7	2.9	9.84	0.06	0.0295	0.00076	1.42E+11	6.74E-05	n.a	n.a	n.a
1.3	Ol	7.58	7.59	0.15	1043.7	0.0	10.05	0.07	0.0303	0.00118	1.53E+08	6.15E-03	n.a	n.a	n.a
1.3	Opx	7.62	7.63	0.17	1975.5	12.8	10.04	0.06	0.0297	0.00109	8.98E+09	5.39E-03	5.09E-07	6.60E+09	-1.94
1.3	Cpx	7.65	7.66	0.16	1780.7	10.5	10.18	0.09	0.0321	0.00161	9.60E+09	6.94E-03	9.47E-07	4.19E+09	-1.94

8.3. Discussion

8.3.1. Evaluation of secondary processes in fluid inclusion composition

8.3.1.1. Diffusive loss of helium

Opx and Cpx 1.1, and Cpx 1.23 clearly differ from the rest of the dataset (Figs. 43 and 44), since they exhibit the lowest helium concentrations (^{3}He < 5.0 x 10^{-18} mol/g; ^{4}He < 5.0 x 10^{-12} mol/g) along with low Rc/Ra values (<6 Ra), ^{4}He/^{20}Ne <60, ^{4}He/^{40}Ar* <0.07, and ^{3}He/^{36}Ar <10^{-3}. All these shreds of evidence are compatible with a preferential loss of helium relative to other noble gases. We highlight that despite a clear loss of helium, Ne, Ar, and CO_2 concentrations are similar or higher than the average calculated in the rest of the dataset, suggesting a limited or negligible influence of this process on these species.

Diffusive loss of noble gases may occur during partial melting or metasomatism of the upper mantle as suggested by Burnard (2004) and Yamamoto et al. (2009), resulting in the isotopic fractionation of ^{3}He, ^{4}He and ^{40}Ar due to differences in their masses and diffusivities (e.g., Faccini et al., 2020). This process has also been highlighted in magmatic crystals resulting in a decrease of ^{3}He/^{4}He at decreasing ^{3}He and ^{4}He concentrations and/or in olivine-pyroxene disequilibria (e.g., Marty et al., 1994; Nuccio et al., 2008; Boudoire et al., 2020).

In our study case, we consider more likely the occurrence of a diffusive fractionation. Therefore, we modeled the curves resulting from this process based on the calculations and analytical procedures proposed by Burnard (2004) and Yamamoto et al. (2009) to verify if this process can explain the variability of our dataset. For the model, we assumed a starting mantle contents of ^{3}He =3.16 x 10^{-17} mol/g, ^{4}He = 3.0 x 10^{-12} mol/g and ^{40}Ar = 2.0 x 10^{-12} mol/g. These values represent the average concentrations of the samples apparently not affected by the helium loss. The corresponding Rc/Ra and ^{4}He/^{40}Ar* ratios are 7.5 and 1.5, respectively, which are compatible with the expected ^{3}He/^{4}He signature for the mantle below El Hierro (^{3}He/^{4}He~7.5 Ra) and the mantle production range (^{4}He/^{40}Ar* = 1 – 5; Marty, 2012). As a result, Opx and Cpx 1.1, and Cpx 1.23 fit the diffusion paths observed in Fig. 44, confirming that their variability is likely produced by a preferential loss of helium through a diffusive fractionation.

8.3.1.2. Cosmogenic and radiogenic helium

As evidenced by several authors, cosmogenic ^{3}He may accumulate in the crystal lattices when rocks are exposed to cosmic rays on the Earth's surface, as well as radiogenic ^{4}He ingrowth may occur over time from the decay of U and Th within the rocks. Then, one or both helium component may diffuse into fluid inclusions, changing the original ^{3}He/^{4}He ratio to higher values, in the case of ^{3}He addition, or lower values, in the case of ^{4}He addition (Kurz, 1986; Dunai and Baur, 1995; Hilton et al., 2002; Correale et al., 2019). The effect of the mixing between the fluid inclusions and cosmogenic and/or radiogenic helium is particularly evident in those samples with long exposure times and low helium concentrations, primarily when multi-step crushing or melting technique is used to extract the fluid inclusions from minerals (e.g,, Dunai and Baur, 1995; Grachev, 2012; Broadley et al., 2016).

Instead, single-step crushing technique is known for preventing the release of cosmogenic and radiogenic helium accumulated in the crystal lattices (Kurz, 1986; Hilton et al., 2002). As in this work we used single-step crushing, we infer that the addition of secondary He in our fluid inclusions can be considered negligible. This conclusion is supported by the fact that samples with the lowest helium concentrations (Opx and Cpx 1.1, and Cpx 1.23) exhibit the lowest Rc/Ra, ^{4}He/^{20}Ne,

^{4}He/^{40}Ar* values, which is a clear evidence of a helium loss. In fact, if the addition of radiogenic ^{4}He would have occurred, we should expect e.g., a progressive decrease of Rc/Ra values at increasing ^{4}He concentration, which is not observed in our sample while can be reasonably assumed for some of the Lanzarote samples analyzed via melting and showing ^{3}He/^{4}He as low as < 0.1 Ra (Grachev, 2012; Fig. 45). Finally, we highlight that our samples have a relatively low age and exposure time since the eruption of hosting lavas 30 – 40 ka ago (Oglialoro et al., 2017; Colombo, 2020).
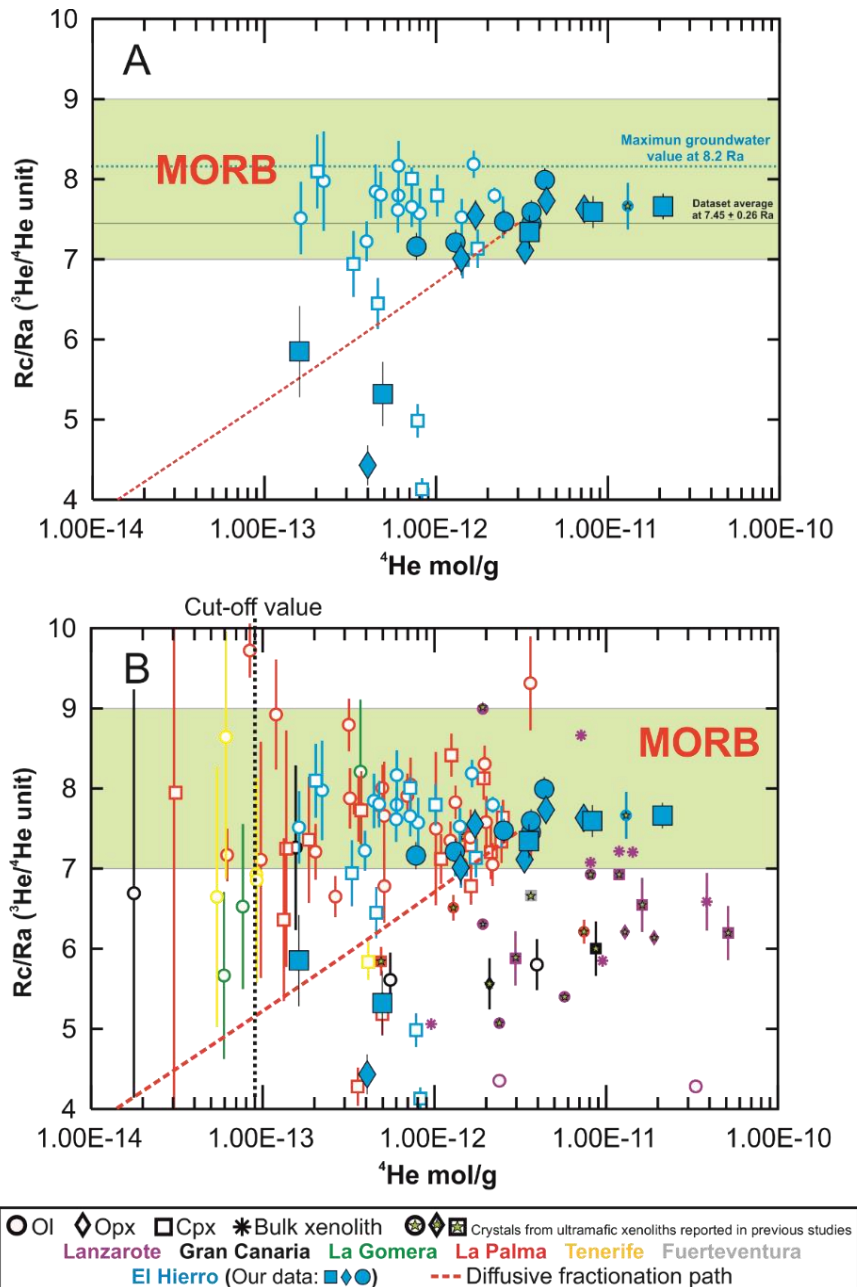
Figure 44. ^{4}He vs Rc/Ra ratios (^{3}He/^{4}He ratio corrected for atmospheric contamination) measured in fluid inclusions. MORB range is reported at Rc/Ra = 8 ± 1 (Graham, 2002). White symbols are lava phenocrysts, the outline colours represent the island where the sample comes from (see legend). Purple asterisks represent the bulk ^{4}He concentrations and Rc/Ra values measured in ultramafic xenoliths from Lanzarote (see Table S1). A) The dotted blue line represents the maximum ^{3}He/^{4}He ratio reported in groundwater samples during the volcanic unrest of 2012 at El Hierro (Padrón et al., 2013). B) An arbitrary cut-off value is proposed at 9.0×10^{-14} mol/g (see subsection 8.3.4).Please see Table S1 for bibliographic references.

Figure 45. [4]He vs Rc/Ra ([3]He/[4]He ratios corrected for atmospheric contamination) diagram showing the variability of fluid inclusions data reported in literature. European SCLM was designed using the information cited in Fig. 43. Please see Table S1 for bibliographic references.

8.3.2. *Atmospheric contamination*

The presence of atmospheric fluids in El Hierro mantle xenoliths is confirmed by [4]He/[20]Ne and Ar-Ne isotopic ratios. As shown in Fig. 46A, most of the samples exhibit [4]He/[20]Ne > 60 and R/Ra > 7, except Opx and Cpx 1.1, and Cpx 1.23, whose [4]He/[20]Ne are lower than 60 and R/Ra between 4.43 and 5.85. However, these samples have [40]Ar/[36]Ar between 826.7 and 5328.4, suggesting much less air contamination than those resembled by [4]He/[20]Ne <60. In Section 8.3.1.1, we recognized the occurrence of a diffusive loss of He from these minerals. For the above line of reasoning, we do not consider Opx and Cpx 1.1, and Cpx 1.23 representative of the mantle features beneath El Hierro, and we exclude these samples from the data interpretation and discussion. On average, the [4]He/[20]Ne values are higher than those in bubbling gases and groundwater from La Palma, El Hierro and Tenerife (Pérez et al., 1996; Padrón et al., 2013; Marrero-Diaz et al., 2015), and lava phenocrysts from La Gomera, Gran Canaria and Tenerife. Our [4]He/[20]Ne values are also similar to those

previously reported in lavas and mantle xenoliths from the European SCLM (Buikin et al., 2005; Gautheron et al., 2005a; Martelli et al., 2011; Rizzo et al., 2018; Faccini et al., 2020). Ne and Ar isotopes mostly confirm the above evidence; however, much fewer data are available from previous studies for comparison. Indeed, in $^{20}Ne/^{22}Ne$ vs $^{21}Ne/^{22}Ne$ (Fig. 46B) and $^{40}Ar/^{36}Ar$ vs $^{3}He/^{36}Ar$ (Fig. 46C) plots, El Hierro samples fall along the air-MORB mixing line overlapping the range of ratios measured in the European SCLM. $^{40}Ar/^{36}Ar$ values reported for El Hierro xenoliths agree with noble gas data previously reported in ultramafic xenoliths from Lanzarote (Grachev, 2012) and are higher if compared with values reported in olivine phenocrysts from La Palma, Tenerife, Gran Canaria and La Gomera.

The presence of an atmospheric component in fluid inclusions of lavas, cumulates or mantle xenoliths from intra-plate magmatism is common to several localities on Earth (Valbracht et al., 1996; Matsumoto et al., 1998, 2000, 2001, 2002; Yamamoto, 2004; Gautheron et al., 2005a; Nuccio et al., 2008; Martelli et al., 2011; Correale et al., 2012, 2016, 2019; Tang et al., 2014; Rizzo et al., 2015, 2018; Broadley et al., 2016; Boudoire et al., 2018; Faccini et al., 2020). The main hypotheses to explain such air contamination involve: i) contamination of xenoliths or melts during their ascent toward the surface; ii) air entrapment in minerals micro-cracks in post-eruptive conditions; iii) air component recycled into the mantle from present or fossil subduction(s). Petrological studies have demonstrated that mafic magmas erupted on the Canary Islands require partial melting of a HIMU-type mantle source, attributed to the recycling of <2Ga old oceanic crust (Gurenko et al., 2006; Day et al., 2010; Day and Hilton, 2011). In this context, it is reasonable to suppose that the subducted slab would also have delivered atmospheric fluids into the mantle source region, resulting in the isotopic signatures observed in El Hierro xenoliths. In fact, we identified a positive trend between ^{3}He and ^{36}Ar concentrations (Fig. 47) that suggests a correlation between the mantle and subducted-related atmospheric gases (Matsumoto et al., 2001) recycled in the lithospheric mantle beneath El Hierro. Moreover, fluid inclusion analysis performed in the same suite of xenoliths used for this study reveal deep (65-60 km), intermediate (37-22 km) and shallow (10-12 km) fluid trapping episodes (Oglialoro et al., 2017). According to these authors, the last fluid-trapping event would reflect a magma accumulation region in the lower oceanic crust where new CO_2-rich fluid inclusions formed along crystal microfractures. Based on this evidence, we cannot discard the infiltration of atmospheric fluids in our mantle xenoliths at crustal depths before the eruption of the transporting magma, as indicated by phenocrysts in lavas from the other islands that systematically show lower $^{40}Ar/^{36}Ar$ values than in mantle xenoliths (Fig. 46C).

8.3.3. A depleted mantle noble gas signature for the El Hierro mantle source beneath and the Canary archipelago

The average (mean±1σ) Rc/Ra measured in El Hierro mantle xenoliths is 7.45±0.26 Ra (Fig. 44). This value is comparable to the $^{3}He/^{4}He$ values reported in lava phenocrysts and cumulates from the same island (7.66±0.35 Ra; Fig. 44A), and slightly below the maximum Rc/Ra value measured in groundwater samples during the 2011-2012 unrest event (~8.2 Ra; Padrón et al., 2013). Averaging these results, we infer the mean $^{3}He/^{4}He$ signature for El Hierro at 7.58±0.34 Ra, which we consider representative of the source mantle. This signature is classically MORB-like, confirming previous indications of a dominant Depleted MORB Mantle (DMM) source (Day and Hilton, 2011, 2020). Therefore, as additionally implied by Ne and Ar isotopes (Fig. 46), we find no evidence of primordial noble gas contribution from the lower mantle, as found instead in the high (Rc/Ra >9) volcanic gases from La Palma (see Table S1).
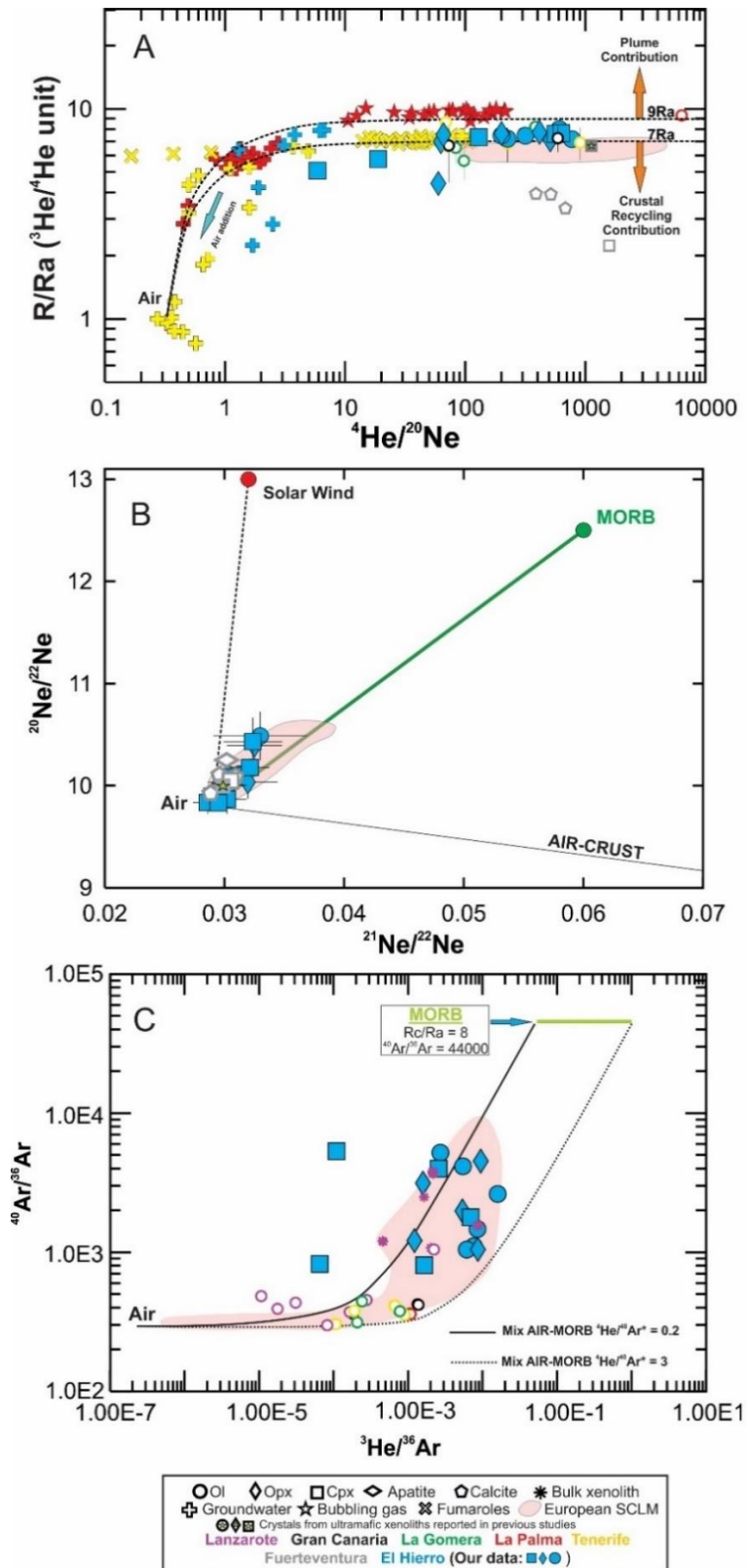
Figure 46. A) $^4He/^{20}Ne$ vs R/Ra ratios, dotted black lines are binary mixing curves between air and an upper mantle source with R/Ra values at 7 and 9. White symbols are lava phenocrysts, the outline colours represent the island where the samples come from (see legend) **B)** Three-isotope plot of neon. The green line represents the binary mixing air-MORB mantle after Sarda et al. (1988) and Moreira et al. (1998) at $^{21}Ne/^{22}Ne_{air} = 0.029$ and $^{20}Ne/^{22}Ne_{air} = 9.8$ and $^{21}Ne/^{22}Ne = 0.06$ and $^{20}Ne/^{22}Ne = 12.5$; Solar wind endmember was plotted at $^{21}Ne/^{22}Ne = 0.0328$ and $^{20}Ne/^{22}Ne = 13.8$ (Heber et al., 2009); the crust endmember was plotted at $^{21}Ne/^{22}Ne = 0.6145$ and $^{20}Ne/^{22}Ne = 0.3$ (Kennedy et al., 1990). **C)** $^3He/^{40}Ar$ vs $^{40}Ar/^{36}Ar$ diagram. European SCLM range was designed using the information cited in Fig. 43. See Table S1 for bibliographical references.
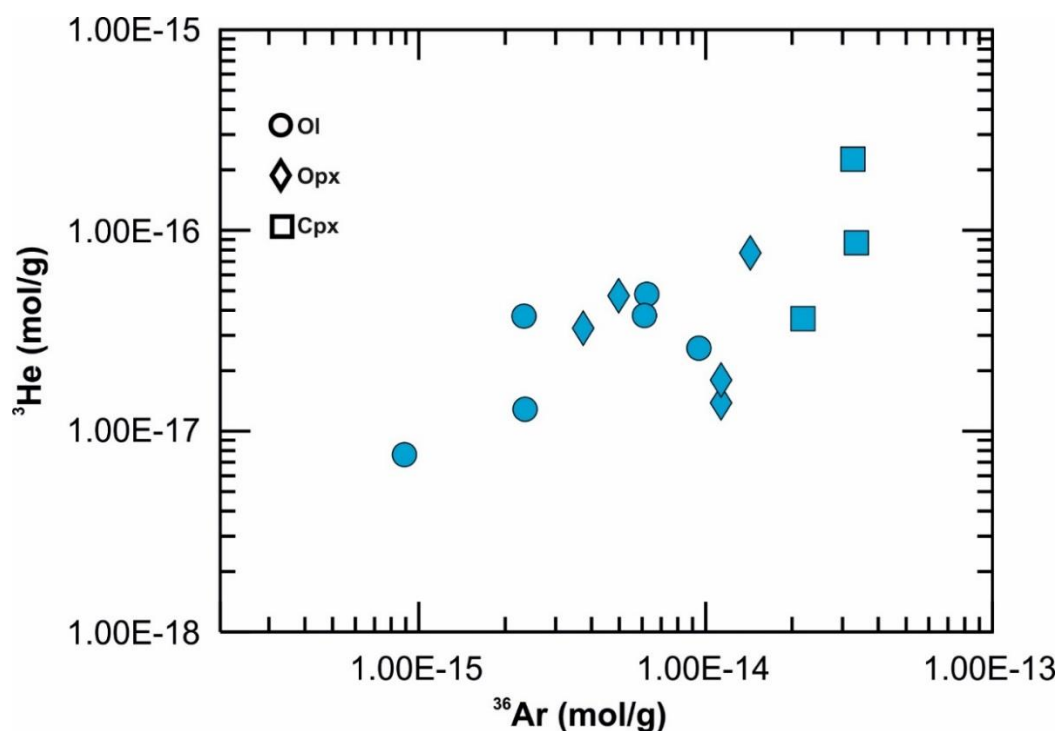
Figure 47. [36]Ar vs [3]He abundances in fluid inclusions hosted in El Hierro mantle xenoliths. Samples affected by diffusive fractionation (1.1 Ox, 1.1 Cpx and 1.23Cpx) were not considered in this diagram.

As discussed in Day and Hilton (2011), the MORB-like Rc/Ra values are evidence for the El Hierro source mantle having been scarcely impacted by any crustal He addition during the past (ancient, 1-2 Ga) oceanic crust/lithosphere subduction events (implied by the HIMU magma affinity; Hofmann, 1997). It is well possible, instead, that Ne and Ar (being well more abundant in air and air-saturated seawater than He) are better records of paleo-subduction(s) events, considering that evidence such as the MORB-air mixing arrays and the correlation between [3]He and [36]Ar contents (see subsection 8.3.2, Figs. 46 and 47) may well reflect recycling of atmospheric gases in the slab. The stable [3]He/[4]He ratios at El Hierro (Fig. 48B) point to a temporally invariant mantle source during the last million years (i.e., since the early Pleistocene).

8.3.4. Catalogue of noble gases and CO_2 isotopes measured along the Canary Islands and data filtering

We put our El Hierro results in a more general context by comparing them with a suitably revised catalogue of [3]He/[4]He ratios measured along the Canary Islands (fumaroles, groundwater, bubbling gas and fluid inclusion information from lavas, cumulates, carbonatites, and mantle xenoliths; Table S1, Figs. 44B, 45 and 46; Vance et al., 1989; Pérez et al., 1994, 1996; Hernández et al., 1998; Hilton et al., 2000; Gurenko et al., 2006; Day and Hilton, 2011, 2020; Melián et al., 2012; Grachev, 2012; Padrón et al., 2013, 2015; Marrero-Diaz et al., 2015; Alonso et al., 2019; Torres-González et al., 2020; Carnevale et al., 2021). This revised dataset is built together after filtering out samples affected by secondary processes (diffusive fractionation, cosmogenic and radiogenic ingrowth of helium) and whose pristine isotopic signature may thus have been compromised (see subsection 8.3.1 for details). Statistical treatment of the data (Fig. 48A) allows further refinement of this data filtering, based on the criteria described below.
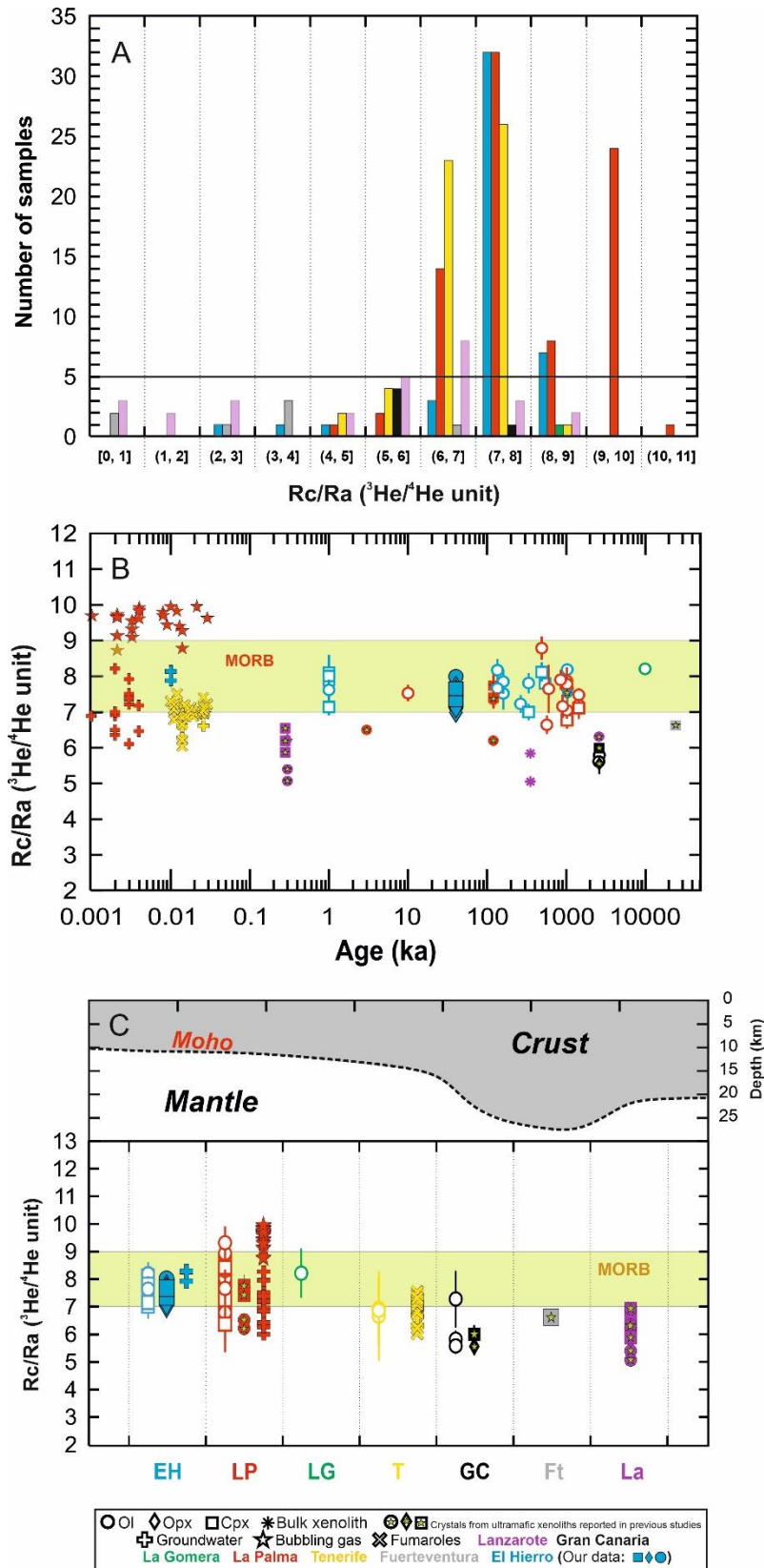
Figure 48. A) Histogram of filtered data, the resulting Rc/Ra values reported in Table S2 were classified in 11 different classes. An arbitrary cut-off value is proposed at five samples per class. Detailed description of data filtering is presented in subsection 8.3.4. B) Age vs Rc/Ra ratios (^{3}He/^{4}He corrected for atmospheric contamination) after data filtering. We plotted the year in which surface gases were sampled (bubbling gas, fumaroles and groundwater) and the age of the outcrop in the case of fluid inclusions. C) Variability of Rc/Ra ratios along the Canarian archipelago. In the upper part of the graph, we designed the thickness of the oceanic crust beneath the Canary Islands based on the seismic information presented by Martinez-Arevalo et al. (2013). EH: El Hierro, LP: La Palma, LG: La Gomera, T: Tenerife, Ft: Fuerteventura, La: Lanzarote. Please see Table S2 for bibliographic references of data.

When comparing our results with those previously reported in other islands, we found three main limitations: 1) data scarcity for some islands such as La Gomera, Tenerife (most of the information derives from Teide volcanic gases), Gran Canaria, and Fuerteventura. 2) Some samples could have suffered diffusive fractionation of helium, or addition of cosmogenic ^{3}He or radiogenic ^{4}He, or atmospheric contamination (some of ^{3}He/^{4}He data reported in previous studies are not corrected for the atmospheric contamination). 3) The use of non-conservative methods in the fluid inclusion extraction (e.g. multi-step crushing, melting), which could lead to a modified isotopic signature in some samples (see subsection 8.3.1).

Due to the above, we attempted a ^{3}He/^{4}He data selection using the following criteria: 1) all samples evidently affected by atmospheric contamination, such as groundwater from Tenerife, were discarded (^{4}He/^{20}Ne < 1 and R/Ra < 4; Fig. 46). 2) In the case of El Hierro, samples suspicious of diffusive fractionation (our Opx and Cpx 1.1, and Cpx 1.23, and phenocrysts fitting the diffusive fractionation path in Fig. 44 were not considered. 3) Samples with ^{4}He concentrations below an arbitrary cut-off value fixed at 9.0 x 10^{-14} mol/g were discarded (Fig. 44B). The latter assumption derives from the fact that crystals with low He contents are more susceptible to secondary changes in the original isotopic signature (see subsection 8.3.1). We highlight that this criterion was already adopted by, e.g., Dunai and Baur (1995) and Martelli et al. (2011)).

The residual samples were classified into eleven classes of Rc/Ra (for those samples for which ^{3}He/^{4}He are provided without air correction, we plotted R/Ra values) and plotted in the histogram of Fig. 48A. Each class can contain a maximum of six bars (one for every island for which ^{3}He/^{4}He data are available), whereas each bar's height indicates the number of ^{3}He/^{4}He measurements carried out for a specific island. To filter anomalous or scattered values and give statistical robustness to the ^{3}He/^{4}He signature in each island, we discarded those bars showing a frequency less than 5 except for La Gomera, Tenerife, Gran Canaria and Fuerteventura, for which only a few measurements are available.

186 samples were selected after the filtering process: 13 from Lanzarote, 1 from Fuerteventura, 5 from Gran Canaria, 49 from Tenerife, 1 from La Gomera, 78 from La Palma and 39 from El Hierro. The resulting (after data filtering) isotopic information is reported in Table S2 and Figs. 48B-C and 49A-B. It is worth mentioning that ultramafic xenoliths reported in Figs. 48B-C also include rocks of cumulitic origin. In detail, in previous studies of El Hierro and La Palma xenoliths, rocks are classified as clinopyroxenites and dunites (Day et al., 2010; Day and Hilton, 2011); the ultramafic xenolith from Fuerteventura is also a clinopyroxenite (Carnevale et al., 2021). Instead, mantle xenoliths from Gran Canaria consist of 1 harzburgite and 1 hornblende-bearing pyroxenite (Vance et al., 1989), and those from Lanzarote consist of 1 lherzolite, 6 harzburgites, 1 gabbro, 1 dunite and 1 unclassiifed mantle rock (sample Lanz560; Vance et al., 1989; Grachev, 2012).

8.3.5. Implications for isotopic variations along the Canary archipelago

The above comparison confirms (Day and Hilton, 2020 and references therein) the presence of a clear lower mantle component only in volcanic gases from La Palma (9.52±0.32Ra), whereas fluid inclusion in phenocrysts from the same island show ratios (7.52±0.66 Ra) comparable to those from El Hierro and La Gomera (Fig. 48C). The different ^{3}He/^{4}He signatures of La Palma and El Hierro have been proposed to derive from mantle sources containing different proportions of (i) recycled oceanic crust and gabbroic lithosphere (ii) a deep mantle source with ^{3}He/^{4}He >9.7 Ra (for La Palma) and (iii) the DMM (dominant at El Hierro) (Day and Hilton, 2011, 2020). This interpretation is reasonably valid also for La Gomera that shows geochemical features similar to the

westernmost islands. Further to the east, from Tenerife to Lanzarote, the ^{3}He/^{4}He ratios decrease at the lower end of the MORB range or even below (Fuerteventura and Lanzarote).

Based on Sr-Nd-Pb-Os isotopic systematics, the lower ^{3}He/^{4}He values in Tenerife and eastern Canary have been suggested to derive from increasing contributions from an enriched mantle (EM) inherited from the incorporation of the continental lithospheric mantle from the West African margin (Hoernle et al., 1991; Simonsen et al., 2000; Gurenko et al., 2006); this is especially observed in lavas from the Anaga massif (Tenerife) and lavas related to the Shield building of Gran Canaria during the Miocene. Sr-Nd-Pb isotopes in carbonatites from Fuerteventura also support the existence of such enriched mantle component (Carnevale et al., 2021). While not ruling out this possibility, we also consider the possible role of ascending magma interactions with the oceanic crust, whose thickness progressively increases eastward (Fig. 48C). As evident in Fig. 48C, the progressive eastward decrease of the Rc/Ra values that starts in Tenerife (in both volcanic gases and fluid inclusions) is paralleled by a corresponding marked increase in crustal thickness (Martinez-Arevalo et al., 2013). Based on this evidence, we argue that the ^{3}He/^{4}He signature presently observed in samples from Tenerife, Gran Canaria, Fuerteventura, and Lanzarote may also be controlled by the addition of crustal He during magma-crust interactions. This inference is plausible if we consider that ascending melts are more prone to be contaminated by the assimilation of crustal-derived radiogenic ^{4}He, lowering the original ^{3}He/^{4}He values. Accordingly, the high ^{3}He/^{4}He values observed mostly in El Hierro and La Palma, but also in La Gomera, would reflect a minimal contribution of crustal materials. Sr-Nd-Pb-O isotopic ratios indicate crustal assimilation is negligible in lavas erupted from El Hierro and La Palma (Gurenko et al., 2006; Day et al., 2010). Instead, volcanic rocks from Gran Canaria and carbonatites from Fuerteventura bring evidence of 5-8% and 10-20% of crustal assimilation, respectively (Thirlwall et al., 1997; Hoernle, 1998; Demény et al., 1998; Gurenko et al., 2006; Day et al., 2010), which could justify the lowering of their ^{3}He/^{4}He values.

Magma ageing also can change the abundance of helium isotopes and can be invoked to explain the low ^{3}He/^{4}He ratios observed in magmatic rocks from the eastern Canary Islands. As discussed by several authors, when magma ponds in the crust for a long time, the ^{3}He/^{4}He ratios eventually decrease due to the accumulation of radiogenic ^{4}He over time (Torgersen and Jenkins, 1982; Hilton et al., 1993; Burnard, 2013). In the case of Gran Canaria, it is possible to estimate the production of radiogenic ^{4}He in magmas based on the U and Th abundances reported in basaltic rocks (Ballentine and Burnard, 2002). Considering an average concentration of 0.8 ppm and 3.4 ppm for U and Th, respectively (Thirlwall et al., 1997), the quantity of ^{4}He produced in Gran Canaria magmas would be 8.93 x 10^{-18} mol/g*yr. Although no information about magma residence time has been reported in the literature, van den Bogaard et al. (1988) proposed an eruptive periodicity of 0.05 Ma, which is closely connected with periods of differentiation and recharge of magma reservoirs. Thus, assuming a starting Rc/Ra = 8, a ^{4}He concentration of 2.5 x 10^{-12} mol/g (the maximum concentration reported in volcanic rocks in Canary Islands, Fig. 44 and 45) and the above ^{4}He production rate, we conclude that a crustal residence time between 0.05 and 0.06 Ma is sufficient to lower the initial ^{3}He/^{4}He to 6.96 Ra, which agrees well with the values reported for Gran Canaria basalts (~6.69 ± 0.46 Ra).

We reiterate our interpretation does not intend to dismiss earlier models that emphasize the role of mantle heterogeneity (Hoernle et al., 1991; Simonsen et al., 2000; Gurenko et al., 2006). These scenarios are not mutually exclusive. Any contribution of crustal He may, in fact, contribute to additionally lowering the ^{3}He/^{4}He values of lavas derive from an already enriched (EM) mantle source. We argue that additional work on fluid inclusions in mantle xenoliths is needed (especially in La Palma, Tenerife, Gran Canaria, Lanzarote, and Fuerteventura) in order to quantify better the relative roles played by crustal interactions and mantle heterogeneities (a continental lithospheric

component in the mantle source) in this portion of the Canary Islands. Mantle xenoliths are indeed much better proxies of the source mantle than lavas, in which a role of shallow crustal processes is often more challenging to dismiss.

8.3.6. Recycled CO_2 in the mantle source

Our results thus bring no evidence of a recycled crustal He component in the El Hierro mantle source. This contrasts with our El Hierro CO_2 isotopic measurements that, being the first fluid inclusions results for Canary Islands, points to a ^{13}C-enriched mantle source (Fig. 49). We find that both olivines and pyroxenes exhibit higher δ^{13}C values than the classical MORB range ($-8\permil <$ δ^{13}C $< -4\permil$; Sano and Marty, 1995), and approaching those of crustal carbonate reservoirs (Marty and Jambon, 1987; Sano and Marty, 1995). Our mantle xenolith results are unique for the Canary Islands, as previous isotopic compositions of CO_2 (δ^{13}C) have only been obtained for volcanic gases and groundwaters (from La Palma and Tenerife) and for some carbonatites (from Fuerteventura) (see Table S1 and Fig. 49). In the remaining Islands, no δ^{13}C information is available due to the lack of surface gas emissions and the technical challenges in extracting CO_2 from (and measuring δ^{13}C in) fluid inclusions in lavas.

The El Hierro results demonstrate a crustal C component in the source mantle, previously un-identified in volcanic gases/groundwater studies in the region (Fig. 49). When comparing our δ^{13}C values with either Rc/Ra (Fig 49A) and $CO_2/^3$He (Fig. 49B), the pyroxene-hosted fluid inclusions fall along a MORB-Limestone mixing line, pointing to a carbonate component in the local mantle. For comparison, volcanic gases from La Palma and Tenerife exhibit $CO_2/^3$He and δ^{13}C values that, although consistent with a mixing MORB-Limestone (Fig. 49B), have less extreme compositions, in which thus the crustal C contribution is less evident. Besides, in the case of groundwaters from Tenerife and La Palma, the low Rc/Ra and more negative δ^{13}C values suggest the addition of crustal-derived radiogenic ^{4}He and organic carbon, as well the fractionation of carbon during CO_2 dissolution in water (Fig. 49A).

The olivine-hosted fluid inclusions exhibit even more extreme ^{13}C-rich compositions (δ^{13}C values of -0.19‰ and +0.96‰) (Fig. 49). Unlike pyroxenes from El Hierro and volcanic gases from Tenerife and La Palma, these unusually positive olivine results cannot result from a classical MORB-limestone mixing (Fig. 49A). In line with the HIMU affinity of the El Hierro mantle source (Day et al., 2010; Day and Hilton, 2011), we propose, instead, that this positive δ^{13}C signature derives from the addition to the local mantle of recycled crustal carbon transported by old subducted altered oceanic crust (AOC) and/or oceanic lithosphere (OL). Recycled AOC and OL components are essential carriers of crustal carbon into the mantle during subduction (Li et al., 2019; Plank and Manning, 2019). This is because AOC and OL precipitate carbonates during hydrothermal alteration at mid-ocean ridges (Alt and Teagle, 1999; Alt et al., 2013). Li et al. (2019) and references therein report the existence of carbonates in AOC and OL with δ^{13}C values as low as -24‰ and as high as +10.3‰, where the extremely positive δ^{13}C values result from the inorganic reduction of CO_2 to methane by either abiotic or biotic processes (Alt and Shanks, 2003) or microbial methanogenesis (Kenward et al., 2009). We show in Fig. 49 model binary mixing lines between MORB and AOC/OL, drawn by considering the range of δ^{13}C carbonate signatures observed in Li et al. (2019). In particular, from the dataset reported by Li et al. (2019), we select the isotopic compositions of two carbonates contained in AOC and two carbonates contained in OL, being characterised by different ages. Carbonates in AOC and OL older than 85 Ma exhibit δ^{13}C values as high as +3.5‰ and +2.1‰, respectively, while carbonates in AOC and OL younger than 85 Ma exhibit δ^{13}C as high as +4.7‰ and +10.9‰, respectively (Li et al., 2019).
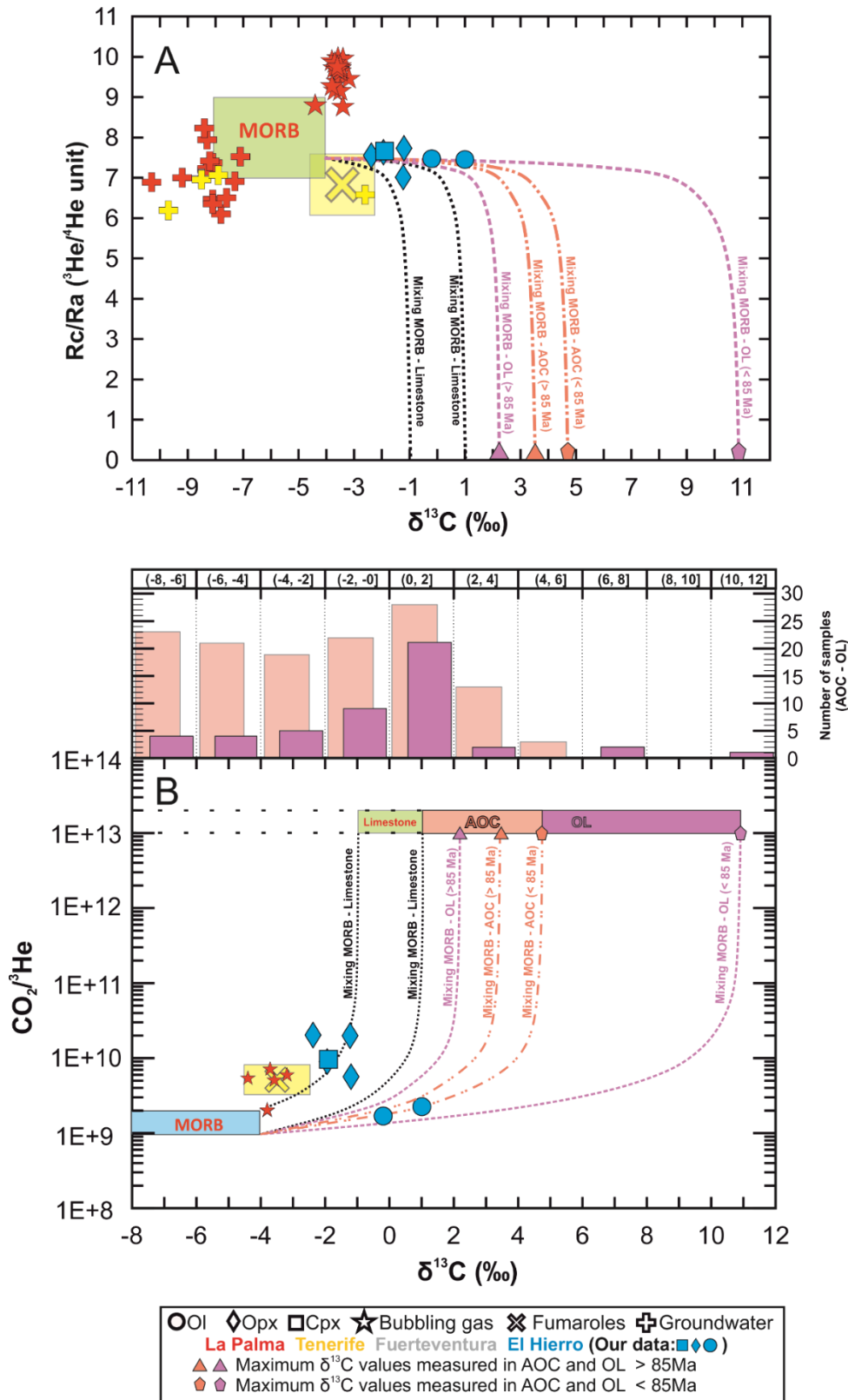
Figure 49. A) $\delta^{13}C$ vs Rc/Ra (^{3}He/^{4}He corrected for atmospheric contamination). Dotted black lines are binary mixing curves between two endmembers: 1) Limestone at $\delta^{13}C$ =-1‰ and 1‰ and Rc/Ra= 0.01 and 2) MORB-like upper mantle at $\delta^{13}C$ = -4‰ and Rc/Ra = 7.45. The yellow square represents the variability of fumarolic samples from El Teide (Tenerife). B) $\delta^{13}C$ vs $CO_2/^3$He. Dotted black lines are binary mixing between two endmembers: 1) Limestone at $\delta^{13}C$ =-1‰ and +1‰ and $CO_2/^3$He = 10-13 and 2) MORB-like upper mantle at $\delta^{13}C$ = -4‰ and $CO_2/^3$He = 1.00 x 10^{-9} and 2.00 x 10^{-9}. Detailed description of MORB-AOC and MORB-OL binary mixing curves is presented in section 8.3.5. The histogram shows the number of samples (AOC-OL) reported for each $\delta^{13}C$ class; $\delta^{13}C$ values measured in AOC and OL were obtained from Li et al. (2019).

88

The Rc/Ra and $CO_2/^3He$ compositions of the AOC/OL end-member are unfortunately undetermined. For the sake of illustration, these AOC/OL components are here assumed (Fig. 49) to have Rc/Ra and $CO_2/^3He$ ratios corresponding to those of crustal limestones (0.01 Ra and 1.0 x 1013, respectively), which is likely to be very rough assumption as, for example, CO_2 and He can undergo fractionation during eclogite formation and melting in the slab. Ultimately, the calculated mixing curves fit the $\delta^{13}C$ values measured in olivines well, supporting the presence of C-rich fluids derived from recycled AOC and/or OL in the mantle beneath El Hierro (Fig. 49). We caution, however, that the AOC/OL end-member can in fact sit in any position along the depicted mixing curve(s), so that (in the most extreme case) the olivines may have recorded the eclogitic component fully (e.g., with no dilution from MORB).

The existence of a C-rich component underneath El Hierro is strongly supported by petrological and fluid inclusion evidence on the same suite of mantle xenoliths (Oglialoro et al., 2017; Remigi et al., 2019; Colombo, 2020). According to these authors, the presence of high-density CO_2-N_2 fluid inclusions and interstitial microveins composed of silicate glass (andesitic-trachytic in composition) and carbonate droplets (calcite and Mg-calcite) are evidence of mantle metasomatism caused by deep infiltration of volatile-rich, carbonate-silicate melts, likely derived from carbonated-eclogite melting at high pressure (Remigi et al., 2019). Mantle metasomatism by C-rich (either carbonatitic or carbonate-silicate) melts underneath the Canary Islands has recurrently been described earlier at El Hierro (Neumann, 1991) and in nearby islands (Frezzotti et al., 2002a, 2002b; Neumann, 2004).

The timing of the paleo-subduction event(s) of AOC-OL recycling is difficult to determine. However, it may coincide with fossil subduction(s) (1-2 Ga old) responsible for the recycling of old oceanic crust and lithosphere, invoked to support the HIMU mantle signature underneath El Hierro and La Palma (e.g., Hoernle et al., 1991; Gurenko et al., 2006; Day et al., 2010; Day and Hilton, 2011, 2020).

8.4. Concluding remarks

We have reported on the first fluid inclusion-based $\delta^{13}C$ evidence for a recycled carbon component in the source mantle feeding El Hierro volcanism. To the best of our knowledge, this is the first direct isotopic evidence for C-rich metasomatic melts having modified the composition of the local mantle, perhaps in response to the past (old, 1-2 Ga old) oceanic subduction events that are implicated by the HIMU affinity of the mantle/magmas.

Pyroxene- and olivine-hosted fluid inclusions record such infiltration of crustal C-rich melts in the mantle but exhibit different extents of ^{13}C enrichment. The cause of this isotopic dissimilarity in the El Hierro xenolith mineral suite is currently undetermined. The El Hierro xenolith suite is, based on petrological and geochemical information (Remigi et al., 2019; Colombo, 2020), thought to represent one single metasomatic event in the mantle, arguing against the involvement of distinct fluids (with contrasting isotopic signature). Also, the negative $\delta^{13}C$ vs $CO_2/^3He$ relationship cannot be explained by trapping of fluids at different pressures, as fluids delivered upon de-compressional degassing should lead to a positive correlation ($\delta^{13}C$ and $CO_2/^3He$ should both decrease with increasing degassing extents). Ultimately, we argue that some mineral specific C isotopic fractionation may occur during metasomatic (mineral-melt-exsolved fluid) interactions deep in the mantle, and we claim for the need of analysing pyroxene vs. olivine isotopic signatures from other xenolith suites to explore the existence of general mineral specific trends.

He, Ar and Ne systematics in our xenoliths confirm a depleted mantle (DMM-type) signature for the lithospheric mantle beneath El Hierro, in agreement with ^{3}He/^{4}He signatures previously reported for groundwater and lava-hosted fluid inclusions. This helium isotopic signature of El Hierro persists in time, suggesting a homogeneity in the local mantle composition at least over the last million years. This MORB-like signature argues against a primordial He source affecting the local lithospheric mantle and suggests a marginal He slab transport during past subduction events. The more radiogenic He signature in the eastern Canary Islands may reflect a combination of an EM source, magma ageing and/or assimilation of radiogenic He upon magma ascent in the crust.

CHAPTER 9. THE RADIOGENIC NATURE OF THE LITHOSPHERIC MANTLE BENEATH LANZAROTE

9.1. Volcanological setting

Lanzarote is the easternmost island of the Canary archipelago and its volcanological history can be subdivided in two periods (Marinoni and Pasquarè, 1994; Troll and Carracedo, 2016): the pre-erosional shield stage (Miocene-Pliocene) and a the post-erosional stage (Quaternary). The island was initially formed by two volcanoes during the shield stage: the Ajaches volcano whose deposits are dated between 14.5 and 0.8 Ma and the Famara volcano with ages between 10.2 Ma and 53 ka (Coello et al., 1992; Troll and Carracedo, 2016). It is believed that both volcanoes grew simultaneously during the late Miocene (Coello et al., 1992; Troll and Carracedo, 2016) until 5.7 Ma ago when the volcanism ceased. This quiescence promoted the beginning of an intense erosional event that lasted a few million years (Marinoni and Pasquarè, 1994). Then, the volcanism reactivated in the Quaternary in the central rift zone with the formation of the Corona volcano and the historical eruptions occurred in 1730-36 (Timanfaya eruption) and 1824 (eruption of Tao, Chinero and Tinguatón volcanoes). Like El Hierro, Lanzarote exhibit tholeiite lavas and alkali basalts that may contain important quantities of ultramafic xenoliths (Siena et al., 1991).

9.1 Petrological characteristics of mantle xenoliths

Petrological data of the same suite of xenoliths are presented in Siena et al. (1991). As described by these authors, xenoliths show protogranular and porphyroclastic textures formed by four main mineral phases: Ol, Opx, Cpx and Sp. Opx is classified as enstatites and Cpx as Cr-diopsides. Some textures such as spongy borders in Opx, interstitial glassy patches and embayed spinels associated with pyrometamorphic processes have been recognized. Based on two-pyroxene geothermometry, Siena et al. (1991) calculated a maximum temperature of 1080°C for the xenoliths and report two groups of fO_2 values (measured in Sp crystals): 1) values that fit the QFM buffer measured in primary interstitial Sp (commonly attributed to upper mantle conditions) and 2) values that fit the NNO buffer (measured in secondary embayed Sp crystals related to pyrometamorphic glassy patches) that indicate more oxidizing conditions likely associated with metasomatic events.

Mantle xenoliths reflect a very complex history. These rocks show depleted patterns of High Field Strength Elements (HFSE) and Heavy Rare Earth Elements (HREE) commonly attributed to 15-20% melting of the mantle source and the extraction of MORB-like magmas (Ottonello et al., 1984; Siena). Xenoliths also record the effect of metasomatic events driven by strongly alkaline silicate melts under hydrous/oxidizing conditions; some evidences of this process are the presence of pyrometamorphic textures, the variable enrichments of HFSE, Nb, P and LREE, and the variability of fO_2 values. Petrographic analyses also revealed that inclusions identified in olivine and pyroxenes are mainly secondary and are composed of three phases (Siena et al., 1991): CO_2, glass and sulphides. Barometric studies in fluid inclusions demonstrated the occurrence of shallow and deep fluid trapping events: shallow fluids were presumably trapped at crustal depths (between 3 - 6 km) while the densest fluids were likely trapped at mantle conditions (between 9.5 and 15 km depth).

9.2. Results

Samples analyzed in this work were collected from Quaternary alkali basic lavas belonging to the cycles III and IV proposed by Fuster et al. (1968) which are recognized as the most recent volcanic

deposits of the island. In total, 7 mantle xenoliths from Lanzarote were investigated in this project: 6 spinel harzburgites and 1 dunite. The noble gas and CO_2 data is reported in Table 8 and Fig. 50. On average, the concentrations of ^3He and ^4He in fluid inclusions (9.82×10^{-12} and 8.25×10^{-17} mol/g, respectively) are higher if compared with the ultramafic nodules collected from El Hierro. Olivines generally exhibit the highest contents of helium when compared with Opx. As observed in xenoliths from Mexico and El Hierro, CO_2 is the predominate phase in fluid inclusions hosted in Lanzarote samples (2.69×10^{-7} mol/g on average); pyroxenes exhibit the highest concentrations when compared with Ol. $^{40}Ar^*$ values vary from 3.99×10^{-12} and 6.30×10^{-10} mol/g. Rc/Ra ratios range from 4.76 to 6.54 and $^4He/^{40}Ar^*$ ratios from 0.01 to 0.58. $^4He/^{20}Ne$ and $^{40}Ar/^{36}Ar$ values are well above the air value (0.318 and 298.56, respectively; Steiger and Jäger, 1977; Ozima and Podosek, 2002) except for sample CL32 Opx which exhibit $^4He/^{20}Ne = 5.2$ and $^{40}Ar/^{36}Ar = 400.1$; this sample also has the lowest Rc/Ra value observed in the dataset (4.76). $^{20}Ne/^{22}Ne$ and $^{21}Ne/^{22}Ne$ vary between 9.82 and 10.50 and from 0.292 to 0.0350, respectively, suggesting a mixing between air and MORB fluids. Like El Hierro xenoliths, the isotopic composition of CO_2 ($\delta^{13}C$) reveals two groups of data: pyroxenes with negative values that vary between -1.1 and -0.6‰ and olivines with positive values (+0.8‰).
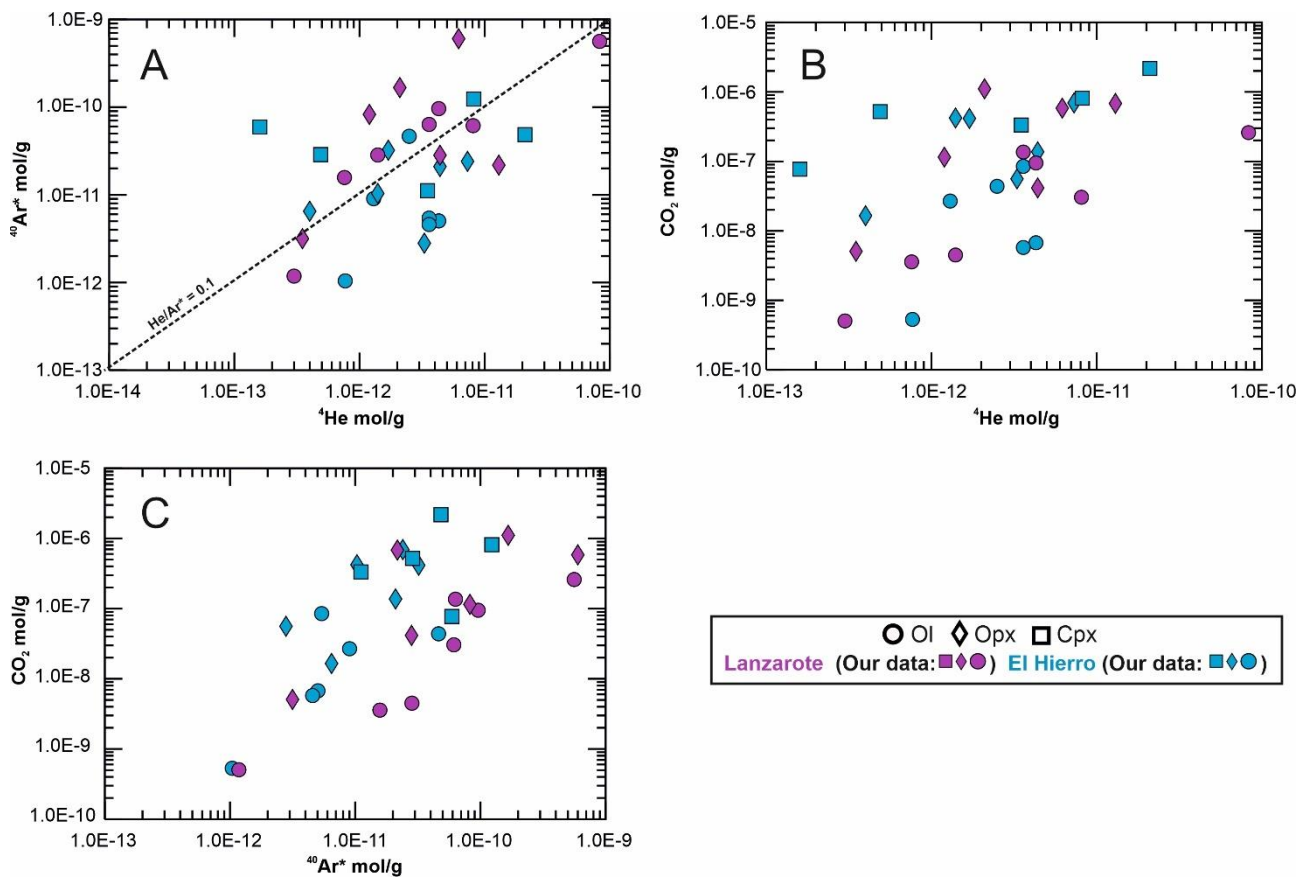
Figure 50. ^4He, $^{40}Ar^*$ and CO_2 contents in fluid inclusions analyzed in mantle xenoliths from Lanzarote and El Hierro.

Table 8. Noble gas and CO_2 compositions of fluid compositions hosted in Lanzarote mantle xenoliths. Concentrations of noble gases isotopes, CO_2 and N_2 are reported in mol/g. [A] First estimation of CO_2 contents in fluid inclusions during noble gas analysis; [B] CO_2 contents and $CO_2/^3He$ ratios measured from the glass line after CO_2 isotopic determinations. Reported errors are 2σ uncertainties. Estimated errors for ^3He, ^4He, ^{20}Ne, ^{21}Ne, ^{22}Ne, ^{40}Ar, ^{36}Ar and CO_2 are <10%, <0.06%, <14%, <10%, <1.4%, <0.14%, <0.2% and <10%, respectively.

Sample	Mineral	Rock type	Weight (g)	^3He	^4He	^{20}Ne	^{21}Ne	^{22}Ne	CO_2^A	^{40}Ar	$^{40}Ar^*$	$^4He/^{20}Ne$	$^4He/^{40}Ar^*$	R/Ra
CL 12	Ol	Sp Harzburgite	1.03855	2.48E-18	3.01E-13	1.16E-14	3.42E-17	1.18E-15	5.05E-10	3.99E-12	1.18E-12	25.9	0.25	5.94
CL 12	Opx	Sp Harzburgite	0.98756	2.92E-18	3.55E-13	1.44E-14	4.33E-17	1.45E-15	5.07E-09	5.83E-12	3.16E-12	24.7	0.11	5.92
CL 33	Ol	Sp Harzburgite	1.07521	6.62E-17	8.05E-12	2.60E-14	8.18E-17	2.56E-15	3.04E-08	6.93E-11	6.14E-11	310.0	0.13	5.91
CL 33	Opx	Sp Harzburgite	0.11669	1.11E-16	1.25E-11	5.88E-14	1.79E-16	5.83E-15	6.80E-07	3.25E-11	2.17E-11	212.7	0.57	6.40
CL 75	Ol	Sp Harzburgite	1.05553	5.75E-18	7.59E-13	1.71E-14	5.10E-17	1.74E-15	3.57E-09	2.24E-11	1.57E-11	44.3	0.05	5.49
CL 75	Opx	Sp Harzburgite	0.51647	9.41E-18	1.18E-12	1.46E-14	4.05E-17	1.48E-15	1.15E-07	8.96E-11	8.25E-11	80.4	0.01	5.75
CL 54	Ol	Sp Harzburgite	1.02179	3.21E-17	3.59E-12	2.13E-14	6.51E-17	2.13E-15	1.36E-07	6.91E-11	6.33E-11	168.5	0.06	6.43
CL 54	Opx	Sp Harzburgite	0.20224	1.77E-17	2.13E-12	7.35E-14	2.30E-16	7.25E-15	1.10E-06	1.77E-10	1.67E-10	29.0	0.01	5.97
CL 27	Ol	Sp Harzburgite	1.01679	3.63E-17	4.28E-12	1.10E-14	3.32E-17	1.11E-15	9.46E-08	1.04E-10	9.60E-11	389.1	0.04	6.09
CL 27	Opx	Sp Harzburgite	0.29024	5.25E-17	6.24E-12	2.74E-14	8.41E-17	2.75E-15	5.83E-07	6.30E-10	6.01E-10	228.1	0.01	6.05
CL 32	Ol	Sp Harzburgite	1.00567	6.95E-16	8.26E-11	9.06E-14	3.01E-16	8.64E-15	2.59E-07	5.95E-10	5.62E-10	912.4	0.15	6.05
CL 32	Opx	Sp Harzburgite	0.05051	2.79E-17	4.44E-12	8.59E-13	2.52E-15	8.62E-14	4.13E-08	1.12E-10	2.82E-11	5.2	0.16	4.51
CL 30	Ol	Dunite	1.02071	1.29E-17	1.43E-12	1.13E-14	3.41E-17	1.14E-15	4.48E-09	3.36E-11	2.84E-11	126.6	0.05	6.52

Sample	Mineral	Rc/Ra	Error (+/-)	$^{40}Ar/^{36}Ar$	Error (+/-)	$^{20}Ne/^{22}Ne$	Error (+/-)	$^{21}Ne/^{22}Ne$	Error (+/-)	$CO_2/^3He^A$	$^3He/^{36}Ar$	CO_2^B	$CO_2/^3He^B$	$\delta^{13}C$ (‰)
CL 12	Ol	6.00	0.19	425.1	0.5	9.87	0.04	0.0292	0.0007	2.03E+08	2.61E-04	n.a	n.a	n.a
CL 12	Opx	5.98	0.20	656.1	0.8	9.91	0.03	0.0299	0.0009	1.74E+09	3.23E-04	n.a	n.a	n.a
CL 33	Ol	5.92	0.13	2622.5	5.1	10.17	0.03	0.0321	0.0004	4.60E+08	2.48E-03	n.a	n.a	n.a
CL 33	Opx	6.41	0.14	910.8	1.1	10.10	0.05	0.0308	0.0009	6.10E+09	3.05E-03	3.77E+09	4.20E-07	-0.60
CL 75	Ol	5.52	0.20	1003.8	5.3	9.84	0.03	0.0294	0.0005	6.20E+08	2.55E-04	n.a	n.a	n.a
CL 75	Opx	5.77	0.19	3810.2	18.2	9.98	0.05	0.0277	0.0003	1.22E+10	3.96E-04	n.a	n.a	n.a
CL 54	Ol	6.44	0.16	3583.8	11.2	10.03	0.03	0.0307	0.0005	4.23E+09	1.65E-03	n.a	n.a	n.a
CL 54	Opx	6.02	0.18	5119.8	54.3	10.12	0.03	0.0317	0.0006	6.24E+10	5.06E-04	9.36E+10	1.66E-06	-1.10
CL 27	Ol	6.10	0.13	3889.6	212.9	9.97	0.03	0.0302	0.0006	2.61E+09	1.34E-03	n.a	n.a	n.a
CL 27	Opx	6.06	0.13	6502.5	296.2	10.00	0.06	0.0308	0.0009	1.11E+10	5.37E-04	1.56E+10	8.20E-07	-2.25
CL 32	Ol	6.05	0.13	5394.4	64.5	10.50	0.02	0.0350	0.0003	3.72E+08	6.23E-03	2.91E+08	2.02E-07	0.80
CL 32	Opx	4.76	0.23	400.1	0.5	9.98	0.03	0.0294	0.0004	1.48E+09	9.81E-05	n.a	n.a	n.a
CL 30	Ol	6.54	0.17	1947.3	7.4	9.89	0.05	0.0300	0.0006	3.46E+08	7.42E-04	n.a	n.a	n.a

9.3. Discussion

9.3.1. Noble gas signature of the Lanzarote lithospheric mantle

The homogeneity of the dataset, particularly regarding the $^{3}He/^{4}He$ ratios, indicates that the fluid inclusions trapped in Lanzarote samples have not been modified by processes such as diffusive fractionation or addition of cosmogenic ^{3}He, therefore, these should represent the composition of the local mantle. When compared to El Hierro xenoliths, ^{4}He, $^{40}Ar^{*}$ and CO_2 contents are also positively correlated and vary in a similar range (Fig. 50). The same observation was made for $^{4}He/^{20}Ne$, $^{20}Ne/^{22}Ne$, $^{21}Ne/^{22}Ne$, $^{40}Ar/^{36}Ar$ and $^{3}He/^{36}Ar$ ratios whose variability also indicates the existence of a recycled atmospheric component in the upper mantle (Fig. 51). As discussed in the following sections, $^{3}He/^{4}He$ values are clearly lower than those measured in El Hierro xenoliths, these vary in a narrow range and support the presence of a radiogenic source in the lithospheric mantle beneath the eastern Canary Islands. $\delta^{13}C$ values, on the other hand, also indicates the existence of crustal carbon in the local mantle and suggests that this component is likely a regional feature (as presumed for the HIMU endmember) that influences the mantle beneath the entire archipelago.

9.3.1.1. Interaction with atmospheric fluids

An atmospheric component is observed in Lanzarote xenoliths. On average, nodules show $^{4}He/^{20}Ne$ $\approx 196.68 \pm 236.85$ and $^{40}Ar/^{36}Ar \approx 2,789.70 \pm 2,003.68$, which are comparable with the averages estimated for El Hierro xenoliths (316.93 ± 245.97 and $2,523.47\pm1,534.39$, respectively). These values are considerably lower than the theorical MORB values (e.g., $^{40}Ar/^{36}Ar = 44,000$; Moreira et al., 1998) and the dataset can be explained using binary mixing trends between two endmembers: 1) MORB and 2) air. The air component is especially observed in samples CL12 Ol/Opx and CL32 Opx whose $^{4}He/^{20}Ne$ and $^{40}Ar/^{36}Ar$ ratios are below 27 and 450, respectively (Fig. 51A-B). The existence of atmospheric fluids is also supported by the variability of the $^{20}Ne/^{22}Ne$ and $^{21}Ne/^{22}Ne$ values since the data falls along the mixing curve MORB-air proposed by Sarda et al. (1988) and Moreira et al. (1998) (Fig. 51C). These results reinforce the hypothesis regarding the existence of an atmospheric component recycled in the lithospheric mantle beneath the Canary Islands (subsection 8.3.2).

We highlight that fluid inclusions analysis performed in Lanzarote xenoliths reflect different fluid trapping episodes under both mantle and crustal conditions (Siena et al., 1991), so it is not possible to discard the introduction of atmospheric fluids at crustal depths or even during the eruption of the transporting magmas. Despite of the above, some evidence indicates a deep origin for the atmospheric component identified in fluid inclusions, for example, the mixing trend observed in Fig. 51B, the occurrence of samples with $^{40}Ar/^{36}Ar$ values over 3,000 (considerably higher than the atmospheric value of 298.56; Steiger and Jäger, 1977; Ozima and Podosek, 2002) and the similarity with the ratios ($^{4}He/^{20}Ne$ and $^{40}Ar/^{36}Ar$) measured in El Hierro xenoliths. Following the reasoning discussed in subsection 8.3.2, we focused on the variability of ^{36}Ar contents since heavy noble gases (e.g., Ar) are more prone to be introduced in the mantle during subduction and can be used as tracers of mantle contamination (Matsumoto et al., 2001; Holland and Ballentine, 2006; Hopp et al., 2007a; Mukhopadhyay and Parai, 2019). Indeed, when comparing ^{3}He and ^{36}Ar abundances, Lanzarote samples follow a positive trend that points to a deep interaction between mantle and subduction related atmospheric noble gases (Fig. 51D; Matsumoto et al., 2001).

The fact that atmospheric fluids have been identified in xenoliths, from both El Hierro and Lanzarote islands, suggests that the atmospheric contamination (via subduction) is a regional

feature that conditions the isotopic signature of the lithospheric mantle located beneath the Canary archipelago. This finding is not unique and many studies have also discussed the role of subduction-related atmospheric fluids in the mantle composition either in sub-continental or sub-oceanic settings, for instance: Mexico, (see subsections 5.4.4.1 and 6.4.2), Europe, West Antarctic Rift System (WARS), Eastern Australia, Red sea region, N/S Kenya rifts and Ethiopia (Afar) (Matsumoto et al., 1998, 2000; Hopp et al., 2004, 2007a, 2007b; Buikin et al., 2005; Gautheron et al., 2005a; Czuppon et al., 2009; Martelli et al., 2011; Halldórsson et al., 2014; Broadley et al., 2016; Rizzo et al., 2018, 2021; Correale et al., 2019; Faccini et al., 2020).
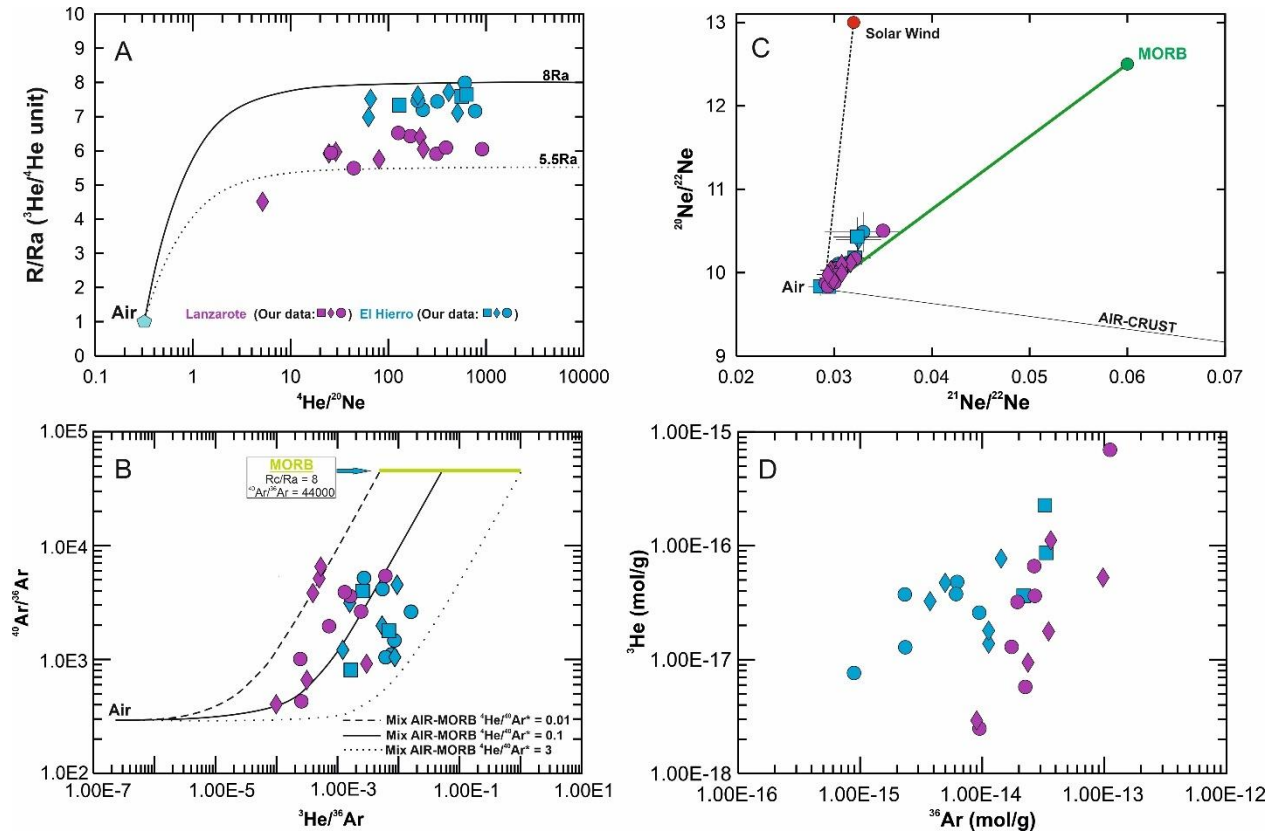
Figure 51. A) $^4He/^{20}Ne$ vs R/Ra ($^3He/^4He$ ratios non corrected to atmospheric contamination). Solid and dotted lines represent binary mixing lines between an upper mantle with 8 and 5.5 Ra, respectively, and air. B) $^{21}Ne/^{22}Ne$ vs $^{20}Ne/^{22}Ne$ ratios. The green line represents the binary mixing air-MORB mantle after Sarda et al. (1988) and Moreira et al. (1998) at $^{21}Ne/^{22}Ne_{air}$ = 0.029 and $^{20}Ne/^{22}Ne_{air}$ = 9.8 and $^{21}Ne/^{22}Ne$ = 0.06 and $^{20}Ne/^{22}Ne$ = 12.5; Solar wind endmember was plotted at $^{21}Ne/^{22}Ne$ = 0.0328 and $^{20}Ne/^{22}Ne$ = 13.8 (Heber et al., 2009); the crust endmember was plotted at $^{21}Ne/^{22}Ne$ = 0.6145 and $^{20}Ne/^{22}Ne$ = 0.3 (Kennedy et al., 1990). C) $^3He/^{40}Ar$ vs $^{40}Ar/^{36}Ar$ diagram. D) ^{40}Ar vs ^3He contents.

9.3.1.2. Partial melting and metasomatism

The residual character of Lanzarote mantle xenoliths was previously observed by Siena et al. (1991). Ultramafic nodules are characterized by low Ti, Al, Na and CaO/Al_2O_3 ratios (the latter compared with the primitive upper mantle) and high Mg, Ni and Cr that coincide with high degrees of partial melting (10-20%) and the extraction of MORB-like magmas (Siena et al., 1991). Noble gases also record this process. In Fig. 52 we compare the Mg# of each mineralogical phase with the corresponding $^3He/^4He$ and $^4He/^{40}Ar*$ ratio measured in fluid inclusions. Mg# generally increases from Ol to Opx and demonstrates the depleted character of the xenoliths with values considerably higher than the expected fertile mantle. Most of the samples exhibit a decrease in $^4He/^{40}Ar*$ when the Mg# increases (from Ol to Opx), which could be interpreted as a partial melting trend. This is supported by the spongy textures identified in Opx by Siena et al. (1991). One exception is sample CL33 Opx, which exhibits an opposite trend, i.e., higher Rc/Ra and $^4He/^{40}Ar*$ and lower Mg# than

95

Ol. This mean that xenolith CL33 possibly records not just a simple partial melting, but also a completely different process capable of modifying the composition of Opx towards the MORB range. Siena et al. (1991) proposes that the mantle beneath Lanzarote was metasomatized by alkali silicate melts (silica oversaturated and high Al_2O_3 and MgO content) likely originated at or below the lithosphere-asthenosphere interface.

Once formed, the melt pervaded the lithospheric mantle reacting with the original mineral paragenesis and modifying the original composition of pyroxenes and spinels; this is evidences by the spongy textures observed in Opx. This hypothesis perfectly fit the variability observed in sample CL33, because a fertile melt that metasomatize/refertilizes the lithospheric mantle is a convenient agent capable of increasing the original Mg#, Rc/Ra and $^4He/^{40}Ar^*$ of the sample CL33 Opx. Metasomatic/refertilization events (driven by volatile-rich silicate melts) are not an isolated discovery in mantle xenoliths from the Canary Islands, as discussed in chapter 8, Colombo (2020) also report the existence of a carbonated-eclogite melt pervading mantle xenoliths from El Hierro. Undoubtedly, all these evidences suggest that episodes of metsomatism/refertilization in the upper mantle are a common phenomenon in the lithospheric mantle in both continental and oceanic settings and have the potential to generate critical changes in their mineralogical, chemical and isotopic composition, including volatiles.

9.3.1.3. Radiogenic $^3He/^4He$ signatures

Petrological observations do not show signs of interaction with the host magma, which discards the entrapment of secondary fluids during the ascent of the xenoliths towards the surface, therefore it is reasonable to consider that volatiles trapped in Lanzarote xenoliths mostly represent a component of the original mantle fluids. The $^3He/^4He$ ratios identified in Lanzarote nodules do not require the involvement of a lower mantle component beneath this island and agree with the observations made by previous studies on noble gases in mantle xenoliths (Fig. 53A-B; Vance et al., 1989; Grachev, 2012). On average, the mantle xenoliths exhibit a Rc/Ra = 5.97±0.44 Ra, which is lower than in all the average other Canary Islands that fall within or at the lower range of MORB. Unlike lavas and volcanic gases, mantle xenoliths are considered as direct samples of the upper mantle (Pearson et al., 2014), so the difference in $^3He/^4He$ ratios observed in these rocks along the archipelago confirms not just the compositional heterogeneity but also the radiogenic nature of the lithospheric mantle beneath the eastern Canary Islands.

The radiogenic signature of Lanzarote samples is not uncommon in oceanic settings as Azores, whereas the eastern S. Miguel Islands records a comparable signature (Moreira et al., 1999, 2012; Madureira et al., 2014). Furthermore, similar findings are registered in some SCLM localities, for instance, the European and the NW African SCLM. Dunai and Baur (1995) and Gautheron et al. (2005a) reported values of 6.32±0.39 Ra for the European SCLM based on the analysis of ultramafic nodules from different Quaternary volcanic provinces including Dreiser Weiher (Germany), Massif Central (France) and Kapfenstein (Austria). Later, Martelli et al. (2011), Rizzo et al. (2018, 2021) and Faccini et al. (2020) found similar ranges when investigating mantle xenoliths from Tallante-Calatrava (Spain), Lower Silesia (Poland), West Eifel-Siebengebirge (Germany) and the Eastern Transylvanian Basin, respectively, confirming that the $^3He/^4He$ signature of European SCLM is lower than that of MORB. It is worth mentioning that studies on Sr-Nd-Pb isotopes in lavas indicate that the European mantle is heterogeneous being formed by different components such as DM (depleted mantle), HIMU and EM (enriched mantle) (Dunai and Baur, 1995). Considering that one of the most accepted model to explain the radiogenic nature of the European SCLM is the addition of ^{4}He-rich fluids inherited from recycled crustal material via paleosubduction events, with

a lithospheric mantle that evolves in steady-state (Gautheron et al., 2005a), the hypothesis of a mixing of different components remains the most plausible.

Figure 52. A) Mg# vs Rc/Ra (^{3}He/^{4}He ratios corrected for atmospheric contamination). B) Mg# vs ^{4}He/^{40}Ar*. C) ^{4}He/^{40}Ar* vs Rc/Ra.

In the case of Africa, Beccaluva et al. (2007, 2008) report values of 5.3-6.5Ra for mantle xenoliths collected in Quaternary alkaline volcanics from North Africa. These authors suggest (also based on

the analysis of Sr-Nd-Pb isotope composition) that the lithospheric mantle has been affected by a HIMU-like metasomatic agent, which extends along the northern–central African lithosphere. Tholeiitic plateau basalts found in these volcanic provinces also indicate the existence of an EM1-type enriched mantle component that is not observed in mantle xenoliths. The authors propose a complex model in which the upwelling asthenosphere displaced the old lithospheric mantle where mantle xenoliths represent shallow mantle depths (a younger and rejuvenated lithosphere), while the tholeiites reflect an old lithospheric domain. Thus, low ^{3}He/^{4}He are likely the result of degassing of shallow mantle domains or the addition of recycled crustal materials in the upper mantle.

As for Europe and NW Africa, the scenario for Canary Islands is far from simple since several authors propose the coexistence of similar mantle components to explain the isotopic variability (Sr-Nd-Pb and noble gas isotope composition) identified in both volcanic materials and mantle-derived rocks (Vance et al., 1989; Hoernle et al., 1991; Hilton et al., 2000; Simonsen et al., 2000; Gurenko et al., 2006; Day and Hilton, 2011, 2020; Grachev, 2012). These components are: HIMU (which is especially recognized in the western islands), EM (enriched mantle), DM (depleted mantle) and a lower mantle within a plume-like geodynamic model. Unfortunately, ^{3}He/^{4}He ratios lower than MORB have been invoked either in presence of a HIMU or EM component, so it is difficult to establish the individual contribution of each component in the helium isotopic signature lower than MORB observed in eastern Canary Islands; two examples of this limitation are the above-mentioned European and NW African SCLM where ^{3}He/^{4}He signatures are relatively constant despite of the coexistence of HIMU or EM components in the local mantle. Thus, the radiogenic ^{3}He/^{4}He ratios may obey to both endmembers: 1) a HIMU-type mantle component derived from the recycling of oceanic crust, which may introduce ^{4}He-rich fluids in the mantle, ultimately lowering the MORB-like pristine ratios, and 2) an EM component, typical of ultramafic xenoliths coming from ancient continental lithospheric mantle, which have become more radiogenic over time due to the in situ radioactive decay of U-Th (Menzies, 1989; Hawkesworth et al., 1990; Hoernle et al., 1991).

It is worth noting that in subsection 9.3.1.1 we already discussed the existence of atmospheric materials in the local mantle (presumably derived from the subducted oceanic crust), which agrees well with the occurrence of a HIMU component beneath Lanzarote. Despite of the above, some authors such as Day and Hilton (2020) attribute the relatively low ^{3}He/^{4}He ratios measured in fumaroles from El Teide to an EM endmember and highlight an increase of the EM contribution in the mantle beneath the eastern Canary Islands (see Fig 53B). This interpretation is based on the investigation performed by Hoernle et al. (1991) and Simonsen et al. (2000), who identified both HIMU-type and EM1-EM2 endmembers when studying the mafic lavas from Tenerife and Gran Canaria. According to Hoernle et al. (1991), the EM component likely reflect the introduction of continental lithospheric mantle (derived from the West African Craton during the break-up of Pangea) into the mantle beneath the eastern part of the archipelago. If this interpretation is correct, then the radiogenic helium ratios measured in our xenoliths would likely reflect the presence of an EM mantle component (i.e., and ancient continental lithospheric mantle), which explains the similarity in ^{3}He/^{4}He with other SCLM localities such as Europe or NW Africa.

Based on the results obtained from the study of mantle xenoliths in Canary Islands, the mantle heterogeneity is the most plausible explanation for the west to east variations of the ^{3}He/^{4}He signature. However, the role of the crustal thickness cannot be discarded (as proposed in subsection 8.3.5) since processes such as magma ageing or crustal assimilation are able to justify the decrease in ^{3}He/^{4}He observed in lava phenocrysts, as observed in olivine-hosted fluid inclusions of La Palma volcanic products that have ratios systematically lower than in gases from Dos Aguas spring (Hilton et al., 2000; Gurenko et al., 2006; Day and Hilton, 2011, 2020; Padrón et al., 2015; Torres-González et al., 2020). More studies, regarding noble gas and carbon isotopes, are required (especially in La

Gomera, Tenerife, Gran Canaria and Fuerteventura) in order to better test the hypothesis of an increasing EM component in the eastern islands.

Figure 53. A) ^{4}He vs Rc/Ra (^{3}He/^{4}He ratios corrected for atmospheric contamination). B) Summary of the variability of Rc/Ra ratios along the Canarian archipelago. EH: El Hierro, LP: La Palma, LG: La Gomera, T: Tenerife, Ft: Fuerteventura, La: Lanzarote. Adapted from Fig. 48C.

9.3.2. Crustal δ^{13}C signatures in fluid inclusions

The fact that CO_2 contents in fluid inclusions from Lanzarote xenoliths are within the same range of El Hierro measurements (Fig. 50B-C) indicates that either the fluids were trapped under mantle

conditions or supports the existence of a comparable C-rich fluid pervading the mantle beneath the eastern islands. This is corroborated by the variability of $\delta^{13}C$ values (-2.25‰ < $\delta^{13}C$ < +0.8‰), which fall in the same range of El Hierro mantle xenoliths and describes similar differences between olivine and pyroxene crystals (Fig. 54). The similarity in $\delta^{13}C$ between mantle xenoliths from both islands indicates that there is a decoupling with the $^3He/^4He$ signatures; although $\delta^{13}C$ values point to a homogeneous signature for the mantle below Canary Islands (which must be verified in xenoliths and lavas from other islands such as Tenerife or La Gomera), derived from the mixing between mantle and crustal carbon (sedimentary carbonates and AOC/OL carbonates; see subsection 8.3.6), the variability of $^3He/^4He$ show a more complex scenario where the isotopic composition is modulated by the interaction between different components (HIMU, MORB, EM, plume; Fig, 55).
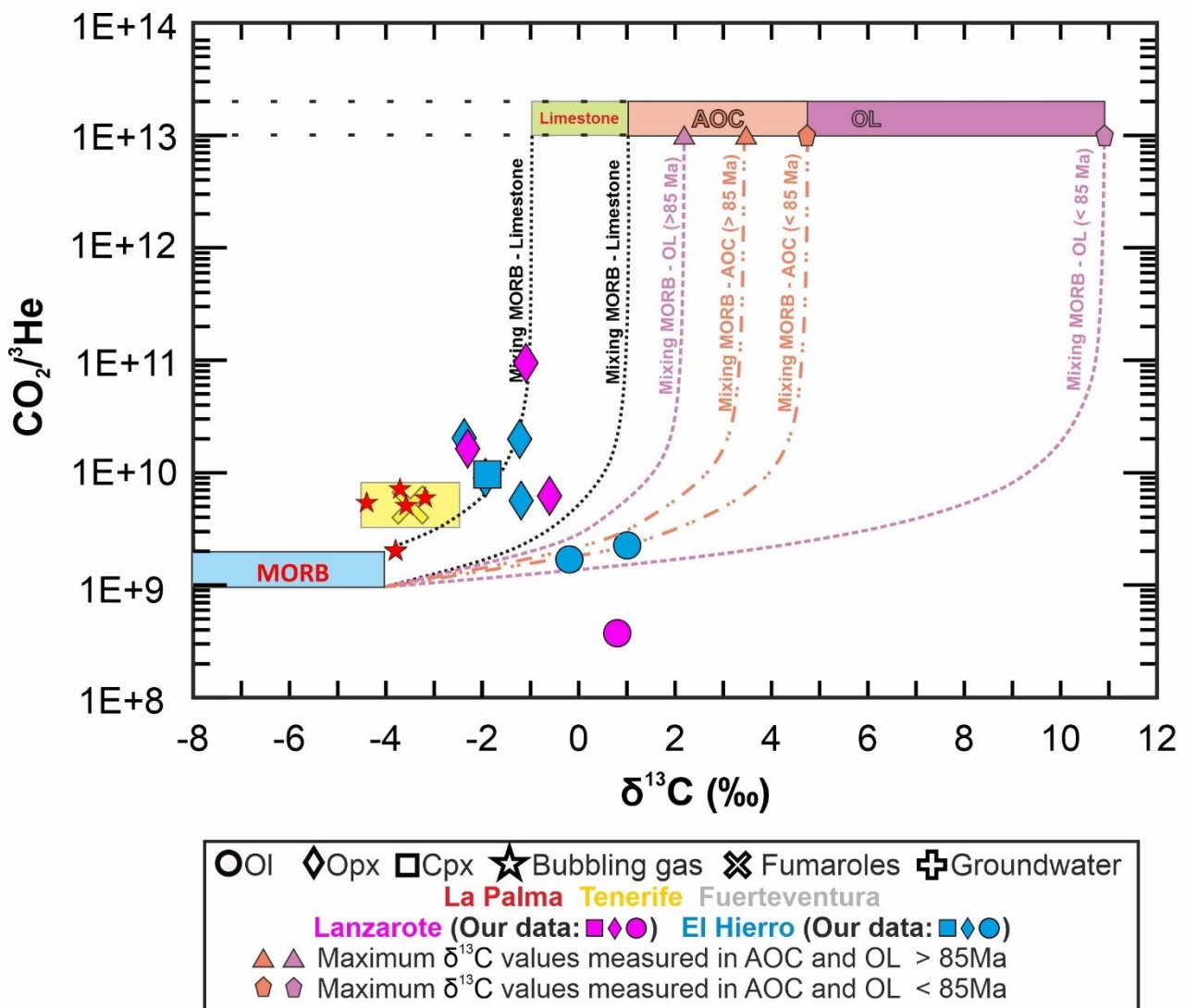
Figure 54. $\delta^{13}C$ vs $CO_2/^3He$ ratios for the Lanzarote samples. Details about the endmembers are provided in the caption of Fig. 49B.

The hypothesis that the recycled crustal carbon is a regional characteristic of the upper mantle beneath the Canary Islands agrees well with the classic "Blob model" (Hoernle and Schmincke, 1993) and the more recent "edge-driven mantle convection model" (Gurenko et al., 2010). This is how a crustal component that is brought to the surface by a HIMU-like mantle plume (which

spreads beneath the archipelago) seems the most plausible scenario to explain the homogeneity observed in El Hierro and Lanzarote xenoliths (Fig. 55). The fact that the recycled carbon component is linked to the HIMU signature leads us to believe that radiogenic ^{3}He/^{4}He ratios may derive from the HIMU component, nevertheless, this connection is not clear since previous studies in volcanic rocks from El Hierro and La Palma demonstrated the HIMU affinity of the islands despite registering MORB-like ^{3}He/^{4}He signatures. We conclude that the introduction of an EM is the most plausible explanation for the radiogenic helium ratios. This EM component does not seem to impact the isotopic composition of the recycled carbon endmember, either because has similar δ^{13}C values, or because this component is not enough to generate appreciable changes in the carbon signatures. In any case, in order to support this idea, it is mandatory to investigate the noble gas and carbon signature of fluid inclusions in mantle xenoliths and lava phenocrysts belonging to other Canary Islands such as Tenerife, La Gomera and Gran Canaria.
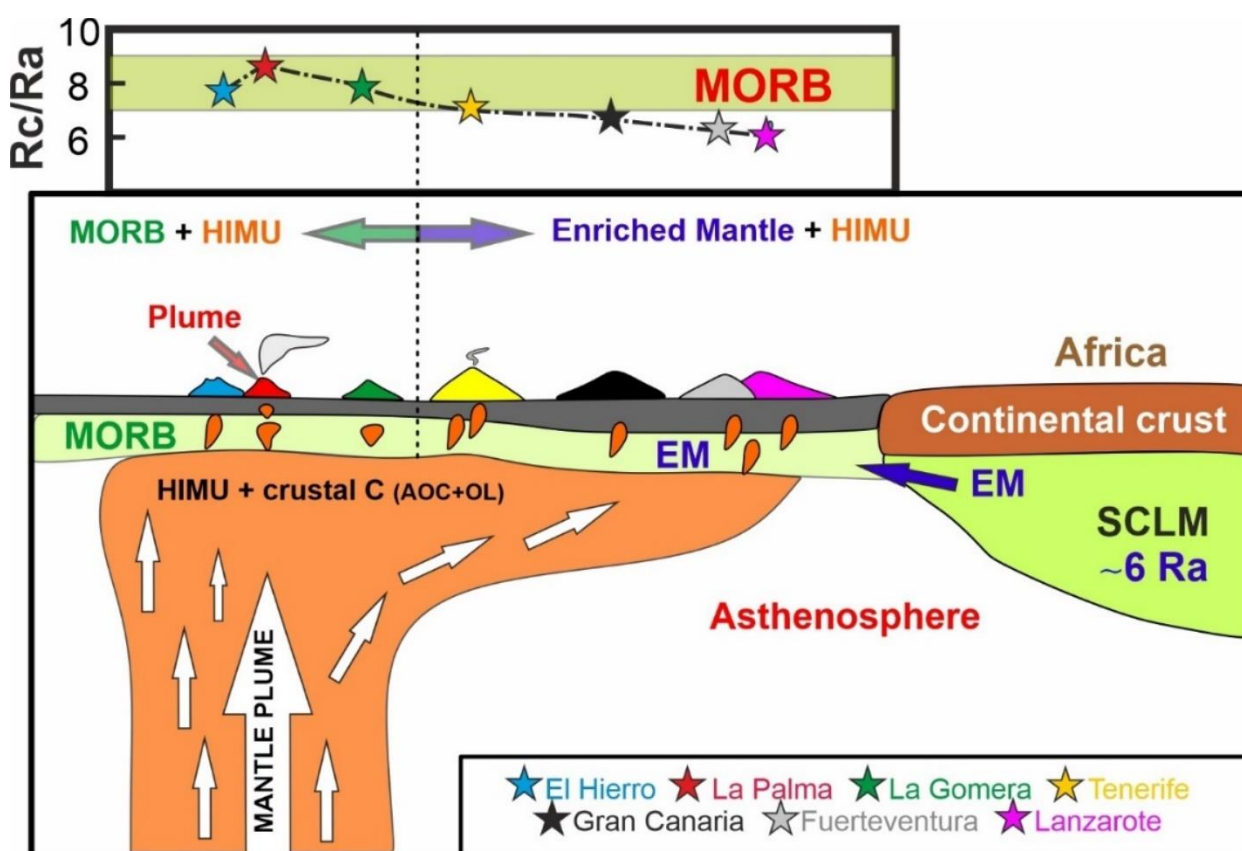
Figure 55. Model for the origin of the crustal carbon identified in fluid inclusions in mantle xenoliths from El Hierro and Lanzarote islands. In the upper section, the stars represent the average Rc/Ra ratio for each island. Modified from Hoernle and Schmincke (1993), Anguita and Hernán (2000) and Troll and Carracedo (2016).

9.4. Conclusions

For the first time, the carbon (of CO_2) and noble gases signatures of fluid inclusions hosted in Lanzarote mantle xenoliths were investigated. ^{4}He/^{20}Ne and ^{40}Ar/^{36}Ar ratios agree with the range of El Hierro xenoliths and suggest the presence of atmospheric noble gases (inherited from paleo-subduction) in the Lanzarote lithospheric mantle. In most of the samples, the variability of ^{4}He/^{40}Ar ratios, which are lower than the reported for El Hierro nodules, decrease from Ol to Opx when the

Mg# increases. This observation has been linked with a partial melting trend that supports the residual character of the spinel harzburgites and dunite here studied.

Rc/Ra values indicate a more radiogenic mantle (5.97±0.44 Ra; 2σ, n = 13) than in El Hierro (7.45±0.26 Ra; 2σ, n = 14). This evidence proves the systematic west to east decrease in ${}^{3}He/{}^{4}He$ ratios along the Canary Islands (from El Hierro to Lanzarote). Considering that fluid inclusions in mantle xenoliths better preserve the isotopic composition of the local mantle, these results point to a source heterogeneity explained by the occurrence of an EM component beneath eastern islands coming from the African SCLM. Finally, $\delta^{13}C$ values are more positive than the MORB-like upper mantle (-2.25‰ < $\delta^{13}C$ < +0.8‰) and vary in a similar range of El Hierro xenoliths. This evidence indicates that the recycled crustal carbon (introduced by the HIMU-like mantle plume) is presumably a regional characteristic of the upper mantle located beneath the Canary Islands.

CHAPTER 10. FINAL CONSIDERATIONS

In this dissertation, I studied the isotopic composition of volatiles (noble gas and CO_2 isotopes) in fluid inclusions hosted in mantle xenoliths from Mexico and the Canary Islands, and a few arc lavas from Sierra Chichinautzin Volcanic Field, a Quaternary monogenetic field located in the Transmexican Volcanic Belt (TMVB). The main outcomes of this study are summarized below:

- In the case of the Mexican Basin and Range, noble gases coupled to petrological data showed a very complex evolution of the local mantle, which has been influenced by the subduction of the Farallon plate and the subsequent tectonic reorganization of the western margin of the North American plate. $^3He/^4He$ ratios measured in three Mexican localities (VESVF = 7.39 ± 0.14 Ra (1σ, n = 30), DVF= 8.39 ± 0.24 Ra (1σ, n = 10), SQVF = 7.43 ± 0.19 Ra (1σ, n = 1)) revealed isotopic differences likely associated with the timing of metasomatic events occurred during the rollback of the Farallon slab and the following evolution of the lithospheric mantle according to a steady-state model. Comparing with the VESVF samples, DVF and SQVF nodules describe a more impacted mantle by atmospheric-derived noble gases. Ne and Ar isotopes revealed the occurrence of different extents of mantle contamination by the infiltration of atmosphere-derived fluids derived from the subducted slab; those areas closer to the western margin of the North American plate (for example, the localities where the DVF and SQVF are emplaced) seems to be more impacted by atmospheric contamination. On average SQVF xenoliths show $^4He/^{20}Ne$ = 28.86 ± 4.36 and $^{40}Ar/^{36}Ar$ = 420.44 ± 67.59, the DVF xenoliths exhibit $^4He/^{20}Ne$ = 73.18 ± 50.07 and $^{40}Ar/^{36}Ar$ = 462.52 ± 128.51 while the VESVF xenoliths show the highest values with $^4He/^{20}Ne$ = 1716.80 ± 2416.13 and $^{40}Ar/^{36}Ar$ = 1962.54 ±1958.53 (1σ). This is corroborated by the increase of oxygen fugacity in mantle xenoliths towards the paleotrench (observed by other authors), that indicates the existence of a more oxidized mantle in the west possibly related to the interaction with crustal fluids from the oceanic slab. Petrography and Raman microspectroscopy analysis in VESVF xenoliths showed the presence of primary carbonates in inclusions and glass veins that testified a metasomatic event driven by silicate carbonate-rich melts at mantle depths. The analysis of CO_2 isotopes (with $\delta^{13}C$ ratios between −0.97 and −2.86‰) revealed that such carbonates are possible linked to a crustal reservoir located in the local mantle derived from paleosubduction events (in this case, the Farallon subduction).

- The SCN lavas belonging to the TMVB show 3He/4He ratios (7.24±0.33Ra; 1σ, n = 4) similar to those reported in the VESVF and other arc volcanoes such as Ceboruco, Colima and Popocatépetl. The SCN olivines likely reflect a subarc mantle with similar noble gas composition to that observed for the VESVF mantle. Probably both localities evolved under similar geodynamic conditions due to their proximity. This scenario would have changed during the tectonic reorganization of the western margin of the North American plate (30 - 7 Ma ago). On the other hand, SCN olivines show MORB-like $\delta^{13}C$ (between -6.3 and -5.0‰) which are explained by magmatic degassing or by the fusion of a different mantle domain characterized by noble gas compositions similar to those reported in the VESVF xenoliths, but different carbon signatures evidently not affected by subduction-related carbonate recycling.

- The Canary Islands offers a completely different perspective of how the mantle changes in response of the influence of both a mantle plume and a paleo-subduction process. Like Mexico, Ne and Ar isotopes measured in ultramafic xenoliths from El Hierro and Lanzarote reflect the occurrence of atmospheric fluids in the local mantle likely recycled from oceanic

crust subducted 1-2 Ga ago. Nodules from both localities show low $^{40}Ar/^{36}Ar$ ratios relative to the MORB-like range (El Hierro: 2523.50 ± 1534.39, Lanzarote: 2789.70 ± 2003.70 (1σ)). The recycling of atmospheric noble gases seems to be a global feature since this phenomenon has been reported in other geodynamic contexts with mantle xenoliths such as Mexico, Europe, West Antarctic Rift System (WARS), Eastern Australia, Kamchatka, Red sea region, N/S Kenya rifts and Ethiopia (Afar). Regarding $^{3}He/^{4}He$ results, a clear west-to-east decrease in helium ratios was observed in ultramafic and volcanic rocks and in superficial emissions along the archipelago. This decrease has been attributed to the existence of different mantle domains that mix at different proportions and create the isotopic complexity observed in volcanic materials: plume, MORB, HIMU and EM. In terms of helium, the plume endmember has only been reported for superficial emissions at La Palma. In this thesis El Hierro shows a MORB-like signature (Rc/Ra = 7.45±0.26 Ra; 2σ, n = 14) similar to that observed in most of La Palma phenocrysts and in La Gomera, while Lanzarote manifests a more radiogenic nature (Rc/Ra = 5.97±0.44 Ra; 2σ, n = 13) similar to that previously reported for Gran Canaria lavas and xenoliths.

- This dissertation reinforces the idea that $^{3}He/^{4}He$ ratios are suitable tools to distinguish plume, MORB and more radiogenic reservoirs in the mantle, however, there exists an important limitation when trying to distinguish EM or HIMU endmembers. For the Canary Islands, although low $^{3}He/^{4}He$ ratios in the eastern islands are possibly associated with an EM component inherited from the African SCLM (as proposed for different authors whose models are based on the study of Sr-Pb-Nd isotopes), it is not possible to discard the effect of HIMU contribution a mantle depths, or the influence of superficial processes such as magma ageing and/or crustal assimilation that potentially can alter the original helium signatures of mantle xenoliths and the host magma.

- The most important finding regarding the study of fluid inclusions in mantle xenoliths from El Hierro and Lanzarote was the recognition of a crustal carbon component in the mantle beneath Canary Islands, showing for the first time the presence of a HIMU reservoir based not only on radiogenic isotopes evidences. The similarity between El Hierro and Lanzarote datasets implies that the recycling of crustal materials in the local mantle is a regional characteristic that extends from the easternmost to the westernmost island as well as the HIMU endmember. This component can reach extreme positive values ($\delta^{13}C$ from -1.1‰ to +0.96‰) at relatively comparable MORB-like $CO_2/^{3}He$ ratios what suggest that this carbon derives from both sedimentary materials and carbonates hosted in recycled altered oceanic crust (AOC) and/or oceanic lithosphere (OL).

- As observed for Mexico and Canary Islands, there is a clear decoupling of helium and carbon signatures since these seem to variate independently from each other. This thesis also reinforces the hypothesis that the lithospheric mantle is not a homogeneous reservoir either beneath continental or oceanic crust, as previously thought for the SCLM, and that its evolution is extremely linked with the local geodynamics and the occurrence of metasomatic processes.

- The findings obtained in Mexican and Canary Islands undoubtedly offer a new perspective of how the Earth's mantle works but also leave some questions still unsolved that must be assessed in the future. For instance, why does the decoupling of helium from CO_2 signatures in both localities occur? What is the main mechanism that governs the extent of crustal

contamination in the mantle? And what controls the difference in $\delta^{13}C$ between different mineralogical phases (e.g., olivines and pyroxenes)?

REFERENCES

Abratis, M., Schmincke, H.-U., Hansteen, T., 2002. Composition and evolution of submarine volcanic rocks from the central and western Canary Islands. Int. J. Earth Sci. 91, 562–582. https://doi.org/10.1007/s00531-002-0286-7

Ackerman, L., ŠpaČek, P., Magna, T., Ulrych, J., Svojtka, M., Hegner, E., Balogh, K., 2013. Alkaline and Carbonate-rich Melt Metasomatism and Melting of Subcontinental Lithospheric Mantle: Evidence from Mantle Xenoliths, NE Bavaria, Bohemian Massif. J. Petrol. 54, 2597–2633. https://doi.org/10.1093/petrology/egt059

Admunsen, H.E.F., 1987. Peridotite xenoliths from Gran Canaria,Canary Islands; evidence for metasomatic processes and partial melting in the lower oceanic crust. Neues Jahrb. Für Mineral. Abh. 156, 121–140.

Aiuppa, A., Fischer, T.P., Plank, T., Bani, P., 2019. CO2 flux emissions from the Earth's most actively degassing volcanoes, 2005–2015. Sci. Rep. 9, 5442. https://doi.org/10.1038/s41598-019-41901-y

Aiuppa, A., Fischer, T.P., Plank, T., Robidoux, P., Di Napoli, R., 2017. Along-arc, inter-arc and arc-to-arc variations in volcanic gas CO2/ST ratios reveal dual source of carbon in arc volcanism. Earth-Sci. Rev. 168, 24–47. https://doi.org/10.1016/j.earscirev.2017.03.005

Albritton, C.C., 1958. Quaternary stratigraphy of the Guadiana valley, Durango, Mexico. Geol. Soc. Am. Bull. 69, 1197. https://doi.org/10.1130/0016-7606(1958)69[1197:QSOTGV]2.0.CO;2

Aldanmaz, E., 2012. Osmium isotope and highly siderophile element geochemistry of mantle xenoliths from NW Turkey: implications for melt depletion and metasomatic history of the sub-continental lithospheric mantle. Int. Geol. Rev. 54, 799–815. https://doi.org/10.1080/00206814.2011.581799

Alemayehu, M., Zhang, H.-F., Sakyi, P.A., 2017. Nature and evolution of lithospheric mantle beneath the southern Ethiopian rift zone: evidence from petrology and geochemistry of mantle xenoliths. Int. J. Earth Sci. 106, 939–958. https://doi.org/10.1007/s00531-016-1342-z

Alonso, M., Padrón, E., Sumino, H., Hernandez, P., Melián, G., Asensio-Ramos, M., Rodriguez, F., Padilla, G., García-Merino, M., Amonte, C., Pérez, N., 2019. Heat and Helium-3 Fluxes from Teide Volcano, Canary Islands, Spain. Geofluids 2019, 1–12. https://doi.org/10.1155/2019/3983864

Alt, J.C., Schwarzenbach, E.M., Früh-Green, G.L., Shanks, W.C., Bernasconi, S.M., Garrido, C.J., Crispini, L., Gaggero, L., Padrón-Navarta, J.A., Marchesi, C., 2013. The role of serpentinites in cycling of carbon and sulfur: Seafloor serpentinization and subduction metamorphism. Lithos, Serpentinites from mid-oceanic ridges to subduction 178, 40–54. https://doi.org/10.1016/j.lithos.2012.12.006

Alt, J.C., Shanks, W.C., 2003. Serpentinization of abyssal peridotites from the MARK area, Mid-Atlantic Ridge: sulfur geochemistry and reaction modeling. Geochim. Cosmochim. Acta 67, 641–653. https://doi.org/10.1016/S0016-7037(02)01142-0

Alt, J.C., Teagle, D.A.H., 1999. The uptake of carbon during alteration of ocean crust. Geochim. Cosmochim. Acta 63, 1527–1535. https://doi.org/10.1016/S0016-7037(99)00123-4

Andersen, T., Neumann, E.-R., 2001. Fluid inclusions in mantle xenoliths. Lithos 55, 301–320. https://doi.org/10.1016/S0024-4937(00)00049-9

Anguita, F., Hernán, F., 2000. The Canary Islands origin: a unifying model. J. Volcanol. Geotherm. Res. 103, 1–26. https://doi.org/10.1016/S0377-0273(00)00195-5

Anguita, F., Hernan, F., 1975. A propagating fracture model versus a hot spot origin for the Canary islands. Earth Planet. Sci. Lett. 27, 11–19. https://doi.org/10.1016/0012-821X(75)90155-7

Arai, S., 1994. Characterization of spinel peridotites by olivine-spinel compositional relationships: Review and interpretation. Chem. Geol. 113, 191–204. https://doi.org/10.1016/0009-2541(94)90066-3

Arai, S., Abe, N., Ishimaru, S., 2007. Mantle peridotites from the Western Pacific. Gondwana Res. 11, 180–199. https://doi.org/10.1016/j.gr.2006.04.004

Arai, S., Ishimaru, S., 2008. Insights into Petrological Characteristics of the Lithosphere of Mantle Wedge beneath Arcs through Peridotite Xenoliths: a Review. J. Petrol. 49, 665–695. https://doi.org/10.1093/petrology/egm069

Araña, V., Ortiz, R., 1991. The Canary Islands: Tectonics, Magmatism and Geodynamic Framework, in: Kampunzu, A.B., Lubala, R.T. (Eds.), Magmatism in Extensional Structural Settings. Springer Berlin Heidelberg, Berlin, Heidelberg, pp. 209–249. https://doi.org/10.1007/978-3-642-73966-8_9

Aranda-Gómez, J., Luhr, J.F., 1996. Origin of the Joya Honda maar, San Luis Potosí, México. J. Volcanol. Geotherm. Res. 74, 1–18. https://doi.org/10.1016/S0377-0273(96)00044-3

Aranda-Gómez, J.J., Henry, C.D., F. Luhr, J., 2000. Evolución tectonomagmática post-paleocénica de la Sierra Madre Occidental y de la porción meridional de la provincia tectónica de Cuencas y Sierras, México. Bol. Soc. Geológica Mex. 53, 59–71. https://doi.org/10.18268/BSGM2000v53n1a3

Aranda-Gómez, J.J., Luhr, J.F., Housh, T.B., Valdez-Moreno, G., Chávez-Cabello, G., 2007. Late Cenozoic intraplate-type volcanism in central and northern México: A review, in: Geology of México: Celebrating the Centenary of the Geological Society of México. Geological Society of America. https://doi.org/10.1130/2007.2422(04)

Aranda-Gómez, J.J., Luhr, J.F., Pier, G., 1992. The La Breña — El Jagüey Maar Complex, Durango, México: I. Geological evolution. Bull. Volcanol. 54, 393–404. https://doi.org/10.1007/BF00312321

Aranda-Gómez, J.J., Ortega-Gutiérrez, F., 1987. Mantle xenoliths in México, in: Mantle Xenoliths. John Wiley, New York, pp. 75–84.

Atwater, T., 1989. Plate tectonic history of the northeast Pacific and western North America, in: Winterer, E.L., Hussong, D.M., Decker, R.W. (Eds.), The Eastern Pacific Ocean and Hawaii. Geological Society of America, North America, pp. 21–72. https://doi.org/10.1130/DNAG-GNA-N.21

Avice, G., Marty, B., 2020. Perspectives on Atmospheric Evolution from Noble Gas and Nitrogen Isotopes on Earth, Mars & Venus. Space Sci. Rev. 216, 36. https://doi.org/10.1007/s11214-020-00655-0

Ballentine, C.J., Burnard, P.G., 2002. Production, Release and Transport of Noble Gases in the Continental Crust. Rev. Mineral. Geochem. 47, 481–538. https://doi.org/10.2138/rmg.2002.47.12

Barboza-Gudino, J.R., Tristán-González, M., Torres-Hernández, J.R., 1999. Tectonic setting of pre-Oxfordian units from central and northeastern Mexico: A review, in: Special Paper 340: Mesozoic Sedimentary and Tectonic History of North-Central Mexico. Geological Society of America, pp. 197–210. https://doi.org/10.1130/0-8137-2340-X.197

Basu, A.R., 1977. Textures, microstructures and deformation of ultramafic xenoliths from San Quintin, Baja California. Tectonophysics 43, 213–246. https://doi.org/10.1016/0040-1951(77)90118-4

Beccaluva, L., Azzouni-Sekkal, A., Benhallou, A., Bianchini, G., Ellam, R.M., Marzola, M., Siena, F., Stuart, F.M., 2007. Intracratonic asthenosphere upwelling and lithosphere rejuvenation beneath the Hoggar swell (Algeria): Evidence from HIMU metasomatised lherzolite mantle xenoliths. Earth Planet. Sci. Lett. 260, 482–494. https://doi.org/10.1016/j.epsl.2007.05.047

Beccaluva, L., Bianchini, G., Ellam, R.M., Marzola, M., Oun, K.M., Siena, F., Stuart, F.M., 2008. The role of HIMU metasomatic components in the North African lithospheric mantle: petrological evidence from the Gharyan lherzolite xenoliths, NW Libya. Geol. Soc. Lond. Spec. Publ. 293, 253–277. https://doi.org/10.1144/SP293.12

Bekaert, D.V., Turner, S.J., Broadley, M.W., Barnes, J.D., Halldórsson, S.A., Labidi, J., Wade, J., Walowski, K.J., Barry, P.H., 2021. Subduction-Driven Volatile Recycling: A Global Mass Balance. Annu. Rev. Earth Planet. Sci. 49, 37–70. https://doi.org/10.1146/annurev-earth-071620-055024

Bell, D.R., Rossman, G.R., 1992. Water in Earth's Mantle: The Role of Nominally Anhydrous Minerals. Science 255, 1391–1397. https://doi.org/10.1126/science.255.5050.1391

Bergman, S.C., Dubessy, J., 1984. CO_2-CO fluid inclusions in a composite peridotite xenolith: implications for upper mantle oxygen fugacity. Contrib. Mineral. Petrol. 85, 1–13. https://doi.org/10.1007/BF00380216

Bishop, F.C., Smith, J.V., Dawson, J.B., 1975. PENTLANDITE–MAGNETITE INTERGROWTH IN DE BEERS SPINEL LHERZOLITE: REVIEW OF SULPHIDES IN NODULES, in: Physics and Chemistry of the Earth. Elsevier, pp. 323–337. https://doi.org/10.1016/B978-0-08-018017-5.50029-8

Bodinier, J.-L., 2004. Silicate, Hydrous and Carbonate Metasomatism at Lherz, France: Contemporaneous Derivatives of Silicate Melt-Harzburgite Reaction. J. Petrol. 45, 299–320. https://doi.org/10.1093/petrology/egg107

Bonadiman, C., Beccaluva, L., Coltorti, M., Siena, F., 2005. Kimberlite-like Metasomatism and 'Garnet Signature' in Spinel-peridotite Xenoliths from Sal, Cape Verde Archipelago: Relics of a Subcontinental Mantle Domain within the Atlantic Oceanic Lithosphere? J. Petrol. 46, 2465–2493. https://doi.org/10.1093/petrology/egi061

Boudoire, G., Rizzo, A.L., Arienzo, I., Di Muro, A., 2020. Paroxysmal eruptions tracked by variations of helium isotopes: inferences from Piton de la Fournaise (La Réunion island). Sci. Rep. 10, 9809. https://doi.org/10.1038/s41598-020-66260-x

Boudoire, G., Rizzo, A.L., Di Muro, A., Grassa, F., Liuzzo, M., 2018. Extensive CO2 degassing in the upper mantle beneath oceanic basaltic volcanoes: First insights from Piton de la Fournaise volcano (La Réunion Island). Geochim. Cosmochim. Acta 235, 376–401. https://doi.org/10.1016/j.gca.2018.06.004

Broadley, M.W., Ballentine, C.J., Chavrit, D., Dallai, L., Burgess, R., 2016. Sedimentary halogens and noble gases within Western Antarctic xenoliths: Implications of extensive volatile recycling to the sub continental lithospheric mantle. Geochim. Cosmochim. Acta 176, 139–156. https://doi.org/10.1016/j.gca.2015.12.013

Buikin, A., Trieloff, M., Hopp, J., Althaus, T., Korochantseva, E., Schwarz, W.H., Altherr, R., 2005. Noble gas isotopes suggest deep mantle plume source of late Cenozoic mafic alkaline volcanism in Europe. Earth Planet. Sci. Lett. 230, 143–162. https://doi.org/10.1016/j.epsl.2004.11.001

Bunge, H.-P., Grand, S.P., 2000. Mesozoic plate-motion history below the northeast Pacific Ocean from seismic images of the subducted Farallon slab. Nature 405, 337–340. https://doi.org/10.1038/35012586

Burnard, P. (Ed.), 2013. The noble gases as geochemical tracers, Advances in isotope geochemistry. Springer, Heidelberg ; New York.

Burnard, P., 2004. Diffusive fractionation of noble gases and helium isotopes during mantle melting. Earth Planet. Sci. Lett. 220, 287–295. https://doi.org/10.1016/S0012-821X(04)00060-3

Burnard, P., Graham, D., Turner, G., 1997. Vesicle-Specific Noble Gas Analyses of "Popping Rock": Implications for Primordial Noble Gases in Earth. Science 276, 568–571. https://doi.org/10.1126/science.276.5312.568

Burnard, P.G., Farley, K.A., Turner, G., 1998. Multiple fluid pulses in a Samoan harzburgite. Chem. Geol. 147, 99–114. https://doi.org/10.1016/S0009-2541(97)00175-7

Canil, D., 2002. Vanadium in peridotites, mantle redox and tectonic environments: Archean to present. Earth Planet. Sci. Lett. 195, 75–90. https://doi.org/10.1016/S0012-821X(01)00582-9

Carnevale, G., Caracausi, A., Correale, A., Italiano, L., Rotolo, S., 2021. An Overview of the Geochemical Characteristics of Oceanic Carbonatites: New Insights from Fuerteventura Carbonatites (Canary Islands). Minerals 11, 203. https://doi.org/10.3390/min11020203

Carracedo, J.C., Day, S., Guillou, H., Rodríguez Badiola, E., Canas, J.A., Pérez Torrado, F.J., 1998. Hotspot volcanism close to a passive continental margin: the Canary Islands. Geol. Mag. 135, 591–604. https://doi.org/10.1017/S0016756898001447

Carrillo-Bravo, J., 1971. La plataforma de Valles-San Luis Potosí. Boletín de la Asociación Mexicana de Geólogos Petroleros. Boletín de la Asociación Mexicana de Geólogos Petroleros 23, 100.

Carteret, C., Dandeu, A., Moussaoui, S., Muhr, H., Humbert, B., Plasari, E., 2009. Polymorphism Studied by Lattice Phonon Raman Spectroscopy and Statistical Mixture Analysis Method. Application to Calcium Carbonate Polymorphs during Batch Crystallization. Cryst. Growth Des. 9, 807–812. https://doi.org/10.1021/cg800368u

Clarke, W.B., Jenkins, W.J., Top, Z., 1976. Determination of tritium by mass spectrometric measurement of 3He. Int. J. Appl. Radiat. Isot. 27, 515–522. https://doi.org/10.1016/0020-708X(76)90082-X

Coello, J., Cantagrel, J.-M., Hernán, F., Fúster, J.-M., Ibarrola, E., Ancochea, E., Casquet, C., Jamond, C., Díaz de Téran, J.-R., Cendrero, A., 1992. Evolution of the eastern volcanic ridge of the Canary Islands based on new K‐Ar data. J. Volcanol. Geotherm. Res. 53, 251–274. https://doi.org/10.1016/0377-0273(92)90085-R

Cohen, R.S., O'Nions, R.K., 1982. Identification of recycled continental material in the mantle from Sr, Nd and Pb isotope investigations. Earth Planet. Sci. Lett. 61, 73–84. https://doi.org/10.1016/0012-821X(82)90040-1

Colombo, E., 2020. Petrological study of peridotite xenoliths of El Hierro island: characterization of the lithospheric mantle beneath the Canary Islands (Spain) (Master's Thesis). University of Milano-Bicocca, Milan.

Coltorti, M., Beccaluva, L., Bonadiman, C., Salvini, L., Siena, F., 2000. Glasses in mantle xenoliths as geochemical indicators of metasomatic agents. Earth Planet. Sci. Lett. 183, 303–320. https://doi.org/10.1016/S0012-821X(00)00274-0

Coltorti, M., Bonadiman, C., Hinton, R.W., Siena, F., Upton, B.G.J., 1999. Carbonatite Metasomatism of the Oceanic Upper Mantle: Evidence from Clinopyroxenes and Glasses in Ultramafic Xenoliths of Grande Comore, Indian Ocean. J. Petrol. 40, 133–165. https://doi.org/10.1093/petroj/40.1.133

Coltorti, M., Downes, H., Grégoire, M., O'Reilly, S.Y. (Eds.), 2010. Petrological evolution of the European lithospheric mantle, Geological Society special publication. Presented at the European Mantle Workshop, Geological Society, London.

Comin-Chiaramonti, P., Lucassen, F., Girardi, V.A.V., De Min, A., Gomes, C.B., 2010. Lavas and their mantle xenoliths from intracratonic Eastern Paraguay (South America Platform) and Andean Domain, NW-Argentina: a comparative review. Mineral. Petrol. 98, 143–165. https://doi.org/10.1007/s00710-009-0061-6

Conceição, R.V., Mallmann, G., Koester, E., Schilling, M., Bertotto, G.W., Rodriguez-Vargas, A., 2005. Andean subduction-related mantle xenoliths: Isotopic evidence of Sr–Nd decoupling during metasomatism. Lithos 82, 273–287. https://doi.org/10.1016/j.lithos.2004.09.022

Correale, A., Martelli, M., Paonita, A., Rizzo, A., Brusca, L., Scribano, V., 2012. New evidence of mantle heterogeneity beneath the Hyblean Plateau (southeast Sicily, Italy) as inferred from noble gases and geochemistry of ultramafic xenoliths. Lithos 132–133, 70–81. https://doi.org/10.1016/j.lithos.2011.11.007

Correale, A., Paonita, A., Rizzo, A., Grassa, F., Martelli, M., 2015. The carbon-isotope signature of ultramafic xenoliths from the Hyblean Plateau (southeast Sicily, Italy): Evidence of mantle heterogeneity. Geochem. Geophys. Geosystems 16, 600–611. https://doi.org/10.1002/2014GC005656

Correale, A., Pelorosso, B., Rizzo, A.L., Coltorti, M., Italiano, F., Bonadiman, C., Giacomoni, P.P., 2019. The nature of the West Antarctic Rift System as revealed by noble gases in mantle minerals. Chem. Geol. 524, 104–118. https://doi.org/10.1016/j.chemgeo.2019.06.020

Correale, A., Rizzo, A.L., Barry, P.H., Lu, J., Zheng, J., 2016. Refertilization of lithospheric mantle beneath the Yangtze craton in south-east China: Evidence from noble gases geochemistry. Gondwana Res. 38, 289–303. https://doi.org/10.1016/j.gr.2016.01.003

Craig, H., Clarke, W.B., Beg, M.A., 1975. Excess 3He in deep water on the East Pacific Rise. Earth Planet. Sci. Lett. 26, 125–132. https://doi.org/10.1016/0012-821X(75)90079-5

Cserna, Z. de, 1989. An outline of the geology of Mexico, in: Bally, A.W., Palmer, A.R. (Eds.), The Geology of North America—An Overview. Geological Society of America, pp. 233–264. https://doi.org/10.1130/DNAG-GNA-A.233

Czuppon, G., Matsumoto, T., Handler, M.R., Matsuda, J., 2009. Noble gases in spinel peridotite xenoliths from Mt Quincan, North Queensland, Australia: Undisturbed MORB-type noble gases in the subcontinental lithospheric mantle. Chem. Geol. 266, 19–28. https://doi.org/10.1016/j.chemgeo.2009.03.029

Dai, H.-K., Zheng, J.-P., 2019. Mantle xenoliths and host basalts record the Paleo-Asian oceanic materials in the mantle wedge beneath northwest North China Craton. Solid Earth Sci. 4, 150–158. https://doi.org/10.1016/j.sesci.2019.09.001

Dasgupta, R., Hirschmann, M.M., 2010. The deep carbon cycle and melting in Earth's interior. Earth Planet. Sci. Lett. 298, 1–13. https://doi.org/10.1016/j.epsl.2010.06.039

Dávalos-Elizondo, M.G., Aranda Gómez, J.J., Levresse, G., Cervantes-de la Cruz, K.E., 2016. Química mineral y geoquímica de xenolitos del manto del campo volcánico Santo Domingo, San Luis Potosí:

evidencias de procesos metasomáticos del manto bajo porciones de la Mesa Central, México. Revista Mexicana de Ciencias Geológicas 33, 81–104.

Davies, G.F., 2011. Mantle Convection for Geologists. Cambridge University Press, Cambridge. https://doi.org/10.1017/CBO9780511973413

Dawson, J.B., 2002. Metasomatism and Partial Melting in Upper-Mantle Peridotite Xenoliths from the Lashaine Volcano, Northern Tanzania. J. Petrol. 43, 1749–1777. https://doi.org/10.1093/petrology/43.9.1749

Day, J.M.D., Barry, P.H., Hilton, D.R., Burgess, R., Pearson, D.G., Taylor, L.A., 2015. The helium flux from the continents and ubiquity of low-3He/4He recycled crust and lithosphere. Geochim. Cosmochim. Acta 153, 116–133. https://doi.org/10.1016/j.gca.2015.01.008

Day, J.M.D., Harvey, R.P., Hilton, D.R., 2019. Melt-modified lithosphere beneath Ross Island and its role in the tectono-magmatic evolution of the West Antarctic Rift System. Chem. Geol. 518, 45–54. https://doi.org/10.1016/j.chemgeo.2019.04.012

Day, J.M.D., Hilton, D.R., 2020. Heterogeneous mantle-derived helium isotopes in the CanaryIslands and other ocean islands. Geology. https://doi.org/10.1130/G47676.1

Day, J.M.D., Hilton, D.R., 2011. Origin of 3He/4He ratios in HIMU-type basalts constrained from Canary Island lavas. Earth Planet. Sci. Lett. 305, 226–234. https://doi.org/10.1016/j.epsl.2011.03.006

Day, J.M.D., Pearson, D.G., Macpherson, C.G., Lowry, D., Carracedo, J.C., 2010. Evidence for distinct proportions of subducted oceanic crust and lithosphere in HIMU-type mantle beneath El Hierro and La Palma, Canary Islands. Geochim. Cosmochim. Acta 74, 6565–6589. https://doi.org/10.1016/j.gca.2010.08.021

Deines, P., 2002. The carbon isotope geochemistry of mantle xenoliths. Earth-Sci. Rev. 58, 247–278. https://doi.org/10.1016/S0012-8252(02)00064-8

Deines, P., 1992. Mantle Carbon: Concentration, Mode of Occurrence, and Isotopic Composition, in: Schidlowski, M., Golubic, S., Kimberley, M.M., McKirdy, D.M., Trudinger, P.A. (Eds.), Early Organic Evolution. Springer Berlin Heidelberg, Berlin, Heidelberg, pp. 133–146. https://doi.org/10.1007/978-3-642-76884-2_10

Demant, A., Cocheme, J.J., Delpretti, P., Piguet, P., 1989. Geology and petrology of the Tertiary volcanics of the northwestern Sierra Madre Occidental, Mexico. Bull. Société Géologique Fr. V, 737–748. https://doi.org/10.2113/gssgfbull.V.4.737

Demény, A., Ahijado, A., Casillas, R., Vennemann, T.W., 1998. Crustal contamination and fluid/rock interaction in the carbonatites of Fuerteventura (Canary Islands, Spain): a C, O, H isotope study. Lithos 44, 101–115. https://doi.org/10.1016/S0024-4937(98)00050-4

Demény, A., Dallai, L., Frezzotti, M.-L., Vennemann, T.W., Embey-Isztin, A., Dobosi, G., Nagy, G., 2010. Origin of CO2 and carbonate veins in mantle-derived xenoliths in the Pannonian Basin. Lithos 117, 172–182. https://doi.org/10.1016/j.lithos.2010.02.013

Demény, A., Vennemann, T.W., Hegner, E., Nagy, G., Milton, J.A., Embey-Isztin, A., Homonnay, Z., Dobosi, G., 2004. Trace element and C–O–Sr–Nd isotope evidence for subduction-related carbonate–silicate melts in mantle xenoliths (Pannonian Basin, Hungary). Lithos 75, 89–113. https://doi.org/10.1016/j.lithos.2003.12.016

Dickinson, W.R., 2002. The Basin and Range Province as a Composite Extensional Domain. Int. Geol. Rev. 44, 1–38. https://doi.org/10.2747/0020-6814.44.1.1

Downes, H., 1997. Shallow Continental Lithospheric Mantle Heterogeneity — Petrological Constraints, in: Fuchs, K. (Ed.), Upper Mantle Heterogeneities from Active and Passive Seismology. Springer Netherlands, Dordrecht, pp. 295–308. https://doi.org/10.1007/978-94-015-8979-6_29

Dunai, T.J., 2010. Cosmogenic Nuclides: Principles, Concepts and Applications in the Earth Surface Sciences. Cambridge University Press, Cambridge. https://doi.org/10.1017/CBO9780511804519

Dunai, T.J., Baur, H., 1995. Helium, neon, and argon systematics of the European subcontinental mantle: Implications for its geochemical evolution. Geochim. Cosmochim. Acta 59, 2767–2783. https://doi.org/10.1016/0016-7037(95)00172-V

Dunai, T.J., Porcelli, D., 2002. Storage and Transport of Noble Gases in the Subcontinental Lithosphere. Rev. Mineral. Geochem. 47, 371–409. https://doi.org/10.2138/rmg.2002.47.10

Eguiluz de Antuñano, S., Aranda García, M., Marrett, R., 2000. Tectónica de la Sierra Madre Oriental, México. Bol. Soc. Geológica Mex. 53, 1–26. https://doi.org/10.18268/BSGM2000v53n1a1

Einstein, A., 2007. The nature and cause of mantle heterogeneity, in: New Theory of the Earth. Cambridge University Press, Cambridge, p. 6.

Faccini, B., Rizzo, A.L., Bonadiman, C., Ntaflos, T., Seghedi, I., Grégoire, M., Ferretti, G., Coltorti, M., 2020. Subduction-related melt refertilisation and alkaline metasomatism in the Eastern Transylvanian Basin lithospheric mantle: Evidence from mineral chemistry and noble gases in fluid inclusions. Lithos 364–365, 105516. https://doi.org/10.1016/j.lithos.2020.105516

Farley, K.A., Neroda, E., 1998. NOBLE GASES IN THE EARTH'S MANTLE. Annu. Rev. Earth Planet. Sci. 26, 189–218. https://doi.org/10.1146/annurev.earth.26.1.189

Farley, K.A., Poreda, R.J., 1993. Mantle neon and atmospheric contamination. Earth Planet. Sci. Lett. 114, 325–339. https://doi.org/10.1016/0012-821X(93)90034-7

Faure, G., 1987. Principles of Isotope Geology. Geol. Mag. 124, 594–595. https://doi.org/10.1017/S0016756800017453

Ferrari, L., López-Martínez, M., Aguirre-Díaz, G., Carrasco-Núñez, G., 1999. Space-time patterns of Cenozoic arc volcanism in central Mexico: From the Sierra Madre Occidental to the Mexican Volcanic Belt. Geology 27, 303–306. https://doi.org/10.1130/0091-7613(1999)027<0303:STPOCA>2.3.CO;2

Ferrari, L., Orozco-Esquivel, T., Manea, V., Manea, M., 2012. The dynamic history of the Trans-Mexican Volcanic Belt and the Mexico subduction zone. Tectonophysics 522–523, 122–149. https://doi.org/10.1016/j.tecto.2011.09.018

Fix, J.E., 1975. The Crust and Upper Mantle of Central Mexico. Geophys. J. Int. 43, 453–499. https://doi.org/10.1111/j.1365-246X.1975.tb00643.x

Foley, S.F., Fischer, T.P., 2017. An essential role for continental rifts and lithosphere in the deep carbon cycle. Nat. Geosci. 10, 897–902. https://doi.org/10.1038/s41561-017-0002-7

Frezzotti, M., Peccerillo, A., 2007. Diamond-bearing COHS fluids in the mantle beneath Hawaii. Earth Planet. Sci. Lett. 262, 273–283. https://doi.org/10.1016/j.epsl.2007.08.001

Frezzotti, M.L., Andersen, T., Neumann, E.-R., Simonsen, S.L., 2002a. Carbonatite melt–CO2 fluid inclusions in mantle xenoliths from Tenerife, Canary Islands: a story of trapping, immiscibility and fluid–rock interaction in the upper mantle. Lithos 64, 77–96. https://doi.org/10.1016/S0024-4937(02)00178-0

Frezzotti, M.L., Ferrando, S., 2015. The chemical behavior of fluids released during deep subduction based on fluid inclusions. Am. Mineral. 100, 352–377. https://doi.org/10.2138/am-2015-4933

Frezzotti, M.L., Ferrando, S., Tecce, F., Castelli, D., 2012b. Water content and nature of solutes in shallow-mantle fluids from fluid inclusions. Earth Planet. Sci. Lett. 351–352, 70–83. https://doi.org/10.1016/j.epsl.2012.07.023

Frezzotti, M.L., Peccerillo, A., Panza, G., 2009. Carbonate metasomatism and CO2 lithosphere–asthenosphere degassing beneath the Western Mediterranean: An integrated model arising from petrological and geophysical data. Chem. Geol. 262, 108–120. https://doi.org/10.1016/j.chemgeo.2009.02.015

Frezzotti, M.L., Tecce, F., Casagli, A., 2012a. Raman spectroscopy for fluid inclusion analysis. J. Geochem. Explor. 112, 1–20. https://doi.org/10.1016/j.gexplo.2011.09.009

Frezzotti, M.-L., Touret, J.L.R., 2014. CO2, carbonate-rich melts, and brines in the mantle. Geosci. Front. 5, 697–710. https://doi.org/10.1016/j.gsf.2014.03.014

Frezzotti, M.-L., Touret, J.L.R., Neumann, E.-R., 2002b. Ephemeral carbonate melts in the upper mantle: carbonate-silicate immiscibility in microveins and inclusions within spinel peridotite xenoliths, La Gomera, Canary Islands. Eur. J. Mineral. 14, 891–904. https://doi.org/10.1127/0935-1221/2002/0014-0891

Fuster, J.M., Cendrero, A., Gastesi, E., Ibanola, E., Lopez-Ruiz, J., 1968. Geology and Volcanology of the Canary Islands-Fuerteventura. Consejo Sup. Invest. Cient., Madrid.

Gautheron, C., Moreira, M., 2002. Helium signature of the subcontinental lithospheric mantle. Earth Planet. Sci. Lett. 199, 39–47. https://doi.org/10.1016/S0012-821X(02)00563-0

Gautheron, C., Moreira, M., Allègre, C., 2005a. He, Ne and Ar composition of the European lithospheric mantle. Chem. Geol. 217, 97–112. https://doi.org/10.1016/j.chemgeo.2004.12.009

Gennaro, M.E., Grassa, F., Martelli, M., Renzulli, A., Rizzo, A.L., 2017. Carbon isotope composition of CO 2 - rich inclusions in cumulate-forming mantle minerals from Stromboli volcano (Italy). J. Volcanol. Geotherm. Res. 346, 95–103. https://doi.org/10.1016/j.jvolgeores.2017.04.001

Giuliani, A., Fiorentini, M.L., Martin, L.A.J., Farquhar, J., Phillips, D., Griffin, W.L., LaFlamme, C., 2016. Sulfur isotope composition of metasomatised mantle xenoliths from the Bultfontein kimberlite (Kimberley, South Africa): Contribution from subducted sediments and the effect of sulfide alteration on S isotope systematics. Earth Planet. Sci. Lett. 445, 114–124. https://doi.org/10.1016/j.epsl.2016.04.005

Goff, F., Janik, C.J., Werner, C., Counce, D., Stimac, J.A., Siebe, C., Love, S.P., Williams, S.N., Fischer, T.P., Johnson, L., 1998. Geochemical surveillance of magmatic volatiles at Popocatépetl volcano, Mexico. GSA Bulletin 110, 695–710. https://doi.org/10.1130/0016-7606(1998)110<0695:GSOMVA>2.3.CO;2

Goff, F., Love, S.P., Warren, R.G., Counce, D., Obenholzner, J., Siebe, C., Schmidt, S.C., 2001. Passive infrared remote sensing evidence for large, intermittent CO2 emissions at Popocatépetl volcano, Mexico. Chem. Geol. 177, 133–156. https://doi.org/10.1016/S0009-2541(00)00387-9

Gómez-Tuena, A., Orozco-Esquivel, Ma.T., Ferrari, L., 2007. Igneous petrogenesis of the Trans-Mexican Volcanic Belt, in: Alaniz-Álvarez, S.A., Nieto-Samaniego, Á.F. (Eds.), Geology of México: Celebrating the Centenary of the Geological Society of México. Geological Society of America, pp. 129–181. https://doi.org/10.1130/2007.2422(05)

Grachev, A.F., 2012. MORB-like mantle beneath Lanzerote Island, Canary Islands. Russ. J. Earth Sci. 12, 1–7. https://doi.org/10.2205/2012ES000515

Graham, D.W., 2002. Noble Gas Isotope Geochemistry of Mid-Ocean Ridge and Ocean Island Basalts: Characterization of Mantle Source Reservoirs. Rev. Mineral. Geochem. 47, 247–317. https://doi.org/10.2138/rmg.2002.47.8

Gregoire, M., 2003. Garnet Lherzolites from the Kaapvaal Craton (South Africa): Trace Element Evidence for a Metasomatic History. J. Petrol. 44, 629–657. https://doi.org/10.1093/petrology/44.4.629

Griffin, W.L., Fisher, N.I., Friedman, J., Ryan, C.G., O'Reilly, S.Y., 1999. Cr-Pyrope Garnets in the Lithospheric Mantle. I. Compositional Systematics and Relations to Tectonic Setting. J. Petrol. 40, 679–704. https://doi.org/10.1093/petroj/40.5.679

Griffin, W.L., O'Reilly, S.Y., Afonso, J.C., Begg, G.C., 2009. The Composition and Evolution of Lithospheric Mantle: a Re-evaluation and its Tectonic Implications. J. Petrol. 50, 1185–1204. https://doi.org/10.1093/petrology/egn033

Guillou, H., Carracedo, J.C., Torrado, F.P., Badiola, E.R., 1996. K-Ar ages and magnetic stratigraphy of a hotspot-induced, fast grown oceanic island: El Hierro, Canary Islands. J. Volcanol. Geotherm. Res. 73, 141–155. https://doi.org/10.1016/0377-0273(96)00021-2

Guo, J., Griffin, W.L., O'Reilly, S.Y., 1999. Geochemistry and Origin of Sulphide Minerals in Mantle Xenoliths: Qilin, Southeastern China. J. Petrol. 40, 1125–1149. https://doi.org/10.1093/petroj/40.7.1125

Gurenko, A.A., Hoernle, K.A., Hauff, F., Schmincke, H.-U., Han, D., Miura, Y.N., Kaneoka, I., 2006. Major, trace element and Nd–Sr–Pb–O–He–Ar isotope signatures of shield stage lavas from the central and western Canary Islands: Insights into mantle and crustal processes. Chem. Geol. 233, 75–112. https://doi.org/10.1016/j.chemgeo.2006.02.016

Gurenko, A.A., Hoernle, K.A., Sobolev, A.V., Hauff, F., Schmincke, H.-U., 2010. Source components of the Gran Canaria (Canary Islands) shield stage magmas: evidence from olivine composition and Sr–Nd–Pb isotopes. Contrib. Mineral. Petrol. 159, 689–702. https://doi.org/10.1007/s00410-009-0448-8

Gutmann, J.T., 1986. Origin of four and five-phase ultramafic xenoliths from Sonora, Mexico. American Mineralogist 71, 1079–1084.

Halldórsson, S.A., Hilton, D.R., Scarsi, P., Abebe, T., Hopp, J., 2014. A common mantle plume source beneath the entire East African Rift System revealed by coupled helium-neon systematics: HELIUM-NEON ISOTOPES IN THE EARS. Geophys. Res. Lett. 41, 2304–2311. https://doi.org/10.1002/2014GL059424

Harvey, J., König, S., Luguet, A., 2015. The effects of melt depletion and metasomatism on highly siderophile and strongly chalcophile elements: S–Se–Te–Re–PGE systematics of peridotite xenoliths

from Kilbourne Hole, New Mexico. Geochim. Cosmochim. Acta 166, 210–233. https://doi.org/10.1016/j.gca.2015.06.028

Hauri, E.H., Cottrell, E., Kelley, K.A., Tucker, J.M., Shimizu, K., Voyer, M.L., Marske, J., Saal, A.E., 2019. Carbon in the Convecting Mantle, in: Orcutt, B.N., Daniel, I., Dasgupta, R. (Eds.), Deep Carbon. Cambridge University Press, pp. 237–275. https://doi.org/10.1017/9781108677950.009

Hawkesworth, C.J., Kempton, P.D., Rogers, N.W., Ellam, R.M., van Calsteren, P.W., 1990. Continental mantle lithosphere, and shallow level enrichment processes in the Earth's mantle. Earth Planet. Sci. Lett. 96, 256–268. https://doi.org/10.1016/0012-821X(90)90006-J

Heber, V.S., Brooker, R.A., Kelley, S.P., Wood, B.J., 2007. Crystal–melt partitioning of noble gases (helium, neon, argon, krypton, and xenon) for olivine and clinopyroxene. Geochim. Cosmochim. Acta 71, 1041–1061. https://doi.org/10.1016/j.gca.2006.11.010

Heber, V.S., Wieler, R., Baur, H., Olinger, C., Friedmann, T.A., Burnett, D.S., 2009. Noble gas composition of the solar wind as collected by the Genesis mission. Geochim. Cosmochim. Acta 73, 7414–7432. https://doi.org/10.1016/j.gca.2009.09.013

Henry, C.D., Aranda-Gomez, J.J., 1992. The real southern Basin and Range: Mid- to late Cenozoic extension in Mexico. Geology 20, 701–704. https://doi.org/10.1130/0091-7613(1992)020<0701:TRSBAR>2.3.CO;2

Henry, C.D., Aranda-Gómez, J.J., 1992. The real southern Basin and Range: Mid- to late Cenozoic extension in Mexico. Geology 20, 701–704. https://doi.org/10.1130/0091-7613(1992)020<0701:TRSBAR>2.3.CO;2

Hernández, P.A., Pérez, N.M., Salazar, J.M., Nakai, S., Notsu, K., Wakita, H., 1998. Diffuse emission of carbon dioxide, methane, and helium-3 from Teide Volcano, Tenerife, Canary Islands. Geophys. Res. Lett. 25, 3311–3314. https://doi.org/10.1029/98GL02561

Hier-Majumder, S., Hirschmann, M.M., 2017. The origin of volatiles in the Earth's mantle. Geochem. Geophys. Geosystems 18, 3078–3092. https://doi.org/10.1002/2017GC006937

Hilton, D., Fischer, T., Marty, B., 2002. Noble Gases and Volatile Recycling at Subduction Zones. Rev. Mineral. Geochem. - REV Miner. GEOCHEM 47, 319–370. https://doi.org/10.2138/rmg.2002.47.9

Hilton, D.R., Hammerschmidt, K., Teufel, S., Friedrichsen, H., 1993. Helium isotope characteristics of Andean geothermal fluids and lavas. Earth Planet. Sci. Lett. 120, 265–282. https://doi.org/10.1016/0012-821X(93)90244-4

Hilton, D.R., Macpherson, C.G., Elliott, T.R., 2000. Helium isotope ratios in mafic phenocrysts and geothermal fluids from La Palma, the Canary Islands (Spain): implications for HIMU mantle sources. Geochim. Cosmochim. Acta 64, 2119–2132. https://doi.org/10.1016/S0016-7037(00)00358-6

Hoernle, K., 1998. Geochemistry of Jurassic Oceanic Crust beneath Gran Canaria (Canary Islands): Implications for Crustal Recycling and Assimilation. J. Petrol. - J Pet. 39, 859–880. https://doi.org/10.1093/petrology/39.5.859

Hoernle, K., Schmincke, H.-U., 1993. The Role of Partial Melting in the 15-Ma Geochemical Evolution of Gran Canaria: A Blob Model for the Canary Hotspot. J. Petrol. 34, 599–626. https://doi.org/10.1093/petrology/34.3.599

Hoernle, K., Tilton, G., Schmincke, H.-U., 1991. SrNdPb isotopic evolution of Gran Canaria: Evidence for shallow enriched mantle beneath the Canary Islands. Earth Planet. Sci. Lett. 106, 44–63. https://doi.org/10.1016/0012-821X(91)90062-M

Hofmann, A.W., 1997. Mantle geochemistry: the message from oceanic volcanism. Nature 385, 219–229. https://doi.org/10.1038/385219a0

Holland, G., Ballentine, C.J., 2006. Seawater subduction controls the heavy noble gas composition of the mantle. Nature 441, 186–191. https://doi.org/10.1038/nature04761

Hopp, J., Ionov, D.A., 2011. Tracing partial melting and subduction-related metasomatism in the Kamchatkan mantle wedge using noble gas compositions. Earth Planet. Sci. Lett. 302, 121–131. https://doi.org/10.1016/j.epsl.2010.12.001

Hopp, J., Trieloff, M., Altherr, R., 2004. Neon isotopes in mantle rocks from the Red Sea region reveal large-scale plume–lithosphere interaction. Earth Planet. Sci. Lett. 219, 61–76. https://doi.org/10.1016/S0012-821X(03)00691-5

Hopp, J., Trieloff, M., Altherr, R., 2007b. Noble gas compositions of the lithospheric mantle below the Chyulu Hills volcanic field, Kenya. Earth Planet. Sci. Lett. 261, 635–648. https://doi.org/10.1016/j.epsl.2007.07.027

Hopp, J., Trieloff, M., Buikin, A., Korochantseva, E., Schwarz, W., Althaus, T., Altherr, R., 2007a. Heterogeneous mantle argon isotope composition in the subcontinental lithospheric mantle beneath the Red Sea region. Chem. Geol. 240, 36–53. https://doi.org/10.1016/j.chemgeo.2007.01.004

Housh, T.B., Aranda-Gómez, J.J., Luhr, J.F., 2010. Isla Isabel (Nayarit, México): Quaternary alkalic basalts with mantle xenoliths erupted in the mouth of the Gulf of California. J. Volcanol. Geotherm. Res. 197, 85–107. https://doi.org/10.1016/j.jvolgeores.2009.06.011

Howarth, G.H., Barry, P.H., Pernet-Fisher, J.F., Baziotis, I.P., Pokhilenko, N.P., Pokhilenko, L.N., Bodnar, R.J., Taylor, L.A., Agashev, A.M., 2014. Superplume metasomatism: Evidence from Siberian mantle xenoliths. Lithos 184–187, 209–224. https://doi.org/10.1016/j.lithos.2013.09.006

Ingrin, J., Skogby, H., 2000. Hydrogen in nominally anhydrous upper-mantle minerals: concentration levels and implications. Eur. J. Mineral. 543–570. https://doi.org/10.1127/ejm/12/3/0543

Inguaggiato, S., Martin-Del Pozzo, A.L., Aguayo, A., Capasso, G., Favara, R., 2005. Isotopic, chemical and dissolved gas constraints on spring water from Popocatepetl volcano (Mexico): evidence of gas–water interaction between magmatic component and shallow fluids. J. Volcanol. Geotherm. Res. 141, 91–108. https://doi.org/10.1016/j.jvolgeores.2004.09.006

Ionov, D.A., 2002a. Mechanisms and Sources of Mantle Metasomatism: Major and Trace Element Compositions of Peridotite Xenoliths from Spitsbergen in the Context of Numerical Modelling. J. Petrol. 43, 2219–2259. https://doi.org/10.1093/petrology/43.12.2219

Ionov, D.A., 2002b. Sr-Nd-Pb Isotopic Compositions of Peridotite Xenoliths from Spitsbergen: Numerical Modelling Indicates Sr-Nd Decoupling in the Mantle by Melt Percolation Metasomatism. J. Petrol. 43, 2261–2278. https://doi.org/10.1093/petrology/43.12.2261

Ionov, D.A., Doucet, L.S., Ashchepkov, I.V., 2010b. Composition of the Lithospheric Mantle in the Siberian Craton: New Constraints from Fresh Peridotites in the Udachnaya-East Kimberlite. J. Petrol. 51, 2177–2210. https://doi.org/10.1093/petrology/egq053

Ionov, D.A., Guo, P., Nelson, W.R., Shirey, S.B., Willbold, M., 2020. Paleoproterozoic melt-depleted lithospheric mantle in the Khanka block, far eastern Russia: Inferences for mobile belts bordering the North China and Siberian cratons. Geochim. Cosmochim. Acta 270, 95–111. https://doi.org/10.1016/j.gca.2019.11.019

Jackson, I. (Ed.), 1998. The Earth's Mantle: Composition, Structure, and Evolution. Cambridge University Press, Cambridge. https://doi.org/10.1017/CBO9780511573101

Jackson, M., Dasgupta, R., 2008. Compositions of HIMU, EM1, and EM2 from global trends between radiogenic isotopes and major elements in ocean island basalts. Earth Planet. Sci. Lett. 276, 175–186. https://doi.org/10.1016/j.epsl.2008.09.023

Jackson, M.G., Shirey, S.B., Hauri, E.H., Kurz, M.D., Rizo, H., 2016. Peridotite xenoliths from the Polynesian Austral and Samoa hotspots: Implications for the destruction of ancient 187Os and 142Nd isotopic domains and the preservation of Hadean 129Xe in the modern convecting mantle. Geochim. Cosmochim. Acta 185, 21–43. https://doi.org/10.1016/j.gca.2016.02.011

Jambon, A., Weber, H.W., Begemann, F., 1985. Helium and argon from an Atlantic MORB glass: concentration, distribution and isotopic composition. Earth Planet. Sci. Lett. 73, 255–268. https://doi.org/10.1016/0012-821X(85)90074-3

Javoy, M., Pineau, F., Agrinier, P., 1989. Volatiles and Stable Isotopes in Recycling, in: Hart, S.R., Gülen, L. (Eds.), Crust/Mantle Recycling at Convergence Zones. Springer Netherlands, Dordrecht, pp. 121–138. https://doi.org/10.1007/978-94-009-0895-6_13

Javoy, M., Pineau, F., Iiyama, I., 1978. Experimental determination of the isotopic fractionation between gaseous CO2 and carbon dissolved in tholeiitic magma: A preliminary study. Contrib. Mineral. Petrol. 67, 35–39. https://doi.org/10.1007/BF00371631

Kaczmarek, M.-A., Bodinier, J.-L., Bosch, D., Tommasi, A., Dautria, J.-M., Kechid, S.A., 2016. Metasomatized Mantle Xenoliths as a Record of the Lithospheric Mantle Evolution of the Northern Edge of the Ahaggar Swell, In Teria (Algeria). J. Petrol. 57, 345–382. https://doi.org/10.1093/petrology/egw009

Karmalkar, N.R., Duraiswami, R.A., Chalapathi Rao, N.V., Paul, D.K., 2009. Mantle-derived mafic-ultramafic xenoliths and the nature of Indian sub-continental lithosphere. J. Geol. Soc. India 73, 657–679. https://doi.org/10.1007/s12594-009-0051-7

Kennedy, B.M., Hiyagon, H., Reynolds, J.H., 1990. Crustal neon: a striking uniformity. Earth Planet. Sci. Lett. 98, 277–286. https://doi.org/10.1016/0012-821X(90)90030-2

Kenward, P.A., Goldstein, R.H., González, L.A., Roberts, J.A., 2009. Precipitation of low-temperature dolomite from an anaerobic microbial consortium: the role of methanogenic Archaea. Geobiology 7, 556–565. https://doi.org/10.1111/j.1472-4669.2009.00210.x

Kiseeva, E.S., Kamenetsky, V.S., Yaxley, G.M., Shee, S.R., 2017. Mantle melting versus mantle metasomatism – "The chicken or the egg" dilemma. Chem. Geol. 455, 120–130. https://doi.org/10.1016/j.chemgeo.2016.10.026

Konzett, J., Armstrong, R.A., Günther, D., 2000. Modal metasomatism in the Kaapvaal craton lithosphere: constraints on timing and genesis from U-Pb zircon dating of metasomatized peridotites and MARID-type xenoliths. Contrib. Mineral. Petrol. 139, 704–719. https://doi.org/10.1007/s004100000160

Kopylova, M.G., Caro, G., 2004. Mantle Xenoliths from the Southeastern Slave Craton: Evidence for Chemical Zonation in a Thick, Cold Lithosphere. J. Petrol. 45, 1045–1067. https://doi.org/10.1093/petrology/egh003

Kurz, M.D., 1986. Cosmogenic helium in a terrestrial igneous rock. Nature 320, 435–439. https://doi.org/10.1038/320435a0

Lages, J., Rizzo, A.L., Aiuppa, A., Samaniego, P., Le Pennec, J.L., Ceballos, J.A., Narváez, P.A., Moussallam, Y., Bani, P., Schipper, C.I., Hidalgo, S., Gaglio, V., Alberti, E., Sandoval-Velasquez, A., 2021. Noble gas magmatic signature of the Andean Northern Volcanic Zone from fluid inclusions in minerals. Chem. Geol. 559, 119966. https://doi.org/10.1016/j.chemgeo.2020.119966

Lal, D., 1987. Production of 3He in terrestrial rocks. Chem. Geol. Isot. Geosci. Sect. 66, 89–98. https://doi.org/10.1016/0168-9622(87)90031-5

Langmuir, C.H., Vocke, R.D., Hanson, G.N., Hart, S.R., 1978. A general mixing equation with applications to Icelandic basalts. Earth Planet. Sci. Lett. 37, 380–392. https://doi.org/10.1016/0012-821X(78)90053-5

le Roex, A., Class, C., 2016. Metasomatic enrichment of Proterozoic mantle south of the Kaapvaal Craton, South Africa: origin of sinusoidal REE patterns in clinopyroxene and garnet. Contrib. Mineral. Petrol. 171, 14. https://doi.org/10.1007/s00410-015-1222-8

Lee, C.A., 2005. Trace Element Evidence for Hydrous Metasomatism at the Base of the North American Lithosphere and Possible Association with Laramide Low-Angle Subduction. J. Geol. 113, 673–685. https://doi.org/10.1086/449327

Lee, H., Muirhead, J.D., Fischer, T.P., Ebinger, C.J., Kattenhorn, S.A., Sharp, Z.D., Kianji, G., 2016. Massive and prolonged deep carbon emissions associated with continental rifting. Nat. Geosci. 9, 145–149. https://doi.org/10.1038/ngeo2622

Lee, J.-Y., Marti, K., Severinghaus, J.P., Kawamura, K., Yoo, H.-S., Lee, J.B., Kim, J.S., 2006. A redetermination of the isotopic abundances of atmospheric Ar. Geochim. Cosmochim. Acta 70, 4507–4512. https://doi.org/10.1016/j.gca.2006.06.1563

Leeman, W.P., Harry, D.L., 1993. A Binary Source Model for Extension-Related Magmatism in the Great Basin, Western North America. Science 262, 1550–1554. https://doi.org/10.1126/science.262.5139.1550

Levresse, G., Cervantes-de la Cruz, K.E., Aranda-Gómez, J.J., Dávalos-Elizondo, M.G., Jiménez-Sandoval, S., Rodríguez-Melgarejo, F., Alba-Aldave, L.A., 2016. CO2 fluid inclusion barometry in mantle xenoliths from central Mexico: A detailed record of magma ascent. J. Volcanol. Geotherm. Res. 310, 72–88. https://doi.org/10.1016/j.jvolgeores.2015.11.012

Li, K., Li, L., Pearson, D.G., Stachel, T., 2019. Diamond isotope compositions indicate altered igneous oceanic crust dominates deep carbon recycling. Earth Planet. Sci. Lett. 516, 190–201. https://doi.org/10.1016/j.epsl.2019.03.041

Li, Z.-X.A., Lee, C.-T.A., Peslier, A.H., Lenardic, A., Mackwell, S.J., 2008. Water contents in mantle xenoliths from the Colorado Plateau and vicinity: Implications for the mantle rheology and hydration-induced thinning of continental lithosphere. J. Geophys. Res. 113, B09210. https://doi.org/10.1029/2007JB005540

Liang, Y., Elthon, D., 1990. Geochemistry and petrology of spinel lherzolite xenoliths from Xalapasco de La Joya, San Luis Potosi, Mexico: Partial melting and mantle metasomatism. J. Geophys. Res. 95, 15859. https://doi.org/10.1029/JB095iB10p15859

López-Doncel, R., 2003. La Formación Tamabra del Cretácico medio en la porción central del margen occidental de la Plataforma Valles. Revista Mexicana de Ciencias Geológias 20, 1–19.

Lu, J., Zheng, J., Griffin, W.L., Yu, C., 2013. Petrology and geochemistry of peridotite xenoliths from the Lianshan region: Nature and evolution of lithospheric mantle beneath the lower Yangtze block. Gondwana Res. 23, 161–175. https://doi.org/10.1016/j.gr.2012.01.008

Luhr, J.F., Aranda-Gomez, J.J., 1997. Mexican Peridotite Xenoliths and Tectonic Terranes: Correlations among Vent Location, Texture, Temperature, Pressure, and Oxygen Fugacity. J. Petrol. 38, 1075–1112. https://doi.org/10.1093/petroj/38.8.1075

Luhr, J.F., Aranda-Gómez, J.J., Housh, T.B., 1995a. San Quintín Volcanic Field, Baja California Norte, México: Geology, petrology, and geochemistry. J. Geophys. Res. Solid Earth 100, 10353–10380. https://doi.org/10.1029/95JB00037

Luhr, J.F., Aranda-Gomez, J.J., Pier, J.G., 1989. Spinel-lherzolite-bearing quaternary volcanic centers in San Luis Potosí, Mexico: 1. Geology, mineralology, and petrology. J. Geophys. Res. 94, 7916. https://doi.org/10.1029/JB094iB06p07916

Lux, G., 1987. The behavior of noble gases in silicate liquids: Solution, diffusion, bubbles and surface effects, with applications to natural samples. Geochim. Cosmochim. Acta 51, 1549–1560. https://doi.org/10.1016/0016-7037(87)90336-X

Marinoni, L.B., Pasquarè, G., 1994. Tectonic evolution of the emergent part of a volcanic ocean island: Lanzarote, Canary Islands. Tectonophysics 239, 111–137. https://doi.org/10.1016/0040-1951(94)90110-4

Márquez, A., Oyarzun, R., Doblas, M., Verma, S.P., 1999a. Alkalic (ocean-island basalt type) and calc-alkalic volcanism in the Mexican volcanic belt: A case for plume-related magmatism and propagating rifting at an active margin? Geology 27, 51–54. https://doi.org/10.1130/0091-7613(1999)027<0051:AOIBTA>2.3.CO;2

Márquez, A., Verma, S.P., Anguita, F., Oyarzun, R., Brandle, J.L., 1999b. Tectonics and volcanism of Sierra Chichinautzin: extension at the front of the Central Trans-Mexican Volcanic belt. J. Volcanol. Geotherm. Res. 93, 125–150. https://doi.org/10.1016/S0377-0273(99)00085-2

Marrero-Diaz, R., López, D., Perez, N.M., Custodio, E., Sumino, H., Melián, G.V., Padrón, E., Hernandez, P.A., Calvo, D., Barrancos, J., Padilla, G., Sortino, F., 2015. Carbon dioxide and helium dissolved gases in groundwater at central Tenerife Island, Canary Islands: chemical and isotopic characterization. Bull. Volcanol. 77, 86. https://doi.org/10.1007/s00445-015-0969-0

Martelli, M., Bianchini, G., Beccaluva, L., Rizzo, A., 2011. Helium and argon isotopic compositions of mantle xenoliths from Tallante and Calatrava, Spain. J. Volcanol. Geotherm. Res. 200, 18–26. https://doi.org/10.1016/j.jvolgeores.2010.11.015

Martelli, M., Rizzo, A.L., Renzulli, A., Ridolfi, F., Arienzo, I., Rosciglione, A., 2014. Noble-gas signature of magmas from a heterogeneous mantle wedge: The case of Stromboli volcano (Aeolian Islands, Italy). Chem. Geol. 368, 39–53. https://doi.org/10.1016/j.chemgeo.2014.01.003

Martin, A.P., Cooper, A.F., Price, R.C., Doherty, C.L., Gamble, J.A., 2021. A review of mantle xenoliths in volcanic rocks from southern Victoria Land, Antarctica. Geol. Soc. Lond. Mem. M56-2019–42. https://doi.org/10.1144/M56-2019-42

Martinez-Arevalo, C., Mancilla, F. de L., Helffrich, G., Garcia, A., 2013. Seismic evidence of a regional sublithospheric low velocity layer beneath the Canary Islands. Tectonophysics 608, 586–599. https://doi.org/10.1016/j.tecto.2013.08.021

Marty, B., 2012. The origins and concentrations of water, carbon, nitrogen and noble gases on Earth. Earth Planet. Sci. Lett. 313–314, 56–66. https://doi.org/10.1016/j.epsl.2011.10.040

Marty, B., 2011. Mantle Volatiles, in: Gargaud, M., Amils, R., Quintanilla, J.C., Cleaves, H.J., Irvine, W.M., Pinti, D.L., Viso, M. (Eds.), Encyclopedia of Astrobiology. Springer Berlin Heidelberg, Berlin, Heidelberg, pp. 959–960. https://doi.org/10.1007/978-3-642-11274-4_934

Marty, B., Jambon, A., 1987. C3He in volatile fluxes from the solid Earth: implications for carbon geodynamics. Earth Planet. Sci. Lett. 83, 16–26. https://doi.org/10.1016/0012-821X(87)90047-1

Marty, B., Tolstikhin, I.N., 1998. CO2 fluxes from mid-ocean ridges, arcs and plumes. Chem. Geol. 145, 233–248. https://doi.org/10.1016/S0009-2541(97)00145-9

Marty, B., Trull, T., Lussiez, P., Basile-Doelsch, I., Tanguy, J.-C., 1994. He, Ar, O, Sr and Nd isotope constraints on the origin and evolution of Mount Etna magmatism. Earth Planet. Sci. Lett. 126, 23–39. https://doi.org/10.1016/0012-821X(94)90240-2

Matsumoto, T., Chen, Y., Matsuda, J.-I., 2001. Concomitant occurence of primordial and recycled noble gasesin the Earth's mantle. Earth Planet. Sci. Lett. 185, 35–47. https://doi.org/10.1016/S0012-821X(00)00375-7

Matsumoto, T., Honda, M., Mcdougall, I., O'Reilly, S.Y., 1998. Noble gases in anhydrous lherzolites from the newer volcanics, southeastern Australia: a MORB-like reservoir in the subcontinental mantle. Geochim. Cosmochim. Acta 62, 2521–2533. https://doi.org/10.1016/S0016-7037(98)00173-2

Matsumoto, T., Honda, M., McDougall, I., O'Reilly, S.Y., Norman, M., Yaxley, G., 2000. Noble gases in pyroxenites and metasomatised peridotites from the Newer Volcanics, southeastern Australia: Implications for mantle metasomatism. Chem. Geol. 168, 49–73. https://doi.org/10.1016/S0009-2541(00)00181-9

Matsumoto, T., Pinti, D.L., Matsuda, J.-I., Umino, S., 2002. Recycled noble gas and nitrogen in the subcontinental lithospheric mantle: Implications from N-He-Ar in fluid inclusions of SE Australian xenoliths. Geochem. J. 36, 209–217. https://doi.org/10.2343/geochemj.36.209

Mazzeo, F.C., Rocco, I., Tucker, R.D., Morra, V., D'Antonio, M., Melluso, L., 2021. Olivine melilitites, mantle xenoliths, and xenocrysts of the Takarindiona district: Petrogenesis, magmatic evolution, and the sub-continental lithospheric mantle of east-central Madagascar. J. Afr. Earth Sci. 174, 104059. https://doi.org/10.1016/j.jafrearsci.2020.104059

McDonough, W.F., Frey, F.A., 1989. Rare earth elements in upper mantle rocks. Rev. Mineral. Geochem. 21, 100–145.

McDonough, W.F., Rudnick, R.L., 1998. Chapter 4. MINERALOGY AND COMPOSITION OF THE UPPER MANTLE, in: Hemley, R.J. (Ed.), Ultrahigh Pressure Mineralogy. De Gruyter, Berlin, Boston, pp. 139–164. https://doi.org/10.1515/9781501509179-006

McKenzie, D., O'Nions, R.K., 1983. Mantle reservoirs and ocean island basalts. Nature 301, 229–231. https://doi.org/10.1038/301229a0

Melián, G., Tassi, F., Pérez, N., Hernandez, P., Sortino, F., Vaselli, O., Padrón, E., Nolasco, D., Barrancos, J., Padilla, G., Rodriguez, F., Dionis, S., 2012. A magmatic source for fumaroles and diffuse degassing from the summit crater of Teide Volcano (Tenerife, Canary Islands): A geochemical evidence for the 2004-2005 seismic-volcanic crisis. Bull. Volcanol. 74. https://doi.org/10.1007/s00445-012-0613-1

Menzies, M.A., 1989. Cratonic, circumcratonic and oceanic mantle domains beneath the western United States. J. Geophys. Res. 94, 7899. https://doi.org/10.1029/JB094iB06p07899

Mercier, J.-C.C., Nicolas, A., 1975. Textures and Fabrics of Upper-Mantle Peridotites as Illustrated by Xenoliths from Basalts. J. Petrol. 16, 454–487. https://doi.org/10.1093/petrology/16.1.454

Meriggi, L., MacÃ\-as, J.L., Tommasini, S., Capra, L., Conticelli, S., 2008. Heterogeneous magmas of the Quaternary Sierra Chichinautzin volcanic field (central Mexico): the role of an amphibole-bearing mantle and magmatic evolution processes. Rev. Mex. Cienc. GeolÃ³gicas 25, 197–216.

Michael, P.J., Graham, D.W., 2015. The behavior and concentration of CO2 in the suboceanic mantle: Inferences from undegassed ocean ridge and ocean island basalts. Lithos 236–237, 338–351. https://doi.org/10.1016/j.lithos.2015.08.020

Moore, G., Marone, C., Carmichael, I.S.E., Renne, P., 1994. Basaltic volcanism and extension near the intersection of the Sierra Madre volcanic province and the Mexican Volcanic Belt. GSA Bull. 106, 383–394. https://doi.org/10.1130/0016-7606(1994)106<0383:BVAENT>2.3.CO;2

Morán-Zenteno, D.J., Cerca, M., Keppie, J.D., 2005. La evolución tectónica y magmática cenozoica del suroeste de México: avances y problemas de interpretación. Bol. Soc. Geológica Mex. 57, 319–341. https://doi.org/10.18268/BSGM2005v57n3a4

Moreira, M., 2013. Noble gas constraints on the origin and evolution of Earth's volatiles. Geochem. Perspect. 2, 229–403. https://doi.org/10.7185/geochempersp.2.2

Moreira, M., Kunz, J., Allègre, C., 1998. Rare Gas Systematics in Popping Rock: Isotopic and Elemental Compositions in the Upper Mantle. Science 279, 1178–1181. https://doi.org/10.1126/science.279.5354.1178

Moreira, M., Sarda, P., 2000. Noble gas constraints on degassing processes. Earth Planet. Sci. Lett. 176, 375–386. https://doi.org/10.1016/S0012-821X(00)00010-8

Moreira, M.A., Kurz, M.D., 2013. Noble Gases as Tracers of Mantle Processes and Magmatic Degassing, in: Burnard, P. (Ed.), The Noble Gases as Geochemical Tracers, Advances in Isotope Geochemistry. Springer Berlin Heidelberg, Berlin, Heidelberg, pp. 371–391. https://doi.org/10.1007/978-3-642-28836-4_12

Mukhopadhyay, S., Parai, R., 2019. Noble Gases: A Record of Earth's Evolution and Mantle Dynamics. Annu. Rev. Earth Planet. Sci. 47, 389–419. https://doi.org/10.1146/annurev-earth-053018-060238

Murck, B.W., Burruss, R.C., Hollister, L.S., 1978. Phase equilibria in fluid inclusions in ultramafic xenoliths. Am. Mineral. 63, 40–46.

Nadeau, S., Pineau, F., Javoy, M., Francis, D., 1990. Carbon concentrations and isotopic ratios in fluid-inclusion-bearing upper-mantle xenoliths along the northwestern margin of North America. Chem. Geol. 81, 271–297. https://doi.org/10.1016/0009-2541(90)90051-8

Nasir, S., Rollinson, H., 2009. The nature of the subcontinental lithospheric mantle beneath the Arabian Shield: Mantle xenoliths from southern Syria. Precambrian Res. 172, 323–333. https://doi.org/10.1016/j.precamres.2009.05.004

Nesterenok, A.V., Yakubovich, O.V., 2016. Production of 3He in rocks by reactions induced by particles of the nuclear-active and muon components of cosmic rays: Geological and petrological implications. Petrology 24, 21–34. https://doi.org/10.1134/S0869591116010057

Neumann, E.-R., 2004. The Evolution of the Upper Mantle beneath the Canary Islands: Information from Trace Elements and Sr isotope Ratios in Minerals in Mantle Xenoliths. J. Petrol. 45, 2573–2612. https://doi.org/10.1093/petrology/egh063

Neumann, E.-R., 1991. Ultramafic and mafic xenoliths from Hierro, Canary Islands: evidence for melt infiltration in the upper mantle. Contrib. Mineral. Petrol. 106, 236–252. https://doi.org/10.1007/BF00306436

Neumann, E.-R., Wulff-Pedersen, E., 1997. The Origin of Highly Silicic Glass in Mantle Xenoliths from the Canary Islands. J. Petrol. 38, 1513–1539. https://doi.org/10.1093/petroj/38.11.1513

Nicolas, A., 1986. Structure and petrology of peridotites: Clues to their geodynamic environment. Rev. Geophys. 24, 875. https://doi.org/10.1029/RG024i004p00875

Nieto-Samaniego, Á.F., Alaniz-Álvarez, S.A., Camprubí í Cano, A., 2005. La Mesa Central de México: estratigrafía, estructura y evolución tectónica cenozoica. Bol. Soc. Geológica Mex. 57, 285–318. https://doi.org/10.18268/BSGM2005v57n3a3

Nieto-Samaniego, Á.F., Ferrari, L., Alaniz-Alvarez, S.A., Labarthe-Hernández, G., Rosas-Elguera, J., 1999. Variation of Cenozoic extension and volcanism across the southern Sierra Madre Occidental volcanic province, Mexico. GSA Bull. 111, 347–363. https://doi.org/10.1130/0016-7606(1999)111<0347:VOCEAV>2.3.CO;2

Nixon, P.H., Rogers, N.W., Gibson, I.L., Grey, A., 1981. Depleted and Fertile Mantle Xenoliths from Southern African Kimberlites. Annu. Rev. Earth Planet. Sci. 9, 285–309. https://doi.org/10.1146/annurev.ea.09.050181.001441

Nuccio, P.M., Paonita, A., Rizzo, A., Rosciglione, A., 2008. Elemental and isotope covariation of noble gases in mineral phases from Etnean volcanics erupted during 2001–2005, and genetic relation with peripheral gas discharges. Earth Planet. Sci. Lett. 272, 683–690. https://doi.org/10.1016/j.epsl.2008.06.007

Oglialoro, E., Frezzotti, M.L., Ferrando, S., Tiraboschi, C., Principe, C., Groppelli, G., Villa, I.M., 2017. Lithospheric magma dynamics beneath the El Hierro Volcano, Canary Islands: insights from fluid inclusions. Bull. Volcanol. 79, 70. https://doi.org/10.1007/s00445-017-1152-6

Oppenheimer, C., Fischer, T.P., Scaillet, B., 2014. Volcanic Degassing: Process and Impact, in: Treatise on Geochemistry. Elsevier, pp. 111–179. https://doi.org/10.1016/B978-0-08-095975-7.00304-1

O'Reilly, S.Y., Griffin, W.L., 2013. Mantle Metasomatism, in: Metasomatism and the Chemical Transformation of Rock, Lecture Notes in Earth System Sciences. Springer Berlin Heidelberg, Berlin, Heidelberg, pp. 471–533. https://doi.org/10.1007/978-3-642-28394-9_12

Ozima, M., Podosek, F.A., 2002. Noble Gas Geochemistry. Cambridge University Press.

Padrón, E., Pérez, N.M., Hernández, P.A., Sumino, H., Melián, G.V., Barrancos, J., Nolasco, D., Padilla, G., Dionis, S., Rodríguez, F., Hernández, Í., Calvo, D., Peraza, M.D., Nagao, K., 2013. Diffusive helium emissions as a precursory sign of volcanic unrest. Geology 41, 539–542. https://doi.org/10.1130/G34027.1

Padrón, E., Pérez, N.M., Rodríguez, F., Melián, G., Hernández, P.A., Sumino, H., Padilla, G., Barrancos, J., Dionis, S., Notsu, K., Calvo, D., 2015. Dynamics of diffuse carbon dioxide emissions from Cumbre Vieja volcano, La Palma, Canary Islands. Bull. Volcanol. 77, 28. https://doi.org/10.1007/s00445-015-0914-2

Paonita, A., 2009. Noble gas solubility in silicate melts:a review of experimentation and theory, and implications regarding magma degassing processes. Ann. Geophys. 48. https://doi.org/10.4401/ag-3225

Paonita, A., Martelli, M., 2007. A new view of the He–Ar–CO2 degassing at mid-ocean ridges: Homogeneous composition of magmas from the upper mantle. Geochim. Cosmochim. Acta 71, 1747–1763. https://doi.org/10.1016/j.gca.2006.12.019

Pardo, M., Suárez, G., 1995. Shape of the subducted Rivera and Cocos plates in southern Mexico: Seismic and tectonic implications. J. Geophys. Res. Solid Earth 100, 12357–12373. https://doi.org/10.1029/95JB00919

Payot, B., Arai, S., Yoshikawa, M., Tamura, A., Okuno, M., Rivera, D., 2018. Mantle Evolution from Ocean to Arc: The Record in Spinel Peridotite Xenoliths in Mt. Pinatubo, Philippines. Minerals 8, 515. https://doi.org/10.3390/min8110515

Pearson, D.G., Canil, D., Shirey, S.B., 2014. Mantle Samples Included in Volcanic Rocks, in: Treatise on Geochemistry. Elsevier, pp. 169–253. https://doi.org/10.1016/B978-0-08-095975-7.00216-3

Pearson, D.G., Canil, D., Shirey, S.B., 2003. Mantle Samples Included in Volcanic Rocks: Xenoliths and Diamonds, in: Treatise on Geochemistry. Elsevier, pp. 171–275. https://doi.org/10.1016/B0-08-043751-6/02005-3

Pérez, N.M., Nakai, S., Wakita, H., Hernández, P.A., Salazar, J.M., 1996. Helium-3 emission in and around Teide Volcano, Tenerife, Canary Islands, Spain. Geophys. Res. Lett. 23, 3531–3534. https://doi.org/10.1029/96GL03470

Pérez, N.M., Nakai, S., Wakita, H., Sano, Y., Williams, S.N., 1994. 3He/4He Isotopic Ratios in Volcanic-Hydrothermal Discharges from the Canary Islands, Spain: Implications on the Origin of the Volcanic Activity. Mineral. Mag. 58, 709–710. https://doi.org/10.1180/minmag.1994.58A.2.107

Pier, J.G., Podosek, F.A., Luhr, J.F., Brannon, J.C., Aranda-Gómez, J.J., 1989. Spinel-lherzolite-bearing quaternary volcanic centers in San Luis Potosí, Mexico: 2. SR and ND Isotopic Systematics. J. Geophys. Res. 94, 7941. https://doi.org/10.1029/JB094iB06p07941

Pineau, F., Mathez, E.A., 1990. Carbon isotopes in xenoliths from the Hualalai Volcano, Hawaii, and the generation of isotopic variability. Geochim. Cosmochim. Acta 54, 217–227. https://doi.org/10.1016/0016-7037(90)90209-4

Plank, T., Manning, C.E., 2019. Subducting carbon. Nature 574, 343–352. https://doi.org/10.1038/s41586-019-1643-z

Porcelli, D.R., O'Nions, R.K., Galer, S.J.G., Cohen, A.S., Mattey, D.P., 1992. Isotopic relationships of volatile and lithophile trace elements in continental ultramafic xenoliths. Contrib. Mineral. Petrol. 110, 528–538. https://doi.org/10.1007/BF00344086

Raisz, E., 1959. Landforms of Mexico.

Regier, M.E., Pearson, D.G., Stachel, T., Luth, R.W., Stern, R.A., Harris, J.W., 2020. The lithospheric-to-lower-mantle carbon cycle recorded in superdeep diamonds. Nature 585, 234–238. https://doi.org/10.1038/s41586-020-2676-z

Remigi, S., Frezzotti, M.L., Ferrando, S., 2019. Generation of CO2 - SO2 fluxes in the lithospheric mantle beneath El Hierro (Canary Islands) on metasomatic reactions of carbonate-rich silicate melts, Intervento presentato a: ECROFI, Budapest. Università di Milano Biccoca, Milan.

Rizzo, A.L., Barberi, F., Carapezza, M.L., Di Piazza, A., Francalanci, L., Sortino, F., D'Alessandro, W., 2015. New mafic magma refilling a quiescent volcano: Evidence from He-Ne-Ar isotopes during the 2011-2012 unrest at Santorini, Greece: RESEARCH ARTICLE. Geochem. Geophys. Geosystems 16, 798–814. https://doi.org/10.1002/2014GC005653

Rizzo, A.L., Faccini, B., Casetta, F., Faccincani, L., Ntaflos, T., Italiano, F., Coltorti, M., 2021. Melting and metasomatism in West Eifel and Siebengebirge Sub-Continental Lithospheric Mantle: Evidence from concentrations of volatiles in fluid inclusions and petrology of ultramafic xenoliths. Chem. Geol. 581, 120400. https://doi.org/10.1016/j.chemgeo.2021.120400

Rizzo, A.L., Pelorosso, B., Coltorti, M., Ntaflos, T., Bonadiman, C., Matusiak-Małek, M., Italiano, F., Bergonzoni, G., 2018. Geochemistry of Noble Gases and CO2 in Fluid Inclusions From Lithospheric Mantle Beneath Wilcza Góra (Lower Silesia, Southwest Poland). Front. Earth Sci. 6, 215. https://doi.org/10.3389/feart.2018.00215

Robock, A., 2000. Volcanic eruptions and climate. Rev. Geophys. 38, 191–219. https://doi.org/10.1029/1998RG000054

Roden, M.F., Murthy, V.R., 1985. Mantle Metasomatism. Annu. Rev. Earth Planet. Sci. 13, 269–296. https://doi.org/10.1146/annurev.ea.13.050185.001413

Rodgers, K.A., Brothers, R.N., Searle, E.J., 1975. Ultramafic nodules and their host rocks from Auckland, New Zealand. Geol. Mag. 112, 163–174. https://doi.org/10.1017/S0016756800045842

Roedder, E., 1984. Fluid Inclusions: An Introduction to Studies of All Types of Fluid Inclusions, Gas, Liquid, Or Melt, Trapped in Materials from Earth and Space, and Their Application to the Understanding of Geologic Processes. Mineralogical Society of America.

Safonov, O., Butvina, V., Limanov, E., 2019. Phlogopite-Forming Reactions as Indicators of Metasomatism in the Lithospheric Mantle. Minerals 9, 685. https://doi.org/10.3390/min9110685

Sandoval-Velasquez, A., Rizzo, A.L., Aiuppa, A., Remigi, S., Padrón, E., Pérez, N.M., Frezzotti, M.L., 2021b. Recycled crustal carbon in the depleted mantle source of El Hierro volcano, Canary Islands. Lithos 400–401, 106414. https://doi.org/10.1016/j.lithos.2021.106414

Sandoval-Velasquez, A., Rizzo, A.L., Frezzotti, M.L., Saucedo, R., Aiuppa, A., 2021a. The composition of fluids stored in the central Mexican lithospheric mantle: Inferences from noble gases and CO2 in mantle xenoliths. Chem. Geol. 576, 120270. https://doi.org/10.1016/j.chemgeo.2021.120270

Sano, Y., Marty, B., 1995. Origin of carbon in Fumarolic gas from island arcs. Chem. Geol. 119, 265–274. https://doi.org/10.1016/0009-2541(94)00097-R

Sano, Y., Nakamura, Y., Wakita, H., Urabe, A., Tominaga, T., 1984. Helium-3 Emission Related to Volcanic Activity. Science 224, 150–151. https://doi.org/10.1126/science.224.4645.150

Sarda, P., 2004. Surface noble gas recycling to the terrestrial mantle. Earth Planet. Sci. Lett. 228, 49–63. https://doi.org/10.1016/j.epsl.2004.09.026

Sarda, P., Staudacher, T., Allegre, C., 1988. Neon isotopes in submarine basalts. Earth Planet. Sci. Lett. 91, 73–88. https://doi.org/10.1016/0012-821X(88)90152-5

Saucedo, R., Macías, J.L., Ocampo-Díaz, Y.Z.E., Gómez-Villa, W., Rivera-Olguín, E., Castro-Govea, R., Sánchez-Núñez, J.M., Layer, P.W., Torres Hernández, J.R., Carrasco-Núñez, G., 2017. Mixed magmatic–phreatomagmatic explosions during the formation of the Joya Honda maar, San Luis Potosí, Mexico. Geol. Soc. Lond. Spec. Publ. 446, 255–279. https://doi.org/10.1144/SP446.11

Schaaf, P., Stimac, J., Siebe, C., Macías, J.L., 2005. Geochemical Evidence for Mantle Origin and Crustal Processes in Volcanic Rocks from Popocatépetl and Surrounding Monogenetic Volcanoes, Central Mexico. J. Petrol. 46, 1243–1282. https://doi.org/10.1093/petrology/egi015

Schmincke, H.-U., 1982. Volcanic and Chemical Evolution of the Canary Islands, in: von Rad, U., Hinz, K., Sarnthein, M., Seibold, E. (Eds.), Geology of the Northwest African Continental Margin. Springer Berlin Heidelberg, Berlin, Heidelberg, pp. 273–306. https://doi.org/10.1007/978-3-642-68409-8_12

Sedlock, R.L., 2003. Geology and tectonics of the Baja California Peninsula and adjacent areas, in: Tectonic Evolution of Northwestern Mexico and the Southwestern USA. Geological Society of America. https://doi.org/10.1130/0-8137-2374-4.1

Sedlock, R.L., Ortega-Gutiérrez, F., Speed, R.C., 1993. Tectonostratigraphic Terranes and Tectonic Evolution of Mexico, Geological Society of America Special Papers. Geological Society of America. https://doi.org/10.1130/SPE278

Severinghaus, J., Atwater, T., 1990. Chapter 1: Cenozoic geometry and thermal state of the subducting slabs beneath western North America, in: Geological Society of America Memoirs. Geological Society of America, pp. 1–22. https://doi.org/10.1130/MEM176-p1

Shaw, C.S.J., Eyzaguirre, J., Fryer, B., Gagnon, J., 2005. Regional Variations in the Mineralogy of Metasomatic Assemblages in Mantle Xenoliths from the West Eifel Volcanic Field, Germany. J. Petrol. 46, 945–972. https://doi.org/10.1093/petrology/egi006

Shurbet, D.H., Cebull, S.E., 1984. Tectonic interpretation of the Trans-Mexicano Volcanic Belt. Tectonophysics 101, 159–165.

Siena, F., Beccaluva, L., Coltorti, M., Marchesi, S., Morra, V., 1991. Ridge to Hot-Spot Evolution of the Atlantic Lithospheric Mantle: Evidence from Lanzarote Peridotite Xenoliths (Canary Islands). J. Petrol. Special_Volume, 271–290. https://doi.org/10.1093/petrology/Special_Volume.2.271

Simon, N.S.C., Carlson, R.W., Pearson, D.G., Davies, G.R., 2007. The Origin and Evolution of the Kaapvaal Cratonic Lithospheric Mantle. J. Petrol. 48, 589–625. https://doi.org/10.1093/petrology/egl074

Simonsen, S., Neumann, E.-R., Seim, K., 2000. Sr–Nd–Pb isotope and trace-element geochemistry evidence for a young HIMU source and assimilation at Tenerife (Canary Island). J. Volcanol. Geotherm. Res. - J VOLCANOL GEOTHERM RES 103, 299–312. https://doi.org/10.1016/S0377-0273(00)00228-6

Smith, D., Alexis Riter, J.C., Mertzman, S.A., 1999. Water–rock interactions, orthopyroxene growth, and Si-enrichment in the mantle: evidence in xenoliths from the Colorado Plateau, southwestern United States. Earth Planet. Sci. Lett. 165, 45–54. https://doi.org/10.1016/S0012-821X(98)00251-9

Snortum, E., Day, J.M.D., Jackson, M.G., 2019. Pacific Lithosphere Evolution Inferred from Aitutaki Mantle Xenoliths. J. Petrol. 60, 1753–1772. https://doi.org/10.1093/petrology/egz047

Stagno, V., 2019. Carbon, carbides, carbonates and carbonatitic melts in the Earth's interior. J. Geol. Soc. 176, 375–387. https://doi.org/10.1144/jgs2018-095

Steiger, R.H., Jäger, E., 1977. Subcommission on geochronology: Convention on the use of decay constants in geo- and cosmochronology. Earth Planet. Sci. Lett. 36, 359–362. https://doi.org/10.1016/0012-821X(77)90060-7

Stern, C.R., Kilian, R., Olker, B., Hauri, E.H., Kurtis Kyser, T., 1999. Evidence from mantle xenoliths for relatively thin (<100 km) continental lithosphere below the Phanerozoic crust of southernmost South America, in: Developments in Geotectonics. Elsevier, pp. 217–235. https://doi.org/10.1016/S0419-0254(99)80013-5

Straub, S.M., Gomez-Tuena, A., Stuart, F.M., Zellmer, G.F., Espinasa-Perena, R., Cai, Y., Iizuka, Y., 2011. Formation of hybrid arc andesites beneath thick continental crust. Earth Planet. Sci. Lett. 303, 337–347. https://doi.org/10.1016/j.epsl.2011.01.013

Straub, S.M., LaGatta, A.B., Martin-Del Pozzo, A.L., Langmuir, C.H., 2008. Evidence from high-Ni olivines for a hybridized peridotite/pyroxenite source for orogenic andesites from the central Mexican Volcanic

Belt: ANDESITE PETROGENESIS IN CENTRAL MVB. Geochem. Geophys. Geosystems 9, n/a-n/a. https://doi.org/10.1029/2007GC001583

Streckeisen, A., 1976. To each plutonic rock its proper name. Earth-Sci. Rev. 12, 1–33. https://doi.org/10.1016/0012-8252(76)90052-0

Sun, S. -s., McDonough, W.F., 1989. Chemical and isotopic systematics of oceanic basalts: implications for mantle composition and processes. Geol. Soc. Lond. Spec. Publ. 42, 313–345. https://doi.org/10.1144/GSL.SP.1989.042.01.19

Swanson, E.R., 1989. A new type of maar volcano from the State of Durango-the El Jagüey-La Breña complex reinterpreted. Universidad Nacional Autónoma de México, Revista del Instituto de Geología 8, 243–248.

Tang, H., Matsumoto, T., Zheng, J., Czuppon, G., Yu, C., Miyakawa, C., Ping, X., 2014. Heterogeneous lithospheric mantle metasomatism in the eastern North China Craton: He–Ar isotopes in peridotite xenoliths from Cenozoic basalts. J. Asian Earth Sci. 80, 185–196. https://doi.org/10.1016/j.jseaes.2013.11.012

Taran, Y., Inguaggiato, S., Varley, N., Capasso, G., Favara, R., 2002. Helium and carbon isotopes in thermal waters of the Jalisco block, Mexico. Geofísica Int. 41.

Thirlwall, M.F., Jenkins, C., Vroon, P.Z., Mattey, D.P., 1997. Crustal interaction during construction of ocean islands: Pb-Sr-Nd-O isotope geochemistry of the shield basalts of Gran Canaria, Canary Islands. Chem. Geol. 135, 233–262. https://doi.org/10.1016/S0009-2541(96)00118-0

Thomson, A.R., Walter, M.J., Kohn, S.C., Brooker, R.A., 2016. Slab melting as a barrier to deep carbon subduction. Nature 529, 76–79. https://doi.org/10.1038/nature16174

Torgersen, T., Jenkins, W.J., 1982. Helium isotopes in geothermal systems: Iceland, The Geysers, Raft River and Steamboat Springs. Geochim. Cosmochim. Acta 46, 739–748. https://doi.org/10.1016/0016-7037(82)90025-4

Torres-González, P.A., Luengo-Oroz, N., Lamolda, H., D'Alessandro, W., Albert, H., Iribarren, I., Moure-García, D., Soler, V., 2020. Unrest signals after 46 years of quiescence at Cumbre Vieja, La Palma, Canary Islands. J. Volcanol. Geotherm. Res. 392, 106757. https://doi.org/10.1016/j.jvolgeores.2019.106757

Touron, S., Renac, C., O'Reilly, S.Y., Cottin, J.-Y., Griffin, W.L., 2008. Characterization of the metasomatic agent in mantle xenoliths from Devès, Massif Central (France) using coupled *in situ* trace-element and O, Sr and Nd isotopic compositions. Geol. Soc. Lond. Spec. Publ. 293, 177–196. https://doi.org/10.1144/SP293.9

Troll, V.R., Carracedo, J.C., 2016. The Geology of the Canary Islands. Elsevier. https://doi.org/10.1016/C2015-0-04268-X

Trull, T., Nadeau, S., Pineau, F., Polve´, M., Javoy, M., 1993. C-He systematics in hotspot xenoliths: Implications for mantle carbon contents and carbon recycling. Earth Planet. Sci. Lett. 118, 43–64. https://doi.org/10.1016/0012-821X(93)90158-6

Trull, T.W., Kurz, M.D., 1993. Experimental measurements of 3He and 4He mobility in olivine and clinopyroxene at magmatic temperatures. Geochim. Cosmochim. Acta 57, 1313–1324. https://doi.org/10.1016/0016-7037(93)90068-8

Tucker, J.M., Mukhopadhyay, S., Gonnermann, H.M., 2018. Reconstructing mantle carbon and noble gas contents from degassed mid-ocean ridge basalts. Earth Planet. Sci. Lett. 496, 108–119. https://doi.org/10.1016/j.epsl.2018.05.024

Urrutia-Fucugauchi, J., Böhnel, H., 1988. Tectonics along the Trans-Mexican volcanic belt according to palaeomagnetic data. Phys. Earth Planet. Inter. 52, 320–329. https://doi.org/10.1016/0031-9201(88)90124-0

Urrutia-Fucugauchi, J., Flores-Ruiz, J.H., Bandy, W.L., Mortera-Gutiérrez, C.A., 1999. Crustal structure of the Colima rift, western Mexico: Gravity models revisited. Geofis. Int. 38, 205–216.

Valbracht, P.J., Staudigel, H., Honda, M., McDougall, I., Davies, G.R., 1996. Isotopic tracing of volcanic source regions from Hawaii: decoupling of gaseous from lithophile magma components. Earth Planet. Sci. Lett. 144, 185–198. https://doi.org/10.1016/0012-821X(96)00126-4

van den Bogaard, P., 2013. The origin of the Canary Island Seamount Province - New ages of old seamounts. Sci. Rep. 3, 2107. https://doi.org/10.1038/srep02107

van den Bogaard, P., Schmincke, H.-U., Freundt, A., Hall, C.M., York, D., 1988. Eruption ages and magma supply rates during the miocene evolution of Gran Canaria: Single-crystal 40Ar/39Ar laser ages. Naturwissenschaften 75, 616–617. https://doi.org/10.1007/BF00366475

Vance, D., Stone, J.O.H., O'Nions, R.K., 1989. He, Sr and Nd isotopes in xenoliths from Hawaii and other oceanic islands. Earth Planet. Sci. Lett. 96, 147–160. https://doi.org/10.1016/0012-821X(89)90129-5

Verma, S.P., 2000. Geochemistry of the subducting Cocos plate and the origin of subduction-unrelated mafic volcanism at the volcanic front of the central Mexican Volcanic Belt, in: Cenozoic Tectonics and Volcanism of Mexico. Geological Society of America. https://doi.org/10.1130/0-8137-2334-5.195

Verma, S.P., Hasenaka, T., 2004. Sr, Nd, and Pb isotopic and trace element geochemical constraints for a veined-mantle source of magmas in the Michoacan-Guanajuato Volcanic Field, west-central Mexican Volcanic Belt. Geochem. J. 38, 43–65. https://doi.org/10.2343/geochemj.38.43

von Gehlen, K., 1992. Sulfur in the Earth's Mantle — A Review, in: Schidlowski, M., Golubic, S., Kimberley, M.M., McKirdy, D.M., Trudinger, P.A. (Eds.), Early Organic Evolution. Springer Berlin Heidelberg, Berlin, Heidelberg, pp. 359–366. https://doi.org/10.1007/978-3-642-76884-2_27

Wallace, R.E., 1990. The San Andreas Fault System, California (Report No. 1515), Professional Paper. U.S. Geological Survey. https://doi.org/10.3133/pp1515

White, W.M., Hofmann, A.W., 1982. Sr and Nd isotope geochemistry of oceanic basalts and mantle evolution. Nature 296, 821–825. https://doi.org/10.1038/296821a0

Williams, Q., Hemley, R.J., 2001. Hydrogen in the Deep Earth. Annu. Rev. Earth Planet. Sci. 29, 365–418. https://doi.org/10.1146/annurev.earth.29.1.365

Williams, S.N., Sano, Y., Wakita, H., 1987. Helium-3 emission from Nevado Del Ruiz Volcano, Colombia. Geophys. Res. Lett. 14, 1035–1038. https://doi.org/10.1029/GL014i010p01035

Witt-Eickschen, G., 2003. Lithospheric Mantle Evolution beneath the Eifel (Germany): Constraints from Sr-Nd-Pb Isotopes and Trace Element Abundances in Spinel Peridotite and Pyroxenite Xenoliths. J. Petrol. 44, 1077–1095. https://doi.org/10.1093/petrology/44.6.1077

Wojdyr, M., 2010. Fityk: a general-purpose peak fitting program. J. Appl. Crystallogr. 43, 1126–1128. https://doi.org/10.1107/S0021889810030499

Wu, D., Liu, Y., Chen, C., Xu, R., Ducea, M.N., Hu, Z., Zong, K., 2017. In-situ trace element and Sr isotopic compositions of mantle xenoliths constrain two-stage metasomatism beneath the northern North China Craton. Lithos 288–289, 338–351. https://doi.org/10.1016/j.lithos.2017.07.018

Yamamoto, J., 2004. Evidence for subduction-related components in the subcontinental mantle from low 3He/4He and 40Ar/36Ar ratio in mantle xenoliths from Far Eastern Russia. Chem. Geol. - CHEM GEOL 207. https://doi.org/10.1016/S0009-2541(04)00108-1

Yamamoto, J., Nishimura, K., Sugimoto, T., Takemura, K., Takahata, N., Sano, Y., 2009. Diffusive fractionation of noble gases in mantle with magma channels: Origin of low He/Ar in mantle-derived rocks. Earth Planet. Sci. Lett. 280, 167–174. https://doi.org/10.1016/j.epsl.2009.01.029

Yang, T.F., Marty, B., Hilton, D.R., Kurz, M.D., 2009. Geochemical Applications of Noble Gases. Chem. Geol. 266, 1–3. https://doi.org/10.1016/j.chemgeo.2009.07.005

Yaxley, G., Kamenetsky, V., Green, D., Falloon, T., 1997. Glasses in mantle xenoliths from western Victoria, Australia, and their relevance to mantle processes. Earth Planet. Sci. Lett. 148, 433–446. https://doi.org/10.1016/S0012-821X(97)00058-7

Zhang, M., Niu, Y., Hu, P.Q., 2009. Volatiles in the mantle lithosphere: Modes of occurrence and chemical compositions, in: The Lithosphere: Geochemistry, Geology and Geophysics. New York, pp. 171–212.

Zindler, A., Hart, S., 1986. Chemical Geodynamics. Annu. Rev. Earth Planet. Sci. 14, 493–571. https://doi.org/10.1146/annurev.ea.14.050186.002425

Zipfel, J., Wörner, G., 1992. Four- and five-phase peridotites from a continental rift system: evidence for upper mantle uplift and cooling at the Ross Sea margin (Antarctica). Contrib. Mineral. Petrol. 111, 24–36. https://doi.org/10.1007/BF00296575

SUPPLEMENTARY TABLES

Table S 1. Noble gas and CO_2 isotopic compositions reported in the literature for the Canary Islands. Reported errors are 2σ uncertainties.

Locality	Sample ID	Rock	Phase	Reference	Extraction Method (FI)	Age (ka)	^{3}He (mol/g)	^{4}He (mol/g)	^{20}Ne (mol/g)	^{40}Ar (mol/g)	^{36}Ar (mol/g)	$^{40}Ar^{*}$ (mol/g)	$^{4}He/^{20}Ne$	$^{4}He/^{40}Ar^{*}$	$^{4}He/CO_2$
Gran Canaria	GC59	Basalt	Ol	Gurenko et al. (2006)	Multistep Crushing	-	1.57E-18	1.56E-13	2.60E-16	4.92E-13	1.17E-15	1.47E-13	599.79	1.05	-
Gran Canaria	GC35	Basalt	Ol	Gurenko et al. (2006)	Multistep Crushing	-	1.66E-19	1.78E-14	2.38E-16	3.38E-13	9.28E-16	6.36E-14	74.86	0.28	-
Gran Canaria	BM69286	Dolerite	Ol	Vance et al. (1989)	Multistep Crushing	-	4.32E-18	5.54E-13	-	-	-	-	-	-	-
Gran Canaria	BM1911160529	Basalt	Ol	Vance et al. (1989)	Multistep Crushing	-	3.20E-17	3.97E-12	-	-	-	-	-	-	-
Gran Canaria	BM1965P8151	Pyroxenite	Cpx	Vance et al. (1989)	Multistep Crushing	2700	7.30E-17	8.75E-12	-	-	-	-	-	-	-
Gran Canaria	BM1965P815j	Harzburgite	Opx	Vance et al. (1989)	Multistep Crushing	2700	1.62E-17	2.10E-12	-	-	-	-	-	-	-
Lanzarote	BM1965P72b	Lherzolite	Cpx	Vance et al. (1989)	Multistep Crushing	0.29	1.38E-16	1.52E-11	-	-	-	-	-	-	-
Lanzarote	BM1965P72	Harzburgite	-	Vance et al. (1989)	Multistep Crushing	-	3.31E-16	3.62E-11	-	-	-	-	-	-	-
Lanzarote	BM1965P74a	Gabbro	Cpx	Vance et al. (1989)	Multistep Crushing	0.29	4.16E-16	4.82E-11	-	-	-	-	-	-	-
Lanzarote	BM1965P77a	Dunite	Cpx	Vance et al. (1989)	Multistep Crushing	0.29	2.26E-17	2.77E-12	-	-	-	-	-	-	-
Lanzarote	L-88-1	Harzburgite	-	Grachev (2012)	Melting	2600	7.26E-17	8.93E-12	-	3.97E-11	3.68E-14	2.89E-11	-	0.31	-
Lanzarote	L-88-1/2	Dunite	-	Grachev (2012)	Melting	2600	6.23E-17	2.01E-11	-	9.73E-11	3.89E-14	8.58E-11	-	0.23	-
Lanzarote	L-88-1/3	Harzburgite	-	Grachev (2012)	Melting	2600	1.12E-16	1.12E-11	-	2.95E-10	2.46E-13	2.22E-10	-	0.05	-
Lanzarote	L-88-1/3	Harzburgite	Ol	Grachev (2012)	Melting	2600	6.28E-18	8.93E-13	-	-	-	-	-	-	-
Lanzarote	L-88-1/4	Dunite	-	Grachev (2012)	Melting	2600	7.47E-17	7.59E-12	-	1.34E-10	3.52E-14	1.24E-10	-	0.06	-
Lanzarote	L-88-2/1	Dunite	-	Grachev (2012)	Melting	-	1.34E-16	1.34E-11	-	2.46E-11	1.57E-14	1.99E-11	-	0.67	-
Lanzarote	L-88-2/4	Dunite	-	Grachev (2012)	Melting	-	8.07E-17	6.70E-12	-	1.40E-10	3.80E-14	1.29E-10	-	0.05	-
Lanzarote	Tim-1	Harzburgite	Ol	Grachev (2012)	Melting	0.3	2.23E-17	1.79E-12	-	-	-	-	-	-	-
Lanzarote	Tim-1	Harzburgite	Opx	Grachev (2012)	Multistep Crushing	0.3	1.04E-16	1.21E-11	-	-	-	-	-	-	-
Lanzarote	Tim-1	Harzburgite	Ol	Grachev (2012)	Multistep Crushing	0.3	4.02E-17	5.36E-12	-	-	-	-	-	-	-
Lanzarote	Tim-2	Harzburgite	Ol	Grachev (2012)	Melting	0.3	1.57E-17	2.23E-12	-	-	-	-	-	-	-
Lanzarote	Tam-1	Harzburgite	Ol	Grachev (2012)	Melting	2600	1.57E-17	1.79E-12	-	-	-	-	-	-	-
Lanzarote	Tam-2	Harzburgite	Ol	Grachev (2012)	Melting	2600	1.72E-17	4.46E-12	-	-	-	-	-	-	-
Lanzarote	Tam-3	Harzburgite	Ol	Grachev (2012)	Melting	2600	5.36E-17	1.34E-11	-	-	-	-	-	-	-
Lanzarote	Lanz560	Mantle xenolith	Cpx	Grachev (2012)	Multistep Crushing	-	1.08E-16	1.12E-11	-	-	-	-	-	-	-
Lanzarote	Lanz560	Mantle xenolith	Opx	Grachev (2012)	Multistep Crushing	-	1.52E-16	1.79E-11	-	-	-	-	-	-	-
Lanzarote	Lanz560	Mantle xenolith	Ol	Grachev (2012)	Multistep Crushing	-	7.31E-17	7.59E-12	-	-	-	-	-	-	-
Lanzarote	L-88-1 BAS	Basalt	Ol	Grachev (2012)	Melting	2600	1.86E-16	3.13E-11	-	9.15E-11	8.55E-14	6.62E-11	-	0.47	-
Lanzarote	L-88-1/2 BAS	Basalt	Ol	Grachev (2012)	Melting	2600	1.35E-17	2.23E-12	-	5.40E-11	1.66E-13	4.90E-12	-	0.46	-

Location	Sample	Rock type	Mineral	Reference	Method										
Lanzarote	L-88-1 BAS	Basalt	Ol	Grachev (2012)	Melting	2600	2.98E-17	1.07E-11	-	4.60E-11	1.09E-13	1.36E-11	-	0.79	-
Lanzarote	L-88-1/2 BAS	Basalt	Ol	Grachev (2012)	Melting	2600	2.61E-17	9.38E-12	-	6.25E-11	1.60E-13	1.51E-11	-	0.62	-
Lanzarote	L-88-1/3 BAS	Basalt	Ol	Grachev (2012)	Melting	2600	1.33E-18	2.23E-12	-	2.68E-11	7.61E-14	4.30E-12	-	0.52	-
Lanzarote	L-88-1/3 BAS	Basalt	Ol	Grachev (2012)	Melting	2600	5.60E-18	9.38E-12	-	7.50E-11	1.83E-13	2.08E-11	-	0.45	-
Lanzarote	L-88-1/4 BAS	Basalt	Ol	Grachev (2012)	Melting	2600	1.09E-18	1.12E-11	-	5.04E-11	1.03E-13	2.01E-11	-	0.56	-
Fuerteventura	FUE1-03	Carbonatite	Apatite	Carnevale et al 2021	Single step Crushing	25000	3.57E-18	9.87E-10	-	-	-	-	45374.6	-	-
Fuerteventura	FUE1-04	Carbonatite	Apatite	Carnevale et al 2021	Single step Crushing	25000	2.23E-17	2.30E-10	-	-	-	-	8294.3	-	-
Fuerteventura	FUE1-03	Carbonatite	Calcite	Carnevale et al 2021	Single step Crushing	25000	3.17E-16	6.79E-11	-	-	-	-	641.1	-	-
Fuerteventura	FUE3-01	Carbonatite	Calcite	Carnevale et al 2021	Single step Crushing	25000	2.04E-16	3.82E-11	-	-	-	-	500.1	-	-
Fuerteventura	FUE3-01	Carbonatite	Calcite	Carnevale et al 2021	Single step Crushing	25000	1.38E-16	2.58E-11	-	-	-	-	388.8	-	-
Fuerteventura	FUE3-01	Carbonatite	Cpx	Carnevale et al 2021	Single step Crushing	25000	6.88E-17	2.21E-11	-	-	-	-	1582.6	-	-
Fuerteventura	FUE4-03	Clinopyroxene	Cpx	Carnevale et al 2021	Single step Crushing	25000	3.39E-17	3.71E-12	-	-	-	-	1120.7	-	-
La Palma	JMDDLP01	Ankaramite	Ol	Day and Hilton (2011)	Crushing	1440	2.05E-18	2.05E-13	-	-	-	-	-	-	-
La Palma	JMDDLP01	Ankaramite	Cpx	Day and Hilton (2011)	Crushing	1440	1.10E-17	1.11E-12	-	-	-	-	-	-	-
La Palma	JMDDLP02	Ankaramite	Ol	Day and Hilton (2011)	Crushing	1440	1.78E-17	1.71E-12	-	-	-	-	-	-	-
La Palma	JMDDLP02	Ankaramite	Cpx	Day and Hilton (2011)	Crushing	1440	3.62E-18	5.04E-13	-	-	-	-	-	-	-
La Palma	JMDDLP03	Picrite	Ol	Day and Hilton (2011)	Crushing	3000	1.15E-18	8.48E-14	-	-	-	-	-	-	-
La Palma	JMDDLP04	Basanite	Ol	Day and Hilton (2011)	Crushing	1020	3.57E-18	3.26E-13	-	-	-	-	-	-	-
La Palma	JMDDLP04	Basanite	Cpx	Day and Hilton (2011)	Crushing	1020	2.14E-18	3.62E-13	-	-	-	-	-	-	-
La Palma	JMDDLP05	Basanite	Ol	Day and Hilton (2011)	Crushing	1020	5.21E-18	4.82E-13	-	-	-	-	-	-	-
La Palma	JMDDLP05	Basanite	Cpx	Day and Hilton (2011)	Crushing	1020	1.56E-17	1.66E-12	-	-	-	-	-	-	-
La Palma	JMDDLP07	Ankaramite	Ol	Day and Hilton (2011)	Crushing	1020	1.42E-17	1.45E-12	-	-	-	-	-	-	-
La Palma	JMDDLP09	Alkali basalt	Ol	Day and Hilton (2011)	Crushing	490	3.92E-18	3.21E-13	-	-	-	-	-	-	-
La Palma	JMDDLP09	Alkali basalt	Cpx	Day and Hilton (2011)	Crushing	490	2.22E-17	1.97E-12	-	-	-	-	-	-	-
La Palma	JMDDLP10	Anjaramite	Ol	Day and Hilton (2011)	Crushing	900	6.22E-19	6.25E-14	-	-	-	-	-	-	-
La Palma	JMDDLP11	Basanite	Ol	Day and Hilton (2011)	Crushing	570	2.47E-18	2.68E-13	-	-	-	-	-	-	-
La Palma	JMDDLP13A	Ol Clinopyroxenite	Ol	Day and Hilton (2011)	Crushing	120	6.55E-17	7.60E-12	-	-	-	-	-	-	-
La Palma	JMDDLP13A	Ol Clinopyroxenite	Cpx	Day and Hilton (2011)	Crushing	120	3.94E-18	3.66E-13	-	-	-	-	-	-	-
La Palma	JMDDLP13B	Ol Clinopyroxenite	Cpx	Day and Hilton (2011)	Crushing	120	1.57E-17	1.53E-12	-	-	-	-	-	-	-
La Palma	JMDDLP14	Basanite	Ol	Day and Hilton (2011)	Crushing	120	1.29E-17	1.26E-12	-	-	-	-	-	-	-
La Palma	JMDDLP21bi	Honrblendite	Ol	Day and Hilton (2011)	Crushing	3	1.18E-17	1.31E-12	-	-	-	-	-	-	-
La Palma	JMDDLP21bi	Gabbro	Cpx	Day and Hilton (2011)	Crushing	3	4.02E-18	4.96E-13	-	-	-	-	-	-	-
La Palma	LP96-66	Lava	Ol	Day and Hilton (2011)	Crushing	850	7.74E-18	7.05E-13	-	-	-	-	-	-	-
La Palma	LP30e	Lava	Ol	Hilton et al. (2000)	Multistep Crushing	-	-	1.65E-12	-	-	-	-	-	-	-
La Palma	LP30e	Lava	Cpx	Hilton et al. (2000)	Multistep Crushing	-	-	2.17E-12	-	-	-	-	-	-	-
La Palma	71LP41	Lava	Ol	Hilton et al. (2000)	Multistep Crushing	-	-	2.04E-12	-	-	-	-	-	-	-

Location	Sample	Rock type	Mineral	Reference	Method										
La Palma	71LP41	Lava	Cpx	Hilton et al. (2000)	Multistep Crushing	-	-	3.73E-12	-	-	-	-	-	-	-
La Palma	LP43e	Lava	Ol	Hilton et al. (2000)	Multistep Crushing	-	-	1.04E-12	-	-	-	-	-	-	-
La Palma	LP43e	Lava	Cpx	Hilton et al. (2000)	Multistep Crushing	-	-	2.50E-12	-	-	-	-	-	-	-
La Palma	151LP69e	Lava	Ol	Hilton et al. (2000)	Multistep Crushing	-	-	1.35E-12	-	-	-	-	-	-	-
La Palma	151LP69e	Lava	Cpx	Hilton et al. (2000)	Multistep Crushing	-	-	2.56E-12	-	-	-	-	-	-	-
La Palma	LP95b	Lava	Ol	Hilton et al. (2000)	Multistep Crushing	-	-	2.22E-12	-	-	-	-	-	-	-
La Palma	LP95b	Lava	Cpx	Hilton et al. (2000)	Multistep Crushing	-	-	1.66E-12	-	-	-	-	-	-	-
La Palma	96LP46	Lava	Ol	Hilton et al. (2000)	Multistep Crushing	-	-	7.37E-13	-	-	-	-	-	-	-
La Palma	96LP46	Lava	Cpx	Hilton et al. (2000)	Multistep Crushing	-	-	3.79E-13	-	-	-	-	-	-	-
La Palma	93LP106	Lava	Ol	Hilton et al. (2000)	Multistep Crushing	-	-	1.21E-13	-	-	-	-	-	-	-
La Palma	93LP106	Lava	Cpx	Hilton et al. (2000)	Multistep Crushing	-	-	3.13E-14	-	-	-	-	-	-	-
La Palma	93LP107	Lava	Ol	Hilton et al. (2000)	Multistep Crushing	-	-	9.82E-14	-	-	-	-	-	-	-
La Palma	93LP107	Lava	Cpx	Hilton et al. (2000)	Multistep Crushing	-	-	1.88E-13	-	-	-	-	-	-	-
La Palma	93LP110	Lava	Ol	Hilton et al. (2000)	Multistep Crushing	-	-	5.18E-13	-	-	-	-	-	-	-
La Palma	93LP110	Lava	Cpx	Hilton et al. (2000)	Multistep Crushing	-	-	1.38E-13	-	-	-	-	-	-	-
La Palma	93LP113	Lava	Ol	Hilton et al. (2000)	Multistep Crushing	-	-	5.04E-13	-	-	-	-	-	-	-
La Palma	93LP113	Lava	Cpx	Hilton et al. (2000)	Multistep Crushing	-	-	1.34E-13	-	-	-	-	-	-	-
La Palma	93LP134	Mafic sill	Ol	Hilton et al. (2000)	Multistep Crushing	-	-	2.00E-12	-	-	-	-	-	-	-
La Palma	93LP134	Mafic sill	Cpx	Hilton et al. (2000)	Multistep Crushing	-	-	1.28E-12	-	-	-	-	-	-	-
La Palma	93LP154	-	Bubbling gases	Hilton et al. (2000)	-	-	-	-	-	-	-	-	-	-	-
La Palma	LP1	Picrite	Ol	Gurenko et al. (2006)	Multistep Crushing	600	5.50E-18	5.17E-13	1.65E-15	1.88E-12	5.19E-15	3.45E-13	312.38	1.50	-
La Palma	LP13	Picrite	Ol	Gurenko et al. (2006)	Multistep Crushing	-	4.78E-17	3.69E-12	5.79E-16	-	-	-	6380.88	-	-
La Palma	A	-	Bubbling gases	Pérez et al. (1994)	-	-	0.029	-	-	-	-	-	-	50.0	-	-
La Palma	B	-	Bubbling gases	Padrón et al. (2015)	-	-	0.021	-	-	-	-	-	-	-	-	-
La Palma	C	-	Bubbling gases	Padrón et al. (2015)	-	-	0.013	-	-	-	-	-	-	119.1	-	-
La Palma	D	-	Bubbling gases	Padrón et al. (2015)	-	-	0.012	-	-	-	-	-	-	78.30	-	-
La Palma	E	-	Bubbling gases	Padrón et al. (2015)	-	-	0.01	-	-	-	-	-	-	181	-	1.45E-05
La Palma	F	-	Bubbling gases	Padrón et al. (2015)	-	-	0.009	-	-	-	-	-	-	169.1	-	1.29E-05
La Palma	G	-	Bubbling gases	Padrón et al. (2015)	-	-	0.008	-	-	-	-	-	-	212.3	-	-
La Palma	H	-	Bubbling gases	Padrón et al. (2015)	-	-	0.008	-	-	-	-	-	-	14.9	-	1.26E-05
La Palma	I	-	Bubbling gases	Padrón et al. (2015)	-	-	0.008	-	-	-	-	-	-	215.7	-	1.02E-05
La Palma	QP60	-	Bubbling gases	Torres-González et al. (2020)	-	-	0.004	-	-	-	-	-	-	25.7	-	-
La Palma	QP60	-	Bubbling gases	Torres-González et al. (2020)	-	-	0.004	-	-	-	-	-	-	73.4	-	-
La Palma	QP60	-	Bubbling gases	Torres-González et al. (2020)	-	-	0.004	-	-	-	-	-	-	102.1	-	-
La Palma	QP60	-	Bubbling gases	Torres-González et al. (2020)	-	-	0.004	-	-	-	-	-	-	160.7	-	-

Location	Sample	Rock type	Phase	Reference	Method										
La Palma	QP60	-	Bubbling gases	Torres-González et al. (2020)	-	0.003	-	-	-	-	-	-	45.6	-	-
La Palma	QP60	-	Bubbling gases	Torres-González et al. (2020)	-	0.003	-	-	-	-	-	-	35.8	-	-
La Palma	QP60	-	Bubbling gases	Torres-González et al. (2020)	-	0.003	-	-	-	-	-	-	34.2	-	-
La Palma	QP60	-	Bubbling gases	Torres-González et al. (2020)	-	0.002	-	-	-	-	-	-	79.0	-	-
La Palma	QP60	-	Bubbling gases	Torres-González et al. (2020)	-	0.002	-	-	-	-	-	-	110.5	-	-
La Palma	QP60	-	Bubbling gases	Torres-González et al. (2020)	-	0.002	-	-	-	-	-	-	96.4	-	-
La Palma	QP60	-	Bubbling gases	Torres-González et al. (2020)	-	0.002	-	-	-	-	-	-	142.9	-	-
La Palma	QP60	-	Bubbling gases	Torres-González et al. (2020)	-	0.002	-	-	-	-	-	-	106.9	-	-
La Palma	QP60	-	Bubbling gases	Torres-González et al. (2020)	-	0.001	-	-	-	-	-	-	55.0	-	-
La Palma	QP63	-	Groundwater	Torres-González et al. (2020)	-	0.004	-	-	-	-	-	-	1.70	-	-
La Palma	QP63	-	Groundwater	Torres-González et al. (2020)	-	0.004	-	-	-	-	-	-	1.23	-	-
La Palma	QP63	-	Groundwater	Torres-González et al. (2020)	-	0.003	-	-	-	-	-	-	1.20	-	-
La Palma	QP63	-	Groundwater	Torres-González et al. (2020)	-	0.003	-	-	-	-	-	-	0.45	-	-
La Palma	QP63	-	Groundwater	Torres-González et al. (2020)	-	0.003	-	-	-	-	-	-	2.75	-	-
La Palma	QP63	-	Groundwater	Torres-González et al. (2020)	-	0.003	-	-	-	-	-	-	2.40	-	-
La Palma	QP63	-	Groundwater	Torres-González et al. (2020)	-	0.003	-	-	-	-	-	-	1.12	-	-
La Palma	QP63	-	Groundwater	Torres-González et al. (2020)	-	0.002	-	-	-	-	-	-	1.34	-	-
La Palma	QP63	-	Groundwater	Torres-González et al. (2020)	-	0.002	-	-	-	-	-	-	1.37	-	-
La Palma	QP63	-	Groundwater	Torres-González et al. (2020)	-	0.002	-	-	-	-	-	-	0.84	-	-
La Palma	QP63	-	Groundwater	Torres-González et al. (2020)	-	0.002	-	-	-	-	-	-	1.93	-	-
La Palma	QP63	-	Groundwater	Torres-González et al. (2020)	-	0.002	-	-	-	-	-	-	1.02	-	-
La Palma	QP63	-	Groundwater	Torres-González et al. (2020)	-	0.002	-	-	-	-	-	-	2.09	-	-
La Palma	QP63	-	Groundwater	Torres-González et al. (2020)	-	0.002	-	-	-	-	-	-	1.55	-	-
La Palma	QP63	-	Groundwater	Torres-González et al. (2020)	-	0.001	-	-	-	-	-	-	0.49	-	-
La Palma	CAN-11	-	Bubbling gases	Day and Hilton (2020)	-	0.014	1.07E-16	8.30E-12	-	-	-	-	12.49	-	3.96E-05
La Palma	CAN-14	-	Bubbling gases	Day and Hilton (2020)	-	0.014	1.28E-16	1.05E-11	-	-	-	-	10.59	-	1.55E-05
La Gomera	LG1	Picrite	Ol	Gurenko et al. (2006)	Multistep Crushing	8600	6.93E-19	7.63E-14	8.92E-16	1.07E-12	3.38E-15	6.59E-14	85.58	1.16	-
La Gomera	LG35	Picrite	Ol	Gurenko et al. (2006)	Multistep Crushing	-	4.67E-19	5.93E-14	5.93E-16	8.82E-13	1.97E-15	2.99E-13	99.95	0.20	-
La Gomera	LG59	Picrite	Ol	Gurenko et al. (2006)	Multistep Crushing	10200	4.21E-18	3.69E-13	9.44E-16	2.10E-12	5.54E-15	4.63E-13	390.81	0.80	-
Tenerife	TF4	Picritic basalt	Ol	Gurenko et al. (2006)	Multistep Crushing	-	8.88E-19	9.23E-14	1.01E-16	3.60E-13	1.01E-15	6.29E-14	918.08	1.47	

Location	Sample	Rock type	Mineral	Reference	Method											
Tenerife	TF7	Picritic basalt	Ol	Gurenko et al. (2006)	Multistep Crushing	-	5.01E-19	5.43E-14	7.30E-16	1.03E-12	2.69E-15	2.33E-13	74.35	0.23	-
Tenerife	TF16	Picritic basalt	Ol	Gurenko et al. (2006)	Multistep Crushing	-	7.36E-19	6.13E-14	8.65E-16	2.13E-12	6.97E-15	7.32E-14	70.85	0.84	-
Tenerife	TF23	Basalt	Ol	Gurenko et al. (2006)	Multistep Crushing	-	8.84E-19	9.28E-14	4.04E-16	5.62E-13	1.36E-15	1.61E-13	229.77	0.58	-
Tenerife	BM1911160529	Basalt	Cpx	Vance et al 1989	Multistep Crushing	-	3.37E-18	4.15E-13					-	-	-
Tenerife	Teide Fumarole	-	Fumaroles	Alonso et al 2019	-	0.005	-	-	-	-	-	-	33.61	-	-
Tenerife	31	-	Diffuse Emission	Hernández et al. (1998)	-	0.025	-	-	-	-	-	-	-	-	-
Tenerife	82	-	Diffuse Emission	Hernández et al. (1998)	-	0.025	-	-	-	-	-	-	-	-	-
Tenerife	86	-	Diffuse Emission	Hernández et al. (1998)	-	0.025	-	-	-	-	-	-	-	-	-
Tenerife	87	-	Diffuse Emission	Hernández et al. (1998)	-	0.025	-	-	-	-	-	-	-	-	-
Tenerife	89	-	Diffuse Emission	Hernández et al. (1998)	-	0.025	-	-	-	-	-	-	-	-	-
Tenerife	90	-	Diffuse Emission	Hernández et al. (1998)	-	0.025	-	-	-	-	-	-	-	-	-
Tenerife	95	-	Diffuse Emission	Hernández et al. (1998)	-	0.025	-	-	-	-	-	-	-	-	-
Tenerife	96	-	Diffuse Emission	Hernández et al. (1998)	-	0.025	-	-	-	-	-	-	-	-	-
Tenerife	97	-	Diffuse Emission	Hernández et al. (1998)	-	0.025	-	-	-	-	-	-	-	-	-
Tenerife	HLA	-	Groundwater	Marrero-Diaz et al. (2015)	-	0.014	-	-	-	-	-	-	-	-	-
Tenerife	LGA	-	Groundwater	Marrero-Diaz et al. (2015)	-	0.014	-	-	-	-	-	-	0.38	-	-
Tenerife	TAG	-	Groundwater	Marrero-Diaz et al. (2015)	-	0.014	-	-	-	-	-	-	-	-	-
Tenerife	NIA	-	Groundwater	Marrero-Diaz et al. (2015)	-	0.014	-	-	-	-	-	-	-	-	-
Tenerife	TAM	-	Groundwater	Marrero-Diaz et al. (2015)	-	0.014	-	-	-	-	-	-	0.36	-	-
Tenerife	ESU	-	Groundwater	Marrero-Diaz et al. (2015)	-	0.014	-	-	-	-	-	-	-	-	-
Tenerife	FFA	-	Groundwater	Marrero-Diaz et al. (2015)	-	0.014	-	-	-	-	-	-	-	-	-
Tenerife	S-2	-	Groundwater	Marrero-Diaz et al. (2015)	-	0.014	-	-	-	-	-	-	-	-	-
Tenerife	ALM	-	Groundwater	Marrero-Diaz et al. (2015)	-	0.014	-	-	-	-	-	-	110.00	-	-
Tenerife	CUM	-	Groundwater	Marrero-Diaz et al. (2015)	-	0.014	-	-	-	-	-	-	-	-	-
Tenerife	FP2	-	Groundwater	Marrero-Diaz et al. (2015)	-	0.014	-	-	-	-	-	-	-	-	-
Tenerife	BVA	-	Groundwater	Marrero-Diaz et al. (2015)	-	0.014	-	-	-	-	-	-	3.70	-	-
Tenerife	FLO	-	Groundwater	Marrero-Diaz et al. (2015)	-	0.014	-	-	-	-	-	-	-	-	-
Tenerife	LCO	-	Groundwater	Marrero-Diaz et al. (2015)	-	0.014	-	-	-	-	-	-	-	-	-
Tenerife	SFN	-	Groundwater	Marrero-Diaz et al. (2015)	-	0.014	-	-	-	-	-	-	1.59	-	-
Tenerife	STA	-	Groundwater	Marrero-Diaz et al. (2015)	-	0.014	-	-	-	-	-	-	-	-	-
Tenerife	VE2	-	Groundwater	Marrero-Diaz et al. (2015)	-	0.014	-	-	-	-	-	-	-	-	-
Tenerife	HON	-	Groundwater	Marrero-Diaz et al. (2015)	-	0.014	-	-	-	-	-	-	-	-	-

Location	Sample		Type	Reference												
Tenerife	AAA	-	Groundwater	Marrero-Diaz et al. (2015)	-	0.014	-	-	-	-	-	-	-	-	-	-
Tenerife	CN2	-	Groundwater	Marrero-Diaz et al. (2015)	-	0.014	-	-	-	-	-	-	-	-	-	-
Tenerife	CLS	-	Groundwater	Marrero-Diaz et al. (2015)	-	0.014	-	-	-	-	-	-	0.72	-	-
Tenerife	POR	-	Groundwater	Marrero-Diaz et al. (2015)	-	0.014	-	-	-	-	-	-	0.45	-	-
Tenerife	RC1	-	Groundwater	Marrero-Diaz et al. (2015)	-	0.014	-	-	-	-	-	-	-	-	-
Tenerife	CHI	-	Groundwater	Marrero-Diaz et al. (2015)	-	0.014	-	-	-	-	-	-	0.38	-	-
Tenerife	MEO	-	Groundwater	Marrero-Diaz et al. (2015)	-	0.014	-	-	-	-	-	-	0.33	-	-
Tenerife	PAS	-	Groundwater	Marrero-Diaz et al. (2015)	-	0.014	-	-	-	-	-	-	0.66	-	-
Tenerife	ARG	-	Groundwater	Marrero-Diaz et al. (2015)	-	0.014	-	-	-	-	-	-	-	-	-
Tenerife	HLN	-	Groundwater	Marrero-Diaz et al. (2015)	-	0.014	-	-	-	-	-	-	-	-	-
Tenerife	HPO	-	Groundwater	Marrero-Diaz et al. (2015)	-	0.014	-	-	-	-	-	-	-	-	-
Tenerife	SF3	-	Groundwater	Marrero-Diaz et al. (2015)	-	0.014	-	-	-	-	-	-	-	-	-
Tenerife	SJC	-	Groundwater	Marrero-Diaz et al. (2015)	-	0.014	-	-	-	-	-	-	-	-	-
Tenerife	LAG	-	Groundwater	Marrero-Diaz et al. (2015)	-	0.014	-	-	-	-	-	-	-	-	-
Tenerife	PIO	-	Groundwater	Marrero-Diaz et al. (2015)	-	0.014	-	-	-	-	-	-	1.60	-	-
Tenerife	FVE	-	Groundwater	Marrero-Diaz et al. (2015)	-	0.014	-	-	-	-	-	-	4.95	-	-
Tenerife	NSL	-	Groundwater	Marrero-Diaz et al. (2015)	-	0.014	-	-	-	-	-	-	0.57	-	-
Tenerife	FVE#	-	Groundwater	Marrero-Diaz et al. (2015)	-	0.014	-	-	-	-	-	-	95.70	-	-
Tenerife	LQO	-	Groundwater	Marrero-Diaz et al. (2015)	-	0.014	-	-	-	-	-	-	0.60	-	-
Tenerife	STO	-	Groundwater	Marrero-Diaz et al. (2015)	-	0.014	-	-	-	-	-	-	0.50	-	-
Tenerife	RAO	-	Groundwater	Marrero-Diaz et al. (2015)	-	0.014	-	-	-	-	-	-	0.50	-	-
Tenerife	SIO	-	Groundwater	Marrero-Diaz et al. (2015)	-	0.014	-	-	-	-	-	-	1.10	-	-
Tenerife	ASW	-	Groundwater	Marrero-Diaz et al. (2015)	-	0.014	-	-	-	-	-	-	0.27	-	-
Tenerife	1	-	Fumaroles	Pérez et al. (1996)	-	0.029	-	-	-	-	-	-	120.00	-	-
Tenerife	2	-	Fumaroles	Pérez et al. (1996)	-	0.026	-	-	-	-	-	-	24.00	-	-
Tenerife	3	-	Groundwater	Pérez et al. (1996)	-	0.026	-	-	-	-	-	-	3.70	-	-
Tenerife	4	-	Groundwater	Pérez et al. (1996)	-	0.026	-	-	-	-	-	-	1.10	-	-
Tenerife	5	-	Groundwater	Pérez et al. (1996)	-	0.026	-	-	-	-	-	-	110.00	-	-
Tenerife	6	-	Groundwater	Pérez et al. (1996)	-	0.026	-	-	-	-	-	-	0.60	-	-
Tenerife	7	-	Groundwater	Pérez et al. (1996)	-	0.026	-	-	-	-	-	-	0.50	-	-

129

Location	ID/Date		Type	Reference											
Tenerife	8	-	Groundwater	Pérez et al. (1996)	-	0.027	-	-	-	-	-	-	0.50	-	-
Tenerife	9	-	Bubbling gases	Pérez et al. (1996)	-	0.027	-	-	-	-	-	-	95.70	-	-
Tenerife	CAN-9	-	Fumaroles	Day and Hilton (2020)	-	0.014	1.08E-16	1.26E-11	-	-	-	-	0.77	-	3.05E-05
Tenerife	CAN-10	-	Fumaroles	Day and Hilton (2020)	-	0.014	9.92E-17	1.08E-11	-	-	-	-	10.27	-	1.55E-05
Tenerife	CAN-12	-	Fumaroles	Day and Hilton (2020)	-	0.014	8.77E-19	1.07E-13	-	-	-	-	0.17	-	1.83E-05
Tenerife	CAN-13	-	Fumaroles	Day and Hilton (2020)	-	0.014	7.91E-17	9.42E-12	-	-	-	-	0.37	-	1.56E-05
Tenerife	15/06/1991	-	Fumaroles	Melián et al. (2012)	-	0.029	-	-	-	-	-	-	120	-	-
Tenerife	27/12/1993	-	Fumaroles	Melián et al. (2012)	-	0.027	-	-	-	-	-	-	20	-	-
Tenerife	08/01/1994	-	Fumaroles	Melián et al. (2012)	-	0.026	-	-	-	-	-	-	113	-	-
Tenerife	20/03/1994	-	Fumaroles	Melián et al. (2012)	-	0.026	-	-	-	-	-	-	126	-	-
Tenerife	07/05/1994	-	Fumaroles	Melián et al. (2012)	-	0.026	-	-	-	-	-	-	36	-	-
Tenerife	23/06/1994	-	Fumaroles	Melián et al. (2012)	-	0.026	-	-	-	-	-	-	24	-	-
Tenerife	13/09/1994	-	Fumaroles	Melián et al. (2012)	-	0.026	-	-	-	-	-	-	43	-	-
Tenerife	13/01/1996	-	Fumaroles	Melián et al. (2012)	-	0.024	-	-	-	-	-	-	38	-	-
Tenerife	24/04/1999	-	Fumaroles	Melián et al. (2012)	-	0.021	-	-	-	-	-	-	24	-	-
Tenerife	03/03/2000	-	Fumaroles	Melián et al. (2012)	-	0.02	-	-	-	-	-	-	55	-	-
Tenerife	26/06/2000	-	Fumaroles	Melián et al. (2012)	-	0.02	-	-	-	-	-	-	105	-	-
Tenerife	24/04/2001	-	Fumaroles	Melián et al. (2012)	-	0.019	-	-	-	-	-	-	76	-	-
Tenerife	07/06/2001	-	Fumaroles	Melián et al. (2012)	-	0.019	-	-	-	-	-	-	40	-	-
Tenerife	14/12/2001	-	Fumaroles	Melián et al. (2012)	-	0.019	-	-	-	-	-	-	14	-	-
Tenerife	03/10/2002	-	Fumaroles	Melián et al. (2012)	-	0.018	-	-	-	-	-	-	53	-	-
Tenerife	01/12/2003	-	Fumaroles	Melián et al. (2012)	-	0.017	-	-	-	-	-	-	-	-	3.02E-05
Tenerife	01/07/2004	-	Fumaroles	Melián et al. (2012)	-	0.016	-	-	-	-	-	-	-	-	2.52E-05
Tenerife	25/01/2005	-	Fumaroles	Melián et al. (2012)	-	0.015	-	-	-	-	-	-	64	-	3.06E-05
Tenerife	28/09/2006	-	Fumaroles	Melián et al. (2012)	-	0.014	-	-	-	-	-	-	76	-	1.35E-05
Tenerife	29/01/2008	-	Fumaroles	Melián et al. (2012)	-	0.012	-	-	-	-	-	-	58	-	1.23E-05
Tenerife	16/04/2008	-	Fumaroles	Melián et al. (2012)	-	0.012	-	-	-	-	-	-	18	-	3.53E-05
Tenerife	29/05/2008	-	Fumaroles	Melián et al. (2012)	-	0.012	-	-	-	-	-	-	36	-	3.23E-05
Tenerife	20/08/2008	-	Fumaroles	Melián et al. (2012)	-	0.012	-	-	-	-	-	-	43	-	2.74E-05
Tenerife	13/11/2008	-	Fumaroles	Melián et al. (2012)	-	0.012	-	-	-	-	-	-	77	-	2.67E-05
Tenerife	16/04/2009	-	Fumaroles	Melián et al. (2012)	-	0.011	-	-	-	-	-	-	28	-	2.76E-05
Tenerife	05/06/2009	-	Fumaroles	Melián et al. (2012)	-	0.011	-	-	-	-	-	-	43	-	3.61E-05
Tenerife	10/07/2009	-	Fumaroles	Melián et al. (2012)	-	0.011	-	-	-	-	-	-	23	-	2.69E-05
Tenerife	07/10/2009	-	Fumaroles	Melián et al. (2012)	-	0.011	-	-	-	-	-	-	29	-	2.96E-05
Tenerife	13/01/2010	-	Fumaroles	Melián et al. (2012)	-	0.01	-	-	-	-	-	-	16	-	2.45E-05
El Hierro	-	-	Groundwater	Padrón et al. (2013)	-	0.009	7.58E-16	1.9E-10	-	-	-	-	2.47	-	-

Location	Sample	Rock type	Phase	Reference	Method										
El Hierro	-	-	Groundwater	Padrón et al. (2013)	-	0.009	4.08E-16	1.3E-10	-	-	-	-	1.72	-	-
El Hierro	-	-	Groundwater	Padrón et al. (2013)	-	0.009	3.97E-16	4.3E-11	-	-	-	-	3.14	-	-
El Hierro	-	-	Groundwater	Padrón et al. (2013)	-	0.009	4.43E-16	5.0E-11	-	-	-	-	1.33	-	-
El Hierro	-	-	Groundwater	Padrón et al. (2013)	-	0.009	3.38E-16	5.8E-11	-	-	-	-	1.85	-	-
El Hierro	-	-	Groundwater	Padrón et al. (2013)	-	0.009	5.15E-16	4.7E-11	-	-	-	-	6.73	-	-
El Hierro	-	-	Groundwater	Padrón et al. (2013)	-	0.009	2.82E-16	2.7E-11	-	-	-	-	3.79	-	-
El Hierro	-	-	Groundwater	Padrón et al. (2013)	-	0.009	5.08E-16	4.6E-11	-	-	-	-	6.19	-	-
El Hierro	JMDDEH01	Ankaramite	Ol	Day and Hilton (2011)	Multistep Crushing	1	2.43E-18	2.19E-13	-				-		
El Hierro	JMDDEH01	Ankaramite	Ol	Day and Hilton (2011)	Multistep Crushing	1	2.32E-17	2.14E-12	-	-	-	-	-	-	-
El Hierro	JMDDEH01	Ankaramite	Cpx	Day and Hilton (2011)	Multistep Crushing	1	2.26E-18	2.01E-13	-	-	-	-	-	-	-
El Hierro	JMDDEH01	Ankaramite	Cpx	Day and Hilton (2011)	Multistep Crushing	1	7.91E-18	7.10E-13	-	-	-	-	-	-	-
El Hierro	JMDDEH03	Basanite	Ol	Day and Hilton (2011)	Multistep Crushing	1030	1.84E-17	1.62E-12	-	-	-	-	-	-	-
El Hierro	JMDDEH04cii	Dunite	Ol	Day and Hilton (2011)	Multistep Crushing	1030	2.51E-17	2.40E-12	-	-	-	-	-	-	-
El Hierro	JMDDEH04ciii	Dunite	Ol	Day and Hilton (2011)	Multistep Crushing	1030	1.35E-16	1.27E-11	-	-	-	-	-	-	-
El Hierro	JMDDEH07	Ankaramite	Ol	Day and Hilton (2011)	Multistep Crushing	1030	8.32E-18	7.90E-13	-	-	-	-	-	-	-
El Hierro	JMDDEH07	Ankaramite	Cpx	Day and Hilton (2011)	Multistep Crushing	1030	3.15E-18	3.26E-13	-	-	-	-	-	-	-
El Hierro	JMDDEH10	Ankaramite	Ol	Day and Hilton (2011)	Multistep Crushing	160	1.68E-18	1.61E-13	-	-	-	-	-	-	-
El Hierro	JMDDEH10	Ankaramite	Cpx	Day and Hilton (2011)	Multistep Crushing	160	4.05E-18	4.51E-13	-	-	-	-	-	-	-
El Hierro	JMDDEH11	Alkali basalt	Ol	Day and Hilton (2011)	Multistep Crushing	160	4.78E-18	4.38E-13	-	-	-	-	-	-	-
El Hierro	JMDDEH11	Alkali basalt	Cpx	Day and Hilton (2011)	Multistep Crushing	160	5.34E-18	7.68E-13	-	-	-	-	-	-	-
El Hierro	JMDDEH13	Ankaramite	Ol	Day and Hilton (2011)	Multistep Crushing	135	7.56E-18	7.10E-13	-	-	-	-	-	-	-
El Hierro	JMDDEH13	Ankaramite	Ol	Day and Hilton (2011)	Multistep Crushing	135	6.75E-18	5.94E-13	-	-	-	-	-	-	-
El Hierro	JMDDEH13	Ankaramite	Cpx	Day and Hilton (2011)	Multistep Crushing	135	4.69E-18	8.13E-13	-	-	-	-	-	-	-
El Hierro	JMDDEH14	Alkali basalt	Ol	Day and Hilton (2011)	Multistep Crushing	265	3.90E-18	3.88E-13	-	-	-	-	-	-	-
El Hierro	JMDDEH15	Ankaramite	Ol	Day and Hilton (2011)	Multistep Crushing	335	5.09E-18	4.69E-13	-	-	-	-	-	-	-
El Hierro	JMDDEH15	Ankaramite	Cpx	Day and Hilton (2011)	Multistep Crushing	335	1.36E-17	1.40E-12	-	-	-	-	-	-	-
El Hierro	JMDDEH16	Basanite	Ol	Day and Hilton (2011)	Multistep Crushing	540	6.44E-18	5.94E-13	-	-	-	-	-	-	-
El Hierro	JMDDEH16	Basanite	Cpx	Day and Hilton (2011)	Multistep Crushing	540	1.08E-17	9.96E-13	-	-	-	-	-	-	-
El Hierro	JMDDEH17	Alkali basalt	Ol	Day and Hilton (2011)	Multistep Crushing	10	1.44E-17	1.38E-12	-	-	-	-	-	-	-
El Hierro	JMDDEH18	Ankaramite	Ol	Day and Hilton (2011)	Multistep Crushing	1	6.24E-18	5.89E-13	-	-	-	-	-	-	-
El Hierro	JMDDEH18	Ankaramite	Cpx	Day and Hilton (2011)	Multistep Crushing	1	1.70E-17	1.71E-12	-	-	-	-	-	-	-

Table S1. Continued.

Locality	Sample ID	^{4}He/CO$_2$	R/Ra	Error (+/-)	Rc/Ra	Error (+/-)	^{40}Ar/^{36}Ar	Error (+/-)	^{20}Ne/^{22}Ne	Error (+/-)	^{21}Ne/^{22}Ne	Error (+/-)	δ^{13}C (‰)	CO$_2$/^{3}He
Gran Canaria	GC59	-	7.26	1.03	7.26	-	422	28	9.14	0.54	-	-	-	-
Gran Canaria	GC35	-	6.69	2.55	6.71	-	364	25	-	-	-	-	-	-
Gran Canaria	BM69286	-	5.61	0.32	-	-	-	-	-	-	-	-	-	-
Gran Canaria	BM1911160529	-	5.8	0.32	-	-	-	-	-	-	-	-	-	-
Gran Canaria	BM1965P8151	-	6.00	0.34	-	-	-	-	-	-	-	-	-	-
Gran Canaria	BM1965P815j	-	5.56	0.32	-	-	-	-	-	-	-	-	-	-
Lanzarote	BM1965P72b		6.55	0.36	-	-	-	-	-	-	-	-	-	-
Lanzarote	BM1965P72	-	6.59	0.36	-	-	-	-	-	-	-	-	-	-
Lanzarote	BM1965P74a	-	6.20	0.34	-	-	-	-	-	-	-	-	-	-
Lanzarote	BM1965P77a	-	5.88	0.34	-	-	-	-	-	-	-	-	-	-
Lanzarote	L-88-1	-	5.85	-	-	-	1080	-	-	-	-	-	-	-
Lanzarote	L-88-1/2	-	2.23	-	-	-	2500	-	-	-	-	-	-	-
Lanzarote	L-88-1/3	-	7.22	-	-	-	1200	-	-	-	-	-	-	-
Lanzarote	L-88-1/3	-	5.06	-	-	-	1000	-	-	-	-	-	-	-
Lanzarote	L-88-1/4	-	7.08	-	-	-	3800	-	-	-	-	-	-	-
Lanzarote	L-88-2/1	-	7.21	-	-	-	1560	-	-	-	-	-	-	-
Lanzarote	L-88-2/4	-	8.67	-	-	-	3680	-	-	-	-	-	-	-
Lanzarote	Tim-1	-	9.00	-	-	-	-	-	-	-	-	-	-	-
Lanzarote	Tim-1	-	6.21	-	-	-	-	-	-	-	-	-	-	-
Lanzarote	Tim-1	-	5.40	-	-	-	-	-	-	-	-	-	-	-
Lanzarote	Tim-2	-	5.07	-	-	-	-	-	-	-	-	-	-	-
Lanzarote	Tam-1	-	6.31	-	-	-	-	-	-	-	-	-	-	-
Lanzarote	Tam-2	-	2.77	-	-	-	-	-	-	-	-	-	-	-
Lanzarote	Tam-3	-	2.88	-	-	-	-	-	-	-	-	-	-	-
Lanzarote	Lanz560	-	6.93	-	-	-	-	-	-	-	-	-	-	-
Lanzarote	Lanz560	-	6.14	-	-	-	-	-	-	-	-	-	-	-
Lanzarote	Lanz560	-	6.93	-	-	-	-	-	-	-	-	-	-	-
Lanzarote	L-88-1 BAS	-	4.28	-	-	-	1070	-	-	-	-	-	-	-
Lanzarote	L-88-1/2 BAS	-	4.35	-	-	-	325	-	-	-	-	-	-	-
Lanzarote	L-88-1 BAS	-	2.00	-	-	-	420	-	-	-	-	-	-	-
Lanzarote	L-88-1/2 BAS	-	2.00	-	-	-	390	-	-	-	-	-	-	-
Lanzarote	L-88-1/3 BAS	-	0.43	-	-	-	352	-	-	-	-	-	-	-

Location	Sample													
Lanzarote	L-88-1/3 BAS	-	0.43	-	-	-	409	-	-	-	-	-	-	-
Lanzarote	L-88-1/4 BAS	-	0.07	-	-	-	491	-	-	-	-	-	-	-
Fuerteventura	FUE1-03	-	0.003	0.002	0.003	-	409.08	0.19	-	-	-	-	-	-
Fuerteventura	FUE1-04	-	0.08	0.02	0.08	-	689.59	0.18	-	-	-	-	-	-
Fuerteventura	FUE1-03	-	3.35	0.03	3.35	-	2067.92	1.34	-	-	-	-	-	-
Fuerteventura	FUE3-01	-	3.84	0.04	3.84	-	614.42	0.06	-	-	-	-	-	-
Fuerteventura	FUE3-01	-	3.86	0.04	3.86	-	713.82	0.05	-	-	-	-	-	-
Fuerteventura	FUE3-01	-	2.23	0.04	2.23	-	650.52	0.61	-	-	-	-	-	-
Fuerteventura	FUE4-03	-	6.66	0.07	6.66	-	431.17	0.06	-	-	-	-	-	-
La Palma	JMDDLP01	-	7.20	0.35	-	-	-	-	-	-	-	-	-	-
La Palma	JMDDLP01	-	7.11	0.31	-	-	-	-	-	-	-	-	-	-
La Palma	JMDDLP02	-	7.48	0.19	-	-	-	-	-	-	-	-	-	-
La Palma	JMDDLP02	-	5.17	0.27	-	-	-	-	-	-	-	-	-	-
La Palma	JMDDLP03	-	9.72	0.34	-	-	-	-	-	-	-	-	-	-
La Palma	JMDDLP04	-	7.87	0.38	-	-	-	-	-	-	-	-	-	-
La Palma	JMDDLP04	-	4.26	0.24	-	-	-	-	-	-	-	-	-	-
La Palma	JMDDLP05	-	7.78	0.26	-	-	-	-	-	-	-	-	-	-
La Palma	JMDDLP05	-	6.77	0.23	-	-	-	-	-	-	-	-	-	-
La Palma	JMDDLP07	-	7.05	0.24	-	-	-	-	-	-	-	-	-	-
La Palma	JMDDLP09	-	8.79	0.33	-	-	-	-	-	-	-	-	-	-
La Palma	JMDDLP09	-	8.12	0.27	-	-	-	-	-	-	-	-	-	-
La Palma	JMDDLP10	-	7.16	0.33	-	-	-	-	-	-	-	-	-	-
La Palma	JMDDLP11	-	6.64	0.26	-	-	-	-	-	-	-	-	-	-
La Palma	JMDDLP13A	-	6.2	0.15	-	-	-	-	-	-	-	-	-	-
La Palma	JMDDLP13A	-	7.74	0.41	-	-	-	-	-	-	-	-	-	-
La Palma	JMDDLP13B	-	7.4	0.17	-	-	-	-	-	-	-	-	-	-
La Palma	JMDDLP14	-	7.34	0.24	-	-	-	-	-	-	-	-	-	-
La Palma	JMDDLP21bi	-	6.5	0.16	-	-	-	-	-	-	-	-	-	-
La Palma	JMDDLP21bi	-	5.83	0.18	-	-	-	-	-	-	-	-	-	-
La Palma	LP96-66	-	7.9	0.28	-	-	-	-	-	-	-	-	-	-
La Palma	LP30e	-	7.38	0.35	-	-	-	-	-	-	-	-	-	-
La Palma	LP30e	-	7.196	0.34	-	-	-	-	-	-	-	-	-	-
La Palma	71LP41	-	7.57	0.33	-	-	-	-	-	-	-	-	-	-
La Palma	71LP41	-	7.37	0.25	-	-	-	-	-	-	-	-	-	-
La Palma	LP43e	-	7.49	0.96	-	-	-	-	-	-	-	-	-	-
La Palma	LP43e	-	7.33	0.27	-	-	-	-	-	-	-	-	-	-
La Palma	151LP69e	-	7.82	0.21	-	-	-	-	-	-	-	-	-	-
La Palma	151LP69e	-	7.63	0.22	-	-	-	-	-	-	-	-	-	-
La Palma	LP95b	-	7.04	0.27	-	-	-	-	-	-	-	-	-	-

La Palma	LP95b	-	7.28	0.33	-	-	-	-	-	-	-	-	-	-
La Palma	96LP46	-	8.04	0.34	-	-	-	-	-	-	-	-	-	-
La Palma	96LP46	-	7.72	0.49	-	-	-	-	-	-	-	-	-	-
La Palma	93LP106	-	8.92	0.69	-	-	-	-	-	-	-	-	-	-
La Palma	93LP106	-	7.94	4.72	-	-	-	-	-	-	-	-	-	-
La Palma	93LP107	-	7.1	1.48	-	-	-	-	-	-	-	-	-	-
La Palma	93LP107	-	7.35	0.79	-	-	-	-	-	-	-	-	-	-
La Palma	93LP110	-	6.77	0.46	-	-	-	-	-	-	-	-	-	-
La Palma	93LP110	-	7.24	1.48	-	-	-	-	-	-	-	-	-	-
La Palma	93LP113	-	8	0.29	-	-	-	-	-	-	-	-	-	-
La Palma	93LP113	-	6.35	1.02	-	-	-	-	-	-	-	-	-	-
La Palma	93LP134	-	8.3	0.23	-	-	-	-	-	-	-	-	-	-
La Palma	93LP134	-	8.41	0.27	-	-	-	-	-	-	-	-	-	-
La Palma	93LP154	-	9.5	0.27	-	-	-	-	-	-	-	-	-	1.70E+10
La Palma	LP1	-	7.65	0.68	7.66	-	362	5	9.22	0.09	-	-	-	-
La Palma	LP13	-	9.31	0.59	9.31	-	-	-	9.69	0.40	-	-	-	-
La Palma	A	-	9.63	0.06	9.68	0.06	-	-	-	-	-	-	-	-
La Palma	B	-	9.5	-	-	-	-	-	-	-	-	-	-	1.70E+10
La Palma	C	-	9.40	0.08	9.42	0.08	-	-	-	-	-	-	-	-
La Palma	D	-	9.82	0.09	9.86	0.09	-	-	-	-	-	-	-	-
La Palma	E	1.45E-05	9.95	0.12	9.96	0.12	-	-	-	-	-	-	-3.6	5.00E+09
La Palma	F	1.29E-05	9.43	0.12	9.45	0.12	-	-	-	-	-	-	-3.2	5.90E+09
La Palma	G	-	9.80	0.07	9.81	0.07	-	-	-	-	-	-	-	-
La Palma	H	1.26E-05	10.04	0.07	10.24	0.07	-	-	-	-	-	-	-2.9	5.70E+09
La Palma	I	1.02E-05	9.70	0.12	9.71	0.12	-	-	-	-	-	-	-3.7	7.30E+09
La Palma	QP60	-	9.61	-	9.72	-	-	-	-	-	-	-	-	-
La Palma	QP60	-	9.85	-	9.89	-	-	-	-	-	-	-	-3.8	-
La Palma	QP60	-	9.92	-	9.95	-	-	-	-	-	-	-	-3.4	-
La Palma	QP60	-	9.82	-	9.84	-	-	-	-	-	-	-	-3.7	-
La Palma	QP60	-	9.32	-	9.38	-	-	-	-	-	-	-	-3.6	-
La Palma	QP60	-	9.55	-	9.63	-	-	-	-	-	-	-	-3.5	-
La Palma	QP60	-	9.09	-	9.16	-	-	-	-	-	-	-	-3.7	-
La Palma	QP60	-	9.67	-	9.71	-	-	-	-	-	-	-	-3.5	-
La Palma	QP60	-	8.73	-	8.76	-	-	-	-	-	-	-	-3.4	-
La Palma	QP60	-	9.73	-	9.76	-	-	-	-	-	-	-	-3.5	-
La Palma	QP60	-	9.13	-	9.15	-	-	-	-	-	-	-	-3.5	-

Location	Sample												
La Palma	QP60	-	9.64	-	9.67	-	-	-	-	-	-	-	-3.6	-
La Palma	QP60	-	9.69	-	9.74	-	-	-	-	-	-	-	-3.6	-
La Palma	QP63	-	6.15	-	7.19	-	-	-	-	-	-	-	-8.3	-
La Palma	QP63	-	5.19	-	6.46	-	-	-	-	-	-	-	-8.1	-
La Palma	QP63	-	5.86	-	7.37	-	-	-	-	-	-	-	-8.1	-
La Palma	QP63	-	2.84	-	6.1	-	-	-	-	-	-	-	-7.8	-
La Palma	QP63	-	6.85	-	7.52	-	-	-	-	-	-	-	-7.1	-
La Palma	QP63	-	6.49	-	7.23	-	-	-	-	-	-	-	-8.3	-
La Palma	QP63	-	5.78	-	7.41	-	-	-	-	-	-	-	-8.2	-
La Palma	QP63	-	6.46	-	7.94	-	-	-	-	-	-	-	-8.3	-
La Palma	QP63	-	5.74	-	6.98	-	-	-	-	-	-	-	-8.5	-
La Palma	QP63	-	5.77	-	8.23	-	-	-	-	-	-	-	-8.4	-
La Palma	QP63	-	5.56	-	6.35	-	-	-	-	-	-	-	-8.1	-
La Palma	QP63	-	5.26	-	6.91	-	-	-	-	-	-	-	-7.3	-
La Palma	QP63	-	5.75	-	6.5	-	-	-	-	-	-	-	-7.6	-
La Palma	QP63	-	5.9	-	7	-	-	-	-	-	-	-	-9.2	-
La Palma	QP63	-	3.47	-	6.89	-	-	-	-	-	-	-	-10.3	-
La Palma	CAN-11	3.96E-05	9.27		9.27	0.11			9.993	0.04	0.029	0.0015	-3.8	1.96E+09
La Palma	CAN-14	1.55E-05	8.78		8.79	0.1			9.861	0.039	0.0291	0.0015	-4.4	5.30E+09
La Gomera	LG1	-	6.53	1.03	6.55	-	315	4	-	-	-	-	-	-
La Gomera	LG35	-	5.67	1.04	5.68	-	447	9	9.83	0.25	-	-	-	-
La Gomera	LG59	-	8.21	0.9	8.22	-	379	6	9.74	0.44	-	-	-	-
Tenerife	TF4		6.92	1.2	6.92	-	358	24	9.57	1.29	-	-	-	-
Tenerife	TF7	-	6.64	1.63	6.66	-	382	10	9.01	0.29	-	-	-	-
Tenerife	TF16	-	8.64	1.77	8.67	-	306	4	9.77	0.3	-	-	-	-
Tenerife	TF23	-	6.85	1.28	6.86	-	414	12	10.32	0.54	-	-	-	-
Tenerife	BM1911160529	-	5.84	0.24	-	-	-	-	-	-	-	-	-	-
Tenerife	Teide Fumarole	-	6.723	0.056	-	-	-	-	-	-	-	-	-3.13	-
Tenerife	31	-	-	-	-	-	-	-	-	-	-	-	-10.54	-
Tenerife	82	-	-	-	-	-	-	-	-	-	-	-	-3.54	-
Tenerife	86	-	-	-	-	-	-	-	-	-	-	-	-2.81	-
Tenerife	87	-	-	-	-	-	-	-	-	-	-	-	-3.85	-
Tenerife	89	-	-	-	-	-	-	-	-	-	-	-	-2.34	-
Tenerife	90	-	-	-	-	-	-	-	-	-	-	-	-2.29	-
Tenerife	95	-	5.87	-	-	-	-	-	-	-	-	-	-12.9	-
Tenerife	96	-	-	-	-	-	-	-	-	-	-	-	-1.34	-
Tenerife	97	-	5.55	-	-	-	-	-	-	-	-	-	-8.54	-
Tenerife	HLA	-	-	-	-	-	-	-	-	-	-	-	-6.9	-

Tenerife	LGA	-	1.206	0.025	1.73	0.186	-	-	-	-	-	-	-6.9	-
Tenerife	TAG	-	-	-	-	-	-	-	-	-	-	-	-6.9	-
Tenerife	NIA	-	-	-	-	-	-	-	-	-	-	-	-5.4	-
Tenerife	TAM	-	1.016	0.013	1.07	0.021	-	-	-	-	-	-	-7.1	-
Tenerife	ESU	-	-	-	-	-	-	-	-	-	-	-	-6.1	-
Tenerife	FFA	-	-	-	-	-	-	-	-	-	-	-	-10.9	-
Tenerife	S-2	-	-	-	-	-	-	-	-	-	-	-	-6.0	-
Tenerife	ALM	-	6.94	-	6.95	0.001	-	-	-	-	-	-	-8.5	-
Tenerife	CUM	-	-	-	-	-	-	-	-	-	-	-	-7.2	-
Tenerife	FP2	-	-	-	-	-	-	-	-	-	-	-	-6.2	-
Tenerife	BVA	-	6.61	-	7.06	0.048	-	-	-	-	-	-	-7.9	-
Tenerife	FLO	-	-	-	-	-	-	-	-	-	-	-	-8.9	-
Tenerife	LCO	-	-	-	-	-	-	-	-	-	-	-	-9.1	-
Tenerife	SFN	-	5.294	0.07	6.19	0.108	-	-	-	-	-	-	-9.7	-
Tenerife	STA	-	-	-	-	-	-	-	-	-	-	-	-8.0	-
Tenerife	VE2	-	-	-	-	-	-	-	-	-	-	-	-8.9	-
Tenerife	HON	-	-	-	-	-	-	-	-	-	-	-	-6.0	-
Tenerife	AAA	-	-	-	-	-	-	-	-	-	-	-	-9.6	-
Tenerife	CN2	-	-	-	-	-	-	-	-	-	-	-	-7.4	-
Tenerife	CLS	-	1.923	0.022	2.49	0.092	-	-	-	-	-	-	-7.0	-
Tenerife	POR	-	0.867	0.014	0.65	0.056	-	-	-	-	-	-	-8.5	-
Tenerife	RC1	-	-	-	-	-	-	-	-	-	-	-	-11.8	-
Tenerife	CHI	-	0.874	0.031	0.55	0.117	-	-	-	-	-	-	-9.7	-
Tenerife	MEO	-	0.953	0.022	0.73	0.13	-	-	-	-	-	-	-20.7	-
Tenerife	PAS	-	1.812	0.026	2.39	0.099	-	-	-	-	-	-	-9.9	-
Tenerife	ARG	-	-	-	-	-	-	-	-	-	-	-	-	-
Tenerife	HLN	-	-	-	-	-	-	-	-	-	-	-	-8.5	-
Tenerife	HPO	-	-	-	-	-	-	-	-	-	-	-	-5.1	-
Tenerife	SF3	-	-	-	-	-	-	-	-	-	-	-	-8.1	-
Tenerife	SJC	-	-	-	-	-	-	-	-	-	-	-	-5.2	-
Tenerife	LAG	-	-	-	-	-	-	-	-	-	-	-	-5.0	-
Tenerife	PIO	-	3.39	0.046	3.89	0.06	-	-	-	-	-	-	-2.5	-
Tenerife	FVE	-	6.275	0.057	6.58	0.033	-	-	-	-	-	-	-2.6	-
Tenerife	NSL	-	0.765	0.016	0.55	0.042	-	-	-	-	-	-	-9.8	-
Tenerife	FVE#	-	6.95	-	6.97	0.002	-	-	-	-	-	-	-	-
Tenerife	LQO	-	4.81	-	7.74	0.589	-	-	-	-	-	-	-	-

136

Tenerife	STO	-	3.19	-	5.97	0.587	-	-	-	-	-	-	-	-
Tenerife	RAO	-	4.34	-	8.06	0.896	-	-	-	-	-	-	-	-
Tenerife	SIO	-	5.18	-	6.57	0.185	-	-	-	-	-	-	-	-
Tenerife	ASW	-	1	-	1	-	-	-	-	-	-	-	-	-
Tenerife	1	-	7.21	-	7.23	-	-	-	-	-	-	-	-	-
Tenerife	2	-	6.96	-	7.04	-	-	-	-	-	-	-	-	-
Tenerife	3	-	6.61	-	7.14	-	-	-	-	-	-	-	-	-
Tenerife	4	-	5.18	-	6.88	-	-	-	-	-	-	-	-	-
Tenerife	5	-	6.94	-	6.96	-	-	-	-	-	-	-	-	-
Tenerife	6	-	4.81	-	9.11	-	-	-	-	-	-	-	-	-
Tenerife	7	-	3.19	-	7.02	-	-	-	-	-	-	-	-	-
Tenerife	8	-	4.34	-	10.18	-	-	-	-	-	-	-	-	-
Tenerife	9	-	6.95	-	6.97	-	-	-	-	-	-	-	-	-
Tenerife	CAN-9	3.05E-05	6.2		6.21	0.11	-	-	9.93	0.04	0.0293	0.002	-4.3	3.80E+09
Tenerife	CAN-10	1.55E-05	6.63		6.63	0.08	-	-	9.99	0.04	0.0293	0.002	-4.1	7.01E+09
Tenerife	CAN-12	1.83E-05	5.89		6.09	0.08	-	-	10.01	0.04	0.029	0.0014	-3.3	6.69E+09
Tenerife	CAN-13	1.56E-05	6.04		6.14	0.08	-	-	9.613	0.038	0.0284	0.0014	-3.7	7.62E+09
Tenerife	15/06/1991	-	7.23	-	7.25	-	-	-	-	-	-	-	-2.7	-
Tenerife	27/12/1993	-	7	-	7.10	-	-	-	-	-	-	-	-2.7	-
Tenerife	08/01/1994	-	7.03	-	7.05	-	-	-	-	-	-	-	-3	-
Tenerife	20/03/1994	-	7.16	-	7.18	-	-	-	-	-	-	-	-2.6	-
Tenerife	07/05/1994	-	7.13	-	7.18	-	-	-	-	-	-	-	-2.9	-
Tenerife	23/06/1994	-	7.04	-	7.12	-	-	-	-	-	-	-	-2.3	-
Tenerife	13/09/1994	-	7.41	-	7.46	-	-	-	-	-	-	-	-3.8	-
Tenerife	13/01/1996	-	6.97	-	7.02	-	-	-	-	-	-	-	-3.7	-
Tenerife	24/04/1999	-	7.02	-	7.10	-	304	-	-	-	-	-	-3.8	-
Tenerife	03/03/2000	-	6.91	-	6.94	-	318	-	-	-	-	-	-4.1	-
Tenerife	26/06/2000	-	6.97	-	6.99	-	333	-	-	-	-	-	-4	-
Tenerife	24/04/2001	-	6.94	-	6.96	-	321	-	-	-	-	-	-3.6	-
Tenerife	07/06/2001	-	6.88	-	6.93	-	309	-	-	-	-	-	-3.8	-
Tenerife	14/12/2001	-	7.02	-	7.16	-	-	-	-	-	-	-	-3.8	-
Tenerife	03/10/2002	-	7.13	-	7.17	-	-	-	-	-	-	-	-4.2	-
Tenerife	01/12/2003	3.02E-05	7.04	-	-	-	-	-	-	-	-	-	-3.2	3.38E+09
Tenerife	01/07/2004	2.52E-05	6.87	-	-	-	-	-	-	-	-	-	-	4.15E+09
Tenerife	25/01/2005	3.06E-05	7.2	-	7.23	-	-	-	-	-	-	-	-	3.27E+09
Tenerife	28/09/2006	1.35E-05	6.84	-	6.86	-	316	-	-	-	-	-	-	7.81E+09

Tenerife	29/01/2008	1.23E-05	7.27	-	7.30	-	311	-	-	-	-	-	-	8.07E+09
Tenerife	16/04/2008	3.53E-05	7.23	-	7.34	-	302	-	-	-	-	-	-	2.82E+09
Tenerife	29/05/2008	3.23E-05	7.24	-	7.30	-	302	-	-	-	-	-	-	3.08E+09
Tenerife	20/08/2008	2.74E-05	6.85	-	6.89	-	305	-	-	-	-	-	-	3.84E+09
Tenerife	13/11/2008	2.67E-05	7.51	-	7.54	-	322	-	-	-	-	-	-	3.59E+09
Tenerife	16/04/2009	2.76E-05	6.78	-	6.85	-	307	-	-	-	-	-	-	3.85E+09
Tenerife	05/06/2009	3.61E-05	7.07	-	7.12	-	312	-	-	-	-	-	-	2.82E+09
Tenerife	10/07/2009	2.69E-05	7.08	-	7.17	-	305	-	-	-	-	-	-	3.78E+09
Tenerife	07/10/2009	2.96E-05	7.2	-	7.27	-	307	-	-	-	-	-	-	3.38E+09
Tenerife	13/01/2010	2.45E-05	7.3	-	7.43	-	303	-	-	-	-	-	-	4.03E+09
El Hierro	-	-	2.826	0.064	3.054	0.081	-	-	-	-	-	-	-	-
El Hierro	-	-	2.242	0.044	2.476	0.065	-	-	-	-	-	-	-	-
El Hierro	-	-	6.7	0.15	7.25	0.18	-	-	-	-	-	-	-	-
El Hierro	-	-	6.38	0.098	7.78	0.28	-	-	-	-	-	-	-	-
El Hierro	-	-	4.225	0.094	4.78	0.14	-	-	-	-	-	-	-	-
El Hierro	-	-	7.906	0.085	8.199	0.099	-	-	-	-	-	-	-	-
El Hierro	-	-	7.53	0.11	8.03	0.14	-	-	-	-	-	-	-	-
El Hierro	-	-	7.878	0.074	8.197	0.09	-	-	-	-	-	-	-	-
El Hierro	JMDDEH01		7.98	0.62	-	-	-	-	-	-	-	-	-	-
El Hierro	JMDDEH01	-	7.8	0.1	-	-	-	-	-	-	-	-	-	-
El Hierro	JMDDEH01	-	8.1	0.46	-	-	-	-	-	-	-	-	-	-
El Hierro	JMDDEH01	-	8.01	0.14	-	-	-	-	-	-	-	-	-	-
El Hierro	JMDDEH03	-	8.19	0.17	-	-	-	-	-	-	-	-	-	-
El Hierro	JMDDEH04cii	-	7.53	0.26	-	-	-	-	-	-	-	-	-	-
El Hierro	JMDDEH04ciii	-	7.67	0.29	-	-	-	-	-	-	-	-	-	-
El Hierro	JMDDEH07	-	7.58	0.31	-	-	-	-	-	-	-	-	-	-
El Hierro	JMDDEH07	-	6.95	0.41	-	-	-	-	-	-	-	-	-	-
El Hierro	JMDDEH10	-	7.52	0.45	-	-	-	-	-	-	-	-	-	-
El Hierro	JMDDEH10	-	6.46	0.32	-	-	-	-	-	-	-	-	-	-
El Hierro	JMDDEH11	-	7.85	0.34	-	-	-	-	-	-	-	-	-	-
El Hierro	JMDDEH11	-	5	0.21	-	-	-	-	-	-	-	-	-	-
El Hierro	JMDDEH13	-	7.66	0.25	-	-	-	-	-	-	-	-	-	-
El Hierro	JMDDEH13	-	8.17	0.31	-	-	-	-	-	-	-	-	-	-
El Hierro	JMDDEH13	-	4.15	0.14	-	-	-	-	-	-	-	-	-	-
El Hierro	JMDDEH14	-	7.23	0.25	-	-	-	-	-	-	-	-	-	-
El Hierro	JMDDEH15	-	7.81	0.29	-	-	-	-	-	-	-	-	-	-
El Hierro	JMDDEH15	-	7	0.23	-	-	-	-	-	-	-	-	-	-

El Hierro	JMDDEH16	-	7.8	0.23	-	-	-	-	-	-	-	-	-	-
El Hierro	JMDDEH16	-	7.8	0.26	-	-	-	-	-	-	-	-	-	-
El Hierro	JMDDEH17	-	7.53	0.23	-	-	-	-	-	-	-	-	-	-
El Hierro	JMDDEH18	-	7.62	0.28	-	-	-	-	-	-	-	-	-	-
El Hierro	JMDDEH18	-	7.14	0.24	-	-	-	-	-	-	-	-	-	-

Table S 2. Noble gas and CO_2 compositions after data filtering. Reported errors are 2σ uncertainties

Locality	Sample ID	Rock	Phase	Reference	Extraction Method (FI)	Age (ka)	^{3}He (mol/g)	^{4}He (mol/g)	^{20}Ne (mol/g)	^{21}Ne (mol/g)	^{22}Ne (mol/g)	^{40}Ar (mol/g)	^{36}Ar (mol/g)	^{40}Ar* (mol/g)	^{4}He/^{20}Ne
Gran Canaria	GC59	Basalt	Ol	Gurenko et al. (2006)	Multistep Crushing	-	1.57E-18	1.56E-13	2.60E-16	-	-	4.92E-13	1.17E-15	1.47E-13	599.79
Gran Canaria	BM69286	Dolerite	Ol	Vance et al. (1989)	Multistep Crushing	-	4.32E-18	5.54E-13	-	-	-	-	-	-	-
Gran Canaria	BM1911160529	Basalt	Ol	Vance et al. (1989)	Multistep Crushing	-	3.20E-17	3.97E-12	-	-	-	-	-	-	-
Gran Canaria	BM1965P8151	Pyroxenite	Cpx	Vance et al. (1989)	Multistep Crushing	2700	7.30E-17	8.75E-12	-	-	-	-	-	-	-
Gran Canaria	BM1965P815j	Harzburgite	Opx	Vance et al. (1989)	Multistep Crushing	2700	1.62E-17	2.10E-12	-	-	-	-	-	-	-
Lanzarote	BM1965P72b	Lherzolite	Cpx	Vance et al. (1989)	Multistep Crushing	0.29	1.38E-16	1.52E-11	-	-	-	-	-	-	-
Lanzarote	BM1965P72	Harzburgite	-	Vance et al. (1989)	Multistep Crushing	-	3.31E-16	3.62E-11	-	-	-	-	-	-	-
Lanzarote	BM1965P74a	Gabbro	Cpx	Vance et al. (1989)	Multistep Crushing	0.29	4.16E-16	4.82E-11	-	-	-	-	-	-	-
Lanzarote	BM1965P77a	Dunite	Cpx	Vance et al. (1989)	Multistep Crushing	0.29	2.26E-17	2.77E-12	-	-	-	-	-	-	-
Lanzarote	L-88-1	Harzburgite	-	Grachev (2012)	Melting	2600	7.26E-17	8.93E-12	-	-	-	3.97E-11	3.68E-14	2.89E-11	-
Lanzarote	L-88-1/3	Harzburgite	Ol	Grachev (2012)	Melting	2600	6.28E-18	8.93E-13	-	-	-	-	-	-	-
Lanzarote	Tim-1	Harzburgite	Opx	Grachev (2012)	Multistep Crushing	0.3	1.04E-16	1.21E-11	-	-	-	-	-	-	-
Lanzarote	Tim-1	Harzburgite	Ol	Grachev (2012)	Multistep Crushing	0.3	4.02E-17	5.36E-12	-	-	-	-	-	-	-
Lanzarote	Tim-2	Harzburgite	Ol	Grachev (2012)	Melting	0.3	1.57E-17	2.23E-12	-	-	-	-	-	-	-
Lanzarote	Tam-1	Harzburgite	Ol	Grachev (2012)	Melting	2600	1.57E-17	1.79E-12	-	-	-	-	-	-	-
Lanzarote	Lanz560	Mantle xenolith	Cpx	Grachev (2012)	Multistep Crushing	-	1.08E-16	1.12E-11	-	-	-	-	-	-	-
Lanzarote	Lanz560	Mantle xenolith	Opx	Grachev (2012)	Multistep Crushing	-	1.52E-16	1.79E-11	-	-	-	-	-	-	-
Lanzarote	Lanz560	Mantle xenolith	Ol	Grachev (2012)	Multistep Crushing	-	7.31E-17	7.59E-12	-	-	-	-	-	-	-
Fuerteventura	FUE4-03	Clinopyroxene	Cpx	Carnevale et al 2021	Single step Crushing	25000	3.39E-17	3.71E-12	-	-	-	-	-	-	1120.7
La Palma	JMDDLP01	Ankaramite	Ol	Day and Hilton (2011)	Multistep Crushing	1440	2.05E-18	2.05E-13	-	-	-	-	-	-	-
La Palma	JMDDLP01	Ankaramite	Cpx	Day and Hilton (2011)	Multistep Crushing	1440	1.10E-17	1.11E-12	-	-	-	-	-	-	-
La Palma	JMDDLP02	Ankaramite	Ol	Day and Hilton (2011)	Multistep Crushing	1440	1.78E-17	1.71E-12	-	-	-	-	-	-	-
La Palma	JMDDLP04	Basanite	Ol	Day and Hilton (2011)	Multistep Crushing	1020	3.57E-18	3.26E-13	-	-	-	-	-	-	-
La Palma	JMDDLP05	Basanite	Ol	Day and Hilton (2011)	Multistep Crushing	1020	5.21E-18	4.82E-13	-	-	-	-	-	-	-

139

La Palma	JMDDLP05	Basanite	Cpx	Day and Hilton (2011)	Multistep Crushing	1020	1.56E-17	1.66E-12	-	-	-	-	-	-	-
La Palma	JMDDLP07	Ankaramite	Ol	Day and Hilton (2011)	Multistep Crushing	1020	1.42E-17	1.45E-12	-	-	-	-	-	-	-
La Palma	JMDDLP09	Alkali basalt	Ol	Day and Hilton (2011)	Multistep Crushing	490	3.92E-18	3.21E-13	-	-	-	-	-	-	-
La Palma	JMDDLP09	Alkali basalt	Cpx	Day and Hilton (2011)	Multistep Crushing	490	2.22E-17	1.97E-12	-	-	-	-	-	-	-
La Palma	JMDDLP11	Basanite	Ol	Day and Hilton (2011)	Multistep Crushing	570	2.47E-18	2.68E-13	-	-	-	-	-	-	-
La Palma	JMDDLP13A	Ol Clinopyroxenite	Ol	Day and Hilton (2011)	Multistep Crushing	120	6.55E-17	7.60E-12	-	-	-	-	-	-	-
La Palma	JMDDLP13A	Ol Clinopyroxenite	Cpx	Day and Hilton (2011)	Multistep Crushing	120	3.94E-18	3.66E-13	-	-	-	-	-	-	-
La Palma	JMDDLP13B	Ol Clinopyroxenite	Cpx	Day and Hilton (2011)	Multistep Crushing	120	1.57E-17	1.53E-12	-	-	-	-	-	-	-
La Palma	JMDDLP14	Basanite	Ol	Day and Hilton (2011)	Multistep Crushing	120	1.29E-17	1.26E-12	-	-	-	-	-	-	-
La Palma	JMDDLP21bi	Honrblendite	Ol	Day and Hilton (2011)	Multistep Crushing	3	1.18E-17	1.31E-12	-	-	-	-	-	-	-
La Palma	LP96-66	Lava	Ol	Day and Hilton (2011)	Multistep Crushing	850	7.74E-18	7.05E-13	-	-	-	-	-	-	-
La Palma	LP30e	Lava	OL	Hilton et al. (2000)	Multistep Crushing	-	-	1.65E-12	-	-	-	-	-	-	-
La Palma	LP30e	Lava	CPX	Hilton et al. (2000)	Multistep Crushing	-	-	2.17E-12	-	-	-	-	-	-	-
La Palma	71LP41	Lava	OL	Hilton et al. (2000)	Multistep Crushing	-	-	2.04E-12	-	-	-	-	-	-	-
La Palma	71LP41	Lava	CPX	Hilton et al. (2000)	Multistep Crushing	-	-	3.73E-12	-	-	-	-	-	-	-
La Palma	LP43e	Lava	OL	Hilton et al. (2000)	Multistep Crushing	-	-	1.04E-12	-	-	-	-	-	-	-
La Palma	LP43e	Lava	CPX	Hilton et al. (2000)	Multistep Crushing	-	-	2.50E-12	-	-	-	-	-	-	-
La Palma	151LP69e	Lava	OL	Hilton et al. (2000)	Multistep Crushing	-	-	1.35E-12	-	-	-	-	-	-	-
La Palma	151LP69e	Lava	CPX	Hilton et al. (2000)	Multistep Crushing	-	-	2.56E-12	-	-	-	-	-	-	-
La Palma	LP95b	Lava	OL	Hilton et al. (2000)	Multistep Crushing	-	-	2.22E-12	-	-	-	-	-	-	-
La Palma	LP95b	Lava	CPX	Hilton et al. (2000)	Multistep Crushing	-	-	1.66E-12	-	-	-	-	-	-	-
La Palma	96LP46	Lava	OL	Hilton et al. (2000)	Multistep Crushing	-	-	7.37E-13	-	-	-	-	-	-	-
La Palma	96LP46	Lava	CPX	Hilton et al. (2000)	Multistep Crushing	-	-	3.79E-13	-	-	-	-	-	-	-
La Palma	93LP106	Lava	OL	Hilton et al. (2000)	Multistep Crushing	-	-	1.21E-13	-	-	-	-	-	-	-
La Palma	93LP107	Lava	OL	Hilton et al. (2000)	Multistep Crushing	-	-	9.82E-14	-	-	-	-	-	-	-
La Palma	93LP107	Lava	CPX	Hilton et al. (2000)	Multistep Crushing	-	-	1.88E-13	-	-	-	-	-	-	-
La Palma	93LP110	Lava	OL	Hilton et al. (2000)	Multistep Crushing	-	-	5.18E-13	-	-	-	-	-	-	-
La Palma	93LP110	Lava	CPX	Hilton et al. (2000)	Multistep Crushing	-	-	1.38E-13	-	-	-	-	-	-	-
La Palma	93LP113	Lava	OL	Hilton et al. (2000)	Multistep Crushing	-	-	5.04E-13	-	-	-	-	-	-	-
La Palma	93LP113	Lava	CPX	Hilton et al. (2000)	Multistep Crushing	-	-	1.34E-13	-	-	-	-	-	-	-
La Palma	93LP134	Mafic sill	OL	Hilton et al. (2000)	Multistep Crushing	-	-	2.00E-12	-	-	-	-	-	-	-
La Palma	93LP134	Mafic sill	CPX	Hilton et al. (2000)	Multistep Crushing	-	-	1.28E-12	-	-	-	-	-	-	-
La Palma	93LP154	-	Bubbling gases	Hilton et al. (2000)	-	-	-	-	-	-	-	-	-	-	-

La Palma	LP1	Picrite	Ol	Gurenko et al. (2006)	Multistep Crushing	600	5.50E-18	5.17E-13	1.65E-15	-	-	1.88E-12	5.19E-15	3.45E-13	312.38
La Palma	LP13	Picrite	Ol	Gurenko et al. (2006)	Multistep Crushing	-	4.78E-17	3.69E-12	5.79E-16	-	-	-	-	-	6380.88
La Palma	A	-	Bubbling gases	Pérez et al. (1994)	-	0.029	-	-	-	-	-	-	-	-	50.0
La Palma	B	-	Bubbling gases	Padrón et al. (2015)	-	0.021	-	-	-	-	-	-	-	-	-
La Palma	C	-	Bubbling gases	Padrón et al. (2015)	-	0.013	-	-	-	-	-	-	-	-	119.1
La Palma	D	-	Bubbling gases	Padrón et al. (2015)	-	0.012	-	-	-	-	-	-	-	-	78.30
La Palma	E	-	Bubbling gases	Padrón et al. (2015)	-	0.01	-	-	-	-	-	-	-	-	181
La Palma	F	-	Bubbling gases	Padrón et al. (2015)	-	0.009	-	-	-	-	-	-	-	-	169.1
La Palma	G	-	Bubbling gases	Padrón et al. (2015)	-	0.008	-	-	-	-	-	-	-	-	212.3
La Palma	I	-	Bubbling gases	Padrón et al. (2015)	-	0.008	-	-	-	-	-	-	-	-	215.7
La Palma	QP60	-	Bubbling gases	Torres-González et al. (2020)	-	0.004	-	-	-	-	-	-	-	-	25.7
La Palma	QP60	-	Bubbling gases	Torres-González et al. (2020)	-	0.004	-	-	-	-	-	-	-	-	73.4
La Palma	QP60	-	Bubbling gases	Torres-González et al. (2020)	-	0.004	-	-	-	-	-	-	-	-	102.1
La Palma	QP60	-	Bubbling gases	Torres-González et al. (2020)	-	0.004	-	-	-	-	-	-	-	-	160.7
La Palma	QP60	-	Bubbling gases	Torres-González et al. (2020)	-	0.003	-	-	-	-	-	-	-	-	45.6
La Palma	QP60	-	Bubbling gases	Torres-González et al. (2020)	-	0.003	-	-	-	-	-	-	-	-	35.8
La Palma	QP60	-	Bubbling gases	Torres-González et al. (2020)	-	0.003	-	-	-	-	-	-	-	-	34.2
La Palma	QP60	-	Bubbling gases	Torres-González et al. (2020)	-	0.002	-	-	-	-	-	-	-	-	79.0
La Palma	QP60	-	Bubbling gases	Torres-González et al. (2020)	-	0.002	-	-	-	-	-	-	-	-	110.5
La Palma	QP60	-	Bubbling gases	Torres-González et al. (2020)	-	0.002	-	-	-	-	-	-	-	-	96.4
La Palma	QP60	-	Bubbling gases	Torres-González et al. (2020)	-	0.002	-	-	-	-	-	-	-	-	142.9
La Palma	QP60	-	Bubbling gases	Torres-González et al. (2020)	-	0.002	-	-	-	-	-	-	-	-	106.9
La Palma	QP60	-	Bubbling gases	Torres-González et al. (2020)	-	0.001	-	-	-	-	-	-	-	-	55.0
La Palma	QP63	-	Groundwater	Torres-González et al. (2020)	-	0.004	-	-	-	-	-	-	-	-	1.70
La Palma	QP63	-	Groundwater	Torres-González et al. (2020)	-	0.004	-	-	-	-	-	-	-	-	1.23
La Palma	QP63	-	Groundwater	Torres-González et al. (2020)	-	0.003	-	-	-	-	-	-	-	-	1.20
La Palma	QP63	-	Groundwater	Torres-González et al. (2020)	-	0.003	-	-	-	-	-	-	-	-	0.45
La Palma	QP63	-	Groundwater	Torres-González et al. (2020)	-	0.003	-	-	-	-	-	-	-	-	2.75
La Palma	QP63	-	Groundwater	Torres-González et al. (2020)	-	0.003	-	-	-	-	-	-	-	-	2.40
La Palma	QP63	-	Groundwater	Torres-González et al. (2020)	-	0.003	-	-	-	-	-	-	-	-	1.12

Location	Sample	Rock type	Phase	Reference	Method										
La Palma	QP63	-	Groundwater	Torres-González et al. (2020)	-	-	0.003	-	-	-	-	-	-	-	1.34
La Palma	QP63	-	Groundwater	Torres-González et al. (2020)	-	-	0.002	-	-	-	-	-	-	-	1.37
La Palma	QP63	-	Groundwater	Torres-González et al. (2020)	-	-	0.002	-	-	-	-	-	-	-	0.84
La Palma	QP63	-	Groundwater	Torres-González et al. (2020)	-	-	0.002	-	-	-	-	-	-	-	1.93
La Palma	QP63	-	Groundwater	Torres-González et al. (2020)	-	-	0.002	-	-	-	-	-	-	-	1.02
La Palma	QP63	-	Groundwater	Torres-González et al. (2020)	-	-	0.002	-	-	-	-	-	-	-	2.09
La Palma	QP63	-	Groundwater	Torres-González et al. (2020)	-	-	0.002	-	-	-	-	-	-	-	1.55
La Palma	QP63	-	Groundwater	Torres-González et al. (2020)	-	-	0.001	-	-	-	-	-	-	-	0.49
La Palma	CAN-11	-	Bubbling gases	Day and Hilton (2020)	-	-	0.014	1.07E-16	8.30E-12	-	-	-	-	-	12.49
La Palma	CAN-13	-	Bubbling gases	Day and Hilton (2020)	-	-	0.014	1.28E-16	1.05E-11	-	-	-	-	-	10.59
La Gomera	LG59	Picrite	Ol	Gurenko et al. (2006)	Multistep Crushing	10200	4.21E-18	3.69E-13	9.44E-16	-	-	2.10E-12	5.54E-15	4.63E-13	390.81
Tenerife	TF7	Picritic basalt	Ol	Gurenko et al. (2006)	Multistep Crushing	-	5.01E-19	5.43E-14	7.30E-16	-	-	1.03E-12	2.69E-15	2.33E-13	74.35
Tenerife	TF23	Basalt	Ol	Gurenko et al. (2006)	Multistep Crushing	-	8.84E-19	9.28E-14	4.04E-16	-	-	5.62E-13	1.36E-15	1.61E-13	229.77
Tenerife	ALM	-	Groundwater	Marrero-Diaz et al. (2015)	-	-	0.014	-	-	-	-	-	-	-	110.00
Tenerife	BVA	-	Groundwater	Marrero-Diaz et al. (2015)	-	-	0.014	-	-	-	-	-	-	-	3.70
Tenerife	SFN	-	Groundwater	Marrero-Diaz et al. (2015)	-	-	0.014	-	-	-	-	-	-	-	1.59
Tenerife	FVE	-	Groundwater	Marrero-Diaz et al. (2015)	-	-	0.014	-	-	-	-	-	-	-	4.95
Tenerife	FVE#	-	Groundwater	Marrero-Diaz et al. (2015)	-	-	0.014	-	-	-	-	-	-	-	95.70
Tenerife	LQO	-	Groundwater	Marrero-Diaz et al. (2015)	-	-	0.014	-	-	-	-	-	-	-	0.60
Tenerife	SIO	-	Groundwater	Marrero-Diaz et al. (2015)	-	-	0.014	-	-	-	-	-	-	-	1.10
Tenerife	1	-	Fumaroles	Pérez et al. (1996)	-	-	0.029	-	-	-	-	-	-	-	120.00
Tenerife	2	-	Fumaroles	Pérez et al. (1996)	-	-	0.026	-	-	-	-	-	-	-	24.00
Tenerife	3	-	Groundwater	Pérez et al. (1996)	-	-	0.026	-	-	-	-	-	-	-	3.70
Tenerife	4	-	Groundwater	Pérez et al. (1996)	-	-	0.026	-	-	-	-	-	-	-	1.10
Tenerife	5	-	Groundwater	Pérez et al. (1996)	-	-	0.026	-	-	-	-	-	-	-	110.00
Tenerife	7	-	Groundwater	Pérez et al. (1996)	-	-	0.026	-	-	-	-	-	-	-	0.50
Tenerife	9	-	Bubbling gases	Pérez et al. (1996)	-	-	0.027	-	-	-	-	-	-	-	95.70
Tenerife	CAN-9	-	Fumaroles	Day and Hilton (2020)	-	-	0.014	1.08E-16	1.26E-11	-	-	-	-	-	0.77
Tenerife	CAN-10	-	Fumaroles	Day and Hilton (2020)	-	-	0.014	9.92E-17	1.08E-11	-	-	-	-	-	10.27
Tenerife	CAN-12	-	Fumaroles	Day and Hilton (2020)	-	-	0.014	8.77E-19	1.07E-13	-	-	-	-	-	0.17

Tenerife	CAN-13	-	Fumaroles	Day and Hilton (2020)	-	0.014	7.91E-17	9.42E-12	-	-	-	-	-	-	0.37
Tenerife	15/06/1991	-	Fumaroles	Melián et al. (2012)	-	0.029	-	-	-	-	-	-	-	-	120
Tenerife	27/12/1993	-	Fumaroles	Melián et al. (2012)	-	0.027	-	-	-	-	-	-	-	-	20
Tenerife	08/01/1994	-	Fumaroles	Melián et al. (2012)	-	0.026	-	-	-	-	-	-	-	-	113
Tenerife	20/03/1994	-	Fumaroles	Melián et al. (2012)	-	0.026	-	-	-	-	-	-	-	-	126
Tenerife	07/05/1994	-	Fumaroles	Melián et al. (2012)	-	0.026	-	-	-	-	-	-	-	-	36
Tenerife	23/06/1994	-	Fumaroles	Melián et al. (2012)	-	0.026	-	-	-	-	-	-	-	-	24
Tenerife	13/09/1994	-	Fumaroles	Melián et al. (2012)	-	0.026	-	-	-	-	-	-	-	-	43
Tenerife	13/01/1996	-	Fumaroles	Melián et al. (2012)	-	0.024	-	-	-	-	-	-	-	-	38
Tenerife	24/04/1999	-	Fumaroles	Melián et al. (2012)	-	0.021	-	-	-	-	-	-	-	-	24
Tenerife	03/03/2000	-	Fumaroles	Melián et al. (2012)	-	0.02	-	-	-	-	-	-	-	-	55
Tenerife	26/06/2000	-	Fumaroles	Melián et al. (2012)	-	0.02	-	-	-	-	-	-	-	-	105
Tenerife	24/04/2001	-	Fumaroles	Melián et al. (2012)	-	0.019	-	-	-	-	-	-	-	-	76
Tenerife	07/06/2001	-	Fumaroles	Melián et al. (2012)	-	0.019	-	-	-	-	-	-	-	-	40
Tenerife	14/12/2001	-	Fumaroles	Melián et al. (2012)	-	0.019	-	-	-	-	-	-	-	-	14
Tenerife	03/10/2002	-	Fumaroles	Melián et al. (2012)	-	0.018	-	-	-	-	-	-	-	-	53
Tenerife	01/12/2003	-	Fumaroles	Melián et al. (2012)	-	0.017	-	-	-	-	-	-	-	-	-
Tenerife	01/07/2004	-	Fumaroles	Melián et al. (2012)	-	0.016	-	-	-	-	-	-	-	-	-
Tenerife	25/01/2005	-	Fumaroles	Melián et al. (2012)	-	0.015	-	-	-	-	-	-	-	-	64
Tenerife	28/09/2006	-	Fumaroles	Melián et al. (2012)	-	0.014	-	-	-	-	-	-	-	-	76
Tenerife	29/01/2008	-	Fumaroles	Melián et al. (2012)	-	0.012	-	-	-	-	-	-	-	-	58
Tenerife	16/04/2008	-	Fumaroles	Melián et al. (2012)	-	0.012	-	-	-	-	-	-	-	-	18
Tenerife	29/05/2008	-	Fumaroles	Melián et al. (2012)	-	0.012	-	-	-	-	-	-	-	-	36
Tenerife	20/08/2008	-	Fumaroles	Melián et al. (2012)	-	0.012	-	-	-	-	-	-	-	-	43
Tenerife	13/11/2008	-	Fumaroles	Melián et al. (2012)	-	0.012	-	-	-	-	-	-	-	-	77
Tenerife	16/04/2009	-	Fumaroles	Melián et al. (2012)	-	0.011	-	-	-	-	-	-	-	-	28
Tenerife	05/06/2009	-	Fumaroles	Melián et al. (2012)	-	0.011	-	-	-	-	-	-	-	-	43
Tenerife	10/07/2009	-	Fumaroles	Melián et al. (2012)	-	0.011	-	-	-	-	-	-	-	-	23
Tenerife	07/10/2009	-	Fumaroles	Melián et al. (2012)	-	0.011	-	-	-	-	-	-	-	-	29
Tenerife	13/01/2010	-	Fumaroles	Melián et al. (2012)	-	0.01	-	-	-	-	-	-	-	-	16
El Hierro	-	-	Groundwater	Padrón et al. (2013)	-	0.009	3.97E-16	4.3E-11	-	-	-	-	-	-	3.14
El Hierro	-	-	Groundwater	Padrón et al. (2013)	-	0.009	4.43E-16	5.0E-11	-	-	-	-	-	-	1.33
El Hierro	-	-	Groundwater	Padrón et al. (2013)	-	0.009	5.15E-16	4.7E-11	-	-	-	-	-	-	6.73
El Hierro	-	-	Groundwater	Padrón et al. (2013)	-	0.009	2.82E-16	2.7E-11	-	-	-	-	-	-	3.79
El Hierro	-	-	Groundwater	Padrón et al. (2013)	-	0.009	5.08E-16	4.6E-11	-	-	-	-	-	-	6.19

El Hierro	JMDDEH01	Ankaramite	Ol	Day and Hilton (2011)	Multistep Crushing	1	2.43E-18	2.19E-13	-	-	-	-	-	-	-
El Hierro	JMDDEH01	Ankaramite	Ol	Day and Hilton (2011)	Multistep Crushing	1	2.32E-17	2.14E-12	-	-	-	-	-	-	-
El Hierro	JMDDEH01	Ankaramite	Cpx	Day and Hilton (2011)	Multistep Crushing	1	2.26E-18	2.01E-13	-	-	-	-	-	-	-
El Hierro	JMDDEH01	Ankaramite	Cpx	Day and Hilton (2011)	Multistep Crushing	1	7.91E-18	7.10E-13	-	-	-	-	-	-	-
El Hierro	JMDDEH03	Basanite	Ol	Day and Hilton (2011)	Multistep Crushing	1030	1.84E-17	1.62E-12	-	-	-	-	-	-	-
El Hierro	JMDDEH04cii	Dunite	Ol	Day and Hilton (2011)	Multistep Crushing	1030	2.51E-17	2.40E-12	-	-	-	-	-	-	-
El Hierro	JMDDEH04ciii	Dunite	Ol	Day and Hilton (2011)	Multistep Crushing	1030	1.35E-16	1.27E-11	-	-	-	-	-	-	-
El Hierro	JMDDEH07	Ankaramite	Ol	Day and Hilton (2011)	Multistep Crushing	1030	8.32E-18	7.90E-13	-	-	-	-	-	-	-
El Hierro	JMDDEH10	Ankaramite	Ol	Day and Hilton (2011)	Multistep Crushing	160	1.68E-18	1.61E-13	-	-	-	-	-	-	-
El Hierro	JMDDEH11	Alkali basalt	Ol	Day and Hilton (2011)	Multistep Crushing	160	4.78E-18	4.38E-13	-	-	-	-	-	-	-
El Hierro	JMDDEH13	Ankaramite	Ol	Day and Hilton (2011)	Multistep Crushing	135	7.56E-18	7.10E-13	-	-	-	-	-	-	-
El Hierro	JMDDEH13	Ankaramite	Ol	Day and Hilton (2011)	Multistep Crushing	135	6.75E-18	5.94E-13	-	-	-	-	-	-	-
El Hierro	JMDDEH14	Alkali basalt	Ol	Day and Hilton (2011)	Multistep Crushing	265	3.90E-18	3.88E-13	-	-	-	-	-	-	-
El Hierro	JMDDEH15	Ankaramite	Ol	Day and Hilton (2011)	Multistep Crushing	335	5.09E-18	4.69E-13	-	-	-	-	-	-	-
El Hierro	JMDDEH15	Ankaramite	Cpx	Day and Hilton (2011)	Multistep Crushing	335	1.36E-17	1.40E-12	-	-	-	-	-	-	-
El Hierro	JMDDEH16	Basanite	Ol	Day and Hilton (2011)	Multistep Crushing	540	6.44E-18	5.94E-13	-	-	-	-	-	-	-
El Hierro	JMDDEH16	Basanite	Cpx	Day and Hilton (2011)	Multistep Crushing	540	1.08E-17	9.96E-13	-	-	-	-	-	-	-
El Hierro	JMDDEH17	Alkali basalt	Ol	Day and Hilton (2011)	Multistep Crushing	10	1.44E-17	1.38E-12	-	-	-	-	-	-	-
El Hierro	JMDDEH18	Ankaramite	Ol	Day and Hilton (2011)	Multistep Crushing	1	6.24E-18	5.89E-13	-	-	-	-	-	-	-
El Hierro	JMDDEH18	Ankaramite	Cpx	Day and Hilton (2011)	Multistep Crushing	1	1.70E-17	1.71E-12	-	-	-	-	-	-	-
El Hierro	1.1	Sp Lherzolite	Ol	This Study	Single step Crushing	<40	1.28E-17	1.28E-12	5.67E-15	1.70E-17	5.65E-16	9.72E-12	2.35E-15	9.03E-12	225.9
El Hierro	1.15	Sp Harzburgite	Ol	This Study	Single step Crushing	<40	3.73E-17	3.60E-12	1.13E-14	3.35E-17	1.13E-15	6.09E-12	2.33E-15	5.41E-12	317.9
El Hierro	1.15	Sp Harzburgite	Opx	This Study	Single step Crushing	<40	1.38E-17	1.42E-12	2.25E-14	6.73E-17	2.28E-15	1.37E-11	1.13E-14	1.03E-11	62.8
El Hierro	1.15	Sp Harzburgite	Cpx	This Study	Single step Crushing	<40	3.62E-17	3.55E-12	2.73E-14	7.92E-17	2.79E-15	1.76E-11	2.18E-14	1.11E-11	129.9
El Hierro	1.2	Sp Lherzolite	Ol	This Study	Single step Crushing	<40	4.80E-17	4.32E-12	7.10E-15	2.19E-17	7.06E-16	6.89E-12	6.24E-15	5.04E-12	608.5
El Hierro	1.2	Sp Lherzolite	Opx	This Study	Single step Crushing	<40	4.72E-17	4.39E-12	1.06E-14	3.30E-17	1.05E-15	2.25E-11	4.98E-15	2.10E-11	415.8
El Hierro	1.2	Sp Lherzolite	Cpx	This Study	Single step Crushing	<40	8.66E-17	8.21E-12	1.45E-14	4.49E-17	1.42E-15	1.33E-10	3.35E-14	1.24E-10	565.4
El Hierro	1.22	Sp Lherzolite	Ol	This Study	Single step Crushing	<40	7.62E-18	7.66E-13	9.87E-16	3.10E-18	9.38E-17	1.31E-12	8.91E-16	1.04E-12	776.1
El Hierro	1.22	Sp Lherzolite	Opx	This Study	Single step Crushing	<40	3.26E-17	3.29E-12	6.44E-15	1.91E-17	6.48E-16	3.91E-12	3.74E-15	2.81E-12	511.8
El Hierro	1.23	Sp Harzburgite	Ol	This Study	Single step Crushing	<40	2.58E-17	2.49E-12	1.24E-14	3.74E-17	1.24E-15	4.92E-11	9.48E-15	4.64E-11	200.7
El Hierro	1.23	Sp Harzburgite	Opx	This Study	Single step Crushing	<40	1.80E-17	1.71E-12	2.59E-14	7.87E-17	2.61E-15	3.55E-11	1.13E-14	3.22E-11	66.0

144

El Hierro	1.3	Sp Harzburgite	Ol	This Study	Single step Crushing	<40	3.76E-17	3.57E-12	6.05E-15	1.82E-17	6.03E-16	6.39E-12	6.12E-15	4.58E-12	589.8
El Hierro	1.3	Sp Harzburgite	Opx	This Study	Single step Crushing	<40	7.71E-17	7.27E-12	3.62E-14	1.07E-16	3.63E-15	2.83E-11	1.43E-14	2.40E-11	200.7
El Hierro	1.3	Sp Harzburgite	Cpx	This Study	Single step Crushing	<40	2.26E-16	2.13E-11	3.37E-14	1.06E-16	3.33E-15	5.81E-11	3.26E-14	4.85E-11	631.8

Table S2: Continued.

Locality	Sample ID	$^4He/^{40}Ar^*$	$^4He/CO_2$	R/Ra	Error (+/-)	Rc/Ra	Error (+/-)	$^{40}Ar/^{36}Ar$	Error (+/-)	$^{20}Ne/^{22}Ne$	Error (+/-)	$^{21}Ne/^{22}Ne$	Error (+/-)	$\delta^{13}C$ (‰)	$CO_2/^3He$
Gran Canaria	GC59	1.05	-	7.26	1.03	7.26	-	422	28	9.14	0.54	-	-	-	-
Gran Canaria	BM69286	-	-	5.61	0.32	-	-	-	-	-	-	-	-	-	-
Gran Canaria	BM1911160529	-	-	5.8	0.32	-	-	-	-	-	-	-	-	-	-
Gran Canaria	BM1965P8151	-	-	6.00	0.34	-	-	-	-	-	-	-	-	-	-
Gran Canaria	BM1965P815j	-	-	5.56	0.32	-	-	-	-	-	-	-	-	-	-
Lanzarote	BM1965P72b	-	-	6.55	0.36	-	-	-	-	-	-	-	-	-	-
Lanzarote	BM1965P72	-	-	6.59	0.36	-	-	-	-	-	-	-	-	-	-
Lanzarote	BM1965P74a	-	-	6.20	0.34	-	-	-	-	-	-	-	-	-	-
Lanzarote	BM1965P77a	-	-	5.88	0.34	-	-	-	-	-	-	-	-	-	-
Lanzarote	L-88-1	0.31	-	5.85	-	-	-	1080	-	-	-	-	-	-	-
Lanzarote	L-88-1/3	-	-	5.06	-	-	-	1000	-	-	-	-	-	-	-
Lanzarote	Tim-1	-	-	6.21	-	-	-	-	-	-	-	-	-	-	-
Lanzarote	Tim-1	-	-	5.40	-	-	-	-	-	-	-	-	-	-	-
Lanzarote	Tim-2	-	-	5.07	-	-	-	-	-	-	-	-	-	-	-
Lanzarote	Tam-1	-	-	6.31	-	-	-	-	-	-	-	-	-	-	-
Lanzarote	Lanz560	-	-	6.93	-	-	-	-	-	-	-	-	-	-	-
Lanzarote	Lanz560	-	-	6.14	-	-	-	-	-	-	-	-	-	-	-
Lanzarote	Lanz560	-	-	6.93	-	-	-	-	-	-	-	-	-	-	-
Fuerteventura	FUE4-03	-	-	6.66	0.07	6.66	-	431.17	0.06	-	-	-	-	-	-
La Palma	JMDDLP01	-	-	7.20	0.35	-	-	-	-	-	-	-	-	-	-
La Palma	JMDDLP01	-	-	7.11	0.31	-	-	-	-	-	-	-	-	-	-
La Palma	JMDDLP02	-	-	7.48	0.19	-	-	-	-	-	-	-	-	-	-
La Palma	JMDDLP04	-	-	7.87	0.38	-	-	-	-	-	-	-	-	-	-
La Palma	JMDDLP05	-	-	7.78	0.26	-	-	-	-	-	-	-	-	-	-
La Palma	JMDDLP05	-	-	6.77	0.23	-	-	-	-	-	-	-	-	-	-
La Palma	JMDDLP07	-	-	7.05	0.24	-	-	-	-	-	-	-	-	-	-
La Palma	JMDDLP09	-	-	8.79	0.33	-	-	-	-	-	-	-	-	-	-
La Palma	JMDDLP09	-	-	8.12	0.27	-	-	-	-	-	-	-	-	-	-

La Palma															
La Palma	JMDDLP11	-	-	6.64	0.26	-	-	-	-	-	-	-	-	-	-
La Palma	JMDDLP13A	-	-	6.2	0.15	-	-	-	-	-	-	-	-	-	-
La Palma	JMDDLP13A	-	-	7.74	0.41	-	-	-	-	-	-	-	-	-	-
La Palma	JMDDLP13B	-	-	7.4	0.17	-	-	-	-	-	-	-	-	-	-
La Palma	JMDDLP14	-	-	7.34	0.24	-	-	-	-	-	-	-	-	-	-
La Palma	JMDDLP21bi	-	-	6.5	0.16	-	-	-	-	-	-	-	-	-	-
La Palma	LP96-66	-	-	7.9	0.28	-	-	-	-	-	-	-	-	-	-
La Palma	LP30e	-	-	7.38	0.35	-	-	-	-	-	-	-	-	-	-
La Palma	LP30e	-	-	7.196	0.34	-	-	-	-	-	-	-	-	-	-
La Palma	71LP41	-	-	7.57	0.33	-	-	-	-	-	-	-	-	-	-
La Palma	71LP41	-	-	7.37	0.25	-	-	-	-	-	-	-	-	-	-
La Palma	LP43e	-	-	7.49	0.96	-	-	-	-	-	-	-	-	-	-
La Palma	LP43e	-	-	7.33	0.27	-	-	-	-	-	-	-	-	-	-
La Palma	151LP69e	-	-	7.82	0.21	-	-	-	-	-	-	-	-	-	-
La Palma	151LP69e	-	-	7.63	0.22	-	-	-	-	-	-	-	-	-	-
La Palma	LP95b	-	-	7.04	0.27	-	-	-	-	-	-	-	-	-	-
La Palma	LP95b	-	-	7.28	0.33	-	-	-	-	-	-	-	-	-	-
La Palma	96LP46	-	-	8.04	0.34	-	-	-	-	-	-	-	-	-	-
La Palma	96LP46	-	-	7.72	0.49	-	-	-	-	-	-	-	-	-	-
La Palma	93LP106	-	-	8.92	0.69	-	-	-	-	-	-	-	-	-	-
La Palma	93LP107	-	-	7.1	1.48	-	-	-	-	-	-	-	-	-	-
La Palma	93LP107	-	-	7.35	0.79	-	-	-	-	-	-	-	-	-	-
La Palma	93LP110	-	-	6.77	0.46	-	-	-	-	-	-	-	-	-	-
La Palma	93LP110	-	-	7.24	1.48	-	-	-	-	-	-	-	-	-	-
La Palma	93LP113	-	-	8	0.29	-	-	-	-	-	-	-	-	-	-
La Palma	93LP113	-	-	6.35	1.02	-	-	-	-	-	-	-	-	-	-
La Palma	93LP134	-	-	8.3	0.23	-	-	-	-	-	-	-	-	-	-
La Palma	93LP134	-	-	8.41	0.27	-	-	-	-	-	-	-	-	-	-
La Palma	93LP154	-	-	9.5	0.27	-	-	-	-	-	-	-	-	-	1.70E+10
La Palma	LP1	1.50	-	7.65	0.68	7.66	-	362	5	9.22	0.09	-	-	-	-
La Palma	LP13	-	-	9.31	0.59	9.31	-	-	-	9.69	0.40	-	-	-	-
La Palma	A	-	-	9.63	0.06	9.68	0.06	-	-	-	-	-	-	-	-
La Palma	B	-	-	9.5	-	-	-	-	-	-	-	-	-	-	1.70E+10
La Palma	C	-	-	9.40	0.08	9.42	0.08	-	-	-	-	-	-	-	-
La Palma	D	-	-	9.82	0.09	9.86	0.09	-	-	-	-	-	-	-	-
La Palma	E	-	1.45E-05	9.95	0.12	9.96	0.12	-	-	-	-	-	-	-3.6	5.00E+09

146

Location	Sample														
La Palma	F	-	1.29E-05	9.43	0.12	9.45	0.12	-	-	-	-	-	-	-3.2	5.90E+09
La Palma	G	-	-	9.80	0.07	9.81	0.07	-	-	-	-	-	-	-	-
La Palma	I	-	1.02E-05	9.70	0.12	9.71	0.12	-	-	-	-	-	-	-3.7	7.30E+09
La Palma	QP60	-	-	9.61	-	9.72	-	-	-	-	-	-	-	-	-
La Palma	QP60	-	-	9.85	-	9.89	-	-	-	-	-	-	-	-3.8	-
La Palma	QP60	-	-	9.92	-	9.95	-	-	-	-	-	-	-	-3.4	-
La Palma	QP60	-	-	9.82	-	9.84	-	-	-	-	-	-	-	-3.7	-
La Palma	QP60	-	-	9.32	-	9.38	-	-	-	-	-	-	-	-3.6	-
La Palma	QP60	-	-	9.55	-	9.63	-	-	-	-	-	-	-	-3.5	-
La Palma	QP60	-	-	9.09	-	9.16	-	-	-	-	-	-	-	-3.7	-
La Palma	QP60	-	-	9.67	-	9.71	-	-	-	-	-	-	-	-3.5	-
La Palma	QP60	-	-	8.73	-	8.76	-	-	-	-	-	-	-	-3.4	-
La Palma	QP60	-	-	9.73	-	9.76	-	-	-	-	-	-	-	-3.5	-
La Palma	QP60	-	-	9.13	-	9.15	-	-	-	-	-	-	-	-3.5	-
La Palma	QP60	-	-	9.64	-	9.67	-	-	-	-	-	-	-	-3.6	-
La Palma	QP60	-	-	9.69	-	9.74	-	-	-	-	-	-	-	-3.6	-
La Palma	QP63	-	-	6.15	-	7.19	-	-	-	-	-	-	-	-8.3	-
La Palma	QP63	-	-	5.19	-	6.46	-	-	-	-	-	-	-	-8.1	-
La Palma	QP63	-	-	5.86	-	7.37	-	-	-	-	-	-	-	-8.1	-
La Palma	QP63	-	-	2.84	-	6.1	-	-	-	-	-	-	-	-7.8	-
La Palma	QP63	-	-	6.85	-	7.52	-	-	-	-	-	-	-	-7.1	-
La Palma	QP63	-	-	6.49	-	7.23	-	-	-	-	-	-	-	-8.3	-
La Palma	QP63	-	-	5.78	-	7.41	-	-	-	-	-	-	-	-8.2	-
La Palma	QP63	-	-	6.46	-	7.94	-	-	-	-	-	-	-	-8.3	-
La Palma	QP63	-	-	5.74	-	6.98	-	-	-	-	-	-	-	-8.5	-
La Palma	QP63	-	-	5.77	-	8.23	-	-	-	-	-	-	-	-8.4	-
La Palma	QP63	-	-	5.56	-	6.35	-	-	-	-	-	-	-	-8.1	-
La Palma	QP63	-	-	5.26	-	6.91	-	-	-	-	-	-	-	-7.3	-
La Palma	QP63	-	-	5.75	-	6.5	-	-	-	-	-	-	-	-7.6	-
La Palma	QP63	-	-	5.9	-	7	-	-	-	-	-	-	-	-9.2	-
La Palma	QP63	-	-	3.47	-	6.89	-	-	-	-	-	-	-	-10.3	-
La Palma	CAN-11	-	3.96E-05	9.27		9.27	0.11			9.993	0.04	0.029	0.0015	-3.8	1.96E+09
La Palma	CAN-13	-	1.55E-05	8.78		8.79	0.1			9.861	0.039	0.0291	0.0015	-4.4	5.30E+09
La Gomera	LG59	0.80	-	8.21	0.9	8.22	-	379	6	9.74	0.44	-	-	-	-
Tenerife	TF7	0.23	-	6.64	1.63	6.66	-	382	10	9.01	0.29	-	-	-	-
Tenerife	TF23	0.58	-	6.85	1.28	6.86	-	414	12	10.32	0.54	-	-	-	-

Location	Sample														
Tenerife	ALM	-	-	6.94	-	6.95	0.001	-	-	-	-	-	-	-8.5	-
Tenerife	BVA	-	-	6.61	-	7.06	0.048	-	-	-	-	-	-	-7.9	-
Tenerife	SFN	-	-	5.294	0.07	6.19	0.108	-	-	-	-	-	-	-9.7	-
Tenerife	FVE	-	-	6.275	0.057	6.58	0.033	-	-	-	-	-	-	-2.6	-
Tenerife	FVE#	-	-	6.95	-	6.97	0.002	-	-	-	-	-	-	-	-
Tenerife	LQO	-	-	4.81	-	7.74	0.589	-	-	-	-	-	-	-	-
Tenerife	SIO	-	-	5.18	-	6.57	0.185	-	-	-	-	-	-	-	-
Tenerife	1	-	-	7.21	-	7.23	-	-	-	-	-	-	-	-	-
Tenerife	2	-	-	6.96	-	7.04	-	-	-	-	-	-	-	-	-
Tenerife	3	-	-	6.61	-	7.14	-	-	-	-	-	-	-	-	-
Tenerife	4	-	-	5.18	-	6.88	-	-	-	-	-	-	-	-	-
Tenerife	5	-	-	6.94	-	6.96	-	-	-	-	-	-	-	-	-
Tenerife	7	-	-	3.19	-	7.02	-	-	-	-	-	-	-	-	-
Tenerife	9	-	-	6.95	-	6.97	-	-	-	-	-	-	-	-	-
Tenerife	CAN-9	-	3.05E-05	6.2		6.21	0.11	-	-	9.93	0.04	0.0293	0.002	-4.3	3.80E+09
Tenerife	CAN-10	-	1.55E-05	6.63		6.63	0.08	-	-	9.99	0.04	0.0293	0.002	-4.1	7.01E+09
Tenerife	CAN-12	-	1.83E-05	5.89		6.09	0.08	-	-	10.01	0.04	0.029	0.0014	-3.3	6.69E+09
Tenerife	CAN-13	-	1.56E-05	6.04		6.14	0.08	-	-	9.613	0.038	0.0284	0.0014	-3.7	7.62E+09
Tenerife	15/06/1991	-	-	7.23	-	7.25	-	-	-	-	-	-	-	-2.7	-
Tenerife	27/12/1993	-	-	7	-	7.10	-	-	-	-	-	-	-	-2.7	-
Tenerife	08/01/1994	-	-	7.03	-	7.05	-	-	-	-	-	-	-	-3	-
Tenerife	20/03/1994	-	-	7.16	-	7.18	-	-	-	-	-	-	-	-2.6	-
Tenerife	07/05/1994	-	-	7.13	-	7.18	-	-	-	-	-	-	-	-2.9	-
Tenerife	23/06/1994	-	-	7.04	-	7.12	-	-	-	-	-	-	-	-2.3	-
Tenerife	13/09/1994	-	-	7.41	-	7.46	-	-	-	-	-	-	-	-3.8	-
Tenerife	13/01/1996	-	-	6.97	-	7.02	-	-	-	-	-	-	-	-3.7	-
Tenerife	24/04/1999	-	-	7.02	-	7.10	-	304	-	-	-	-	-	-3.8	-
Tenerife	03/03/2000	-	-	6.91	-	6.94	-	318	-	-	-	-	-	-4.1	-
Tenerife	26/06/2000	-	-	6.97	-	6.99	-	333	-	-	-	-	-	-4	-
Tenerife	24/04/2001	-	-	6.94	-	6.96	-	321	-	-	-	-	-	-3.6	-
Tenerife	07/06/2001	-	-	6.88	-	6.93	-	309	-	-	-	-	-	-3.8	-
Tenerife	14/12/2001	-	-	7.02	-	7.16	-	-	-	-	-	-	-	-3.8	-
Tenerife	03/10/2002	-	-	7.13	-	7.17	-	-	-	-	-	-	-	-4.2	-
Tenerife	01/12/2003	-	3.02E-05	7.04	-	-	-	-	-	-	-	-	-	-3.2	3.38E+09
Tenerife	01/07/2004	-	2.52E-05	6.87	-	-	-	-	-	-	-	-	-	-	4.15E+09
Tenerife	25/01/2005	-	3.06E-05	7.2	-	7.23	-	-	-	-	-	-	-	-	3.27E+09

Tenerife	28/09/2006	-	1.35E-05	6.84	-	6.86	-	316	-	-	-	-	-	-	7.81E+09
Tenerife	29/01/2008	-	1.23E-05	7.27	-	7.30	-	311	-	-	-	-	-	-	8.07E+09
Tenerife	16/04/2008	-	3.53E-05	7.23	-	7.34	-	302	-	-	-	-	-	-	2.82E+09
Tenerife	29/05/2008	-	3.23E-05	7.24	-	7.30	-	302	-	-	-	-	-	-	3.08E+09
Tenerife	20/08/2008	-	2.74E-05	6.85	-	6.89	-	305	-	-	-	-	-	-	3.84E+09
Tenerife	13/11/2008	-	2.67E-05	7.51	-	7.54	-	322	-	-	-	-	-	-	3.59E+09
Tenerife	16/04/2009	-	2.76E-05	6.78	-	6.85	-	307	-	-	-	-	-	-	3.85E+09
Tenerife	05/06/2009	-	3.61E-05	7.07	-	7.12	-	312	-	-	-	-	-	-	2.82E+09
Tenerife	10/07/2009	-	2.69E-05	7.08	-	7.17	-	305	-	-	-	-	-	-	3.78E+09
Tenerife	07/10/2009	-	2.96E-05	7.2	-	7.27	-	307	-	-	-	-	-	-	3.38E+09
Tenerife	13/01/2010	-	2.45E-05	7.3	-	7.43	-	303	-	-	-	-	-	-	4.03E+09
El Hierro	-	-	-	6.7	0.15	7.25	0.18	-	-	-	-	-	-	-	-
El Hierro	-	-	-	6.38	0.098	7.78	0.28	-	-	-	-	-	-	-	-
El Hierro	-	-	-	7.906	0.085	8.199	0.099	-	-	-	-	-	-	-	-
El Hierro	-	-	-	7.53	0.11	8.03	0.14	-	-	-	-	-	-	-	-
El Hierro	-	-	-	7.878	0.074	8.197	0.09	-	-	-	-	-	-	-	-
El Hierro	JMDDEH01			7.98	0.62	-	-	-	-	-	-	-	-	-	-
El Hierro	JMDDEH01	-	-	7.8	0.1	-	-	-	-	-	-	-	-	-	-
El Hierro	JMDDEH01	-	-	8.1	0.46	-	-	-	-	-	-	-	-	-	-
El Hierro	JMDDEH01	-	-	8.01	0.14	-	-	-	-	-	-	-	-	-	-
El Hierro	JMDDEH03	-	-	8.19	0.17	-	-	-	-	-	-	-	-	-	-
El Hierro	JMDDEH04cii	-	-	7.53	0.26	-	-	-	-	-	-	-	-	-	-
El Hierro	JMDDEH04ciii	-	-	7.67	0.29	-	-	-	-	-	-	-	-	-	-
El Hierro	JMDDEH07	-	-	7.58	0.31	-	-	-	-	-	-	-	-	-	-
El Hierro	JMDDEH10	-	-	7.52	0.45	-	-	-	-	-	-	-	-	-	-
El Hierro	JMDDEH11	-	-	7.85	0.34	-	-	-	-	-	-	-	-	-	-
El Hierro	JMDDEH13	-	-	7.66	0.25	-	-	-	-	-	-	-	-	-	-
El Hierro	JMDDEH13	-	-	8.17	0.31	-	-	-	-	-	-	-	-	-	-
El Hierro	JMDDEH14	-	-	7.23	0.25	-	-	-	-	-	-	-	-	-	-
El Hierro	JMDDEH15	-	-	7.81	0.29	-	-	-	-	-	-	-	-	-	-
El Hierro	JMDDEH15	-	-	7	0.23	-	-	-	-	-	-	-	-	-	-
El Hierro	JMDDEH16	-	-	7.8	0.23	-	-	-	-	-	-	-	-	-	-
El Hierro	JMDDEH16	-	-	7.8	0.26	-	-	-	-	-	-	-	-	-	-
El Hierro	JMDDEH17	-	-	7.53	0.23	-	-	-	-	-	-	-	-	-	-
El Hierro	JMDDEH18	-	-	7.62	0.28	-	-	-	-	-	-	-	-	-	-
El Hierro	JMDDEH18	-	-	7.14	0.24	-	-	-	-	-	-	-	-	-	-

El Hierro	1.1	0.14	4.78E-05	7.20	-	7.21	0.16	4141.0	0.0	10.11	0.07	0.0304	0.00106	n.a	2.09E+09
El Hierro	1.15	0.67	4.26E-05	7.44	-	7.45	0.15	2620.4	0.0	9.99	0.04	0.0296	0.00081	0.96	2.26E+09
El Hierro	1.15	0.14	3.37E-06	6.98	-	7.01	0.21	1210.0	11.8	9.94	0.06	0.0297	0.00120	-1.23	3.04E+10
El Hierro	1.15	0.32	1.07E-05	7.33	-	7.34	0.21	805.0	6.4	9.84	0.11	0.0286	0.00121	n.a	9.19E+09
El Hierro	1.2	0.86	6.42E-04	7.99	-	7.99	0.15	1103.1	0.0	10.12	0.05	0.0312	0.00095	n.a	1.40E+08
El Hierro	1.2	0.21	3.21E-05	7.72	-	7.73	0.18	4516.6	76.2	10.40	0.13	0.0325	0.00230	-1.43	2.90E+09
El Hierro	1.2	0.07	1.01E-05	7.59	-	7.59	0.20	3979.1	39.8	10.43	0.24	0.0323	0.00245	n.a	9.38E+09
El Hierro	1.22	0.73	1.44E-03	7.16	-	7.16	0.17	1465.4	0.0	10.49	0.24	0.0330	0.00390	n.a	6.96E+07
El Hierro	1.22	1.17	5.89E-05	7.11	-	7.11	0.16	1044.6	12.7	9.98	0.09	0.0296	0.00143	n.a	1.72E+09
El Hierro	1.23	0.05	5.69E-05	7.46	-	7.47	0.15	5187.2	0.0	10.09	0.04	0.0304	0.00081	-0.19	1.69E+09
El Hierro	1.23	0.05	4.14E-06	7.52	-	7.55	0.19	3137.1	37.6	10.01	0.07	0.0304	0.00136	-2.38	2.30E+10
El Hierro	1.3	0.78	6.20E-04	7.58	-	7.59	0.15	1043.7	0.0	10.05	0.07	0.0303	0.00118	n.a	1.53E+08
El Hierro	1.3	0.30	1.05E-05	7.62	-	7.63	0.17	1975.5	12.8	10.04	0.06	0.0297	0.00109	-1.94	8.98E+09
El Hierro	1.3	0.44	9.78E-06	7.65	-	7.66	0.16	1780.7	10.5	10.18	0.09	0.0321	0.00161	-1.94	9.60E+09